

University of Southampton Research Repository ePrints Soton

Copyright © and Moral Rights for this thesis are retained by the author and/or other copyright owners. A copy can be downloaded for personal non-commercial research or study, without prior permission or charge. This thesis cannot be reproduced or quoted extensively from without first obtaining permission in writing from the copyright holder/s. The content must not be changed in any way or sold commercially in any format or medium without the formal permission of the copyright holders.

When referring to this work, full bibliographic details including the author, title, awarding institution and date of the thesis must be given e.g.

AUTHOR (year of submission) "Full thesis title", University of Southampton, name of the University School or Department, PhD Thesis, pagination

UNIVERSITY OF SOUTHAMPTON

Faculty of Natural and Environmental Science

School of Chemistry

High Throughput Synthesis and Corrosion Studies on Alloys

by

Talal Awad M Aljohani

Thesis for the degree of Doctor of Philosophy

June 2013

UNIVERSITY OF SOUTHAMPTON

ABSTRACT

FACULTY OF NATURAL AND ENVIRONMENTAL SCIENCE

Doctor of philosophy

HIGH THROUGHPUT SYNTHESIS AND CORROSION STUDIES ON ALLOYS

Talal Awad M Aljohani

A range of Ni-Cr, Ni-W, Al-Mg, and Al-Mg-Zr thin film alloys have been synthesised using a controllable compositional gradient method based on MBE sources allowing the deposition of compositional gradients of a large range of thin film materials. The alloy materials are characterised by X-ray diffraction, including phase identification and crystallite size, and energy dispersive x-ray spectroscopy (EDX). The corrosion resistance of 100 discrete alloy compositions has been measured simultaneously in identical environments using a high-throughput screening protocol based on cyclic voltammetry (CV). The corrosion resistances and potentials are extracted from voltametric data by both the Linear Polarisation Resistance (LPR) and Tafel Extrapolation methods. Results from these are shown to be consistent. In general, the corrosion (polarisation) resistance behaviour is shown to be directly related to the bulk alloy structures or morphologies.

In the case of the NiCr alloys, besides the b.c.c α -Cr (Im3m) phase and its Ni solid solutions, which exhibit the highest polarisation resistances, the σ Cr_3Ni_2 (P42/mnm) phase exhibits the next best polarisation resistance.

The incorporation of W in the Ni-W solid solution at low W compositions resulted in a small reduction in corrosion resistance while a significant increase in the corrosion resistance was observed for alloy compositions greater than 24 %_{at.} W.

The best corrosion resistance of Al-Mg alloys was observed for alloy compositions comprise 35%_{at.} Al, which corresponds to the formation of γ $\text{Al}_{12}\text{Mg}_{17}$ (i.e. also named β phase). The incorporation of Zr in the Al-Mg resulted in forming five Al-Zr metastable phases i.e. Al_3Zr , Al_2Zr , Al_3Zr_2 , Al_4Zr_5 , and Al_3Zr_5 . The Al-Mg-Zr alloys composition contained Al_3Zr_2 and Al_3Zr_5 exhibit highest cathodic activity, corrosion resistance, and passivity.

Contents

ABSTRACT	iii
Contents.....	iv
List of tables.....	viii
List of figures.....	ix
DECLARATION OF AUTHORSHIP	xix
Acknowledgements	xxi
Definitions and Abbreviations	xxii
Symbols	xxiii
1. Introduction	1
1.1 Definition of Corrosion	1
1.2 Types of Corrosion	1
1.2.1 Uniform Corrosion.....	1
1.2.2 Galvanic Corrosion	2
1.2.3 Crevice Corrosion	3
1.2.4 Pitting Corrosion	3
1.2.5 Environmentally Induced Cracking	4
1.2.6 Hydrogen Damage.....	5
1.2.7 Intergranular Corrosion	5
1.2.8 Dealloying	6
1.2.9 Erosion Corrosion and Fretting Corrosion	7
1.3 Potential vs. pH (Pourbaix) Diagrams.....	7
1.4 Corrosion Rate Measurement	8
1.4.1 Weight Loss	8
1.4.2 Electrical Resistance Probes	8
1.4.3 Electrochemical Polarisation Methods	9
1.4.3.1 Tafel Method.....	9
1.4.3.2 Polarisation Resistance (PR)	11
1.5 Motivation	13
1.5.1 Combinatorial or High-Throughput Method History	13
1.6 Literature Review of Metal Alloys.....	15
1.6.1 NiCr Alloys	15
1.6.2 Ni-W Alloys	19
1.6.3 Al-Mg Alloys	22

1.6.3.1	The corrosion Properties of Al-Mg and Mg-Al Alloys	23
1.6.3.2	The Corrosion Mechanism of Mg and Mg Alloys	26
1.6.3.2.1	Partially protective films	28
1.6.3.2.2	Monovalent magnesium ion:.....	29
1.6.3.2.3	Undermining and falling particles:.....	29
1.6.3.2.4	Forming magnesium hydride (MgH ₂):.....	29
1.6.3.3	The structure of Al-Mg and Mg-Al alloys	30
1.6.4	Al-Mg-Zr Alloys	32
1.6.4.1	The Corrosion Properties of Al-Mg-Zr Alloys	32
1.6.4.2	The Structure of Al-Mg-Zr Alloys.....	33
2.	Experimental	35
2.1	High-Throughput Physical Vapour Deposition (HT-PVD) system.....	35
2.2	The combinatorial or High-Throughput Methodology.....	37
2.3	Preparation of Thin Film Alloys and Substrate Types	40
2.4	Bulk “Commercial” Samples	42
2.5	Characterisation Instruments	42
2.5.1	X-ray Diffraction (XRD).....	42
2.5.2	Energy Dispersive X-ray Spectroscopy (EDS).....	44
2.5.3	Atomic Force Microscope (AFM).....	44
2.5.4	Potentiostat.....	44
2.5.5	Electrochemical Cell	45
2.5.6	Reference and Counter Electrodes	46
2.6	Corrosion Electrolyte	46
2.7	Corrosion (Polarisation) Resistance (R _p) Determining Methods.....	48
2.7.1	Corrosion Resistance (R _p) Determining by Tafel extrapolation Method 48	
2.7.2	Corrosion Resistance (R _p) Determined by Linear Polarisation Resistance (LPR) Method.....	50
3.	Ni-Cr Thin Film Alloys.....	51
3.1	Introduction	51
3.2	Structure Characterization of As-deposited Ni-Cr Film Alloys.....	51
3.3	Electrochemical Measurements of Ni-Cr Thin Film in Phosphoric Acid pH 3 at 293K.....	56
3.3.1	Cyclic Voltammetry	56
3.3.2	Corrosion Resistance.....	62
3.3.2.1	Linear Polarization Resistance (LPR).....	62

3.3.2.2	Polarization (Corrosion) Resistance Obtained by Tafel and LPR	66
3.3.3	Zero Current Potential ($E_{i=0}$)	68
3.4	Electrochemical Measurements of Ni-Cr Thin Film Alloys in Sodium Chloride [50 mM] at 293 K.	71
3.4.1	Cyclic Voltammetry	71
3.4.2	Zero Current (Corrosion) Potential	73
3.4.3	Corrosion (Polarisation) Resistance	74
3.4.3.1	Polarization Resistance Obtained by LPR	74
3.4.3.2	Polarization Resistance Obtained by LPR and Tafel Extrapolation	76
3.5	Electrochemical Measurements of Bulk “Commercial” Samples in Sodium Chloride [50 mM] at 293 K.	77
3.5.1	Cyclic Voltammetry	77
3.5.2	Corrosion Resistance of Nickel, Chromium and Ni-Cr Bulk Alloys	79
3.6	Comparison between Bulk and As-deposited NiCr Alloys Studied in Sodium Chloride.	80
3.7	Conclusion	83
4.	Ni-W Thin Film System	85
4.1	Introduction	85
4.2	Structure Characterisation of As-deposited Ni-W Film Alloys	85
4.3	Electrochemical Measurements of As-deposited a 10x10 Ni-W Array in Phosphoric Acid Solution [pH 3] at 293 K.	89
4.3.1	Cyclic Voltammetry	89
4.3.2	Corrosion (zero current) potential	93
4.3.3	Corrosion Resistance	94
4.4	Conclusion	97
5.	Binary Al-Mg Alloys	99
5.1	Introduction	99
5.2	X-ray diffraction of Binary Al-Mg Alloy	99
5.3	Corrosion Resistance (Polarisation) of the Al-Mg Alloys	105
5.4	Conclusion	117
6.	Ternary Al-Mg-Zr Alloys	119
6.1	Introduction	119
6.1.1	X-ray Diffraction of Al-Mg-Zr Alloys	120
6.2	Electrochemical Screening of Al-Mg-Zr Alloys	128
6.2.1	Electrochemical Screening of As-deposited Al-Mg-Zr Alloys	128
6.2.1.1	The Corrosion Resistance (R_p) Screening of As-deposited Al-Mg-Zr Alloys	128

6.2.2	Electrochemical Screening of Annealed Al-Mg-Zr Alloys	141
6.2.2.1	The Corrosion Resistance (R_p) of the Annealed Al-Mg-Zr Alloys 144	
6.3	Comparison between the As-deposited and Annealed Al-Mg-Zr Alloys 146	
6.4	Conclusion	149
7.	General Conclusion	151
7.1	Future Work.....	152
7.1.1	Open Circuit Potential (E_{opc}).....	152
7.1.2	The Potential Scan Rate	153
	Appendices	155
	Appendix 1	155
	Appendix 2	159
	Bibliography	163

List of tables

Table 1.1 The identified phases in the Ni-Cr phase diagram and their compositional range at the temperature of 500 to 1900 °C. Adapted from [81].	17
Table 1.2: The identified Phases in Ni-W phase diagram versus tungsten composition.....	21
Table 1.3: Chemical composition of some Al-Mg-Zn alloys i.e. AZ21, AZ31, AZ501, AZ81 and AZ91 alloys.....	23
Table 1.4: Structural details of intermetallic and solid solutions of Zr-Al system.....	34
Table 2.1: Deposition conditions, substrates, aperture value, and film material types.....	41
Table 2.2: Materials and chemicals specification and suppliers name	47
Table 3.1: XRD data and identified phases for selected Ni-Cr alloys.....	55
Table 3.2: The corrosion and breakdown potentials, and polarization resistance of Ni, Cr, and Ni-Cr alloys.	80
Table 5.1: The EDX analysis before and after the electrochemical screening of the Al-Mg alloys deposited on gold substrate.	115
Table 6.1: Summary of the x-ray diffraction results of Al-Mg-Zr alloys.	121

List of figures

Figure 1.1: A grain boundary of sensitised stainless steel, type 304. Adapted from Fontana, M. G. (1978); Corrosion Engineering. New York, McGraw-Hill [3].	6
Figure 1.2 NiCr phase diagram at equilibrium, adapted from [81].	17
Figure 1.3: Theoretically predicted free energy versus Ni/Cr composition [91]	18
Figure 1.4: Binary Ni-W alloy phase diagram, adapted from [104].	21
Figure 1.5: Electrochemical behaviour of magnesium at potentials higher than E_{corr} . The solid and dashed line are the expected and obtained behaviour respectively. Adapted from [128].	28
Figure 2.1: Schematic of high-throughput physical vapour deposition (HT-PVD) system.	36
Figure 2.2: (A) Growth chamber of high throughput PVD in which parallel co-deposition of binary alloys was prepared, (B) Top view of high throughput PVD chamber. Sources were arranged in 120° geometry.	36
Figure 2.3: (A) Gradients growth methodology from single off-axis source [170], (B) gradients growth when aperture situated at B1.	38
Figure 2.4: The composition of calibrated NiCr array as (A) map (B) wedge “ramp” shape.	39
Figure 2.5: (A) Silicon/silicon nitride substrate used for XRD study. (B) Silicon micro-fabricated array used for electrochemical screening [170].	40
Figure 2.6: Diffraction caused by crystallised planes.	43
Figure 2.7: D8 diffractometer measurement diagram.	43

Figure 2.8: Electrochemical cell used in a parallel high-throughput electrochemical screening, adapted from[41].	45
Figure 2.9: Example of how corrosion current (i_{corr}) is extrapolated from Tafel plot. This plot is for Ni ₆₇ W ₃₃ alloy.	49
Figure 2.10: Example of linear polarisation resistance (LPR) behaviour, from which corrosion resistance has been obtained. This data is shown for Ni ₆₇ W ₃₃ alloy. The scan rate is 20 mV s ⁻¹ .	50
Figure 3.1: X-ray diffraction patterns of as-deposited Ni-Cr on a 10x10 array (#6648) silicon nitride substrate at 323 K. Chromium composition is measured and enclosed in each square. Composition is divided to Four zones namely green (4-22 % _{at.} Cr), orange (28-45 % _{at.} Cr), grey (~ 47-70 % _{at.} Cr), and gold (74-90 % _{at.} Cr). The scale are (X = 35-70 and Y = 0-300).	52
Figure 3.2: X-ray diffraction patterns of a series of as-deposited Ni-Cr thin film alloys of composition range of 4-89 % _{at.} Cr. The films are deposited on a silicon nitride substrate at ~ 300 K. Four regions are identified, namely Cr solid solution in γ -Ni (111), a preferred orientation of the γ -Ni (111) phase, two σ phases (Cr ₃ Ni ₂ and Cr ₇ Ni ₃), and Ni solid solution in α -Cr). Compositions in % _{at.} are determined by EDS.	54
Figure 3.3: The first anodic sweep of the cyclic voltammograms of 100 Ni-Cr alloys (#7149) deposited at room temperature. The electrolyte is phosphoric acid (pH 3) solution purged with Ar for 20 min at room temperature. The scan rate was 20 mV s ⁻¹ . Compositions were determined by EDS.	56
Figure 3.4: Selected cyclic voltammograms of NiCr alloys (#7149) in the composition orange 31-78 % _{at.} measured in phosphoric acid (pH3) solution purged for 20 min with Ar to remove oxygen at room temperature. The scan rates was 20 mV s ⁻¹ . Note that the y scale (current density) varies between plots.	58
Figure 3.5: The first anodic sweep of the cyclic voltammograms of 100 NiCr alloys (#7150) deposited at room temperature. The electrolyte is	

phosphoric acid (pH 3) solution purged with Ar for 20 min at room temperature. The scan rates were 20 mV s ⁻¹	59
Figure 3.6: Selected cyclic voltammograms from a 10x10 as-deposited Ni-Cr array (B). Note that y scale (current density) varies between plots.....	60
Figure 3.7: Selected cyclic voltammograms from a 10x10 as-deposited Ni-Cr array (#6763) in the composition range of 31-78 % _{at.} Cr. The solution is phosphoric acid [pH 3] purged for 2 min in the presence of the sample before applying the CV. Note that y scale (current density) varies between plots. The scan rates was 20 mV s ⁻¹	61
Figure 3.8: The Polarization Resistances (R _p) determined by the LPR method of as-deposited nickel, chromium and NiCr alloys of composition of 28-83 % _{at.} Cr. The electrolyte was de-aerated phosphoric acid (pH 3) at room temperature. The R _p was extracted after performing cyclic voltammetry in the potential range -600 to +100 vs. SCE/mV at scan rates of 20 mV s ⁻¹ . The compositions were determined by EDS.	63
Figure 3.9: The Polarization Resistances (R _p) determined by the LPR method of as-deposited nickel, chromium and NiCr alloys of composition of 42-87 % _{at.} Cr. The electrolyte was de-aerated phosphoric acid (pH 3) at room temperature.....	64
Figure 3.10: The Polarization Resistances (R _p) determined by the LPR method of as-deposited nickel, NiCr alloys of composition of 2-90 % _{at.} Cr. The corrosion electrolyte was de-aerated phosphoric acid (pH 3) at room temperature.....	66
Figure 3.11: The polarization Resistance(s) (R _p) obtained by the LPR method (■), and from the Tafel method assuming the limits of B = 26 mV (▼) and B = 13 mV (▲) for Ni, Cr and NiCr alloys of compositions in the range of 31-83 % _{at.} Cr for (A and B), and 2-90 % _{at.} Cr array (C). Note that y scale (polarisation resistance) in array (C) differs from arrays (A and B).	67

- Figure 3.12:** The zero current potential ($E_{i=0}$) of as-deposited Ni-Cr arrays examined in phosphoric acid pH 3 at 293 K. Chromium composition determined by EDS..... 69
- Figure 3.13:** Comparison between open circuit and zero current potential for Ni-Cr alloys of compositions in the range of 31-83 % Cr, array A (#7149). The open circuit potentials were obtained after 20 min. The electrolyte is phosphoric acid pH 3 at 293 K..... 70
- Figure 3.14:** Comparison between open circuit and zero current potential for Cr and Ni-Cr alloys of compositions in the range of 42-85 % Cr, array B (#7150). The open circuit potentials were obtained after 20 min. The electrolyte is phosphoric acid pH 3 at 293 K..... 70
- Figure 3.15:** The forward sweep of the cyclic voltammograms of 100 Ni-Cr alloys deposited at room temperature. The electrolyte is sodium chloride [50mM]. The solution was purged with Ar for 2 min at room temperature. The scan rate was 20 mV s⁻¹..... 71
- Figure 3.16:** Selected cyclic voltammograms from a 10x10 as-deposited Ni-Cr array in sodium chloride [50 mM]. The solution was purged for 2 min in the presence of the sample before applying the CV. The corrosion potential (E_{corr}) and breakdown potential (E_{bd}) are labelled..... 73
- Figure 3.17:** The zero current potential(s) extracted from voltametric data of single array of 100 fields studied in sodium chloride [50 mM] at 293 K. The corrosion electrolyte was purged with Ar for 2 min.74
- Figure 3.18:** The polarization resistance extracted from voltametric data by LPR method from a single array of 100 fields studied in sodium chloride [50 mM] at 293 K. Chromium compositions were determined by EDS. Solution purged with Ar for 2 min. 75
- Figure 3.19:** The polarization Resistance(s) (R_p) obtained by the LPR method (a), and from the Tafel extrapolation method assuming the $B = 26$ mV (b) for NiCr alloys of compositions in the range of 2-83 %_{at.} Cr. R_p was extracted after performing cyclic voltammetry in the potential range -1250 to +1000 vs. SCE/mV at a scan rate of 20

mV s⁻¹. The compositions were determined by EDS. The corrosion electrolyte is sodium chloride [50 mM] at 293 K. 76

- Figure 3.20:** Cyclic voltammograms of nickel, chromium, and three Ni-Cr bulk alloys examined in aerated sodium chloride [50 mM] at 293 K. Arrow indicates Ni dissolution. 77
- Figure 3.21:** Potentiodynamic curves of Ni, Cr, and Ni-Cr bulk alloys studied in aerated sodium chloride [50 mM] at 293 K. Arrows indicate the breakdown potential (E_{bd}). Compositions are in (%_{wt.}). 78
- Figure 3.22:** Polarization resistance of Ni, Cr, and Ni-Cr alloys examined in aerated sodium chloride solution [50 mM] at 293 K. The error bar reflects standard error (SE) obtained from linear regression. 79
- Figure 3.23:** zero current (corrosion) potentials of (a) as-deposited NiCr alloys in the composition range 2-89 %_{at.} Cr, (b) nickel, chromium, and NiCr bulk alloys at different compositions in atomic percentage (%_{at.}). 81
- Figure 3.24:** Polarisation resistance(s) extracted from cyclic voltammograms data by LRP approach (a) for as-deposited Ni-Cr alloys (b) for nickel, chromium, and NiCr bulk alloys. Both systems investigated in sodium chloride [50 mM] at 293 K. 83
- Figure 4.1:** X-ray diffraction patterns of a series of as-deposited NiW thin film alloys of composition range from 3-37 %_{at.} W. The films were deposited on a silicon nitride substrate at ~ 300 K. Three phases were identified, namely Ni (W) solid solution γ -Ni (111) and Ni (200), Ni₄W (211), and amorphous phase where no peaks can be seen for a composition $\geq 26\%$ _{at.} W. Compositions in %_{at.} were determined by EDS. 86
- Figure 4.2:** (A) The grain size of the NiW solid solution phase determined using the Scherrer equation from the half width of the <111> Bragg peak as a function of composition. (b) The peak position of the <111> Bragg peak of the NiW solid solution as a function of composition. Note that error will be higher close to zero nm. . 87

Figure 4.3: Cyclic voltammograms of a 10x10 Ni-W array studied in phosphoric acid pH 3 at 293 K. All the squares have same scale where x axis ranges from (- 900 to + 800 vs. SCE/ mV) and y varies by $\pm 6 \text{ mA cm}^{-2}$ around the zero current. The 20 mV s^{-1} was used as scan rate. Gold was used as substrate for the electrochemical array. Tungsten compositions were determined by EDS and are enclosed above. Electrode with a coordinate (4, 4) from bottom left is dead electrode due to bad connection... 90

Figure 4.4: Selected cyclic potentiodynamic curves for a composition from 6-33 %_{at.} W and pure Ni. Currents are normalised to geometric area. The electrolyte is phosphoric acid pH 3. Anodic activity decreases for the compositions $\geq 21 \text{ %}_{\text{at.}}$ W. The corrosion potential (E_{corr}) and breakdown potential (E_{bd}) are labelled..... 92

Figure 4.5: The corrosion potentials (E_{corr}) extracted from the potentiodynamic curves for a composition of 5-35 %at W and pure Ni. 94

Figure 4.6: Polarisation resistances determined by LPR of as-deposited 100 pads on Ni-W array of a compositions range of 5-35 %_{at.} W. All electrochemical measurements are performed in phosphoric acid pH 3 electrolyte at 293 K. The electrolyte was purged with Ar for 3 min in the presence of the array. The error bar was obtained from standard error..... 96

Figure 4.7: Selected polarisation resistances determined by LPR (■) compared to ones obtained by Tafel (▲, ▼) where B equals 13 and 26 mV respectively. The error bar was obtained from standard error.. 96

Figure 5.1:X-ray diffraction patterns of a series of as-deposited Mg-Al thin film alloys of composition range of 10-79 %_{at.} Al. The films were deposited on a silicon/ silicon nitride substrate at $\sim 300 \text{ K}$ (#7358). Three phases have been identified, namely solid solution of Al in Mg as hexagonal (002), $\gamma \text{ Al}_{12}\text{Mg}_{17}$ with structure of (330), and Mg solid solution in Al of f.c.c (111). The alloys composition in %_{at.} was determined by EDS. 101

Figure 5.2: The Al-Mg phase diagram (a) ref.[104] and (b) ref.[143]..... 101

- Figure 5.3:** The integrated areas under the peaks located at ca. $2\theta = 34.42^\circ$ correspond to (002) of hexagonal Mg (Al) solid solution and 34.72° corresponds intermetallic γ $\text{Al}_{12}\text{Mg}_{17}$ phase as function of Al compositions..... 102
- Figure 5.4:** The X-ray diffraction pattern of the $\text{Al}_{16}\text{Mg}_{84}$ alloy. Two phases have been identified namely solid solution of Al in Mg as (002) and γ $\text{Al}_{12}\text{Mg}_{17}$ with structure of (330). 103
- Figure 5.5:** The integrated area under the peak located at $2\theta = 38.36^\circ$ which corresponds to the (111) of Al f.c.c. as function of Al compositions..... 104
- Figure 5.6 :** The corrosion resistances of Al-Mg alloys (#7355) versus Al compositions (A) determined by LPR and (B) extracted from Tafel extrapolation, where $B = 26$ mV. The corrosion electrolyte is [0.005 M] of sodium chloride. The pH and temperature were kept at 9 and 293 K respectively. 106
- Figure 5.7 :** The corrosion resistances of Al-Mg (#7355) alloys versus Mg compositions (A) determined by LPR and (B) extracted from Tafel extrapolation where $B = 26$ mV. The corrosion electrolyte is [0.005 M] of sodium chloride. The pH and temperature were kept at 9 and 293 K. 107
- Figure 5.8:** The corrosion potentials of the Al-Mg alloys (#7355) for the composition range of 5–79 %_{at.} Al and 25–95 %_{at.} Mg. The saturated calomel electrode (SCE) was used as reference electrode. The corrosion electrolyte is [0.005 M] of sodium chloride. 108
- Figure 5.9:** The potentiodynamic curves of series Al-Mg alloys for a composition range of 5–77 %_{at.} Al. The corrosion electrolyte is sodium chloride [0.005 M] where the SCE is used as reference electrode. Compositions were determined by EDS. 111
- Figure 5.10:** Scanning electron microscope (SEM) images of selected Al-Mg alloys after electrochemical screening (a) $\text{Al}_5\text{Mg}_{95}$ (b) $\text{Al}_{24}\text{Mg}_{76}$ (c) $\text{Al}_{32}\text{Mg}_{68}$ (d) $\text{Al}_{48}\text{Mg}_{52}$ (e) $\text{Al}_{52}\text{Mg}_{48}$ (f) $\text{Al}_{77}\text{Mg}_{23}$. The substrate is gold.113

- Figure 5.11:** A plot of $\log R_p$ vs. $\log (i_{corr})$ for a series of Al-Mg alloys: The slope and B derived from (Equation 5-2) are -1.04 and 26 mV respectively. The electrolyte is sodium chloride [0.005 M] at 293 K..... 116
- Figure 6.1:** X-ray diffraction patterns of as-deposited Al-Mg-Zr alloys (#7541). Silicon nitride was used as the substrate. The detected phases are designated and included (at the right). Compositions, in atomic %, were determined by EDX..... 123
- Figure 6.2:** X-ray diffraction patterns of annealed Al-Mg-Zr alloys (#7544). Silicon nitride was used as the substrate. The detected phases are designated and included (at the right). Compositions, in atomic %, were determined by EDX. Array annealed at 423 K for 30 min. 125
- Figure 6.3:** X-ray diffraction of selected Al-Mg-Zr alloys as-annealed (A, B, C, D) and as-deposited (E, F, G, H). Silicon nitride was used as the substrate. The annealed alloys were heated linearly at 423 K for 30 minutes in a vacuum. 126
- Figure 6.4:** Summary of the phases identified in the binary Al-Mg and ternary Al-Mg-Zr systems. 127
- Figure 6.5:** The composition maps of the components of Al-Mg-Zr alloys (#7537) across the 10x10 array. The compositions were determined by EDX. Gold pads on silicon/silicon nitride chip were used as the substrate. The film thicknesses are 100–150 nm..... 128
- Figure 6.6:** The corrosion resistance values as a function of the constituents of Al-Mg-Zr alloys (#7537). The data were determined using the LPR method. De-aerated sodium chloride [0.1 M] was used as the corrosion electrolyte. Measurements were obtained at 293 K. The XRD results are included..... 130
- Figure 6.7:** The corrosion resistance values as a function of the constituents of Al-Mg-Zr alloys (#7537). The data were determined using the Tafel extrapolation method assuming $B = 24$ mV. De-aerated

sodium chloride [0.1 M] was used as the corrosion electrolyte. Measurements were obtained at 293 K. 131

Figure 6.8: Topography of as-deposited Al-Mg-Zr alloys obtained by AFM where (a) $\text{Al}_{80}\text{Mg}_1\text{Zr}_{19}$ (b) $\text{Al}_{65}\text{Mg}_9\text{Zr}_{26}$ (c) $\text{Al}_{44}\text{Mg}_{16}\text{Zr}_{40}$ (d) $\text{Al}_{42}\text{Mg}_{23}\text{Zr}_{35}$ (e) $\text{Al}_{23}\text{Mg}_{32}\text{Zr}_{45}$ and (f) $\text{Al}_{31}\text{Mg}_{15}\text{Zr}_{54}$. Silicon nitride was used as the substrate. The roughness factor unit is nm. 133

Figure 6.9: The corrosion resistance values as a function of the constituents of Al-Mg-Zr alloys (#7534) where (A, B, C) are determined using the LPR method and (D, E, F) are determined using the Tafel method assuming $B = 24$ mV. The corrosion electrolyte solution was de-aerated sodium chloride [0.02 M]. Measurements were obtained at 293K..... 134

Figure 6.10: The composition maps of the components of Al-Mg-Zr alloys (#7534) across the 10x10 array. The compositions were determined by EDX and silicon nitride was used as the substrate. Black arrows show the selected compositions. 135

Figure 6.11: The selected corrosion resistances as a function of the components of Al-Mg-Zr alloys (#7534) where (A, B, C) are determined using the LPR method and (D, E, F) are determined using the Tafel method. The corrosion electrolyte solution was de-aerated sodium chloride [0.02 M]. Measurements were obtained at 293 K..... 136

Figure 6.12: Potentiodynamic curves of as-deposited Al-Mg-Zr alloys (#7537) studied in sodium chloride solution [0.1 M]. The scan rate was 20 mVs^{-1} . The solution was purged with N_2 for five minutes. The pH and temperature were adjusted at 6.35 and 293 K. Alloys composition was determined by EDX. 137

Figure 6.13: Corrosion potentials of the selected Al-Mg-Zr alloys (#7537) versus (A) Mg, (B) Al, and (C) Zr compositions. 138

Figure 6.14: The corrosion potentials (E_{corr}) extracted from the potentiodynamic curves of Al-Mg-Zr alloys (#7537). The electrolyte is sodium

chloride solution [0.1 M]. Alloys composition was determined by EDX. The XRD results are included. 140

Figure 6.15: Potentiodynamic curves of annealed Al-Mg-Zr alloys investigated in de-aerated sodium chloride solution [0.05 M]. The scan rate was 20 mVs^{-1} . The pH and temperature were adjusted at 6.35 and 293 K. Alloy composition was determined by EDX. 141

Figure 6.16: Corrosion potentials of the selected Al-Mg-Zr alloys versus (A) Mg, (B) Al, and (C) Zr compositions 142

Figure 6.17: A plot of $\log R_p$ vs. $\log (i_{\text{corr}})$ for a series of Al-Mg-Zr alloys: The slope and B derived from (Equation 6-1) are -0.922 and 24 mV respectively. The electrolyte is sodium chloride [0.1 M] at room temperature. 143

Figure 6.18: The corrosion resistance values obtained by LPR as a function of the components of Al-Mg-Zr alloys. De-aerated sodium chloride solution [0.05 M] was used as corrosion electrolyte. The pH and temperature were kept at 6.30 and 293 K. The XRD results are included..... 145

Figure 6.19: Topography of (a) as-deposited and (b) annealed $\text{Al}_{80}\text{Mg}_1\text{Zr}_{19}$ alloy. Silicon nitride was used as the substrate. 147

Figure 6.20: Potentiodynamic curves of selected as-deposited and annealed Al-Mg-Zr alloys investigated in de-aerated sodium chloride solution [0.05M]. The scan rate was 20 mVs^{-1} . The pH and temperature were adjusted at 6.35 and 293K. Alloys composition was determined by EDX..... 148

DECLARATION OF AUTHORSHIP

I, Talal Awad M Aljohani, declare that the thesis entitled

High Throughput Synthesis and Corrosion Studies on Alloys

and the work presented in the thesis are both my own, and have been generated by me as the result of my own original research. I confirm that:

- this work was done wholly or mainly while in candidature for a research degree at this University;
- where any part of this thesis has previously been submitted for a degree or any other qualification at this University or any other institution, this has been clearly stated;
- where I have consulted the published work of others, this is always clearly attributed;
- where I have quoted from the work of others, the source is always given. With the exception of such quotations, this thesis is entirely my own work;
- I have acknowledged all main sources of help;
- where the thesis is based on work done by myself jointly with others, I have made clear exactly what was done by others and what I have contributed myself;
- Parts of this work have been published as:
 - (1) T.A. Aljohani, B.E. Hayden, A. Anastasopoulos, The high throughput electrochemical screening of the corrosion resistance of Ni-Cr thin film alloys, *Electrochimica Acta*, 76 (2012) 389-393.
 - (2) Talal Aljohani, Brian. E. Hayden., Derek Pletcher, Alexandros Anastasopoulos, Combinatorial Electrochemical Corrosion Screening of Library Ni-Cr Thin Film Alloys Prepared by High-Throughput Physical Vapour Deposition Electrochemical Horizon 2011, Bath 2011, Poster.
 - (3) Talal A Aljohani, B. E. H., Derek Pletcher, Alexandros Anastasopoulos, High-Throughput Measurement of Corrosion Resistance of Metal Alloy Thin Film Materials, Conference, EUROCORR 2012, 1022.
 - (4) T.A. Aljohani, B.E. Hayden; A Simultaneous Screening of the Corrosion Resistance of Ni-W Thin Film Alloys, *Electrochimica Acta*,(accepted).

Signed:



Date:.....21/08/13.....

Acknowledgements

I would like to express my sincere gratitude to my supervisor Professor Brian E. Hayden for his valuable and constructive supervision, and his unlimited support throughout this project. Also, I would like to offer my special thanks to Professor Derek Pletcher for his valuable advice. I would like also to thank my adviser Dr. Guy Denuault for his willingness to give time and offer suggestions. Also, I must not forget to offer special thanks to Dr. Alexandros Anastasopoulos for his assistance and encouragement during the preparation of samples. Also I would like to give a special thanks to the mechanical and glassblowing workshops staff for their help which I have greatly appreciated. I would like to thank Sandy Kerr for proofreading Chapter five; also my acknowledgement extends to Hayden's group members for their encouragement and support. Also I would like to acknowledge the staff of the Chemistry department and to everyone who helped me throughout my project.

I would like to acknowledge King Abdulaziz City for Science and Technology (KACST) for funding this project.

I am deeply grateful to my wife whose encouragement has played an essential role in helping me to survive the PhD challenges. Also I would like to thank my little kids Hesham and Abdulrahman, who always ensure that I have a fun time.

I owe my gratitude to all my brothers and sisters, who are always close to me and have given me the spirit to accomplish this thesis.

Finally, and yet importantly, I would like to express my exceptional thanks and appreciation to my mother for her unlimited kindness; and I also would like to devote this thesis to the soul of my father who convinced me that a person can do anything if he/she really wants to do so.

Definitions and Abbreviations

Passivity: Passivity defines as state where metal/alloy forms thin film of oxide under oxidizing condition and high anodic polarisation.

Breakdown potential: The potential after the passive region where current densities increase sharply.

Corrosion or zero current potential: The surface potential of corroding metal.

Grain boundary: A region separates two grains or crystals which interface in different orientation.

Negative difference effect (NDE): The increase of hydrogen evolution reaction (HER) with applying potential, and has only been observed in Mg and its alloys.

MBE: Molecular Beam Epitaxy

PVD: Physical Vapour Deposition

HT: High-Throughput

IGC: Intergranular Corrosion

IGSCC: Intergranular Stress Cracking Corrosion

SCC: Stress Cracking Corrosion

AFM: Atomic Force Microscope

XRD: X-ray Diffraction

EDX or EDS: X-ray Dispersive Energy Spectroscopy

SCE: Saturated Calomel Electrode

LPR: Linear Polarization Resistance

Symbols

E_{corr} : Corrosion Potential

$E_{i=0}$: Zero Current Potential

E_{opc} : Open Circuit Potential

E_{app} : Applied Potential

η : Overpotential

R_p : Polarisation (corrosion) Resistance

b_a : Tafel anodic constant

b_c : Tafel cathodic constant

B : Tafel constant

I_{corr} : Corrosion current density

I_o : Exchange current density

I : Current density

λ : Wave length of the incident x-rays

K : Numerical constant = 0.93

B : Half width of half maximum of the diffracted peak

$x/2$: Bragg's angle

d : Interplanar distance between crystal planes

θ : Bragg's angle, between the lattice plane and x-rays

1. Introduction

1.1 Definition of Corrosion

Corrosion is generally defined as a destructive reaction between a metal or metal alloy and its environment[1]. This eventually leads to a deterioration of material properties. Two reactions take place during the corrosion process. The first is the anodic reaction (Equation 1-1) where the metal is oxidised and loses electrons (ne^-):



The second is the reduction reaction (Equation 1-2). Hydrogen evolution is the most common reduction reaction in acidic environment where the hydrogen ion (H^+) is reduced to (H_2) gas:



The reduction of oxygen is sometimes observed in neutral (Equation 1-3) and acidic (Equation 1-4) solutions.



Water can also be reduced in the following way:



1.2 Types of Corrosion

1.2.1 Uniform Corrosion

This sort of corrosion is the most common and results in a uniform corrosive attack which takes place all-over the metal surface [2]. The best example of this corrosion is atmospheric corrosion of steel from which iron oxide (i.e. rust) results. The rate of this corrosion is predictable; therefore it does not

cause much concern from a practical point of view. Cathodic protection, painting, and coating can be applied to reduce this sort of corrosion.

1.2.2 Galvanic Corrosion

This corrosion occurs when two metals or phases[2] with different potentials (E) are attached together in the presence of a corrosive electrolyte[3]. The active metal (i.e. more negative E) becomes the anode and gives electrons while the other metal (more positive E) becomes the cathode and receives electrons. For example, if Al (less active) and Mg (very active) are both in a corrosive solution (e.g. NaCl solution) galvanic corrosion more likely would occur. Therefore Al-Mg and Mg-Al alloys usually suffer from this form of corrosion [4-6]. Moreover, the presence of active and passive phases (i.e. β Al_3Mg_2 and γ $\text{Al}_{12}\text{Mg}_{17}$ respectively) could form micro-galvanic corrosion [6]. The latter may be classified under intergranular corrosion. The severity of this form of corrosion depends on the potential difference between the two metals, the corrosive environment, the distance and metal area[3]. A large difference in potential between metals means a large corrosion rate. Also, a more severe environment accelerates the corrosion reaction rate. The corrosion severity is reduced by distance; for example this corrosion occurs at joints or junctions between two different metals but is reduced far from the site of the corrosive attack. The area plays a significant role in accelerating galvanic corrosion. The current density increases with decreasing electrode (i.e. metal) area. Therefore, the large passive metal fastened with small and active metal results high anodic current density. Consequently this type of corrosion can be avoided or reduced if the suggestions below are implemented:

- Reduce the potential difference by choosing two metals with similar potentials in the galvanic series.
- Reduce the area or size difference of metals used as jointers and avoid shapes that may cause corrosion to take place.
- Use an insulator between two metals with similar potentials.
- The coating between two similar metals should be applied with caution and should not create any small anode and large cathode effects.
- Use inhibitors to reduce environment aggressiveness.

1.2.3 Crevice Corrosion

This type of corrosion often exists inside crevices located in covered areas exposed to corrosive media[7]. The shield could be deposits, sands, insoluble solids or non-metallic materials (e.g. plastic gasket, wood, rubber, concrete etc.). Stainless steel covered with rubber inside sea water often suffers from this corrosion[3]. The ions migration (e.g. Cl^- and M^+) into and out of the crevice cell controls the rate of this corrosion, which often occurs after oxygen depletion. The common example of this type of corrosion is filiform corrosion or often called underfilm corrosion. Avoiding sharp corners, stagnant areas, and porosity in fasteners with regular basis maintenance will minimize crevice corrosion problems.

1.2.4 Pitting Corrosion

Pitting corrosion occurs as a result of rigorous localized attack from which small holes result. The initiation of these pits is normally due to compositional heterogeneities, scratches, and environmental variation[8]. The pitting corrosion and crevice corrosion are difficult to predict and forms in concealed places. Also, they share similar propagation mechanisms (i.e. ions diffusion). Pitting corrosion is common in stainless steel, nickel alloys containing chromium and aluminium alloys. The pit propagation rate depends on migration of corrosion products into and out of the pit, frequently named the occluded cell. Therefore, if metal/alloys have not been repassivated quickly the metal dissolution increases rapidly. Once the pit is initiated other factors such as diffused corrodents (i.e. Corrosion products) in and out the pit controls pitting corrosion rates. The mechanism of pitting corrosion is not clear yet. Also the pitting corrosion mechanism varies from metal to metal. Song and Atrens[4] believe that magnesium localized corrosion differs from stainless steel corrosion because it is self-limiting and grows laterally. However, some other hypothesis have been reported[7]. The pitting corrosion in stainless steel instigated by low pH and high chloride ion concentration results from the hydrolysis reaction (Equation 1-6)



The next step is the autocatalytic process. The $\text{Fe}(\text{OH})_2$ oxide layer reacts with a chloride ion and produces excess positive charge inside the pit (Fe^{3+}) blocked

by $\text{Fe}(\text{OH})_2$. As a result the chloride ion migrates from the surface into the pit to balance electroneutrality.



The pH inside the pit decreases largely where hydrogen and chloride ions are concentrated. Such an environment stimulates the corrosion of most metals. The rate-determining step in this mechanism is the Fe^{3+} release reaction catalysed by the chloride ion. In other words, the quality and stability of the formed passive film play a significant role in pitting corrosion. However, Smialowska[9] argues that the lower solubility of oxidised species controls the pitting corrosion rate. This conclusion was drawn after studying the pitting corrosion behaviour of Al-Cr, Al-Zr, Al-W, and Al-Zn. Results show a correlation between pitting potential and oxide layer formed on the surface. The alloys with less soluble oxides such as CrOOH or Cr_2O_3 show high pitting corrosion. However, this argument cannot explain the effectiveness of inhibitors which totally depend on preventing corrosive species like Cl^- from interacting with metals/alloys surface. The pits usually grow toward gravity[3]. The alloy/ metal type and environment determine the pit shape. The common shapes resulting from pitting corrosion are shallow, elliptical, undercut, narrow deep, and subsurface[7].

1.2.5 Environmentally Induced Cracking

Environmentally induced cracking (EIC) is a brittle mechanical failure generated by the presence of tensile stress and a corrosive environment. EIC has three forms, namely stress cracking corrosion (SCC), corrosion fatigue cracking (CFC) and hydrogen induced cracking (HIC). All of these forms are induced environmentally. Stress cracking corrosion is similar to corrosion fatigue cracking, however, the latter results after cyclic stresses while stress cracking corrosion occurs under static stress. The hydrogen induced cracking is a result of hydrogen diffusion into metal/alloy lattices during cathodic polarisation. This makes HIC different from SCC and CFC which are suppressed during cathodic polarisation[7]. Alloys are more susceptible to stress cracking corrosion than pure metals[7]. Also, stress corrosion cracking is intergranular. This is called intergranular stress cracking corrosion (IGSCC) and is common in

Al alloys, for instance. IGSCC is triggered by precipitating Mg-rich β phase (Al_3Mg_2) within a grain boundary, in which anodic attack occurs [10, 11]. The electrochemical potential plays an important role in stress corrosion cracking. Therefore, the anodic polarisation technique is widely used to investigate these types of corrosion[12]. The mechanism of SCC is not well known yet, and this is due to many factors which are associated with this type of corrosion. The mechanism also depends on the alloy/ metal behaviour with respect to corrosive media, which varies making the situation more complex.

1.2.6 Hydrogen Damage

This corrosion is mainly caused by hydrogen. The hydrogen interacts with the metal in different ways producing four forms of corrosion[3]:

- Hydrogen blistering
- Hydrogen embrittlement
- Decarburization
- Hydrogen attack

The diffusion of hydrogen into a metal/alloy creates swelling, often named blistering. In a similar way hydrogen embrittlement reduces ductility and tensile strength properties. Removing carbon from steel by moist hydrogen at elevated temperatures is referred to as decarburization. Hydrogen attack also refers to interactions between an alloy constituent and hydrogen at high temperature. Decarburization and hydrogen attack occur at high temperatures.

1.2.7 Intergranular Corrosion

This corrosion occurs within or adjacent to grains boundaries[8] due to an alloy element, impurities or rich phase segregates or precipitates at grain boundaries. As a result, grain boundaries become more reactive than interior grains, hence localized attack results. This form of corrosion is widely witnessed after heat treatment of some alloys such as austenitic stainless steel and aluminium alloys containing magnesium. Chromium carbides (Cr_{23}C_6) precipitate at grains boundaries when austenitic stainless steel is heated in the range of 550-800 °C. As a result, chromium depletes from the region near to grain boundaries (**Figure 1.1**), therefore it becomes less resistant and preferentially attacked. This process often is called sensitisation[13, 14].

Similar phenomena have been observed in Al-Mg alloys [10, 11, 15, 16]. Most researchers believe that susceptibility to sensitisation or intergranular corrosion in Al-Mg alloys is a result of β phase (Al_3Mg_2) precipitation at grain boundaries and not because of Mg segregation. However, others [8, 10, 17] argue that it is because of potential differences between grains boundaries and matrices. Moreover, Mg segregation is the main cause of susceptibility to sensitisation or intergranular corrosion.

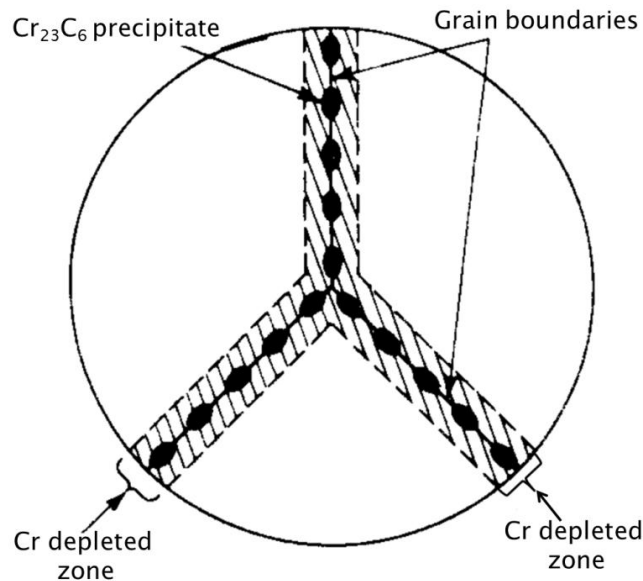


Figure 1.1: A grain boundary of sensitised stainless steel, type 304. Adapted from Fontana, M. G. (1978); Corrosion Engineering. New York, McGraw-Hill [3].

There are three solutions to minimise intergranular corrosion (IGC)[3]. The first involves applying high temperature treatment to dissolve chromium carbide and produce a homogenous alloy. The second involves the use of stabilizers having strong affinity to carbide. The last solution involves reducing the carbon content below 0.03 %.

1.2.8 Dealloying

Dealloying or selective leaching refers to the corrosion form during which one element from an alloy constituent corrodes selectively. Dezincification is the most common example of this type of corrosion. Dezincification occurs by removing zinc from brass alloys which consist of 30 % zinc and 70 % copper.

This process also is named parting as metallurgical term[8]. Zinc preferentially corrodes because it is more active (i.e. more negative electrochemical potential) than copper. Similar phenomena are seen when other active elements such as aluminium, nickel or silicon alloy with copper[7]. Another example of element leaching is the removal of iron selectively from grey cast iron, which is named misleadingly as graphitization.

1.2.9 Erosion Corrosion and Fretting Corrosion

Erosion corrosion takes place when a high flow rate of corrosive fluid removes or disrupts a protective film (e.g. corrosion product). This can be accelerated when sands or suspended slurries exist within the corrosive fluid. Fretting corrosion refers to abrasion between multicomponent devices. Therefore the protective film is removed due to repeated friction.

Also, cavitation corrosion is considered as a form of erosion corrosion. This type results from pressurised water bubbles which fall onto a surface. Consequently, metal particles are removed from the surface leaving a hole or cavity which increases with time. This form of corrosion often occurs in condenser and heat exchanger tubes.

1.3 Potential vs. pH (Pourbaix) Diagrams

The Pourbaix diagram provides information about the possibility of corrosion reactions occurring from a thermodynamic point of view. However, it provides no expectation of corrosion rates or any kinetic information. Nevertheless, the potential/pH diagrams are used for fuel cells, batteries, and electroplating applications [7]. Pourbaix diagrams are constructed based on the Nernst equation (Equation 1-9):

$$E_r = E_o + \frac{RT}{nF} \ln \frac{[\text{Oxidized}]}{[\text{reduced}]} \quad \text{Equation 1-9}$$

Some diagrams related to the alloy systems being studied are enclosed (see Appendix 1).

1.4 Corrosion Rate Measurement

Corrosion rate is often determined by weight loss or electrochemical polarisation methods. Each method has advantages and limitations[18].

1.4.1 Weight Loss

This is a conventional method which involves measuring the sample weight before and after corrosion or exposure tests. Samples often undergo four steps, namely sample preparation, sample exposure, sample cleaning or corrosion product removing, and sample weighing. The corrosion rate is calculated by Equation 1-10[3]:

$$\text{Mils per year} = \frac{534 W}{DAT} \quad \text{Equation 1-10}$$

Where W is weight loss (in milligrams), D is density (in grams per cubic square g/cm^3), A is sample exposed area (in square inches) and T is the exposure or immersion time in hours. MPY i.e. mils per year is a common term among engineers. This unit can be converted to the metric system or daily rates as described by Fontana[3]. The main limitations of the weight loss method are the lower weight sensitivity viz. up to only 0.1mg, time consuming, and does not provide any information about intergranular corrosion.

Atmospheric corrosion is the most common example of this method [7, 19, 20]. However, atmospheric conditions are not fully controlled, hence the salt fog cabinet is used to control corrosion environment[21].

1.4.2 Electrical Resistance Probes

Electrical resistance probes are considered as non-electrochemical corrosion measurements which are used to monitor corrosion rates [22]. Electrical resistance increases proportionately with a uniform loss of the probed cross-sectional area. In other words the measured resistance is equivalent to weight loss. This technique has similar drawbacks to the weight loss method, which is a long time is required to measure the corrosion rate.

1.4.3 Electrochemical Polarisation Methods

Tafel extrapolation and linear polarisation resistance (LPR) are the two methods used to measure corrosion rates by electrochemical polarisation. The polarisation methods have certain advantages over the conventional weight loss methods. Firstly, polarisation methods do not require a long time and can be executed within a few minutes. Therefore, it is appropriate for corrosion monitoring, and corrosion kinetic investigation. It is also a non-destructive measurement, particularly the LPR method where only small potentials are needed to be applied i.e. less than 30 mV versus open circuit potential.

1.4.3.1 Tafel Method

Tafel extrapolation is a special application of the mixed potential theory firstly described by Wagner and Traud [23]. It describes the relationship between the net current resulting from cathodic and anodic reactions under activation control. This is also a kin to the Butler- Volmer equation (Equation 1-11):

$$i = i_{corr} \left\{ \exp \left(\frac{2.303(E - E_{corr})}{b_a} \right) - \exp \left(- \frac{2.303 (E - E_{corr})}{b_c} \right) \right\} \quad \text{Equation 1-11}$$

Where i , i_{corr} , E , and E_{corr} , are net current, corrosion current, applied potential, and corrosion potential.

b_a , and b_c are anodic and cathodic constant respectively, which are the average of the Tafel slopes where $\log |i|$ is plotted vs. η . This can be obtained at potentials (η) away from the corrosion potential (E_{corr}) by $50 < \eta > -50$ mV. Tafel behaviour exists where $\log (i)$ versus applied potential varies linearly. This equation is the well-known Tafel law (Equation 1-12):

$$\eta = a \pm b \log |i| \quad \text{Equation 1-12}$$

$\eta = (E - E_{corr})$ is the overpotential where a is a constant and b depends on the applied polarity, either b_c or b_a .

For example, at cathodic polarisations of $(E - E_{corr}) \leq -50$ mV the anodic current is insignificant and Equation 1-11 reduces to Equation 1-13:

$$i = i_{corr} \left\{ \exp \left(-\frac{2.303 (E - E_{corr})}{b_c} \right) \right\} \quad \text{Equation 1-13}$$

By taking the ln and substituting $(E - E_{corr})$ by η Equation 1-13 becomes

$$\ln \left(\frac{-i}{i_{corr}} \right) = -\frac{2.303}{b_c} \eta \quad \text{Equation 1-14}$$

Rearrangement of Equation 1-14 gives

$$\eta = -\frac{b_c}{2.303} [\ln(-i) - \ln i_{corr}] \quad \text{Equation 1-15}$$

Equation 1-15 simplifies to Equation 1-16

$$\eta = \frac{b_c}{2.303} \ln(i_{corr}) - \frac{b_c}{2.303} \ln(-i) \quad \text{Equation 1-16}$$

And as known from the logarithmic laws $\ln x = 2.303 \log x$ thus Equation 1-16 becomes:

$$\eta = b_c \log(i_{corr}) - b_c \log(-i) \quad \text{Equation 1-17}$$

or

$$\log(-i) = \log i_{corr} - \frac{\eta}{b_c} \quad \text{Equation 1-18}$$

Therefore, the corrosion current (i_{corr}) is found by extrapolating the linear line of $\log(-i)$ vs. η at (E_{corr}) , and the slope of linear line is b_c^{-1} .

At anodic polarisations of $(E - E_{corr}) \geq +50$ mV the cathodic current is insignificant and Equation 1-11 reduces to Equation 1-19 as well. Similarly the corrosion current (i_{corr}) can be obtained by extrapolating the linear line of $\log(i)$ vs. η at (E_{corr}) :

$$\eta = b_b \log(i_{corr}) + b_b \log(i) \quad \text{Equation 1-19}$$

Tafel behaviour is examined by carrying out potentiodynamic polarisation scans over a potential range of ± 250 mV vs. open circuit potential or corrosion potential (E_{corr}). Slow scan rates, often between 0.1 to 1 mV, should be used in

order to achieve the steady state, and also to avoid a charging current contribution, which increases with scan rate (Equation 1-20). Tafel behaviour should be extended over at least one order of magnitude of current density in order to gain appropriate extrapolation. However, Tafel slopes may not be accessible or obtainable in some cases, e.g. in fast metal/alloy dissolution, oxide reduction and passivation.

$$I = C \, dE/dt \quad \text{Equation 1-20}$$

Where C is capacitance of the double layer formed in electrode/solution interface.

Also high scan rates increase charging current contribution as shown in Equation 1-20. Therefore this effect distorts the total current which in turn increases the unwanted potential drop (IR) as presented in Equation 1-21. Consequently, corrosion or zero current potential (E_{corr} , $E_{i=0}$) might not be equal to open circuit potential. This difference increases with increasing scan rate as thoroughly discussed by Zhang et al [24].

$$\Delta\eta_{\text{true}} = \Delta\eta_{\text{applied}} - IR \quad \text{Equation 1-21}$$

The η and IR are overpotential and potential drop respectively.

$$i_{\text{total}} = i_{\text{faradic}} + i_{\text{charging}} \quad \text{Equation 1-22}$$

Moreover, Tafel behaviour can only be obtained when the reaction is under activation control not mass transport control.

1.4.3.2 Polarisation Resistance (PR)

It has been observed that the applied potential within a few millivolts from the zero current potential varies linearly with measured current[1]. Polarisation resistance is the slope of the linear line at corrosion or zero current potential, which is inversely proportional to corrosion rate. Stern and Geary [25] simplify the Butler-Volmer equation (Equation 1-11) by assuming that at corrosion potential (where $\eta = 0$) the Butler-Volmer equation can be linearized using $e^x = 1+x+x^2/2!+x^3/3!$. Therefore at low overpotential or at corrosion potential the higher terms can be ignored therefore the Butler-Volmer equation (Equation 1-11) reduces to Equation 1-23.

$$\left(\frac{di}{dE}\right)_{E_{\text{corr}}} = \frac{1}{R_p} = 2.303 i_{\text{corr}} \left[\frac{1}{b_a} + \frac{1}{b_c} \right] \quad \text{Equation 1-23}$$

Where B , i_{corr} , R_p are Tafel constant, corrosion current and polarisation resistance respectively.

Despite early criticism by Hoar[26], the linear polarisation resistance (LPR) method is widely used to determine corrosion rates. This method is non-destructive and easy to use, therefore it is extensively used by corrosion metres for corrosion monitoring[7, 22]. Moreover, Tafel slopes or constants (B) can be determined from potentials near to the corrosion potential, which is before the Tafel polarisation region. This has been proven by many researchers [27-32]. Mansfeld has suggested a four step method to calculate corrosion currents by knowing the polarisation resistance at two potentials[29]. Also, Oldham and Mansfeld[33] have proposed a graphical method by which corrosion currents can be determined without any need of the Tafel constant.

However, the corrosion current estimated by Equation 1-23 can be overestimated in the presence of other redox reactions occurring near the corrosion potential[7]. Mansfeld and Oldham[27] modified Equation 1-23 to include cases where the reversible potentials of oxidation and reduction reactions are near to the corrosion potential.

Linear polarisation resistance (LPR) is a very useful method to monitor corrosion despite its limitations[28]. Polarisation curves in the vicinity of the corrosion potential (E_{corr}) implies a corrosion behaviour, albeit the polarisation curve is non-linear[34].

As mentioned in the Tafel method, high scan rates may cause variation between zero current potential and open circuit potential. Consequently the slope value i.e. polarisation resistance, will be also different. The error will be high when the polarisation curve is non-linear. Therefore, low scan rates always are recommended.

1.5 Motivation

Corrosion has potential consequences in our daily lives. The direct economic cost of corrosion in the United States is \$276 billion according to a study performed by CC Technologies Laboratories, Inc. from 1999 to 2001[35]. In the UK, the annual cost of corrosion is 3.5 % of the UK GNP according to a survey published by Hoar[36] and performed in 1970. The estimated cost of corrosion in Saudi Arabia by 2011 is \$24.84 billion [37]. Moreover, corrosion can cause fatal accidents such as the airline accident in Hawaii, the bridge collapse at Point Pleasant, West Virginia, the steam pipe burst at a Virginia nuclear power generating plant, and the gasoline pipeline burst in Minnesota[7]. All these accidents are results of corrosion. However, good practice by choosing the right materials and employing appropriate maintenance can make enormous expenses avoidable [38], and increase the safety of human life.

Time and material types play significant roles in corrosion processes. Therefore, fast corrosion assessment methods will result in detecting material failure at an early stage and where treatment may be possible. However, identifying the material failure may not solve the problem completely and novel materials with robust corrosion resistance are required in some aggressive environments.

Consequently, this project involves the development of high throughput electrochemical screening methodology to measure corrosion characteristics of thin film alloys on a micro-fabricated array comprised of a 100 electrodes. The thin film alloys are synthesised by high-throughput physical vapour deposition (HT-PVD) methodology based on MBE sources. This method satisfies both conditions i.e. time and materials type, which control corrosion processes.

1.5.1 Combinatorial or High-Throughput Method History

The combinatorial or high-throughput approach was firstly used in the pharmaceutical industry in the 1980s [39]. The astonishing success of the combinatorial method has attracted other academic and industrial research. Materials development and discovery have largely implemented this approach to examine certain properties or activities[40]. Combinatorial methods have

been applied to the screening and optimisation of metal alloys [41] and supported metal nano-particle electrocatalysts[42-46].

Recently, the combinatorial approach has been implemented for the purpose of investigating the corrosion behaviour of materials [47, 48]. A scanning droplet cell [49] was successfully employed to investigate the passivation behaviour of some thin film alloys [47, 50-52]. An optical screening method has been used to assess the corrosion behaviour of a library of thin films by image analysis of electrodes before and after exposure to the corrosion environment [48]. A multi-electrode method has been applied to evaluate corrosion behaviour before and after adding inhibitors where pairs of identical wires embedded in an insulator are interrogated by applying potentials which activate both anodic and cathodic responses [53, 54].

However, the offered corrosion screening methodology provides two advantages over other high-throughput approaches. Firstly, considerable numbers of samples of up to a 100 fields per single array can be explored while a quarter of this number could only be evaluated by multi-electrode high-throughput methods [53, 54]. Additionally, simultaneous parallel electrochemical screening ensures not only simple procedures but also an identical electrochemical environment, which is hard to achieve in the sequential measurements of a scanning droplet cell (SDC) [49]. This approach also has been extensively developed to study the compositional, particles size support dependence in electro-catalysis [46, 55, 56].

The rest of this chapter presents background on the alloy systems investigated in this thesis.

1.6 Literature Review of Metal Alloys

1.6.1 NiCr Alloys

Ni-Cr alloys have good electrical, mechanical, high temperature, and corrosion resistance. As a result they are being used in several applications whether as thin films [57-62] or bulk [63-66] alloys. For instance, they have low temperature coefficients of resistance (TCR) and large resistivity, hence are widely used in microelectronics as resistors, filaments and humidity sensors [57-59, 67]. Also, cold sprays of Ni₈₀-Cr₂₀ and Ni₅₀-Cr₅₀ exhibit high oxidation resistance in severe environment at temperatures as high as 900 °C [68]. At similar to the previous condition, steam oxidation resistance of 9Cr-1Mo steel was enhanced after applying thin films of Ni₅₀-Cr₅₀ alloy [62]. Similar observations revealed that oxidation resistance is induced by sputtering a thin layer of Ni₈₀-Cr₂₀ on Ti₃Al-based intermetallic alloys [69]. Besides good oxidation resistance, Ni-50Cr thin film coatings display good corrosion resistance at severe conditions of 900 °C for 1000 hours in a hostile environment of Na₂SO₄-60% V₂O₅ [70]. In a similar study, the corrosion resistance of Ni-20Cr examined at 900 °C for 1000 hours in the presence of SO_x, NO_x, O₂ and CO₂ showed good performance [71]. Nichrome alloys are widely used in high temperature applications where hot corrosion occurs. As a boiler tube coated by detonation spray and used at an incineration plant, 50Ni-50Cr alloy has passed hot corrosion tests for 7 years without any faults [72]. Also, observation of corrosion resistance of 80Ni-20Cr films exposed to Na₂SO₄-60% V₂O₅ revealed that the 80Ni-20Cr alloy exhibits better corrosion resistance than the Cr₃C₂-Ni-20Cr film alloy [60]. Furthermore, Ni-20Cr alloy has been used as a bond coat in thermal barrier coating (TBCs), preventing the hot gases penetrating the bond coat and showing good corrosion resistance by using a gas shroud system [73]. It seems from previous literature that Ni₈₀-Cr₂₀ and Ni₅₀-Cr₅₀ are the most promising alloys.

Amorphous Ni-(15-20) Cr-P alloys studied in hot concentrated phosphoric acid shows very similar polarisation behaviour. This indicates that no change takes place by increasing Cr content from 15 to 20%_{at.} [74]. No other paper concerning NiCr alloy corrosion in phosphoric acid has been found. Bojinov et al. [75] investigated transpassive dissolution of NiCr bulk alloys and it was

shown that the Ni-10Cr alloy demonstrates a larger passive area compared to the Ni-20Cr alloy.

Ni-Cr bulk alloys also have demonstrated good resistance in different environments and applications. In fusion reactors, as an alternative to stainless steel (00Cr16Ni15Mo3Nb, 06Cr18Ni10Ti) XHM-1, a Ni-Cr chromium-enriched alloy (44% Cr, Ni-Base, 1-2 Mo) called Bochvalloy, was used in the water coolant working at 150 to 350°C with various chloride and oxygen contents. No cracking corrosion appeared even after 86 000 hours of testing [65].

In addition, Ni-Cr alloys are being used broadly as an alternative to precious metals, like gold, in dental restoration. In 0.9% saline solution, alloys with high Cr content > 20%, are used as soldered joints, showed better resistance to galvanic corrosion [76]. Another study using the electrolyte at 37°C reported that a marginal effect was observed to the electrochemical behaviour of the Ni-Cr alloy, related to the use of a different casting method[77]. Also, the corrosion behaviour of Ni-Cr in 3% NaCl at ambient temperature was evaluated as lower than Co-Cr [78]. The corrosion resistance of Euro-Cream Ni-Cr alloy (72.5Ni-23.1Cr-1.1Fe) and Ultratek Ni-Cr alloy (80.1Ni-11.4Cr-2.5Mo-1.7Be) was investigated in 0.02, 0.2 and 1 M of NaCl [79]. Also, the influence of using three different manufacturing procedures for Ni-Cr alloy (63Ni-16Cr-8Co-5Mo-3Al3.5Mn-1.5Be) on their corrosion resistance was examined [80].

The NiCr alloy structure varies based on composition and heat treatment. From a compositional point of view and at equilibrium, in which free energy is at a minimum and there is sufficient mobility, three phases were found. These are f.c.c. γ -Ni solid solution (0-50% Cr), Ni_2Cr or γ^- (21-40% Cr), and b.c.c. α -Cr (65-100% Cr) [81]. Moreover, metastable phases were identified. The phase diagram is shown in **Figure 1.2**. Compositions versus detected phase details are presented in **Table 1.1**. The existence of the metastable phases at equilibrium depends on the substrate temperature and nature[82].

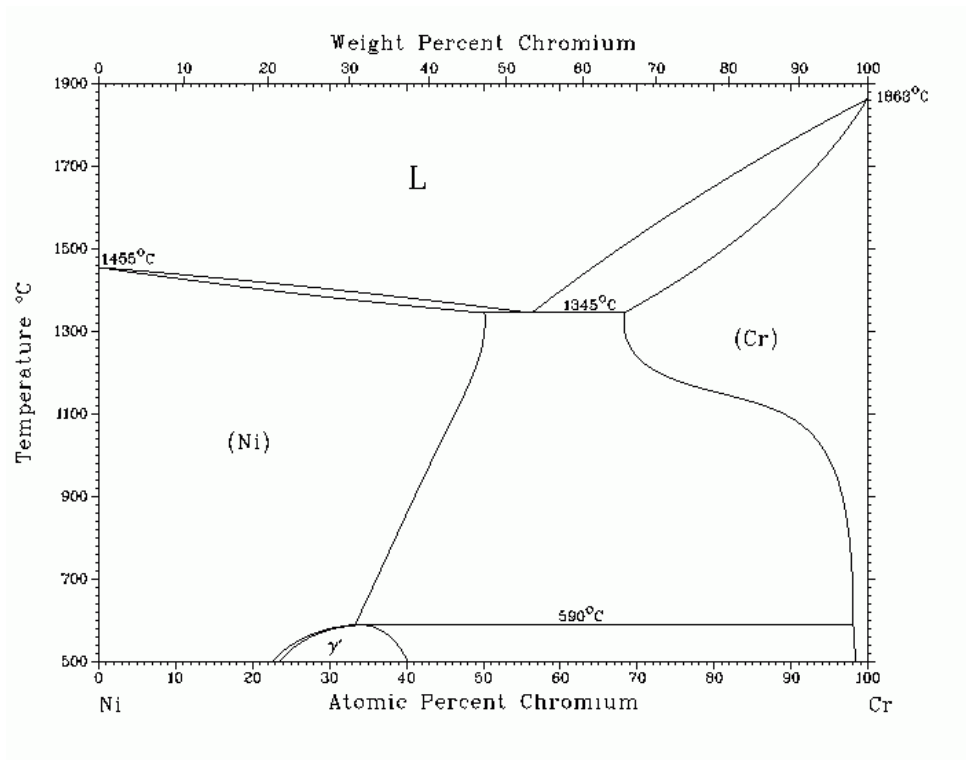


Figure 1.2 NiCr phase diagram at equilibrium, adapted from [81].

Table 1.1 The identified phases in the Ni-Cr phase diagram and their compositional range at the temperature of 500 to 1900 °C. Adapted from [81].

Phase	Composition % _{wt.} Cr	Pearson Symbol	Space group
Ni	0 to 47	cF4	Fm3m
Ni ₂ Cr or γ	21 to 37	oI6	Immm
Cr	65 to 100	cI2	Im3m
Metastable phases			
σ	~28	tP30	P4 ₂ /mnm
δ	100	cP8	Pm3m

At non-equilibrium, unheated films or those deposited at low temperature, it has been reported that from 0-40% Cr, the f.c.c. γ -Ni solid was predominant, while from 40-70% Cr, sigma phases existed. At rich chromium alloys > 70% Cr, in addition to the b.c.c. α -Cr solid solution, δ -Cr was observed regardless of the method with which Ni-Cr films were prepared [83-88]. The sigma phases were noticed at 30% Cr with a tetragonal structure and lattice parameter ($a = 0.882$ nm and $c = 0.4567$ nm). Furthermore, a preferred orientation, affected significantly by substrate nature, was detected [89, 90]. Also, the δ -Cr phase structure was identified as Cr_3Ni [82]. As shown in **Figure 1.3**, sigma phases were thermodynamically predicted in addition to the Ni and Cr extremity solid solution by plotting free energy versus composition phase formation [91]. In this figure the sigma phase displays the lower free energy in the composition range of 50 to 85% Cr although the reported sigma phase has found in a shorter compositional range. The conclusion drawn here is that the sigma phase more likely exists in the composition range of 50-75%at. Cr where it shows lower free energy compared to other phases i.e. b.c.c Cr and f.c.c Ni. This probably is true with NiCr alloys prepared at low temperature.

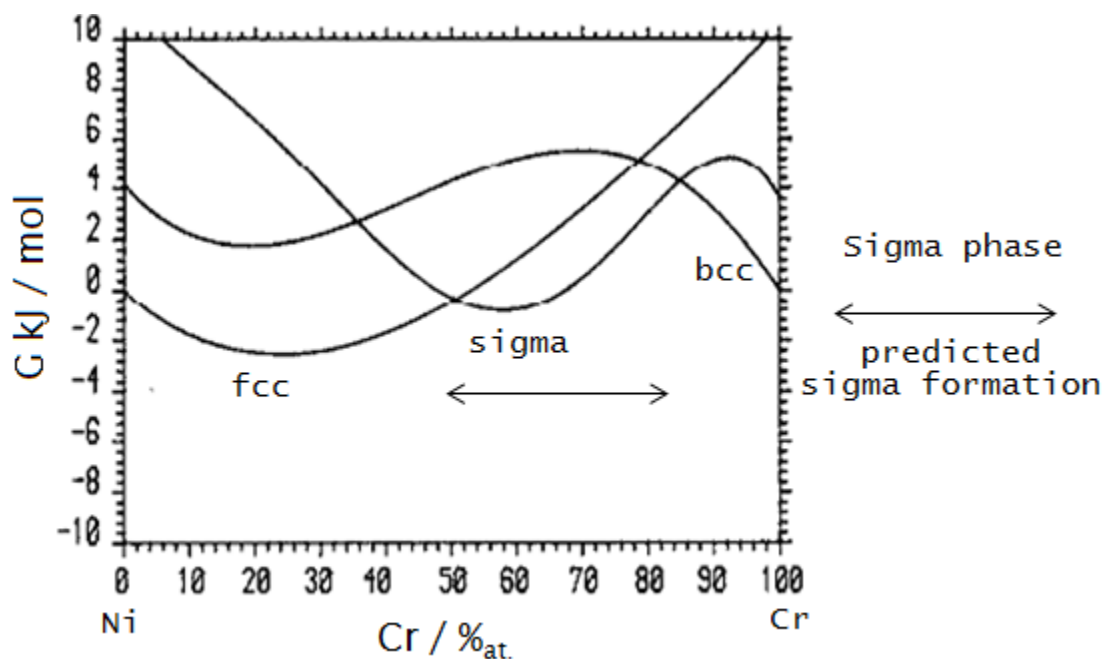


Figure 1.3: Theoretically predicted free energy versus Ni/Cr composition [91]

1.6.2 Ni-W Alloys

Ni-W alloys have been suggested as a successful substitute to electrodeposited chromium which is usually prepared from toxic hexavalent chromium Cr(VI) [92]. Electrodeposition and thermal sputtering, or spraying, are the most common methods by which Ni-W alloys are usually synthesized.

The corrosion and mechanical properties of the Ni-W alloys are good [93] but largely these properties depend on alloy structures, for instance, nanocrystalline or amorphous structures [94]. For example, the amorphous Ni-W alloy films in which W content is in the range of 44-67 %_{wt.}, demonstrate better corrosion and wear resistance than nickel film [93]. Two types of nanostructure phases of Ni-W alloys were prepared, named single phase nanostructure and two phase nanostructure. The first type was formed at 6.7% and demonstrates good corrosion resistance. The second type, formed at more than 7% and consists of pure amorphous tungsten and separated Ni nanoparticles, demonstrates low corrosion resistance, although tungsten content is increased. The low corrosion resistance of the second type was attributed to the galvanic corrosion provoked by the existence of the two phases in the second type [95]. Similar observations [96] showed that the corrosion resistance of Ni-W alloys examined in 3.5% sodium chloride increases by increasing the tungsten content up to 7.54 %_{at.} and thereafter decreases. This is in contrast to a study by Pedro et al [97] where the corrosion resistance of the Ni-W(86:14 %_{at.}) alloy containing more tungsten is better than the Ni-W(93:7 %_{at.}) alloy. The X-ray diffraction results show that the Ni-W (86:14 %_{at.}) alloy has only one broad peak at ca. = 43.5 2 θ corresponding to the amorphous phase, whereas Ni-W (93:7 %_{at.}) has two peaks at ca. = 44.5 and 52 2 θ corresponding to Ni (W) solid solution. This indicates adding more W leads to the formation of the amorphous phase of the Ni-W (86:14 %_{at.}) alloy which increases corrosion resistance compared to the Ni-W (93:7 %_{at.}) alloy. This observation agrees with others [98]. The increase in corrosion resistance of the Ni-W (86:14 %_{at.}) alloy has been ascribed to the significant reduction of segregation and grain boundary energy which is attained by forming amorphous phases. This is related to the tungsten composition and is discussed thoroughly by Detor et al [99].

The influence of pH saline solution on the corrosion resistance of nanocrystalline Ni-W alloys was investigated by Amnuaysak et al [94]. The results revealed that, generally, nanocrystalline Ni-W alloys in acidic media exhibit greater corrosion resistance than alkaline ones. Carrier and plasma gas flow rate is evidently affected by the Ni-W composite coating structure and corrosion behaviour. Results revealed a noticeable increase in coating hardness and corrosion resistance when using high carrier and plasma gas flow rates [100]. As catalysts for the hydrogen evolution reaction, sputtered Ni-W films in the range 5-25% W were tested in an alkaline solution [101]. Electroactivity reached a maximum value at 10% W, after which point the exchange current density dramatically decreased. The effect of composite material on NiW alloy corrosion resistance has been investigated [102]. The co-deposition of SiC nano-particulates improves the corrosion resistance.

The structure of Ni-W alloys, as prepared by magnetron sputtering, in a wide range (0-75% W) were reported [103]. Four distinctive compositions were identified: 0-25%, 25-50%, 50-75%, and 75-100% W. All the compositions, whether as-sputtered or annealed, showed “at least partially crystalline states”, except that 50-75% W showed only an amorphous phase i.e. non-crystalline state. In the first composition range, and according to X-ray diffraction results, only Ni (W) solid solution was observed. The second range of composition containing 25-50 W % demonstrated a broad peak, believed to be for the Ni(W) solid solution or the Ni_4W (211). This can happen either by making a supersaturated solid solution of Ni(W) or making the Ni_4W (211) phase as explained by several authors [103, 104]. A rich tungsten composition i.e. 75-100% β -W for as-sputtered, which was reverted to α -W after annealing was obtained. Similar observations were reported by Yamasaki et al [105] where the onset of amorphous phase was obtained at 20%_{at.}.

At equilibrium, five phases were identified according to the Ni-W phase diagram shown in Figure 1.4 [104]. A solid solution of tungsten in Ni has been observed in the composition range of 0 to ~39.9 %_{wt.} W, which equals (0~17.7%_{at.} W). In addition, three intermetallic phases i.e. Ni_4W , NiW, and NiW_2 have been found. The first intermetallic phase was observed at ~44 %_{wt.} (~20 %_{at.}) W, which also has been identified in films prepared at the non-equilibrium

state. With unknown space group, NiW was detected at $\sim 75.8\%$ wt. of tungsten. NiW₂ with I4 space group was observed at 86.3% wt. At very rich tungsten content $> 99.9\%$ W only (W) phase was detected. All phases and their features are summarised in Table 1.2.

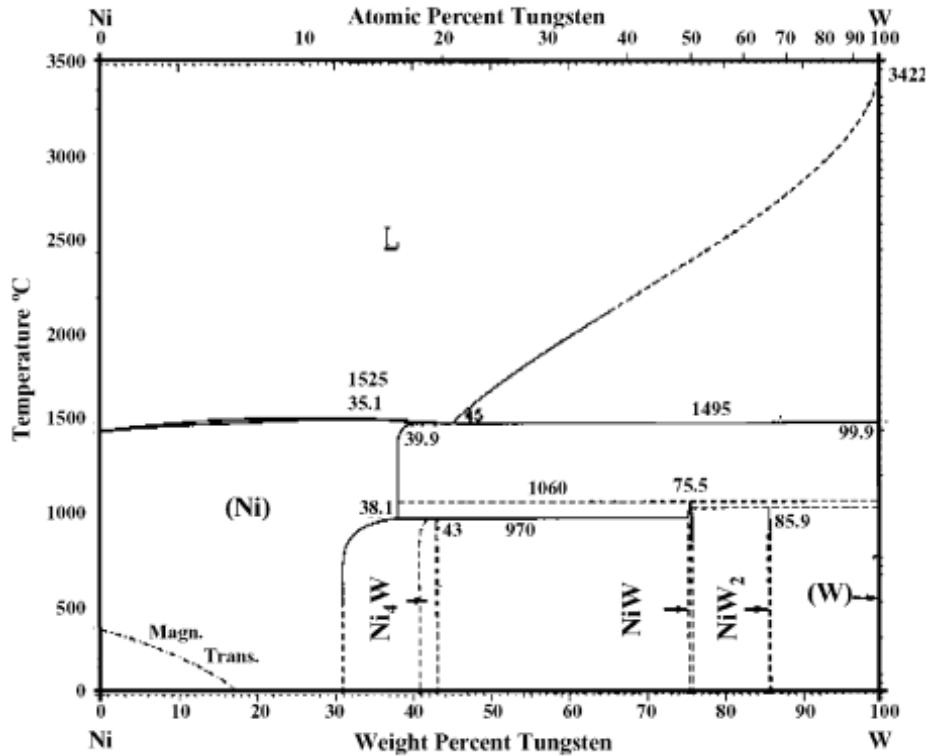


Figure 1.4: Binary Ni-W alloy phase diagram, adapted from [104].

Table 1.2: The identified Phases in Ni-W phase diagram versus tungsten composition.

Phase	Composition of tungsten % _{wt.}	Pearson Symbol	Space group
Ni	0 to 39.9	cF4	Fm3m
Ni ₄ W	~44	tI10	I4/m
NiW	~75.8	o**
NiW ₂	86.3	tI96	I4
(W)	99.9 to 100	cI2	Im3m

1.6.3 Al-Mg Alloys

Unique characteristics such as abundance, high strength/ weight ratio, good machinability, thermal conductivity, and electromagnetic shielding features make magnesium highly used in numerous industries. For example, because of its high strength/ weight ratio magnesium is used in the automobile, aerospace and electronic industries for reducing the weight of products while maintaining excellent mechanical properties[106]. Also, magnesium is used in clinical applications such as biodegradable implants for cardiovascular, musculoskeletal, and general surgery [107, 108]. However, the low corrosion resistance of magnesium is its main defect limitation. The reasons of the low corrosion resistance of magnesium are firstly the very negative standard potential of magnesium i.e. -2.37 V. Therefore in the presence of another metal galvanic corrosion occurs. Secondly, magnesium protective oxide is easily breakable particularly in acid and neutral media[109].

Aluminium intrinsically forms a good protective film and it is widely used to improve magnesium corrosion resistance. However, the mechanical properties of aluminium are low hence it is very often enhanced by adding magnesium which has superb mechanical properties. Therefore this system is interesting and worthwhile to be studied comprehensively.

Table 1.3 displays the most common Mg-Al alloys which usually comprise low amounts of Al. These alloys known as AZ alloys have small amounts of Zn (0.4-0.9 wt. %).

Table 1.3: Chemical composition of some Al-Mg-Zn alloys i.e. AZ21, AZ31, AZ501, AZ81 and AZ91 alloys.

Al-Mg system	Al % _{wt.}	Zn % _{wt.}	Mg % _{wt.}
AZ21	1.33	0.59	balance
AZ31	3.1	0.72	balance
AZ501	51.04	0.38	48.58
AZ81	8.2	0.46	balance
AZ91	8.8	0.68	balance

On the other hand, there are a number of Al-Mg alloys in which low amounts of Mg are added in order to improve their mechanical properties. This is referred to as solid-solution strengthening. Four types of Al alloys contain Mg, namely 3xxx, 5xxx, 6xxx, and 7xxx. But these alloys also may comprise other elements like Cu, Zn, Si, Mn, and Cr. The wrought type having a four digit system and the first digit indicates the principal alloying elements. For example the 3xxx is a wrought Al-Cu-X alloy in which copper is the principal alloying element. The X element always has a low concentration compares to copper. More details about Al alloys and their applications are given elsewhere[7, 110].

1.6.3.1 The corrosion Properties of Al-Mg and Mg-Al Alloys

The Al-Mg alloys which contain Mg ≥ 3 % undergo intergranular corrosion (IGC) or intergranular stress corrosion cracking (IGSCC) when exposed to heat treatments even at low temperature, which is usually referred to as sensitization [15]. As a result, the β phase i.e. Mg_2Al_3 precipitates at grain boundaries. Also, magnesium segregates during the heat treatment to the grain boundaries and Al free zone[111]. However, the direct effect of magnesium segregation on the intergranular corrosion (IGC) or intergranular stress corrosion cracking (IGSCC) is still debatable. Two theories explain

magnesium segregation. The conventional theory assumes magnesium segregates to grain boundaries during heat treatment i.e. it is an equilibrium process. However this theory cannot explain the occurrence of magnesium segregation observed at non-equilibrium [112]. The existence of magnesium segregation at non-equilibrium is believed to be attributed to increasing solubility in the liquid state when solidus temperature is reached. In other words, magnesium segregation may occur at large ratios of solid solubility to liquid solute when solidus temperature is reached[112]. Also, the vacancy drag or vacancy pump model has been proposed [113]. This model assumes magnesium segregation is controlled by energy interaction between magnesium atoms and vacancies. The role of magnesium segregation in the IGSCC of Al alloys has been reviewed by Scamans et al[111] and show that Mg segregation was detected in both as-quenched and non-treated alloys. Despite the low level they have noticed Mg segregation at non-equilibrium condition. However, no direct evidence indicates that Mg segregation instigates the IGSCC but it promotes hydrogen entry into Al. Another study [114] suggests that Mg segregation has little impact to induce the stress corrosion cracking (SCC) where the main reason for it is the hydrogen generated in the Mg rich β phase (i.e. Mg_2Al_3). However, Jones et al [11] argued that magnesium segregation does not have any role in the stress corrosion cracking of Al-Mg alloys, which result from the anodic attack along the β phase precipitation. This agrees with the observation reported by Searles et al. [16] where a clear correlation between sensitisation time and β phase dissolution was identified. Similar results were obtained by Oguocha et al. [15]. However, some researchers [10, 12, 115] assumed that susceptibility of Al- Mg alloys to intergranular stress corrosion cracking (IGSCC) is caused by a difference in the breakdown potentials (E_{bd}), which leads to pitting dissolution of the depleted zone within the grain boundaries. In other words, intergranular stress corrosion cracking (IGSCC) does not result from the difference in the corrosion potential (E_{corr}) between the Mg rich β phase (i.e. Mg_2Al_3) and solid solution matrix. Urushino and Sugimoto [115] found that the initiation potential ($= E_{bd}$ of G.B) of intermetallic Al_2CuMg appears at -880 mV/SCE while for Al_2Cu it starts at -580 mV/SCE. Therefore the dissolution of the Al_2Cu is expected to happen during SCC but results show that susceptibility to IGSCC was observed at higher potentials i.e. pitting potential for grain boundaries. Consequently,

intergranular stress cracking corrosion is induced not by dissolution of the precipitates but by pitting corrosion in the solute-depleted area.

Nevertheless, a large body of literature tends to the opinion that intergranular stress cracking corrosion (IGSCC) in Al-Mg alloys results from the dissolution of the precipitated Mg_2Al_3 phase at grain boundaries. Recently, Lyndon et al. [116] explored the corrosion behaviour of the Mg_2Al_3 phase as a function of pH in sodium chloride electrolyte. The results reveal that the Mg_2Al_3 phase dissolution and corrosion potential (E_{corr}) largely depend on the pH. This indicates the importance of the role of the cathodic reaction in the Mg_2Al_3 phase dissolution. This confirms that intergranular corrosion (IGC) or stress cracking corrosion is a consequence of the galvanic reaction between the Mg_2Al_3 phase (i.e. active and acts as anode) at grain boundaries and the matrix acting as cathode. Also, the annealing impact on corrosion resistance of intergranular corrosion (IGC) was studied by Shuangping et al [117]. The anodic activity increases with an increase in annealing temperature although the E_{corr} shifts to nobler potentials. The uniform distribution of the Mg_2Al_3 phase, which is enhanced by the annealing process, causes E_{corr} to shift to nobler potentials.

Stress corrosion cracking (SCC) is problematic in both the Al-Mg and Mg-Al alloys, which limits their usage particularly in structural applications [118]. Stress corrosion cracking (SCC) is induced by Mg_2Al_3 and $\gamma Al_{12}Mg_{17}$ precipitated at grain boundaries of the Al-Mg and Mg-Al alloys respectively. However, the Mg_2Al_3 acts as an anode whereas the $\gamma Al_{12}Mg_{17}$ acts as the cathode with respect to the matrix i.e. the solid solution.

The Mg-Al alloys are usually comprised of low amounts of Al (i.e. 1-9 %_{at.}) such as AZ21, AZ3, AZ81, and AZ91, except AZ501 which is comprised of 50 % Al. The AZ is defined as (A = Al) and (Z = Zn i.e. less than 1 %_{at.}) and the digits reflect the composition percentage. The Mg-Al alloys also undergo intergranular corrosion (IGC) and stress corrosion cracking (SCC) [118]. However, $\gamma Al_{12}Mg_{17}$ plays a significant role in the corrosion behaviour of the Mg-Al alloys. Therefore, the corrosion resistance of some Mg-Al alloys is still debatable. For example, AZ31 displays better corrosion resistance than AZ91 as observed by Cheng Ying-liang et al. [119] but opposite results were found by Pardo et al [20] where AZ91 shows better corrosion resistance. The latter is

in agreement with other observations reported by Pardo et al and Zhu and Song [120, 121]. This difference in corrosion resistance of Mg-Al alloys is due to the dual role of γ $\text{Al}_{12}\text{Mg}_{17}$ named frequently as the β phase. Normally the γ $\text{Al}_{12}\text{Mg}_{17}$ phase acts in two ways, which largely depends on the microstructure environment. γ $\text{Al}_{12}\text{Mg}_{17}$ acts as a corrosion barrier when it disperses equally in the matrix producing a continuous network. Consequently, corrosion progress is hampered and corrosion resistance is improved compared to pure magnesium. However, γ $\text{Al}_{12}\text{Mg}_{17}$ can act as a cathode with respect to the matrix (i.e. solid solution of Al in Mg). As a result, micro-galvanic corrosion occurs, therefore corrosion resistance could be lower than for pure magnesium. This results when a small fraction of the γ $\text{Al}_{12}\text{Mg}_{17}$ interfaces with the matrix. The role of the β phase i.e. γ $\text{Al}_{12}\text{Mg}_{17}$ on the corrosion resistance has received enormous attention [4, 6, 20, 119-127].

The effect of the chloride concentration and temperature on the corrosion of Mg-Al alloys was explored by the salt fog test[126]. Results reveal that corrosion attack increases with increasing chloride ion concentration and temperature. Moreover, the β phase i.e. γ $\text{Al}_{12}\text{Mg}_{17}$ plays a significant role in controlling corrosion attack on the AZ81 and AZ91 alloys.

1.6.3.2 The Corrosion Mechanism of Mg and Mg Alloys

Magnesium has very negative standard electrode potential (Mg^{2+}/Mg) specifically -2.37 V/ vs. SCE. Therefore it is very reactive and undergoes galvanic corrosion when in contact with other metals such as Al. Magnesium hydroxide and hydrogen gas result from magnesium dissolution in water. Magnesium hydroxide $\text{Mg}(\text{OH})_2$ is more stable in water than MgO [109]. The overall corrosion reaction is shown below (Equation 1-26) along with partial reactions present in (Equation 1-24 and Equation 1-25):



However, the corrosion mechanism of magnesium and magnesium alloys is not simple and still debatable[2]. Moreover, magnesium shows a very abnormal electrochemical phenomenon, which has never been seen with any other metal. This phenomenon is defined as the negative difference effect (NDE). For most metals applied potentials suppress the hydrogen evolution reaction (i.e. cathodic reaction) and increase the anodic reaction (i.e. metal dissolution). However, for magnesium corrosion both the hydrogen evolution reaction (HER) and metal dissolution increase with applying positive potential [128]. The negative difference term reflects the relationship between the hydrogen evolution rate (I_0) at the corrosion potential of magnesium (E_{corr}) and the hydrogen evolution rate ($I_{\text{H,app}}$) at applied potential ($E_{\text{corr}} < E_{\text{app}}$) as defined by Equation 1-27. Normally, the hydrogen evolution rate ($I_{\text{H,app}}$) is lower than the spontaneous hydrogen evolution (I_0) at potentials more than the corrosion potential ($E_{\text{corr}} < E_{\text{app}}$), hence, the difference should be positive not negative. But electrochemical experiments for Mg show that at ($E_{\text{corr}} < E_{\text{app}}$) the hydrogen evolution rate ($I_{\text{H,app}}$) is higher than the spontaneous hydrogen evolution (I_0). Moreover it increases with increased applied positive potential rather than decreases[128].

$$\Delta = I_0 - I_{\text{H,app}} \quad \text{Equation 1-27}$$

I_0 : exchange current density of hydrogen evolution at E_{corr}

$I_{\text{H,app}}$: hydrogen evolution at ($E_{\text{corr}} < E_{\text{app}}$)

The NDE phenomenon was explained by Bender et al. [128] as presented in Figure 1.5 . As one would expect the hydrogen evolution current decreases with applying positive potentials, where the magnesium dissolution current increases as shown by the solid line. However, the hydrogen evolution rate (gas collected) increases at potentials higher than E_{corr} as shown by the dashed line. Moreover, the corrosion rate of magnesium obtained by the weight loss method is greater than the one determined by the electrochemical approach[2].

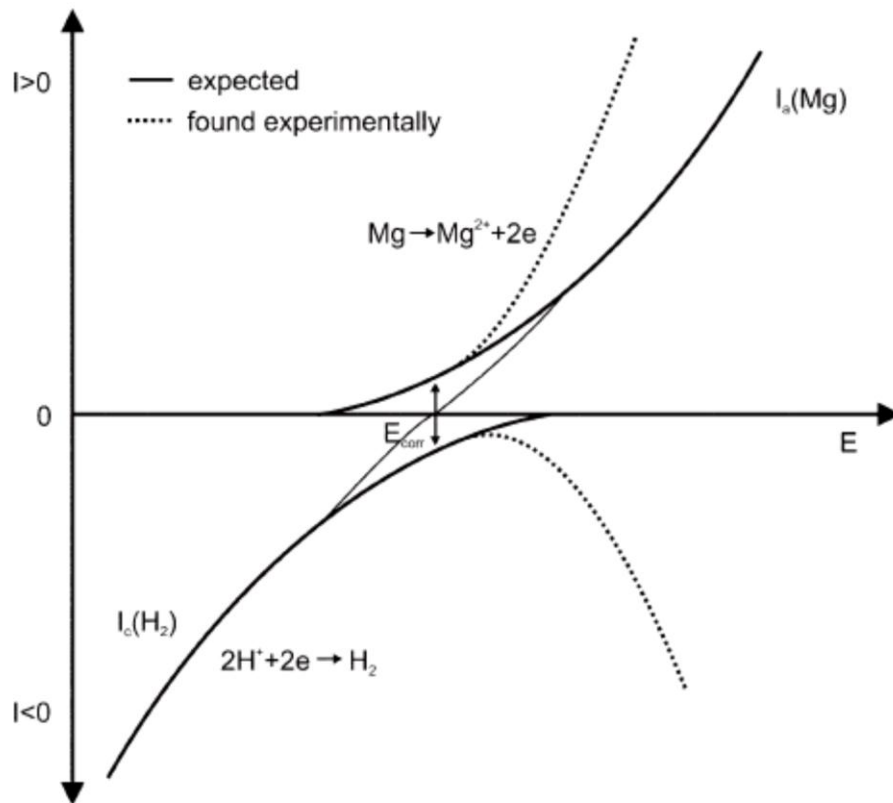


Figure 1.5: Electrochemical behaviour of magnesium at potentials higher than E_{corr} . The solid and dashed line are the expected and obtained behaviour respectively. Adapted from [128].

Four mechanisms have been proposed to explain the negative difference effect (NDE) and the high dissolution rate of magnesium [128-131]. Although none of them have answered all the raised questions, some mechanisms give plausible explanations. The following is a brief description of these mechanisms.

1.6.3.2.1 Partially protective films

This mechanism assumes that the negative difference effect (NDE) is due to partial breakdown of the passive film forming $Mg(OH)_2$ or MgO . Therefore, by applying more potential the oxide layer coverage decreases. The evidence of porous and partially protective films of $Mg(OH)_2$ or MgO observed by [132, 133] give grounding to this mechanism. However, this mechanism has failed to explain the existence of the NDE in acidic and neutral media where $Mg(OH)_2$ or MgO thermodynamically are not stable as proved by Perrault [130].

1.6.3.2.2 Monovalent magnesium ion:

Forming monovalent magnesium ions (Mg^+) as intermediate species (Equation 1-28) during magnesium dissolution may explain the NDE. This ion reacts chemically with ($2H^+$) or (H_2O) producing hydrogen gas (Equation 1-29). This mechanism has been experimentally proved by Bender et al. [134] and Song and Atrens[135]. Moreover it explains the hydrogen evolution increase with increased applied positive potential.



However, there is no evidence regarding the existence of the monovalent magnesium ion (Mg^+) and this notion has been experimentally proved wrong by Williams and McMurray [136] using the scanning vibrating electrode technique (SVET). Moreover, the analysis of magnesium dissolution by atomic emission spectroelectrochemistry has revealed no sign of monovalent magnesium ions[137].

1.6.3.2.3 Undermining and falling particles:

This mechanism assumes the high mass loss is due to the galvanic corrosion between the second phase particles (e.g. $Al_{12}Mg_{17}$) and magnesium matrix. As a result, the second phase particles are undermined and peel off in side corrosion solution. This agrees with SEM observations of partially undermined particles reported by Makar and Kruger [138]. Similar results were obtained by Song et al [132] where small ratios of such fragments were observed at high anodic currents. Moreover, higher ratios of those fragments were detected at more cathodic currents.

1.6.3.2.4 Forming magnesium hydride (MgH_2):

The Hydrogen evolution based on this mechanism results from magnesium hydride decomposition. This involves two steps. Firstly, magnesium is reduced to magnesium hydride as in Equation 1-30. Then magnesium

hydride decomposes chemically when in contact with water producing hydrogen gas (Equation 1-31).



The ex situ x-ray diffraction performed by Gulbrandsen [131] confirms the formation of MgH_2 at cathodic polarisation. But this mechanism cannot explain hydrogen evolution increasing at anodic polarisation at which magnesium hydride reaction (Equation 1-30) should be suppressed. Therefore this mechanism can explain the NDE at cathodic polarisation as suggested by Chen et al. [129] where the other three previous mechanisms explain the NDE at corrosion potential and anodic polarisation.

1.6.3.3 The structure of Al-Mg and Mg-Al alloys

The solid solution of Mg in Al extends to 18.9 %_{at.} Mg according to the Mg-Al phase diagram shown in Figure 1.5 [139]. The structure is face-centered cubic of (Al) with Fm3m space group. At the other extreme the solid solution of Al in Mg prevails from 88.2 up to 100 %_{at.} Mg as a close-packed hexagonal structure. The β phase, namely Al_3Mg_2 , appears at the compositions of 38.5 to 40.3 %_{at.} Mg. Note that β phase is sometimes used to refer to the second phase of the Mg-Al system (i.e. Al_3Mg_2 and $\text{Al}_{12}\text{Mg}_{17}$) and is used specifically to refer to the Al_3Mg_2 phase. The β phase i.e. Al_3Mg_2 has f.c.c. structure and transforms to structure with lower symmetry [139] at low temperature. This may be compared to the unknown metastable phase obtained at ~34.3 %_{at.} Mg [140]. The second intermetallics namely γ $\text{Al}_{12}\text{Mg}_{17}$ extends from 45 up to 60 %_{at.} Mg. The former perfect structure has been obtained at 58.6 %_{at.} Mg.

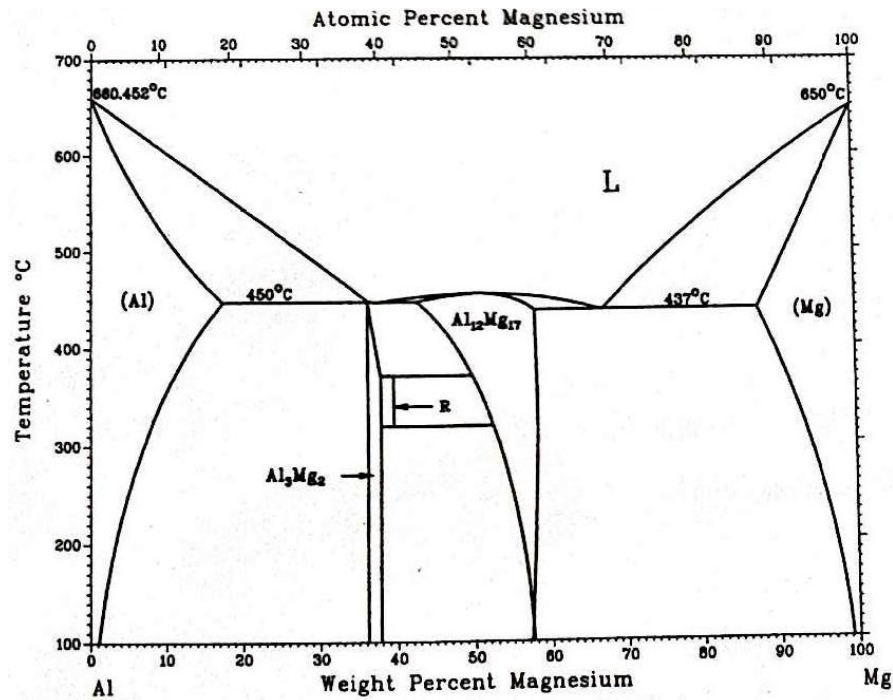


Figure 1.5: The phase diagram of binary Mg-Al alloy[139].

A combinatorial gradient of non-equilibrium Mg-Al alloys was prepared by Olk and Haddad [141]. The X-ray diffraction results showed five phases. From the Mg compositional point of view the compositions of (71 to 52 %_{at.} Mg) contains a mixture of γ $\text{Al}_{12}\text{Mg}_{17}$ and Al solid solution in Mg. The γ $\text{Al}_{12}\text{Mg}_{17}$ was exclusively identified at limited compositions (~ 50 to 40 %_{at.} Mg). Besides γ $\text{Al}_{12}\text{Mg}_{17}$, the amorphous phase arises at lower Mg compositions (35 to 38 %_{at.} Mg). The addition of more Al into the Mg-Al matrix produces the amorphous phase at ~33 %_{at.} Mg. The f.c.c. structure of Mg solid solution in Al was obtained at low Mg compositions (i.e. Mg < 26 %_{at.}). The Mg solid solution in Al extends to higher Mg compositions (up to 40 %_{at.} Mg) as obtained by Scudino et al.[142].

However, at high temperature, the solid solution comprising 40 %_{at.} Mg transforms to the β' phase. Therefore, they concluded that the solid solution is a metastable phase which transforms to a more stable phase at equilibrium.

The intermetallics of γ $\text{Al}_{12}\text{Mg}_{17}$ and β Al_3Mg_2 are repeatedly identified in the Mg-Al or Al-Mg alloys [143-146]. The rhombohedral phase (i.e. R phase) named in the literature as ϵ was detected at ~ 56 %_{at.} Al[147] at 410 °C. This phase is rarely reported in the literature.

1.6.4 Al-Mg-Zr Alloys

1.6.4.1 The Corrosion Properties of Al-Mg-Zr Alloys

Zirconium is often used as a grain refiner through adding small amounts (i.e. 0.1 up to 2 %_{wt.}) to Mg alloys[148]. This effect leads to improved corrosion resistance[149, 150] via stabilising the Mg matrix. However, zirconium has a limited solubility in Mg, therefore adding Zr in great amounts to Mg would lead Zr to precipitate out of the Mg matrix. As a result, corrosion resistance would also increase due to galvanic corrosion. This is in agreement with observations by Eimutis et al [151] where Mg-4Al-1Zr and Mg-3Al-5Zr showed better corrosion performance compared to their free Zr counterparts. However, corrosion resistance deteriorated by adding more Zr (7 and 21 %_{at.}). This is owing to the formation of nanostructured or amorphous Zr phases besides the Mg-Al matrix. Nevertheless, X-ray diffractions have shown no sign of such structures. Similar results were reproduced afterwards [152]. There are a few articles in the literature which concern the Al-Mg-Zr corrosion performance.

Adding Zr to aluminium decreases the corrosion rate significantly in [1M] HCl solution[153]. The corrosion rate of some Al-Zr alloys was three orders of magnitude lower than the aluminium corrosion rate. Moreover, adding higher amounts of Zr (57 and 71 %_{at.}) increases passivity and pitting corrosion resistance. The corrosion behaviour of arc-melted and sputtered Al-Zr alloys containing 5–71 %_{at.} Zr was explored in borate-boric acid and NaCl solution[154]. The sputtered alloys form solid solutions of Zr in Al of up to 11 %_{at.} Zr after which an amorphous phase was obtained. Contrary arc-melted alloys comprising Zr < 24 %_{at.} have had Al₃Zr and α-Al while AlZr, Al₂Zr₃, and Al₂Zr phases were identified at rich Zr (57 and 71 %_{at.}) alloys. The sputtering alloys demonstrated higher corrosion resistance and pitting corrosion potential in comparison with its arc-melted counterpart alloys. The simultaneous existence of two or three intermetallics causes lower pitting potential in the arc-melted alloys. The Al-Zr alloys usually undergo pitting corrosion[155] but its mechanism is not yet clear. Smialowska [9] reviewed this area and suggested a new mechanism of Al alloys which similar to the Al-Zr alloys ones. He concluded that pitting corrosion development is governed by the stability degree of oxidized species inside the corrosion pit and the dimension of the pit. Additionally, he did not rule out the passive film role in stopping ions

diffusing into the bulk but he downgrades its effect in preventing pitting corrosion.

1.6.4.2 The Structure of Al-Mg-Zr Alloys

There are no ternary intermetallic compounds for Al-Mg-Zr systems[156, 157]. Zirconium has limited solubility in Mg as displayed in the Mg-Zr phase diagram[104]. However, the solubility of Zr can be extended using the non-equilibrium preparation method[158]. In contrast Zr forms several intermetallics with Al. According to the Zr-Al phase diagram [159, 160] ten intermetallics of Al-Zr have been identified at equilibrium. Besides the solid, two extreme solutions of Al and Zr, those intermetallic phases versus Al composition (in atomic %) are shown **Table 1.4**. All those phases have been verified experimentally and theoretically [161-163].

Moreover, most of those phases have been obtained as metastable phases[160]. For example fast quenching of alloys comprising 27 %_{at.} Al consists of β Zr matrix and Al_2Zr . Also, Zr_5Al_3 was obtained at low temperature as hexagonal with Mn_5Si_3 structure at composition 37.5 %_{at.} Al. There is controversy about the Zr_5Al_3 structure in the literature. Murray et al [160], and some other researchers suggested hexagonal Mn_5Si_3 as the structure. However, others such as Edshammar, and Potzschke and Schubert [164, 165] have argued that the crystal structure of the Zr_5Al_3 is a tetragonal Si_3W_5 type, proving that contamination with interstitial impurities works as a stabiliser to the hexagonal Mn_5Si_3 type. A recent study revealed that Zr_5Al_3 has a tetragonal structure at temperature $> 800^\circ\text{C}$, while it has a hexagonal structure at low temperatures as metastable[166]. Schuster et al [166] confirmed that the Al_3Zr_5 phase with a Mn_5Si_3 type structure is stable only in the low temperature phase. Also, Zr_5Al_3 is stabilised by oxygen positioned inside the octahedral structure[167]. A similar effect was observed with nitrogen where Zr_5Al_3 was stabilised with about 2 %_{at.} N_2 at high temperature as $\text{Zr}_5\text{Al}_3\text{N}_{1-x}$. Other intermediate phases such as Zr_2Al_3 , ZrAl_2 and ZrAl_3 have been obtained at ≥ 60 %_{at.} Al[160].

Zr_5Al_3 and Zr_3Al_2 are used as hydrogen getters[168]. Zr_5Al_3 absorbs hydrogen even at 1 atm forming $\text{Zr}_5\text{Al}_3\text{H}_8$ [169].

Table 1.4: Structural details of intermetallic and solid solutions of Zr-Al system.

Phase	Composition % _{at.} Al	Pearson symbol	Space group	prototype
α Zr	0 to 10.5	hP2	$P6_3/mmc$	Mg
β Zr	0 to 26	cI2	Im3m	W
Zr ₃ Al	25	cP4	Pm3m	AuCu ₃
Zr ₂ Al	33.3	hP6	$P6_3/mmc$	Ni2In
Zr ₅ Al ₃	37.5	tI32	I4/mcm	W ₃ Si ₃
Zr ₃ Al ₂	40	tP20	$P4_2/mmm$	Al ₂ Zr ₃
Zr ₄ Al ₃	42.9	hP7	P6	Al ₃ Zr ₄
Zr ₅ Al ₄	44.4	hP18	$P6_3/mmc$	Ga ₄ Ti ₅
ZrAl	50	oC8	Cmcm	CrB
Zr ₂ Al ₃	60	oF40	Fdd2	Al ₃ Zr ₂
ZrAl ₂	66.7	hP12	$P6_3/mmc$	MgZn ₂
ZrAl ₃	75	tI16	I4/mmm	Al ₃ Zr
Al	99.93 to 100	cF4	Fm3m	Cu

2. Experimental

2.1 High-Throughput Physical Vapour Deposition (HT-PVD) system

The thin film alloys were prepared by the high throughput physical vapour deposition as shown in **Figure 2.1**. This system contains two chambers which are connected with a Cryo-Pump (Helix Tech. Corporation) and titanium sublimation (Varian) pump, in order to obtain the ultrahigh vacuum (UHV) condition. Chamber (A) was used in this study. Samples were transferred to the chamber through the buffer line, where a base pressure of around 1×10^{-8} mBar was applied using a homemade trolley. After venting the isolated buffer line adjacent to the transfer load lock, samples were loaded onto named specimen holders sitting on the trolley. Subsequently, the load lock was closed and the buffer line was pumped down from atmosphere pressure to UHV. Then the samples were delivered to chamber (A) by driving a trolley on a fixed railway inside the buffer line. In the front of the chamber gate, the sample was picked up from the trolley and placed in a transfer arm, after which the sample was transported into the chamber. The PVD chamber, whose pressure was kept at 1×10^{-10} mBar, consists of six off-axis sources: three electron beam guns (e-gun; Temescal) and three effusion “Knudsen” cells (K-cells; DCA HTKS). These are shown in **Figure 2.2** (B). Also six HT “wedges”, which are controllable shutters, were incorporated above each source. The sample was held at the top of the chamber and was positioned in a depositing height using a manipulator. An oil free rotary pump (Pfeiffer) and turbo-molecular pump (Pfeiffer) were used to pump down the load lock buffer line and growth chamber after venting.

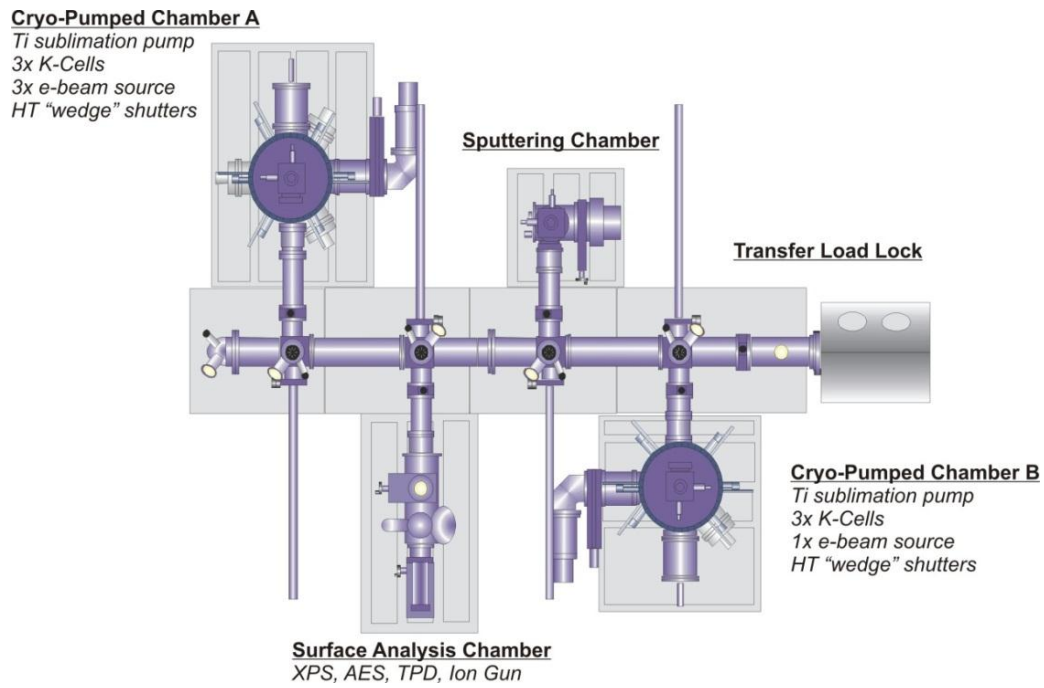


Figure 2.1: Schematic of high-throughput physical vapour deposition (HT-PVD) system.

(A)



(B)

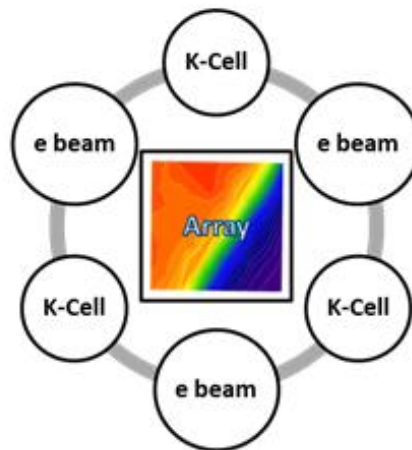


Figure 2.2: (A) Growth chamber of high throughput PVD in which parallel co-deposition of binary alloys was prepared, (B) Top view of high throughput PVD chamber. Sources were arranged in 120° geometry.

2.2 The combinatorial or High-Throughput Methodology

The gradient growth of Ni-Cr, Ni-W, and Mg-Al thin film alloys was achieved by adapting the fixed shutters and deposition rate methodology. This is clearly described elsewhere [170]. **Figure 2.3 (A)** defines the notion of this method using a single off-axis source [170]. The flux of evaporated material from the source (C) can be changed by the aperture or wedge shutter (B). Consequently, the deposit concentration on sample (A) will vary and create a shadow. At B_{min} , no wedge “shutter” is applied. Therefore, a uniform deposition would perform. However, at B_{max} the source is completely covered and, as such, no deposition would occur. Therefore, wedge “ramp shape” can be obtained by adjusting the aperture “wedge shutter” between B_{min} and B_{max} . For example, if the aperture is positioned at (B_1), then the C_1 side of the source would see the entire sample from A_1 to A_2 , but C_2 would see only A_1 . As a result, more deposits would occur at A_1 side compared to A_2 side, hence creating ramp shape (**Figure 2.3(B)**). Nevertheless, a uniform film can be achieved by creating two similar ramp “wedge” shapes from two opposite sources (e.g. A, B) on A sample (A_1 to A_2) as shown in **Figure 2.3(B)**. This is accomplished by calibration. This is the first essential step in every deposition course. The calibration performs by altering the B value of the aperture “shutter” and measuring film composition by Energy Dispersive X-ray Spectroscopy (EDX). This would reveal the wedge “ramp” shape, which provides a quantitative analysis of how gradients grow on the sample. After obtaining the desirable compositional range, the deposition rate and the B value of the aperture must be kept unchanged during the deposition course. The deposition rate is monitored by quartz micro-balance (provided by Kurt J. Lesker Company). Two types of substrate (i.e. glass and used silicon) were used in the calibration process. The film thickness is usually checked by atomic force microscope (AFM) before making real samples.

Figure 2.4 shows an example of calibrated sample where both composition map (A) and wedge “ramp” shape (B) are shown.

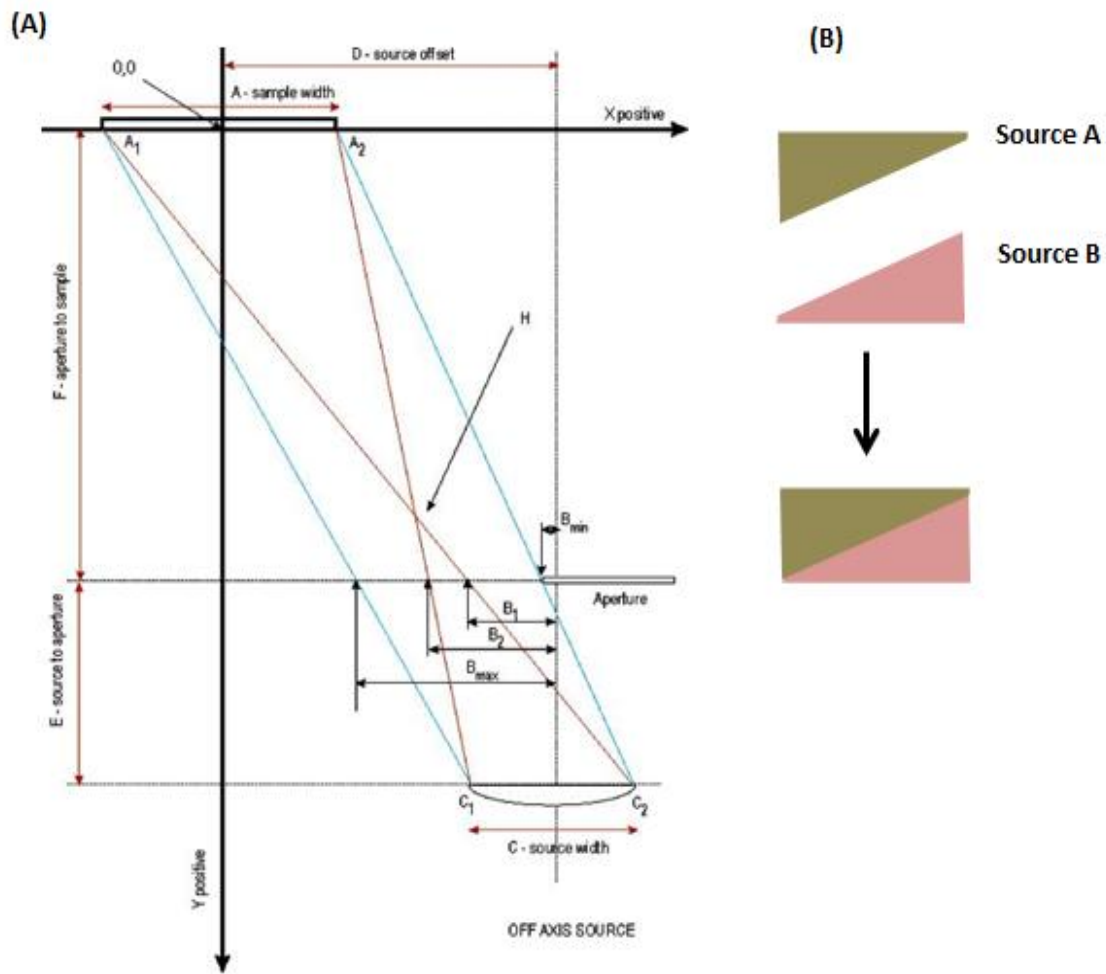


Figure 2.3: (A) Gradients growth methodology from single off-axis source [170], (B) gradients growth when aperture situated at B_1 .

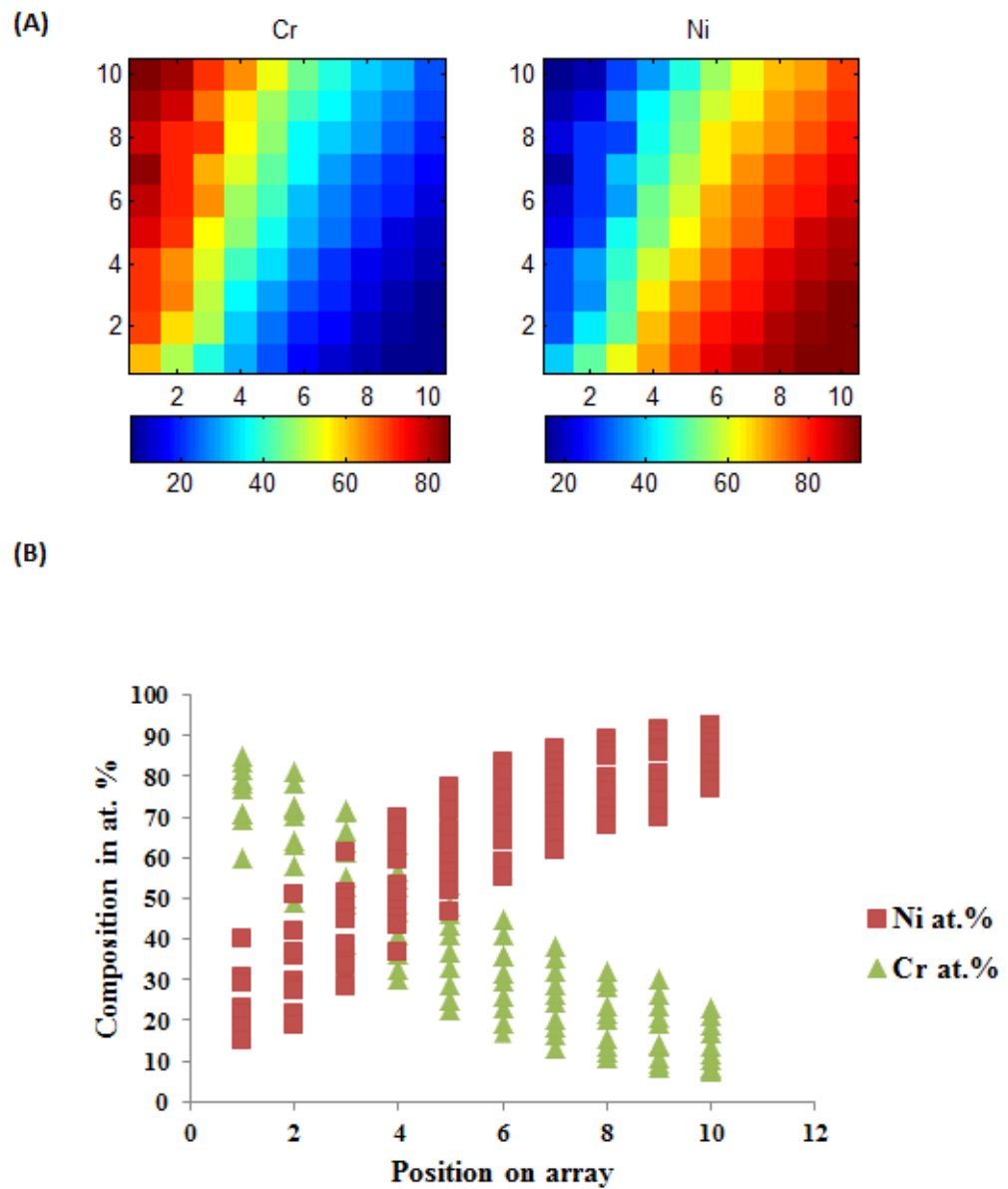


Figure 2.4: The composition of calibrated NiCr array as (A) map (B) wedge “ramp” shape.

2.3 Preparation of Thin Film Alloys and Substrate Types

Ni-Cr and Ni-W alloys were prepared by simultaneously depositing the elements Cr (Alfa Aesar 99.99% purity), Ni (Alfa Aesar 99.95%), Ni (Alfa Aesar 99.95%), and W (Alfa Aesar 99.97% purity) respectively from the electron beam sources arranged in a 120° geometry. The thin film alloys of Al-Mg (i.e., the low temperature elements) were co-evaporated simultaneously from K-cell sources. However, for ternary Al-Mg-Zr alloys, Zirconium was co-evaporated from the electron beam source.

This way of depositing allows the complete mixing of elements, which minimises surface segregation and eliminates any need for post-deposition annealing.

Thin films were deposited on two substrates. A 32 mm² silicon/silicon nitride substrate (Nova Electronic Materials), covered by a (10 × 10) metallic mask, were used for the X-ray diffraction study (**Figure 2.5(A)**). Films were also deposited on the (10 × 10) silicon micro-fabricated array of independently addressable working electrodes (Ilika Technologies Ltd.), which is used for high throughput combinatorial electrochemical screening (**Figure 2.5(B)**)[170]. The working electrode “fields” and contacts are made from gold. This array is called an electrochemical array, which from now on will be presented as E-chem. Each electrode has the same area which is equal to 0.014 cm². All the samples’ “arrays” were washed with ethanol and water before depositing. Deposition conditions, aperture “shutter” value B, and material types are summarised in **Table 2.1**.

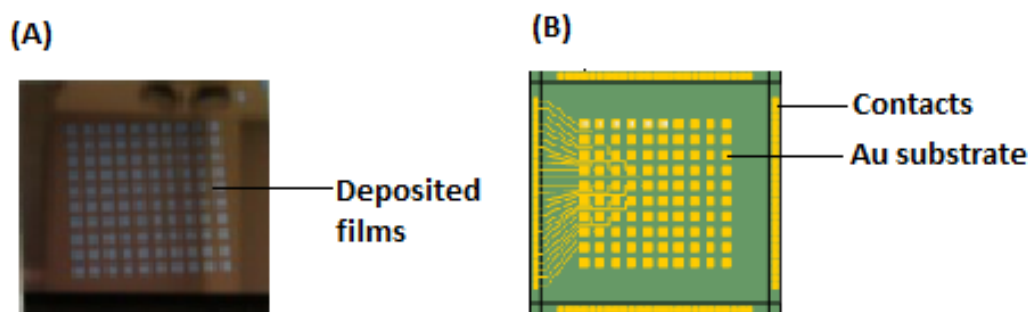


Figure 2.5: (A) Silicon/silicon nitride substrate used for XRD study. (B) Silicon micro-fabricated array used for electrochemical screening[170].

Table 2.1: Deposition conditions, substrates, aperture value, and film material types.

Sample number	Film type	Substrate	Aperture B (mm)	Deposition time (min.)	Substrate temperature (K)	Evaporating temperature (K)
6648	Ni-Cr	Si-nitride*	Ni = 37 Cr = 37	90	323	E-beam
7149 (=A)	Ni-Cr	E-chem ^x	Ni = 37	90	323	E-beam
7150 (=B)			Cr = 37			
6763 (=C)						
6718	Ni-W	Si-nitride*	W = 0 Ni = 37	120	323	E-beam
6722	Ni-W	E-chem ^x	W = 0 Ni = 37	120	323	E-beam
6723	Ni-W	E-chem ^x	W = 0 Ni = 37	120	323	E-beam
6730	Ni-W	E-chem ^x	W = 0	120	323	E-beam
6731			Ni = 37			
7358	Al-Mg	Si-nitride*	Al = 42 Mg = 40	80	300	Al = 1568 Mg = 798
7355	Al-Mg	E-chem ^x	Al = 42 Mg = 40	90	300	Al = 1568 Mg = 798
7522	Al-Mg	Si-nitride*	Al = 39 Mg = 40	90	300	Al = 1578 Mg = 793
7521	Al-Mg	E-chem ^x	Al = 39 Mg = 40	120	300	Al = 1578 Mg = 793
7541, 7544	Al-	Si-nitride*	Al = 39	120	323	Al = 1578
7537, 7534	Mg-Zr	E-chem ^x	Mg = 40			Mg = 793
7543			Zr = 30			Zr = E-beam

*Silicon/silicon nitride substrate, ^x electrochemical array with gold as substrate.

2.4 Bulk “Commercial” Samples

Commercial rods Ni (99.9% purity) and three Ni-Cr alloys (90:10 %_{wt.}, 80:20 %_{wt.}, 50:50 %_{wt.}) were provided by Goodfellow. The chromium rod (99.9% purity) was supplied by Testbourne Ltd. The diameter of the samples was 12 mm, except for NiCr (50:50 %_{wt.}) which was 10 mm. All samples were manually polished with three types of silicon carbide paper 800, 1200, and 2000, for one minute each. Afterwards, samples were manually polished with three Alumina powder 1, 0.3, and 0.05 micron, for three minutes each in order to produce a smooth and reproducible surface.

2.5 Characterisation Instruments

2.5.1 X-ray Diffraction (XRD)

A Bruker D8 powder diffractometer combined with a C2 area detector was used to characterise the films' structure, phases, and grain sizes. X-ray diffraction was carried out using Cu K α ($\lambda = 1.5418 \text{ \AA}$) operating at 40 kV, 30 mA. Macro analysis of 100 fields “alloys” was achieved using a sequential scan. The scan rate was 600 s per point. Integration was achieved by GADDS software connected to the X-ray machine.

The interaction between X-ray beams and matter are firstly described by H.W Bragg and William Lawrence (Equation 2-1), now known as Bragg's law.

$$n\lambda = 2d \sin \theta \quad \text{Equation 2-1}$$

Where

λ = wavelength of X-ray beam

d = interplanar distance between crystal planes

θ = Bragg's angle, between the lattice plane and X-rays

Figure 2.6 shows a constructive interference for $(n\lambda)$ diffracted by crystal planes as described by Bragg. The second ray travels further which equals $(AB + BC)$. Therefore, Bragg's angle can be calculated as follows:

$$\sin \theta = \frac{AB}{d} \text{ or } d \sin \theta = AB \quad \text{Equation 2-2}$$

Thus, constructive interference only occurs if

$$2d \sin \theta = (AB + BC) = n\lambda \quad \text{Equation 2-3}$$

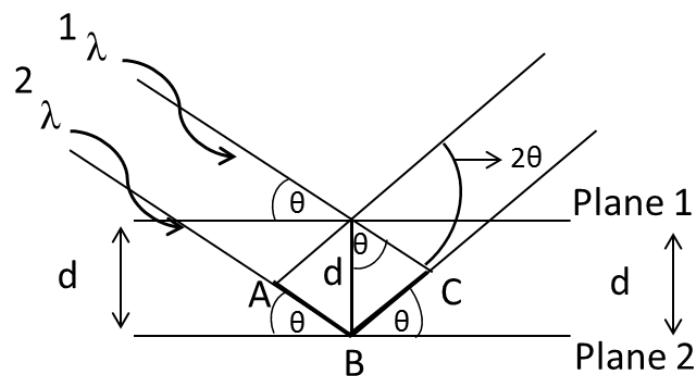


Figure 2.6: Diffraction caused by crystallised planes.

The Bruker D8 powder diffractometer, which uses Bragg-Brentano geometry, is shown in **Figure 2.7**. It uses a scintillation counter as detector instead of a film.

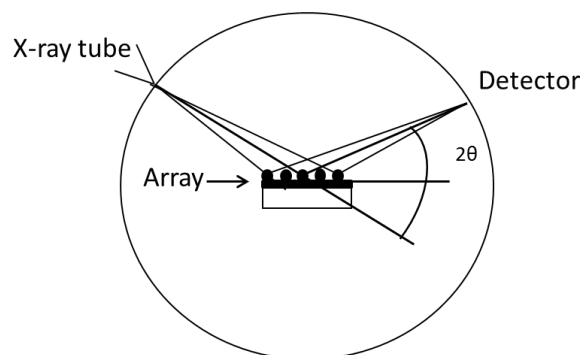


Figure 2.7: D8 diffractometer measurement diagram.

The grain sizes (L) were determined using the Scherrer Equation 2-4. The full width of half maximum (FWHM) values was extracted from the main Bragg peak for each alloys' system.

$$L = K\lambda / (B \cos \frac{\theta}{2}) \quad \text{Equation 2-4}$$

Where

λ = wave length of the incident X-rays

K= numerical constant = 0.93

B= half width of half maximum of the diffracted peak

$\theta/2$ = Bragg's angle

2.5.2 Energy Dispersive X-ray Spectroscopy (EDS)

Composition analysis was carried out using Electron Dispersive X-ray Spectroscopy (EDS) using a JEOL JSM5910 and Oxford Instruments INCA 300. EDX analysis was obtained using 10 kV. Thin film compositions are always presented as an atomic percentage.

2.5.3 Atomic Force Microscope (AFM)

Thickness calibration was carried out using a Thermomicroscope Autoprobe (M5) (Park Scientific Instruments) equipped with a high resolution camera that allows the researcher to situate a cantilever near to the film edges. Measurements were carried out using the top scan mode. Also, AFM was used to examine surface topographies for Al-Mg-Zr samples. This allows the measurement of the roughness factor as well.

2.5.4 Potentiostat

Two types of Potentiostat were utilised in this study. A multichannel current follower/potentiostat system (Ilika Technologies Ltd.) which is described elsewhere [55] was used to apply high-throughput electrochemical screening on a 100 electrodes micro-fabricated array. The potential is applied simultaneously to all electrodes, while current is sequentially recorded using a

fast multiplexed current follower. Data is monitored and collected by a PC supported by Paradise software (written by Ilika Technologies Ltd). The current sensitivity is $10 \mu\text{A V}^{-1}$.

Another potentiostat, which was utilised to perform electrochemical measurements of commercial bulk samples, was a Uniscan instrument model PG581.

2.5.5 Electrochemical Cell

A three compartment glass cell, specially designed to accommodate the high-throughput array was used, and is shown in **Figure 2.8** [41]. A reference electrode was mounted in a Luggin capillary with a tip situated a few millimetres away from the E-chem array. The counter electrode (Gold mesh, 2 cm^2) was separated by a glass sinter. A gasket was used to ensure no leakage could occur. The cell was jacketed although all experiments were performed at 298 K.

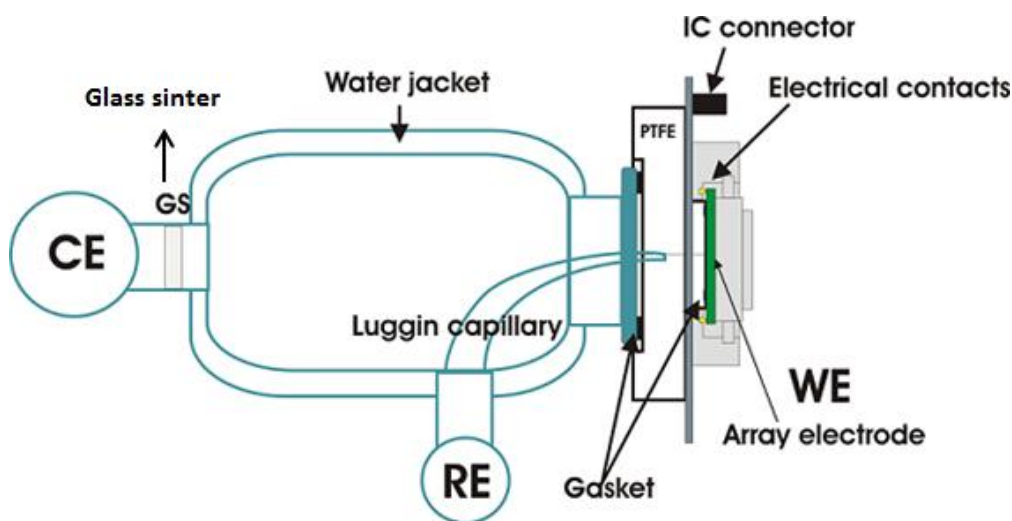


Figure 2.8: Electrochemical cell used in a parallel high-throughput electrochemical screening, adapted from[41].

2.5.6 Reference and Counter Electrodes

A saturated calomel electrode Hg/Hg₂Cl₂ sat. KCl [(SCE)/ 0.24V vs. SHE] (provided by Fisher Scientific) and a homemade mercury mercurous sulphate electrode Hg/Hg₂SO₄, K₂SO₄ (saturated) [MMSE/0.64V vs. SHE] were used as reference electrodes (RE). The counter electrode (CE) was a 2 cm² mesh gold.

2.6 Corrosion Electrolyte

Three electrolytes were used to perform electrochemical measurements. A phosphoric acid solution (pH 3) electrolyte was prepared from orthophosphoric acid H₃PO₄ with an assay of 86.2% supplied by Fisher Scientific and ultra-pure water. Besides this, four sodium chloride solutions with a concentration of [0.1, 0.05, 0.02, 0.005 M] were used and prepared from pure dried vacuum salt (PDV) supplied by INEOS enterprises. All solutions were made using ultra-pure water (18.2 MΩ cm, ELGA). Details of the materials and chemicals utilised in this study are presented in **Table 2.2**.

Table 2.2: Materials and chemicals specification and suppliers name

Material name	State	Purity (%)	Supplier name
Nickel	Solid	99.95	Alfa Aesar
Chromium	Solid	99.99	Alfa Aesar
Tungsten	Solid	99.97	Alfa Aesar
Magnesium	Solid	99.98	Alfa Aesar
Aluminium	Solid	99.99	Alfa Aesar
Zirconium	solid	99.8	Alfa Aesar
Nickel	Solid “rod”	99.99	Goodfellow
Chromium	Solid “rod”	99.99	Testbourne Ltd
NiCr	Solid “rod”	90:10	Goodfellow
NiCr	Solid “rod”	80:20	Goodfellow
NiCr	Solid “rod”	50:50	Goodfellow
Orthophosphoric acid	Liquid	86.2	Fisher Scientific
Sodium chloride	Solid “powder”	99.9	INEOS enterprises

2.7 Corrosion (Polarisation) Resistance (R_p) Determining Methods

A cyclic voltammetry (CV) technique (i.e. a reversal of linear sweep voltammetry) (LSV) was employed. A wide potential window of cyclic voltammetry scan was performed in every new alloy system, in order to inspect the electrochemical behaviour of the system being studied. Subsequently, the potential window reduces to $\sim \pm 500$ mV vs. open circuit “corrosion” potential (E_{corr}). Currents were normalised to geometric current densities.

The corrosion (polarisation) resistance (R_p) was extracted from the CV data using both the Tafel extrapolation and linear polarisation resistance (LPR) methods.

2.7.1 Corrosion Resistance (R_p) Determining by Tafel extrapolation Method

Initially, the corrosion current density (i_{corr}) was extrapolated from the Tafel plot (Equation 2-5). Subsequently, it was converted to a corrosion resistance (R_p) using (Equation 2-6) after assuming the two extreme values of B from (Equation 2-7), which can lie in the range 13 to 26 mV, following Stern and Wiesert [171] and assuming $b_a = b_c = 60$ mV, and $b_a = 120$ mV, $b_c = 120$ respectively. Therefore B values are always assumed to be either 13 or 26 mV.

$$\log | -i | = \log i_{\text{corr}} - \frac{\eta}{b_c} \quad \text{Equation 2-5}$$

$$R_p = \frac{B}{i_{\text{corr}}} \quad \Omega \text{ cm}^2 \quad \text{Equation 2-6}$$

$$B = \frac{b_a b_c}{2.303(b_a + b_c)} \quad \text{Equation 2-7}$$

Figure 2.9 displays an example Tafel plot (Equation 2-5) from which the corrosion current density was obtained from the intercept. In this example $i_{\text{corr}} = 43.77 \mu\text{A cm}^{-2}$. Assuming the limiting values of B from (Equation 2-7), the corrosion current is converted to corrosion resistance (R_p) by (Equation 2-6). The corrosion current (i_{corr}) and corrosion resistance (R_p) are relatively

insensitive to the values of b_a and b_c (Equation 2-7), where both appear in the numerator and denominator. In other words, the general trend of the data set of corrosion resistances (R_p), determined by the two limiting values of B , will be the same, and the only difference will be in the R_p absolute values.

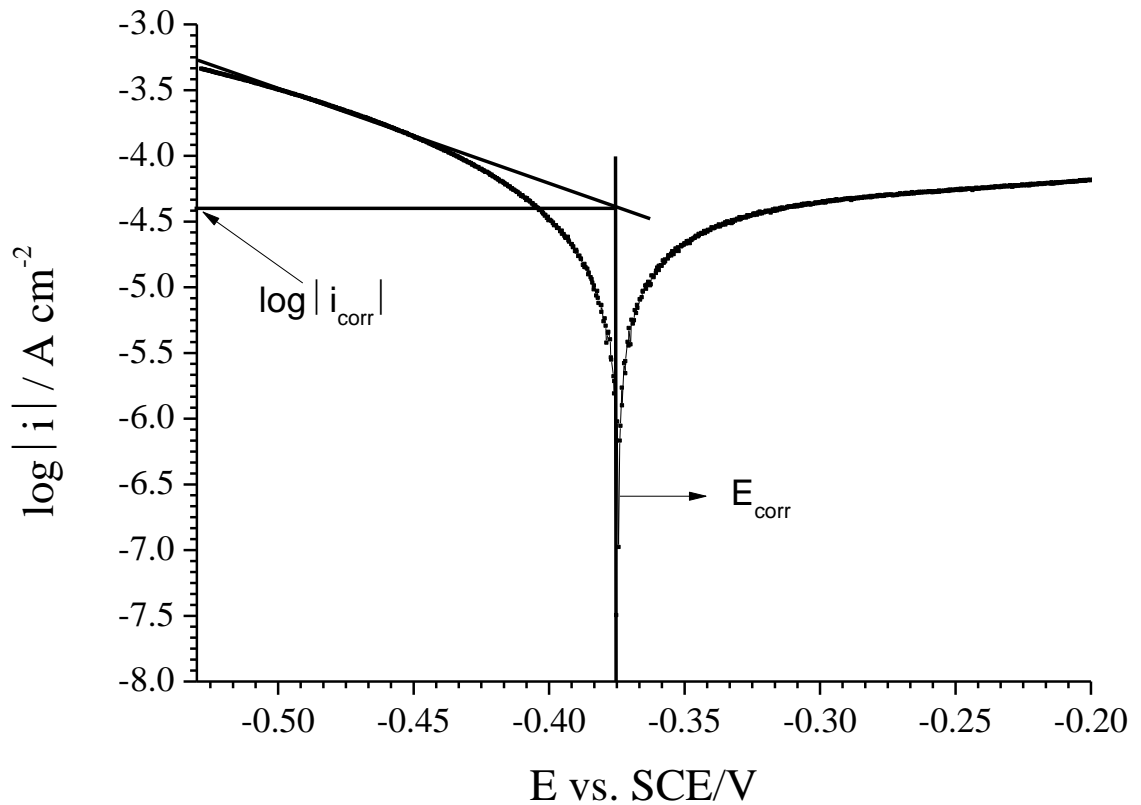


Figure 2.9: Example of how corrosion current (i_{corr}) is extrapolated from Tafel plot. This plot is for Ni₆₇W₃₃ alloy.

2.7.2 Corrosion Resistance (R_p) Determined by Linear Polarisation Resistance (LPR) Method.

The second method by which the corrosion resistances (R_p) were extracted from the cyclic voltammograms data was linear polarisation resistance (LPR), i.e., the slope of the linear current-potential dependence at the zero current limit, as expressed in Equation 2-8.

$$R_p = \left(\frac{\Delta E}{\Delta i} \right)_{i=0} \quad \Omega \text{ cm}^2 \quad \text{Equation 2-8}$$

The linear relationship is limited within a few millivolts away from the zero current potential ($E_{i=0}$), or what is also called corrosion potential (E_{corr}). **Figure 2.10** shows an example of the linear current-potential dependence at the zero current limit (inset figure), as expressed in Equation 2-8 for anodic and cathodic over-potentials of ± 10 mV. The zero current potential ($E_{i=0}$) is -0.385 V vs. SCE. Therefore, the corrosion resistance (R_p) is the reciprocal of the slope of a linear fit to the data shown in the inset figure (**Figure 2.10**). In this example, $R_p = 1063 \Omega \text{ cm}^2$.

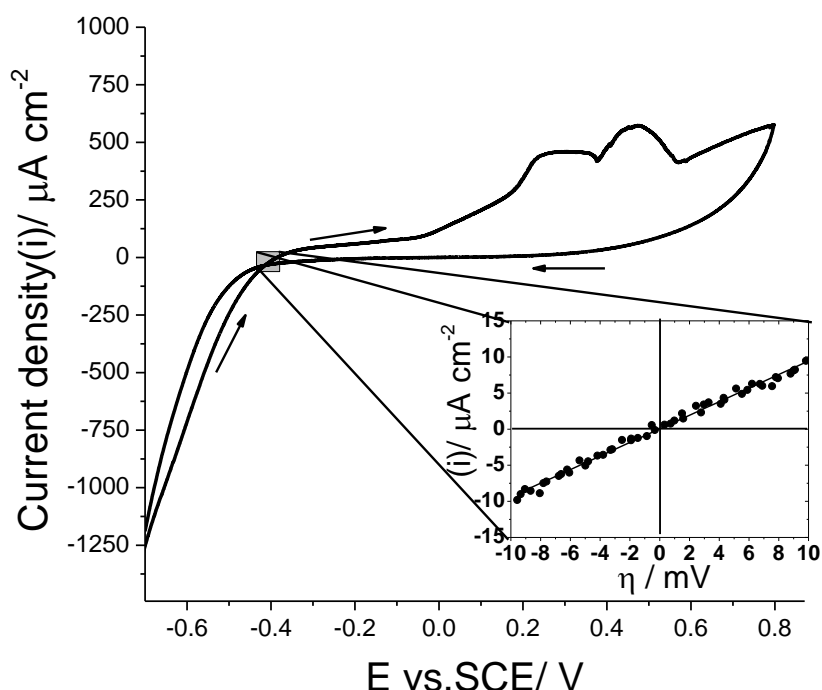


Figure 2.10: Example of linear polarisation resistance (LPR) behaviour, from which corrosion resistance has been obtained. This data is shown for $\text{Ni}_{67}\text{W}_{33}$ alloy. The scan rate is 20 mV s^{-1} .

3. Ni-Cr Thin Film Alloys

3.1 Introduction

The Ni-Cr alloys are widely used, particularly in a very aggressive corrosion environment. However, their corrosion resistance relies on their chromium composition. Therefore, this chapter introduces an assessment of the corrosion behaviour of a series of Ni-Cr thin film alloys manufactured by a combinatorial gradient method based on MBE sources. The alloy's structure and composition are characterised by X-ray diffraction (XRD) and energy dispersive X-ray spectroscopy (EDS). In addition, the corrosion behaviour of nickel, chromium, and selected Ni-Cr bulk "commercial" alloys are measured and compared to their equivalents from the Ni-Cr thin film alloys. The effect of chemical composition and structure on corrosion behaviour is discussed as well.

3.2 Structure Characterization of As-deposited Ni-Cr Film Alloys

High throughput X-ray diffraction measurements on a 10x10 array Ni-Cr film array have been recorded and are presented in **Figure 3.1**. Chromium composition (in atomic %) was measured by EDS and is printed over each field. Four distinctive zones were found, labelled here in green, orange, grey, and gold. Each zone represents one or two unique patterns. For example, the green and gold zones show diffraction comprising two peaks at $2\theta = 44.5^\circ$ and 52° and 44.5° and 65° respectively. The orange zone shows only one peak at 44.1° 2θ , demonstrating high intensity. The grey zone consists of four unique diffraction patterns whose peaks appear at $(40^\circ, 44^\circ)$, (40°) , $(39.9^\circ, 45^\circ)$, and $(40^\circ, 45^\circ, 66^\circ)$.

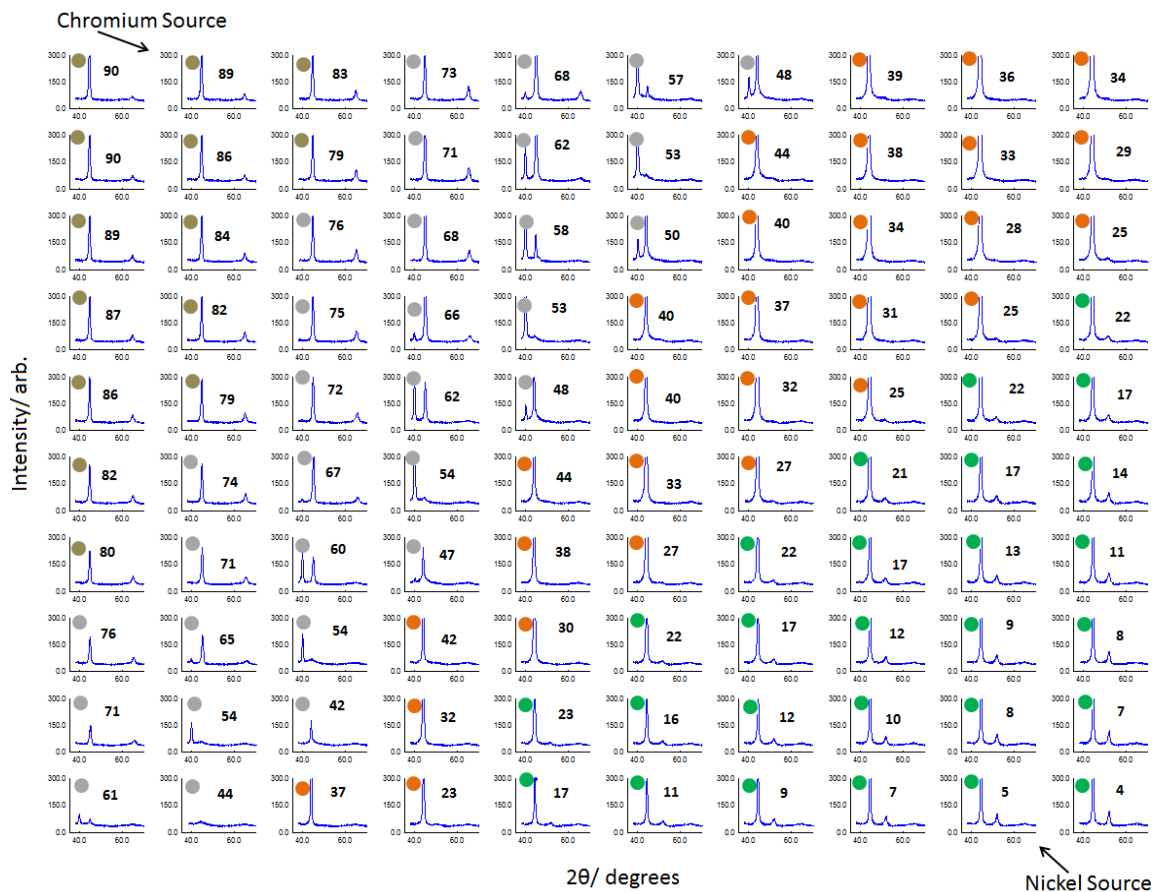


Figure 3.1: X-ray diffraction patterns of as-deposited Ni-Cr on a 10x10 array (#6648) silicon nitride substrate at 323 K. Chromium composition is measured and enclosed in each square. Composition is divided to Four zones namely green (4-22 %_{at.} Cr), orange (28-45 %_{at.} Cr), grey (~ 47-70 %_{at.} Cr), and gold (74-90 %_{at.} Cr). The scale are (X = 35-70 and Y = 0-300).

For further investigation, the selected alloy(s) “field(s)” which represent each zone are presented in **Figure 3.2**. Also, the detected phase and its compositional range are included in the right side of **Figure 3.2**.

The green zone (4-22 %_{at.} Cr) has two peaks at $2\theta = 44.5^\circ$ and 52° related to f.c.c. γ -Ni solid solution containing chromium [83, 172]. These two peaks shift to a lower angle by 0.2° 2θ with increasing chromium content. The f.c.c. (Fm3m) γ -Ni structure associated with the solid solution is expected at equilibrium [81] (0 to 47 %_{at.} Cr) and non-equilibrium (0 to 50 %_{at.} Cr) [84, 85].

The diffraction pattern observed in the orange zone (28 to 45 %_{at.} Cr) displays only one peak. This peak appears at $2\theta = 44-44.2^\circ$ and demonstrates high intensity, which is not possible to be noticed in **Figure 3.2** where the

logarithmic scale has been applied. This peak associates to oriented γ -Ni(111) Bragg peak as a result of a preferred growth orientation in the thin film. This is a phenomena which has been observed in several Ni-Cr thin films and reported elsewhere [89, 173]. This is in contrast with the Ni_2Cr or γ phase corresponding to the (Immm) space group and expected under equilibrium conditions in the range 21 to 37 %_{at.} Cr [81].

From the grey zone ~48-70 %_{at.} Cr, five alloy compositions have been chosen to represent the five X-ray diffraction patterns existing in that compositional range (as shown in **Figure 3.2**). Firstly, at 48% Cr (e.g. $\text{Ni}_{52}\text{-Cr}_{48}$) two peaks appear at $2\theta = 40^\circ, 44.1^\circ$. The first peak is the onset of a $\sigma\text{-Cr}_3\text{Ni}_2$ phase [87-89] and relates precisely to (002) structure. The second peak associates to the oriented γ -Ni (111) Bragg peak. Incorporation of more Cr (e.g. $\text{Ni}_{47}\text{-Cr}_{53}$) resulted in an increase of the intensity of the (002) peak and a complete disappearing of oriented γ -Ni (111) at $44.1^\circ 2\theta$. Besides, a new peak for the $\sigma\text{-Cr}_3\text{Ni}_2$ phase has surfaced at $2\theta = 44.8^\circ$ as displayed by $\text{Ni}_{42}\text{-Cr}_{58}$. This indicates that at ~ 60 %_{at.} Cr the $\sigma\text{-Cr}_3\text{Ni}_2$ phase is prevailed.

Another σ metastable phase has been observed at ~ 62 %_{at.} Cr as displayed by the $\text{Ni}_{38}\text{-Cr}_{62}$. Three peaks appear at $2\theta = 40^\circ, 45^\circ, \text{ and } 66^\circ$. According to the PDF cards [174, 175], which include all diffraction peaks data for predetermined phases and published by International Centre for diffraction data (ICDD), and [89], the first peak is for (002) of the $\sigma\text{-Cr}_3\text{Ni}_2$ while others are for (041) and (410) structures of $\sigma\text{-Cr}_7\text{Ni}_3$ phase. Similar results have been observed elsewhere [87-89].

From the fourth zone (gold) two diffraction patterns are selected and presented in **Figure 3.2**. The diffraction pattern of the $\text{Ni}_{26}\text{-Cr}_{74}$ shows two peaks at $2\theta = 44.75^\circ, 65.2^\circ$. These peaks shift to a lower angle at rich chromium alloys (e.g. $\text{Ni}_{11}\text{-Cr}_{89}$). According to the PDF card [176] this relates to $\alpha\text{-b.c.c.}(110)$ structure with space group of (Im3m), which is corresponding to nickel solid solution in chromium. This in agreement with observations by Vollaro et al. [83]. Moreover, this phase is expected at compositional region 75-90 % of Cr irrespective of the method by which Ni-Cr films are prepared [83-88].

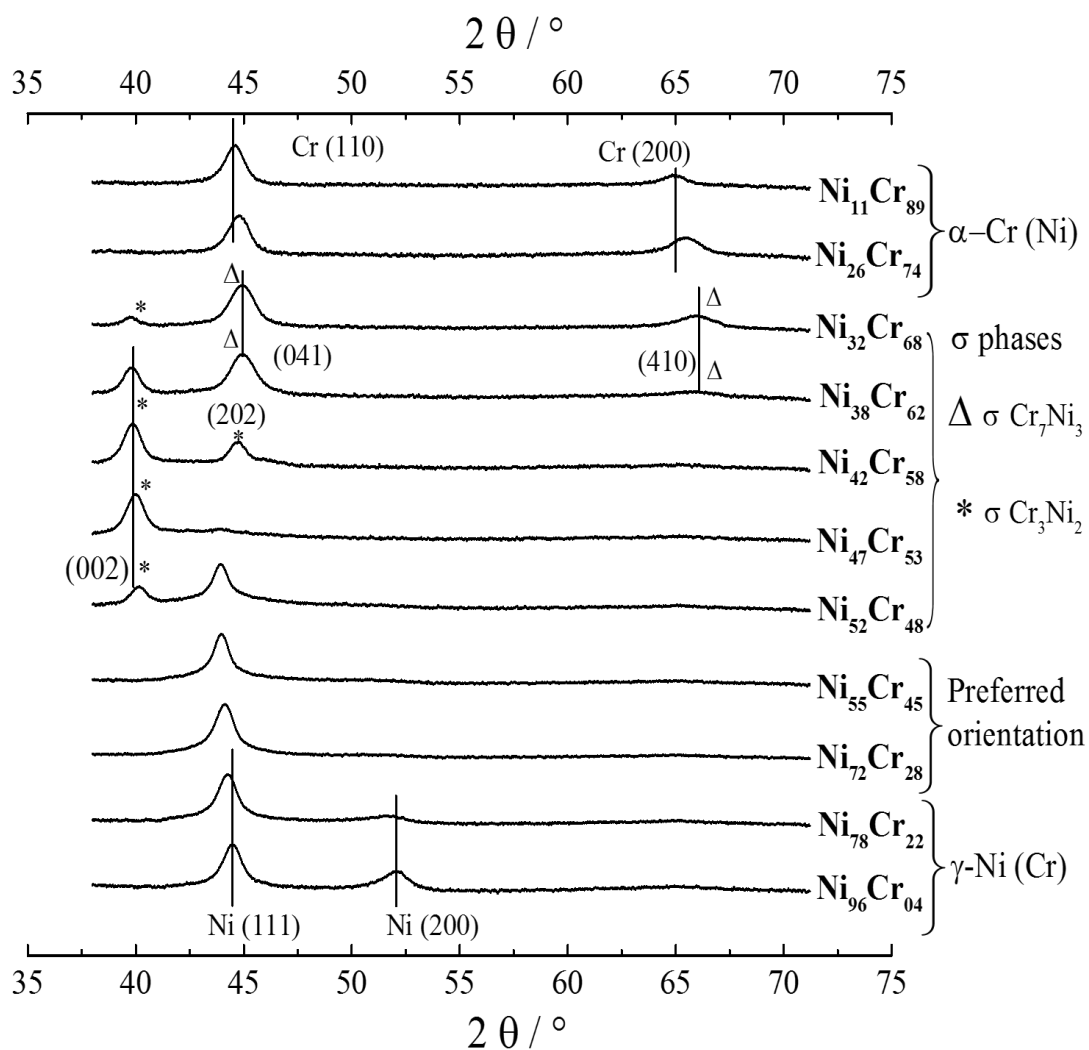


Figure 3.2: X-ray diffraction patterns of a series of as-deposited Ni-Cr thin film alloys of composition range of 4-89 %_{at.} Cr. The films are deposited on a silicon nitride substrate at ~ 300 K. Four regions are identified, namely Cr solid solution in γ -Ni (111), a preferred orientation of the γ -Ni (111) phase, two σ phases (Cr_3Ni_2 and Cr_7Ni_3), and Ni solid solution in α -Cr. Compositions in %_{at.} are determined by EDS.

All the previous patterns are defined and enclosed in the right side of **Figure 3.2**. Moreover, a summary of X-ray diffraction data, phases, and alloy compositions is presented in **Table 3.1**.

Table 3.1: XRD data and identified phases for selected Ni-Cr alloys.

Compositional ranges of Cr (% _{at.})	Peaks position (2 θ)	Phase	Structure	Space group	Reference
4 to 22	44.5° and 52°	γ -Ni(111)	cubic	Fm3m*	[81, 84, 85]
28 to 45	44-44.2°	oriented γ -Ni(111)			[89, 173]
53 to 58	40°, 44.8°	σ -Cr ₃ Ni ₂	tetragonal	P4 ₂ /mnm*	[87-89]
62 to 68	40°, 45°, and 66°	σ -Cr ₃ Ni ₂ σ -Cr ₇ Ni ₃	tetragonal	P4 ₂ /mnm*	[87-89]
74 to 89	44.75°, 65.2°	α -b.c.c(110)	cubic	Im3m*	[83-88]

* Details about structure and space groups are included in the appendix.

3.3 Electrochemical Measurements of Ni-Cr Thin Film in Phosphoric Acid pH 3 at 293K.

3.3.1 Cyclic Voltammetry

The electrochemical measurements are obtained by performing a cyclic voltammetry (CV) scan. The phosphoric acid solution [pH 3] at 293 K is used as a corrosion electrolyte. Before applying the scan, the solution was purged with argon for 20 min in the presence of the sample. **Figure 3.3** displays the first anodic sweep of cyclic voltammograms recorded on a 10x10 Ni-Cr array as a function of chromium composition. The currents are normalised to geometric area. At the compositions $31 \leq \text{Cr } \%_{\text{at.}} \leq 65$ the voltammetry does not significantly change. However, an abrupt change in behaviour appears at ca. 50 $\%_{\text{at.}}$ Cr.

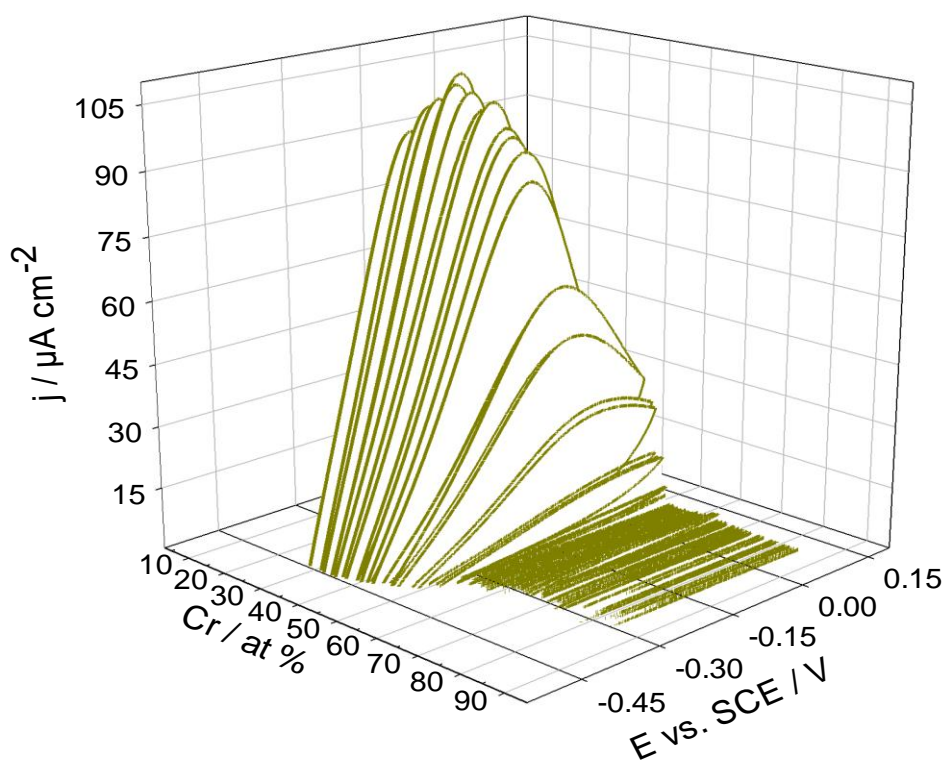


Figure 3.3: The first anodic sweep of the cyclic voltammograms of 100 Ni-Cr alloys (#7149) deposited at room temperature. The electrolyte is phosphoric acid (pH 3) solution purged with Ar for 20 min at room temperature. The scan rate was 20 mV s^{-1} . Compositions were determined by EDS.

To investigate the alloy composition effect, six cyclic voltammograms are chosen from the compositional regions where the change in redox and corrosion behaviour is greatest. Results are shown in **Figure 3.4**. Note that the current scale is not the same for each composition. As one would expect, both the anodic and cathodic processes are strongly influenced by the composition of the Ni-Cr alloy. For compositions $< \text{ca. } 50 \text{ \%}_{\text{at.}} \text{Cr}$, the cathodic current density increases rapidly and becomes irreversible. This change is accompanied by the appearance of a large anodic polarisation wave. Also the anodic or oxidation peak shifted to more negative potentials for nickel rich alloys. However, the size of the anodic wave at rich nickel $\geq 65 \text{ \%}_{\text{at.}} \text{Ni}$ has been slightly reduced (**Figure 3.3**).

Wylie et al.[177] similarly observed an apparent oxidation wave for the Ni-based dental casting alloy with $< 18 \text{ \% at Cr}$ whereas the alloy containing $> 30 \text{ \% at Cr}$ shows passive behaviour with low current density; the modified Fusayama's artificial saliva was used as a corrosion electrolyte at 310 K.

Comparison of this change (from active to passive voltametric behaviour as a function of composition) with the structural data obtained from XRD (**Figure 3.2**) reveals that it appears to correspond to the compositional onset of formation of the Ni-Cr σ - phases, namely $\sigma\text{-Cr}_3\text{Ni}_2$ and $\sigma\text{-Cr}_7\text{Ni}_3$. The onset of $\sigma\text{-Cr}_3\text{Ni}_2$ appears at $\sim 50 \text{ \%}_{\text{at.}} \text{Cr}$, which coincides with the massive reduction of anodic polarisation (as shown in **Figure 3.3** and **Figure 3.4**). This compares to the passive behaviour of the austenitic stainless steel, in which above 12 % Cr largely was enhanced[7].

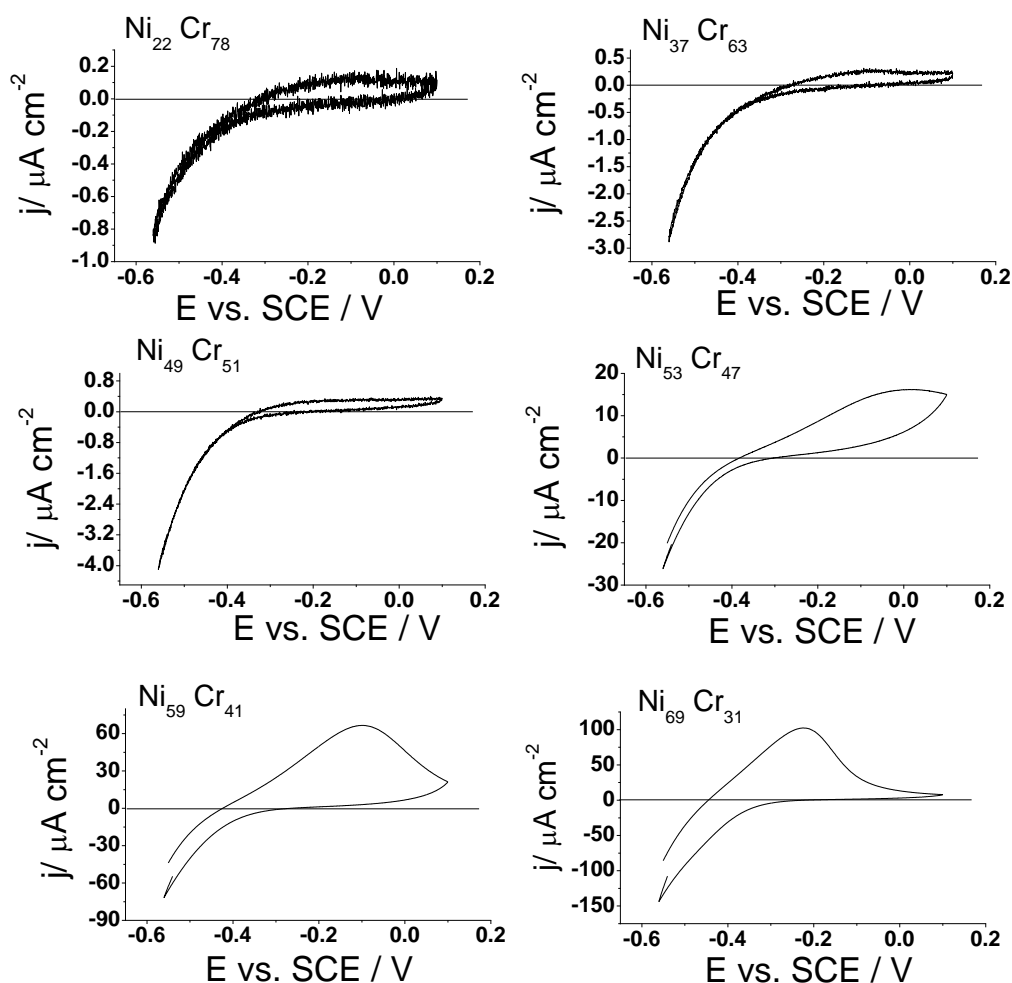


Figure 3.4: Selected cyclic voltammograms of NiCr alloys (#7149) in the composition range 31-78 %_{at.} measured in phosphoric acid (pH3) solution purged for 20 min with Ar to remove oxygen at room temperature. The scan rates was 20 mV s⁻¹. Note that the y scale (current density) varies between plots.

These results have been reproduced with another Ni-Cr array prepared by the same approach and investigated under the same conditions. There is no difference in any part of the compositional ranges extending over a shorter range. The anodic sweeps of voltammograms recorded on the second Ni-Cr array versus chromium composition are shown in **Figure 3.5**. The comparison between the anodic sweeps obtained from the first and second arrays show a consistent result (as shown in **Figure 3.3** and **Figure 3.5**). Results from both

arrays emphasise that 50 %_{at.} chromium is a critical composition at which electrochemical behaviour significantly changes.

The oxidation's current density (j) largely increases for the Ni-Cr alloys containing lower than 50 % Cr (**Figure 3.5**).

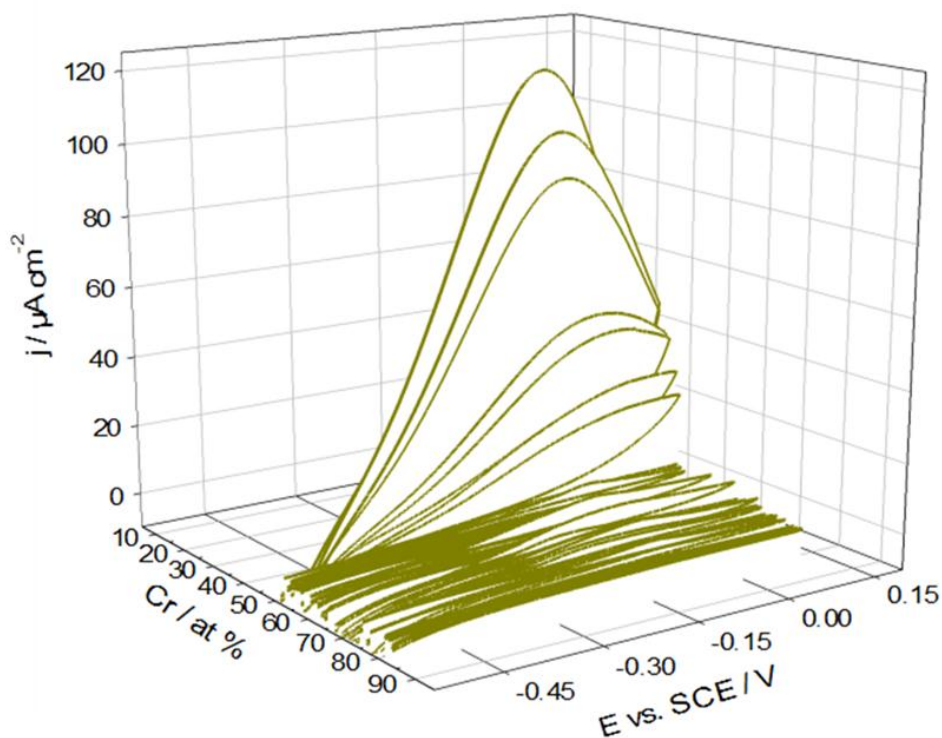


Figure 3.5: The first anodic sweep of the cyclic voltammograms of 100 NiCr alloys (#7150) deposited at room temperature. The electrolyte is phosphoric acid (pH 3) solution purged with Ar for 20 min at room temperature. The scan rates were 20 mV s^{-1} .

Selected alloy compositions in the range 44 to 78 %_{at.} Cr are chosen and presented in **Figure 3.6**. There is no significant change in the current densities of anodic and cathodic at the three top alloys. However, the anodic polarisation rises clearly at 48 %_{at.} Cr as displayed by the Ni₅₂Cr₄₈ alloy (**Figure 3.6**). The latter peak current density of oxidation wave is ca. = $50 \mu\text{A cm}^{-2}$ while the Ni₄₉Cr₅₁ ones is ca. = $7.5 \mu\text{A cm}^{-2}$ which is about seven times less. Consequently the 50 ± 1 %_{at.} chromium is a critical composition of as-deposited Ni-Cr alloys.

The correlation between the abrupt reduction in anodic current densities and the onset of the σ -Cr₃Ni₂ metastable is obvious. This indicates that this phase creates a stable passive layer; as a result, the oxidation or anodic current density decreases. This is obvious by comparing XRD results (Figure 3.2) and anodic sweep measurements shown in Figure 3.3.

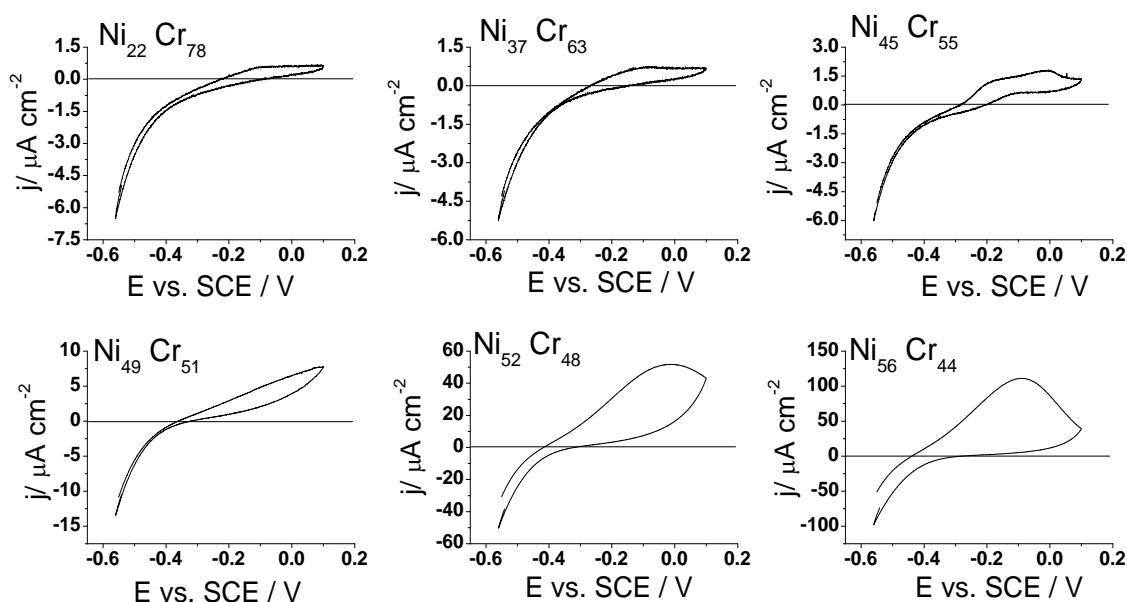


Figure 3.6: Selected cyclic voltammograms from a 10x10 as-deposited Ni-Cr array (B). Note that y scale (current density) varies between plots.

For further investigation a new 10x10 Ni-Cr array (#6763) is screened immediately after contacting the corrosion solution (i.e. 2 min) in order to reduce irreversible changes caused through long periods in the corrosion electrolyte. Selected cyclic voltammograms of NiCr alloys in the composition range of 31-78 % Cr, which is similar to the previous arrays, are presented in Figure 3.7. Results are comparable to those observed in the previous arrays (Figure 3.4 and Figure 3.6). However, as expected, the anodic and cathodic current densities of the last array are greater. This is a result of a smaller corrosion film formed during a short period in the electrolyte solution before conducting cyclic voltammetry screenings. In other words, when the sample is left for a long time (i.e. 20 min), a thick corrosion film (often metal oxide) is accumulated on the surface. This oxide has a lower conductivity. Therefore, the current densities decrease by increasing the thickness of the oxide film. In agreement with previous results, at above 50 % Cr both anodic and cathodic

polarisations have reduced (**Figure 3.7**). Abrupt changes are displayed by the $\text{Ni}_{54}\text{-Cr}_{46}$ alloys, where both anodic and cathodic current densities largely increase.

The consistency in the results confirms the reproducibility of the high-throughput screening method. Also 50 % Cr is a critical composition above which cathodic and anodic reactions decline. Contrarily, at below 50 % Cr cathodic and anodic reactions increase.

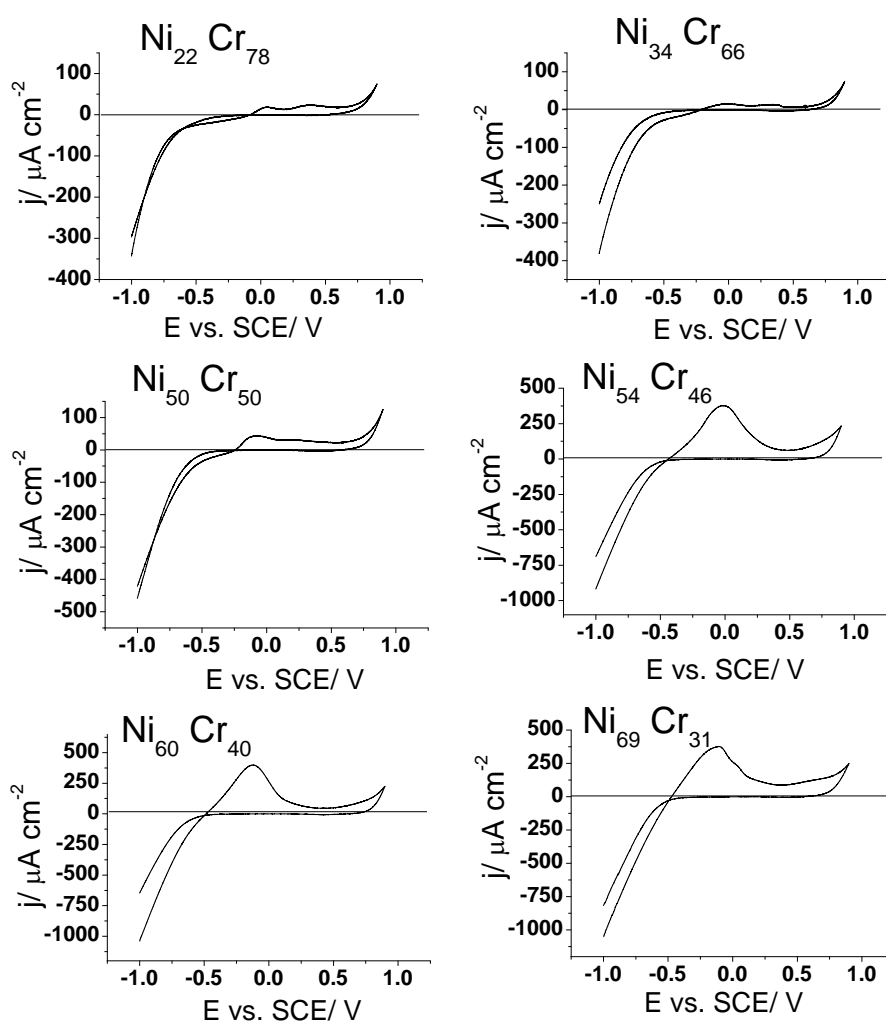


Figure 3.7: Selected cyclic voltammograms from a 10x10 as-deposited Ni-Cr array (#6763) in the composition range of 31-78 %_{at.} Cr. The solution is phosphoric acid [pH 3] purged for 2 min in the presence of the sample before applying the CV. Note that y scale (current density) varies between plots. The scan rates was 20 mV s⁻¹.

3.3.2 Corrosion Resistance

3.3.2.1 Linear Polarization Resistance (LPR)

Polarisation resistance of the alloys has been extracted from the voltammetry by the linear polarisation method (LPR). The methodology of extracting polarisation (corrosion) resistance by LPR is explained in the experimental section. The error bars reflect the average of polarisation resistance measured at different film thickness. The results are extracted from the voltammetry scans which were obtained on a single array of 100 fields (#7149), and plotted as functions of chromium compositions as shown in **Figure 3.8**. This has been reproduced on a number of separate arrays from which three arrays are presented here.

Incorporation of Cr into the NiCr matrix affects the polarisation resistance of the NiCr alloy differently, which can be divided into a number of compositional regions (**Figure 3.8**). The addition of chromium by $0 < \text{Cr } \%_{\text{at.}} < 45$ in the Ni and the NiCr alloy results in a small reduction in the polarisation resistance. This coincides with the NiCr compositions characterised by the solid solution of Cr in the f.c.c γ -Ni (Fm3m) phase (**Figure 3.2**), where de-alloying of chromium at the grain boundaries results in intergranular corrosion (IGC), a well-known phenomenon in the NiCr alloys [7, 178].

As shown in **Figure 3.8**, the polarisation resistance at the compositional range (from 28 to 45 % Cr) where preferred orientation of the solid solution phase observed has not changed (**Figure 3.2**). An abrupt increase in the polarisation resistance is observed between $45 < \text{Cr } \%_{\text{at.}} < 50$. This is corresponding to the onset of the formation of the σ Cr_3Ni_2 metastable phase. The latter major increase in the polarisation resistance compares to the enormous reduction of anodic current densities (**Figure 3.3** and **Figure 3.5**). This can be seen clearly in the inset, which shows an expanded plot of the polarisation resistance at low Cr compositions.

A maximum in polarisation resistance is observed at ca. 60 $\%_{\text{at.}}$ Cr which corresponds to the ideal alloy concentration for the Cr_3Ni_2 metastable phase. This conforms to the XRD results (**Figure 3.2**). Yamada et al.[72] observed a similar result where $\text{Ni}_{50}\text{Cr}_{50}$ displays the highest corrosion resistance in a very

aggressive solution ($8\%CO_2+8\%O_2+18\%H_2O+0.1\%HCl+N_2$ corrosive gas) at 773, 873 K.

Above 60 %_{at.} Cr, the polarisation resistance initially decreases, and subsequently increases sharply for compositions above 80 %_{at.} Cr. These two compositional regions correspond to the formation of the σ Cr_7Ni_3 metastable phase beside the Cr_3Ni_2 metastable phase, and the region of solid solution of Ni in b.c.c α -Cr (Im3m) (Figure 3.2). Therefore, the initial decreases owing to intergranular corrosion (IGC) are influenced by the simultaneous existence of the two metastable phases i.e. Cr_3Ni_2 and Cr_7Ni_3 . This sort of corrosion (i.e. IGC) exists in heterogeneity situations[178]. Above 80 %_{at.} solely b.c.c α -Cr exists, (Figure 3.2) hence the polarisation resistance increases sharply.

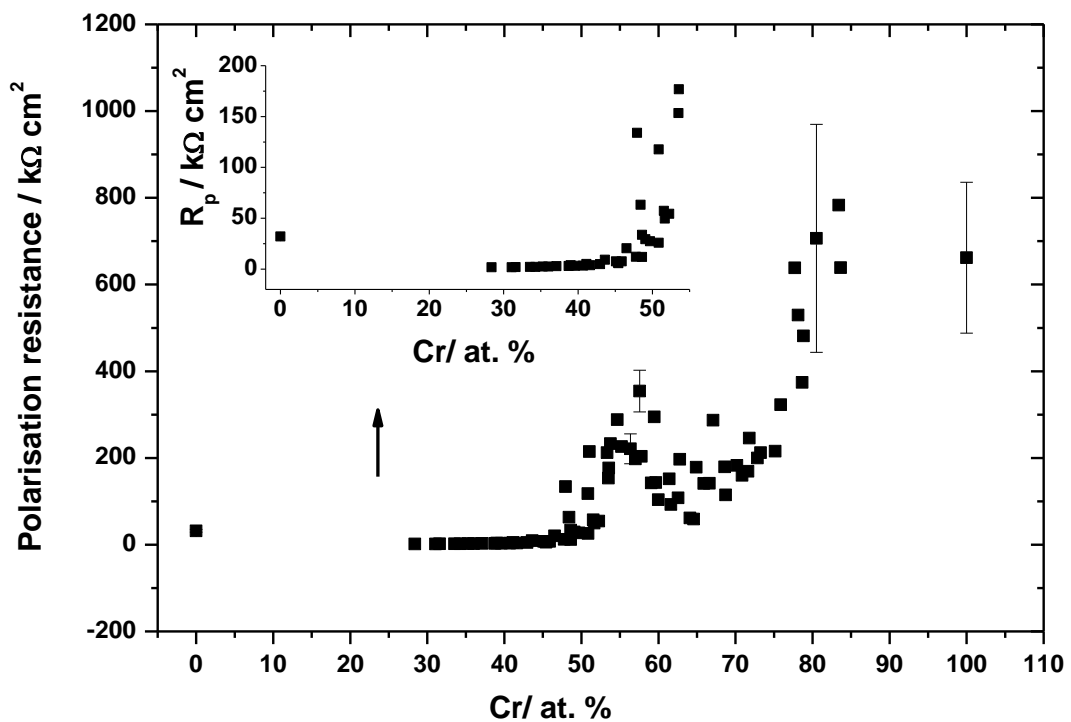


Figure 3.8: The Polarization Resistances (R_p) determined by the LPR method of as-deposited nickel, chromium and NiCr alloys of composition of 28-83 %_{at.} Cr. The electrolyte was de-aerated phosphoric acid (pH 3) at room temperature. The R_p was extracted after performing cyclic voltammetry in the potential range -600 to +100 vs. SCE/mV at scan rates of 20 mV s^{-1} . The compositions were determined by EDS.

The polarisation resistance recorded is shown to be directly related to the bulk alloy structures. The intervention of the background and charging current into the submicron current densities of chromium and high resistance Ni-Cr alloys result in a large error bar. Recede

The polarization (corrosion) resistance has been reproduced on another Ni-Cr array (#7150) synthesised under similar conditions. The compositional range of the second array is slightly shorter.

The polarisation resistances extracted from a 100 field on the second array are plotted versus chromium composition (**Figure 3.9**). In comparison to polarisation resistances obtained from the first array (**Figure 3.8**), the alloy compositional dependence of the polarisation resistance as a function of composition is very consistent. The addition of Cr into the Ni-Cr matrix results in reduction of the polarisation resistance over a compositional range of (0 to 45 %_{at.} Cr). Also, sharp increases in the polarisation resistance appear at 50 and 80 % Cr (**Figure 3.9**). Moreover, identical behaviour also is detected above 60 %_{at.} Cr where the polarisation resistance firstly reduces then sharply increases.

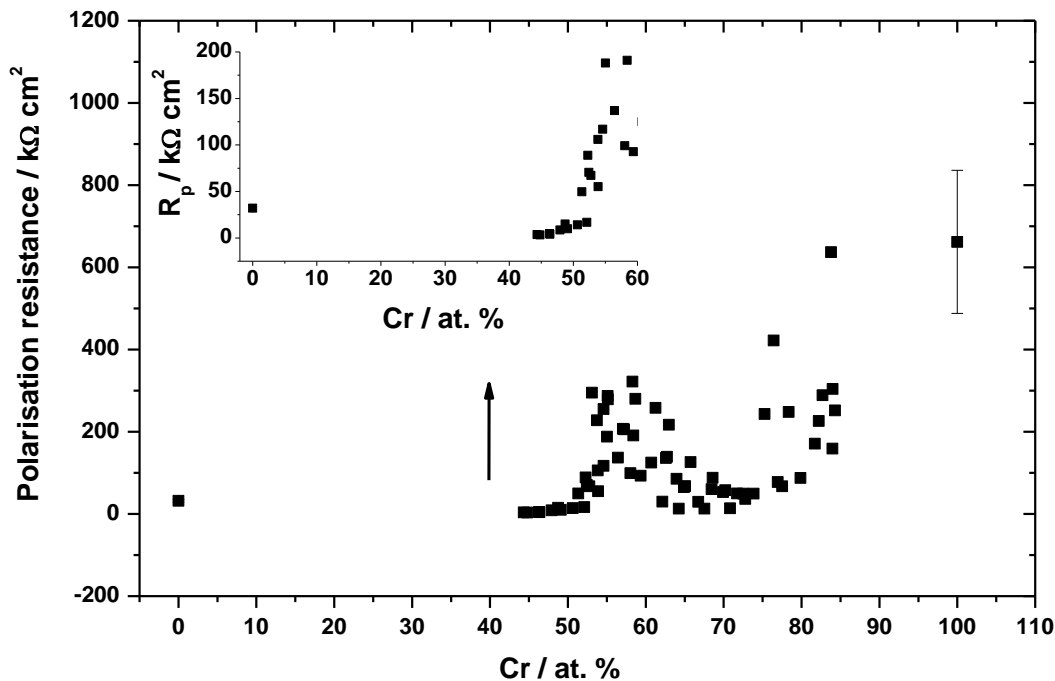


Figure 3.9: The Polarization Resistances (R_p) determined by the LPR method of as-deposited nickel, chromium and NiCr alloys of composition of 42-87 %_{at.} Cr. The electrolyte was de-aerated phosphoric acid (pH 3) at room temperature.

In order to investigate further the corrosion performance of the NiCr alloys, cyclic voltametry has been applied on a separate array (#6763) immediately after being in the electrolyte, unlike the prior two arrays where cyclic voltametry was executed after 20 min. This is to minimise the surface irreversible changes that have taken place due to longer periods in the electrolyte, which definitely has an effect on electrochemical measurement.

Note that for the sake of simplicity, the first and second arrays examined after long periods in the electrolyte will be called from now on (A=7149) and (B=7150) while the third array screened after a short period will be named as (C=6763).

The polarisation resistances extracted by LPR from the third array (C) are presented in **Figure 3.10**. In general, the polarisation resistance behaviour is similar to those observed in previous arrays (A and B). Besides the maximum polarisation resistance increase obtained at 80 %_{at.} Cr, the Ni-Cr alloy comprised of ≥ 50 %_{at.} Cr displays the second best polarisation resistance. Moreover, similar reduction in the polarisation resistance was observed following the incorporation of Cr into the Ni-Cr matrix at low Cr content.

Nevertheless, there appear to be some differences. The absolute value of polarisation resistances extracted from the last array (C) is much smaller. However, this is expected, and it relates to the thickness of the oxide layer (or corrosion product) which increases with time. Therefore the immediate screen did not allow this layer to grow, hence the alloys resistance appears lower. On the other hand, the previous arrays (A and B) are left for 20 min in electrolyte before taking a measurement; therefore, the thicker oxide layer has already formed which results in higher polarisation resistances.

Another difference from what is observed in **Figure 3.8** and **Figure 3.9** is that the polarisation resistance above 60 %_{at.} Cr shows a smaller reduction (**Figure 3.10**). This is yet again owing to the difference in soak time of the arrays in corrosion solution before applying the CV. The arrays (A and B) are left for long periods (i.e.20 min), providing a chance for micro-galvanic corrosion to occur between the σ -phases existing within this region (**Figure 3.2**). However, this could not take place in the last array (C) on which measurements are immediately performed.

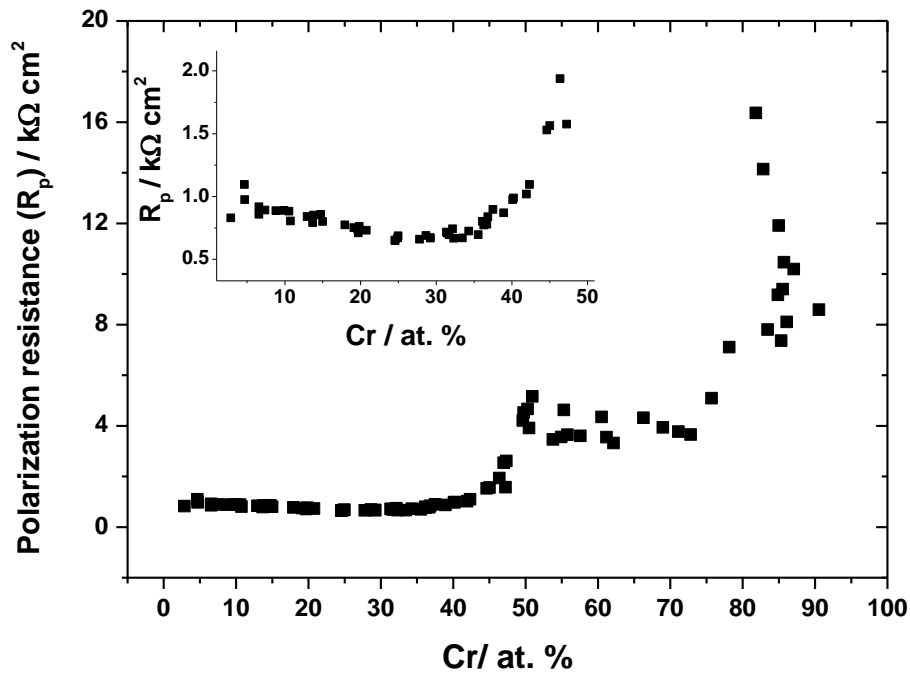


Figure 3.10: The Polarization Resistances (R_p) determined by the LPR method of as-deposited nickel, NiCr alloys of composition of 2-90 %_{at.} Cr. The corrosion electrolyte was de-aerated phosphoric acid (pH 3) at room temperature.

3.3.2.2 Polarization (Corrosion) Resistance Obtained by Tafel and LPR

The trend in the compositional dependence of the polarisation resistance determined by the LPR method is also reproduced by extracting the polarisation resistance from the Tafel method for a series of NiCr alloys. Results are compared to the polarisation resistance determined by the LPR approach (**Figure 3.11**). This comparison between the two methods is to ensure the polarization resistance behaviour of Ni-Cr alloys over the whole compositional range are studied. The compositional dependence of the polarisation resistance determined by the Tafel extrapolation method for the selected Ni-Cr alloys are the same as those determined by LPR (**Figure 3.11**), demonstrating the reproducibility of the methods.

In addition, all changes in the polarisation resistance are observed by both methods at the same compositional range. For example, the polarisation

resistance increases sharply at 50 and 80 % Cr. A small reduction in the polarisation resistance occurs by incorporating Cr at a low composition range.

There is a systematic increase in the absolute values of corrosion resistances extracted by LPR, which are likely to be a result of irreversible changes that occurred during the cathodic scan which precedes the linear polarisation resistance region. As a result, a thin corrosion film is formed on the alloys surface, producing an increase of the corrosion resistances extracted by LPR, in agreement with the assessment of Mansfeld [37]. Nevertheless, while there may be errors associated with the absolute values of the polarisation resistances derived from LPR, the identical environments of the alloy fields in the screening measurement ensure that the trends in the polarisation resistance obtained as a function of composition appear to be reliable.

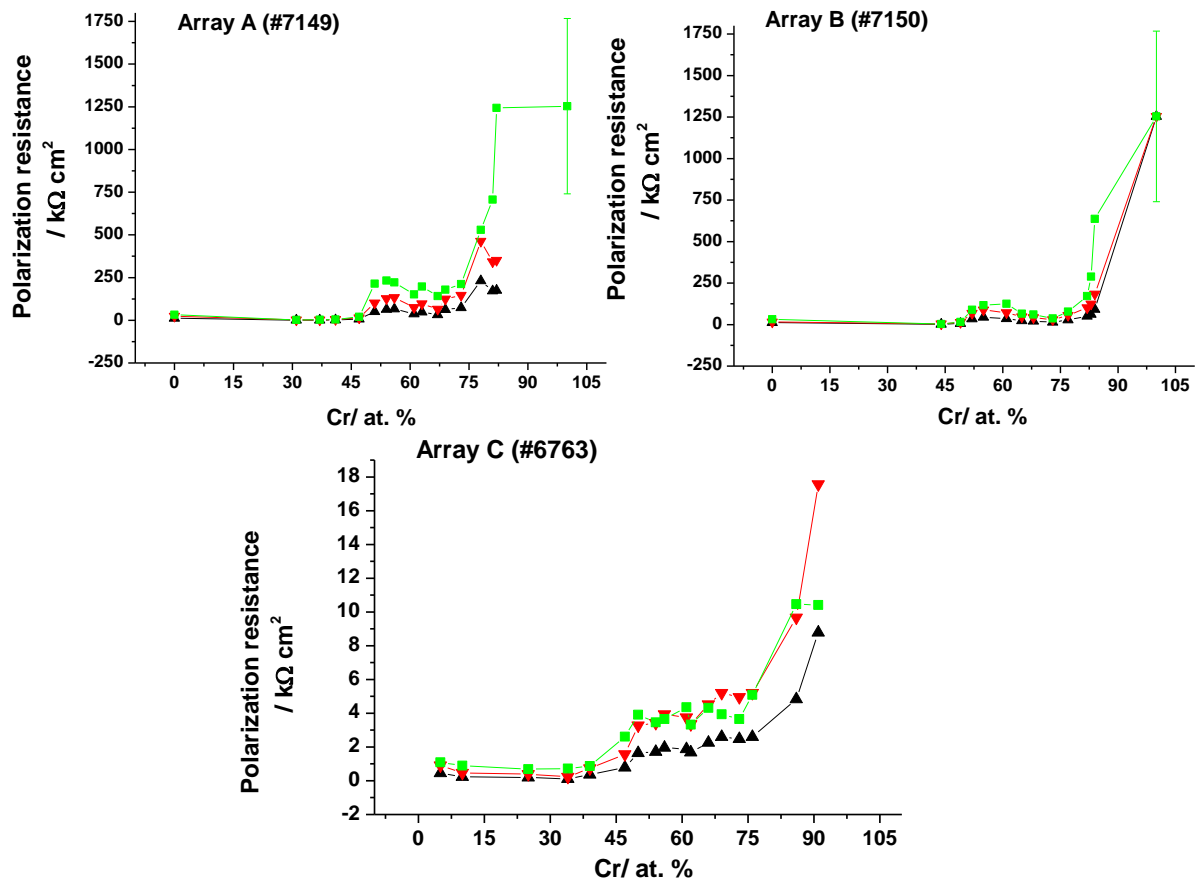


Figure 3.11: The polarization Resistance(s) (R_p) obtained by the LPR method (■), and from the Tafel method assuming the limits of $B = 26\text{ mV}$ (▼) and $B = 13\text{ mV}$ (▲) for Ni, Cr and NiCr alloys of compositions in the range of 31-83 %_{at.} Cr for (A and B), and 2-90 %_{at.} Cr array (C). Note that y scale (polarisation resistance) in array (C) differs from arrays (A and B).

3.3.3 Zero Current Potential ($E_{i=0}$)

The zero current potential ($E_{i=0}$) of three separate Ni-Cr arrays are extracted from voltametric measurements of the previous arrays and presented in **Figure 3.12**. The error bar reflects the effect of thickness variation on the Ni and Cr zero current potential. Note that the arrays (A and B) are measured with the same procedure and conditions.

The addition of Cr into Ni-Cr matrix by $< \sim 45 \%_{\text{at}}$ results in a 100 mV shift to negative potentials (**Figure 3.12**), which coincide with the formation of chromium solid solution of in nickel as shown in XRD results (**Figure 3.2**). Apparent rise (i.e. 200 mV) in the zero current potential is observed at $\geq 50 \%$ Cr; subsequently a small decrease appears above 60 % Cr for arrays (A and B). Similar behaviour has been noticed in the polarisation resistance data (**Figure 3.8** and **Figure 3.9**). Therefore the corrosion (polarisation) resistance and zero current potential are related to the characteristic of Ni-Cr bulk structure. For example, the decrease in the zero current potential at low Cr content indicates the formation of Ni (Cr) solid solution, which is susceptible to intergranular corrosion (IGC)[12, 179, 180]. Also, the positive shift in potentials is associated with the formation of the $\text{Cr}_3\text{-Ni}_2$ metastable phase at $\geq 50 \%_{\text{at}}$ of chromium (**Figure 3.2**). It is difficult to assess the exact mechanism or relationship between the $\text{Cr}_3\text{-Ni}_2$ formation and the increase of the zero current potential. Nevertheless, the $\text{Cr}_3\text{-Ni}_2$ formation probably forms a protective chromium rich layer, which may be positively charged. This protective layer is often obtained in Ni-Cr alloys [181]. Above 60 %_{at} Cr the potential slightly shifts to negative potentials as displayed by the arrays (A, B **Figure 3.12**). This compares to a small decrease in the polarisation resistance (**Figure 3.8** and **Figure 3.9**), which corresponds with micro-galvanic corrosion caused by the simultaneous presence of metastable phases. There is no significant change of zero current potential at 60 to 70 %_{at} Cr for the array (C) where only flat behaviour persists. This is due to a short presence in corrosion electrolyte campers to arrays (A and B).

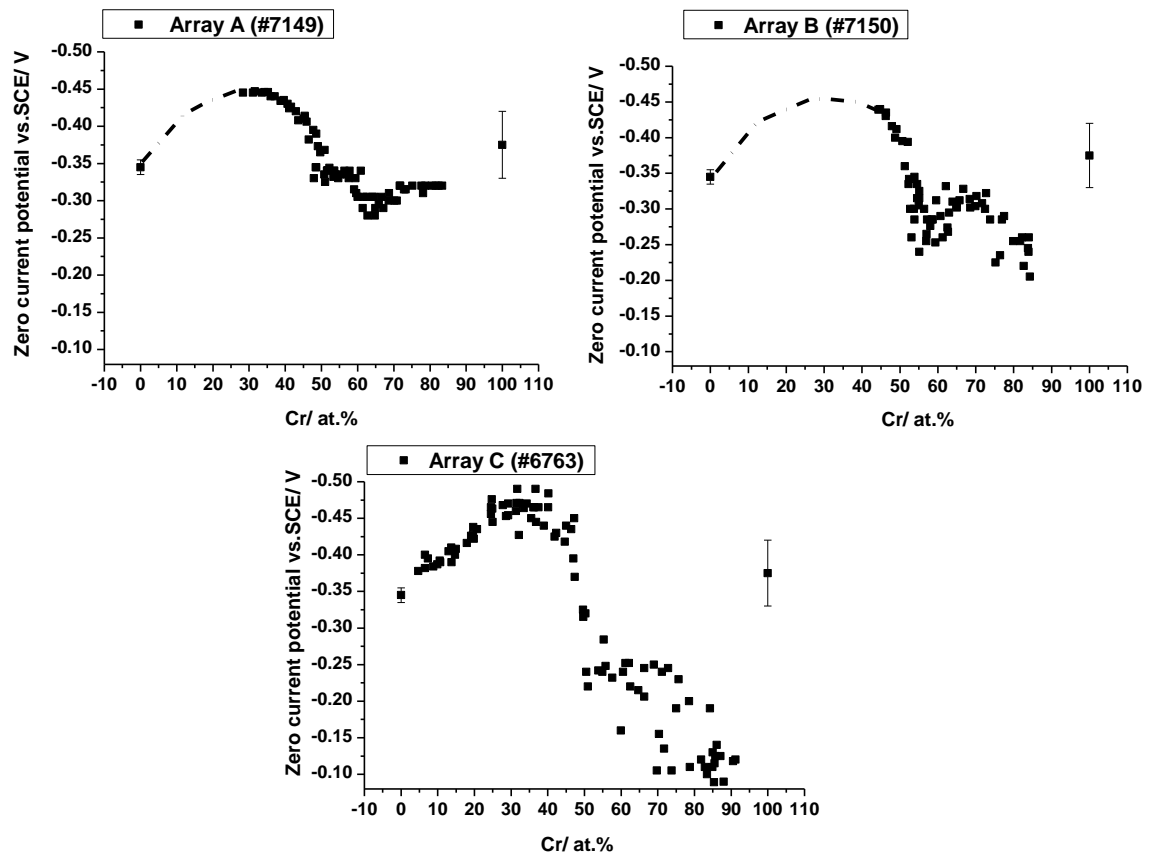


Figure 3.12: The zero current potential ($E_{i=0}$) of as-deposited Ni-Cr arrays examined in phosphoric acid pH 3 at 293 K. Chromium composition determined by EDS.

Moreover, the open circuit potentials (E_{opc}) have been measured for some Ni-Cr arrays, although this experimental arrangement is still under examination. Nevertheless, the initial results appear very optimistic. A comparison between open circuit and zero current potential for arrays (A, B) are shown in **Figure 3.13** and **Figure 3.14**. Results are consistent in demonstrating a similar behaviour. There is, however, a systematic difference in the absolute value of the potentials obtained from $E_{i=0}$ and E_{opc} . The zero current potential ($E_{i=0}$) appears more negative owing to the irreversible changes (i.e. Corrosion) that have taken place during cathodic scan.

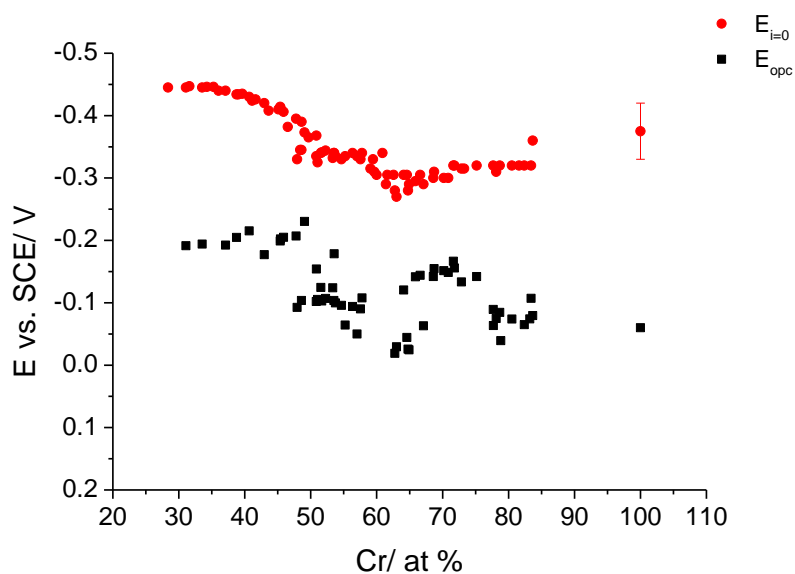


Figure 3.13: Comparison between open circuit and zero current potential for Ni-Cr alloys of compositions in the range of 31-83 % Cr, array A (#7149). The open circuit potentials were obtained after 20 min. The electrolyte is phosphoric acid pH 3 at 293 K.

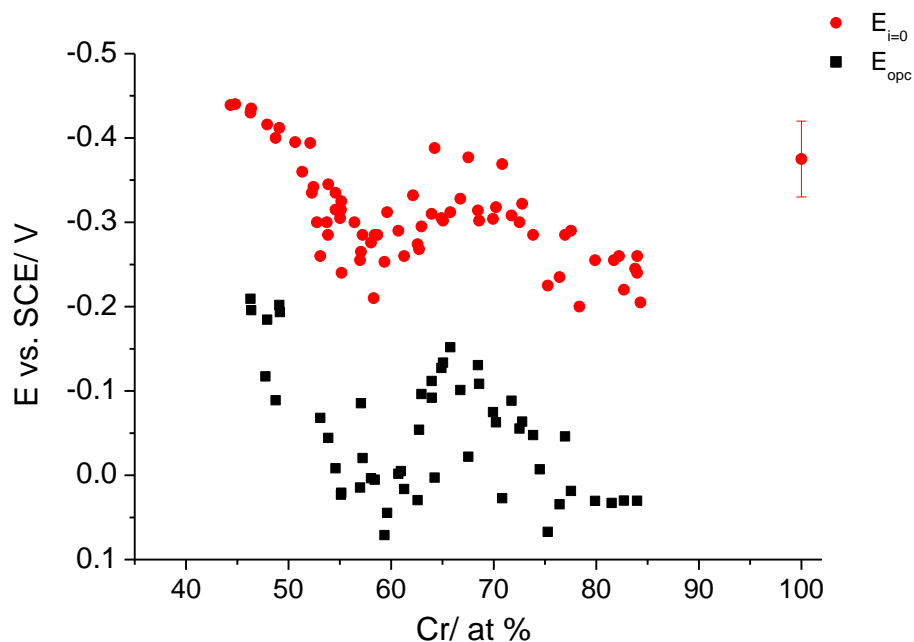


Figure 3.14: Comparison between open circuit and zero current potential for Cr and Ni-Cr alloys of compositions in the range of 42-85 % Cr, array B (#7150). The open circuit potentials were obtained after 20 min. The electrolyte is phosphoric acid pH 3 at 293 K.

3.4 Electrochemical Measurements of Ni-Cr Thin Film Alloys in Sodium Chloride [50 mM] at 293 K.

3.4.1 Cyclic Voltammetry

Sodium electrolytes are probably the most common electrolyte type for a corrosion study and therefore have been used to examine the corrosion properties of Ni-Cr thin film alloys. **Figure 3.15** shows forward sweep voltammograms recorded on a 10x10 Ni-Cr array in sodium chloride [50mM]. Note that chromium composition, in atomic percent (%_{at.}), is enclosed and increases as indicated. The solution was purged with argon for 2 min before applying the cyclic voltammetry scan. Current scale is the same for each square normalised to (-31–70 μA). Small anodic and cathodic polarisations are shown by rich chromium alloys (upper left) while the rich nickel alloys (bottom right) show great oxidation and reduction currents.

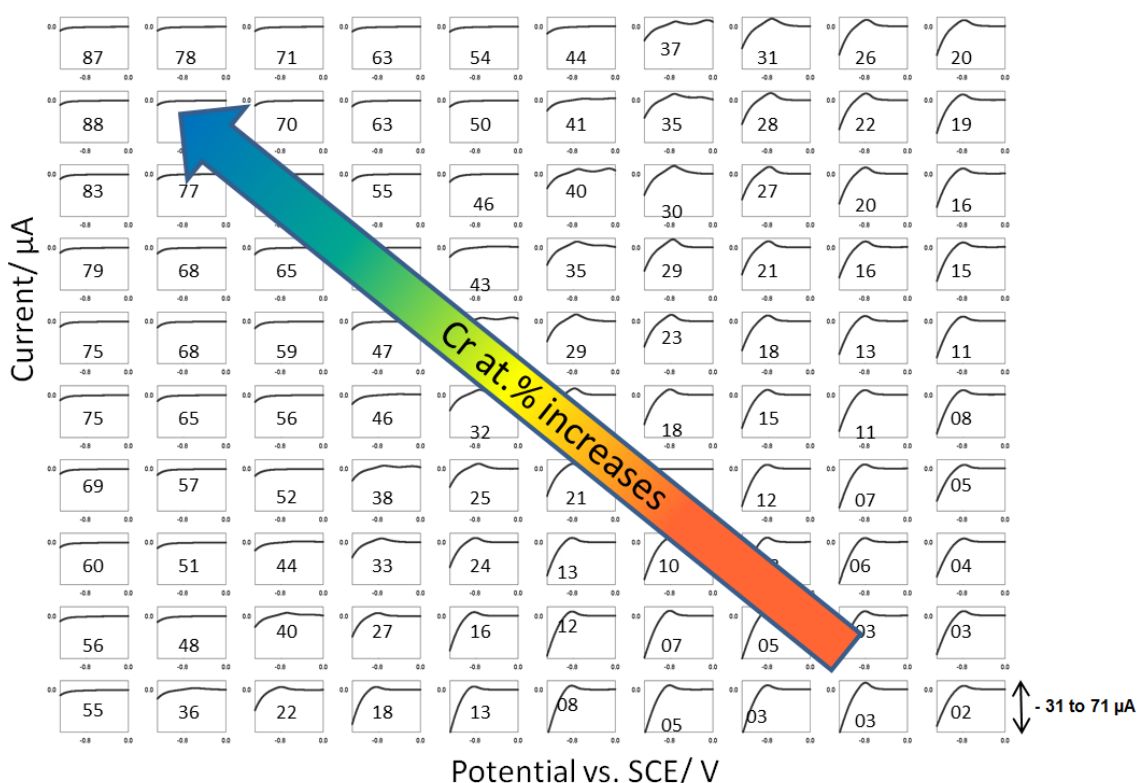


Figure 3.15: The forward sweep of the cyclic voltammograms of 100 Ni-Cr alloys deposited at room temperature. The electrolyte is sodium chloride [50mM]. The solution was purged with Ar for 2 min at room temperature. The scan rate was 20 mV s^{-1} .

For further investigation selected potentiodynamic curves are presented in **Figure 3.16**. Results are for alloy compositions in the range of 2-87 %_{at.} Cr.

The alloys containing $50 \geq \%_{\text{at.}} \text{Cr}$ displayed large passive behaviour proximate to the corrosion potential (E_{corr}), and very low passive current densities i.e. $0.03 \mu\text{A cm}^{-2}$. A significant increase in the anodic polarisation appears at 39 %_{at.} Cr (as displayed by the Ni₆₁-Cr₃₉ alloy). Moreover, a breakdown of passive film is observed at the potential of (-0.3 vs. SCE/ V). Additionally the E_{corr} shifts about 350 mV to negative potentials (**Figure 3.16**). This indicates that at lower than 39 % Cr, the Ni-Cr alloys corrode in activity while above 50 %_{at.} Cr they corrode in passivity. This is observable by comparing the anodic current densities of Ni₅₀-Cr₅₀ and Ni₆₁-Cr₃₉, which are $0.03 \mu\text{A cm}^{-2}$ and $3 \mu\text{A cm}^{-2}$ respectively. Accordingly, above 50 %_{at.} Cr an anodic wave has not appeared while large anodic waves have been obtained for alloy compositions $< 39 \%_{\text{at.}} \text{Cr}$.

The alloys that contained $25 \geq \%_{\text{at.}} \text{Cr} \geq 50$ show positive breakdown potential (E_{bd}) i.e. at which anodic current densities rise greatly; while alloys that consist of 30 to 40 % Cr show negative breakdown potential. The high positive breakdown potential indicates great corrosion performance[1].

The incorporation of Ni < 20 at % results in a small increase of the corrosion potential and a marginal decrease of the anodic polarisation current densities.

The cathodic polarisation i.e. more likely proton reduction increases by incorporating Ni, indicating the good electrocatalytic activity of Ni for hydrogen evolution reaction (HER) [182].

The great reduction of anodic polarisation displayed by Ni₅₀-Cr₅₀ and shown in **Figure 3.16** is similarly noticed at the alloy same composition examined in phosphoric acid (**Figure 3.3**).

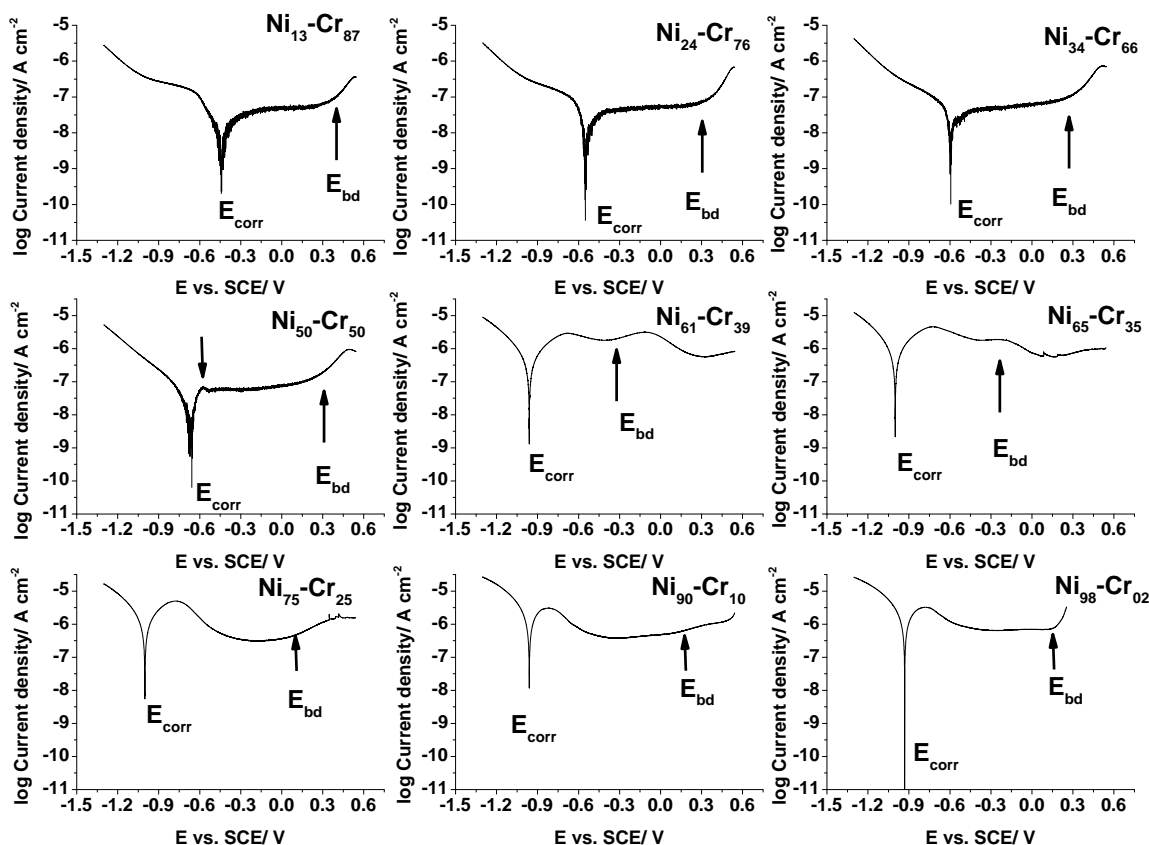


Figure 3.16: Selected cyclic voltammograms from a 10x10 as-deposited Ni-Cr array in sodium chloride [50 mM]. The solution was purged for 2 min in the presence of the sample before applying the CV. The corrosion potential (E_{corr}) and breakdown potential (E_{bd}) are labelled.

3.4.2 Zero Current (Corrosion) Potential

The zero current potentials ($E_{i=0}$) which are equivalent to E_{corr} were obtained from voltametric data on a single array of 100 field and are shown in **Figure 3.17**. The addition of Cr by $\leq 30\%_{\text{at}}$ resulted in a small reduction of the zero current potential. The potential, however, increases sharply at $\geq 45\%_{\text{at}}$ Cr. This compares to the enormous difference observed between the Ni₅₀-Cr₅₀ and Ni₆₁-Cr₃₉ alloys (**Figure 3.16**) where considerable reduction of the anodic polarisation and corrosion potential are noticed. Subsequently, above $50\%_{\text{at}}$ Cr the corrosion potential decreases gradually with increasing Cr content. Results are similar to the ones demonstrated by Ni-Cr alloys studied in phosphoric acid (**Figure 3.12 C**) although the latter are more positive.

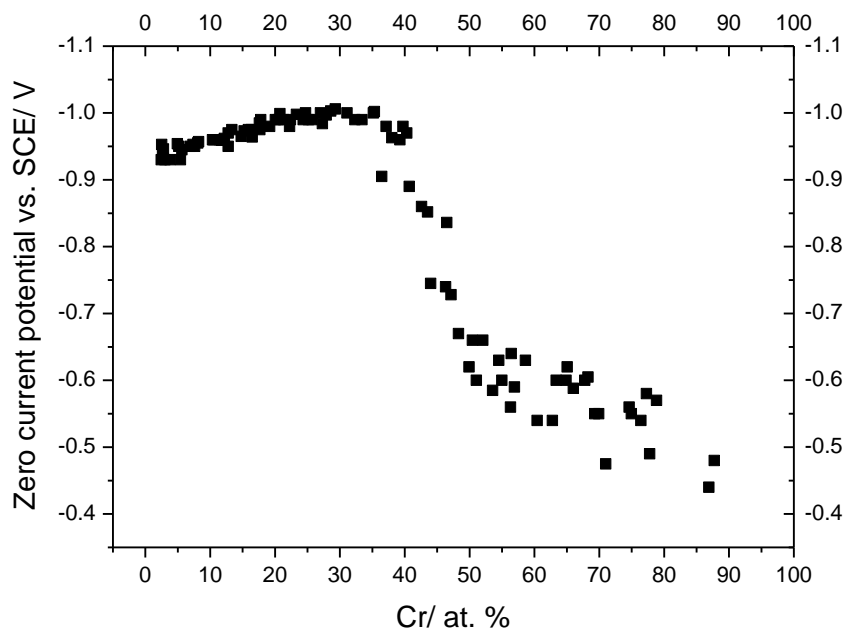


Figure 3.17: The zero current potential(s) extracted from voltametric data of single array of 100 fields studied in sodium chloride [50 mM] at 293 K. The corrosion electrolyte was purged with Ar for 2 min.

3.4.3 Corrosion (Polarisation) Resistance

3.4.3.1 Polarization Resistance Obtained by LPR

In order to investigate further the corrosion resistance of the NiCr alloys, the polarisation resistance of the alloys has been extracted from the voltammetry by the linear polarisation resistance (LPR) methodology. Results are shown in **Figure 3.18** for a series of NiCr alloys in the range 2-83 %_{at.} Cr. The inset shows an expanded plot of the polarisation resistance at low Cr compositions.

There is no significant change of the corrosion resistance at lower than 20 %_{at.} Cr where the polarisation resistance remained constant at ca. 0.25 kΩ cm² (**Figure 3.18**). Next, the polarization resistance initially increases gradually in the range 30-40 %_{at.} Cr (inset figure) and subsequently the polarization resistance increases considerably for alloy compositions above 45 %_{at.} Cr. This

sharp increase of the corrosion resistance associates with the large reduction of corrosion potential observed in **Figure 3.17**.

The comparison between the polarisation resistance of the alloy compositions above 50 %_{at.} Cr and the ones for alloy compositions below 30 %_{at.} Cr confirms that alloys below 30 % corrode actively where alloys above 50 % corrode in passivity. This complies with the observation shown in **Figure 3.16**, where alloys containing above 50 %_{at.} Cr show complete passivation while alloys containing <30 %_{at.} Cr display large anodic dissolution.

The increase of the polarisation resistance initially taken place at 30 % Cr associates with the preferred orientation of the solid solution phase (**Figure 3.2**). The abrupt increase of the polarisation resistance observed at 45 %_{at.} Cr relates probably to the formation of the σ Cr_3Ni_2 metastable phase (**Figure 3.2**).

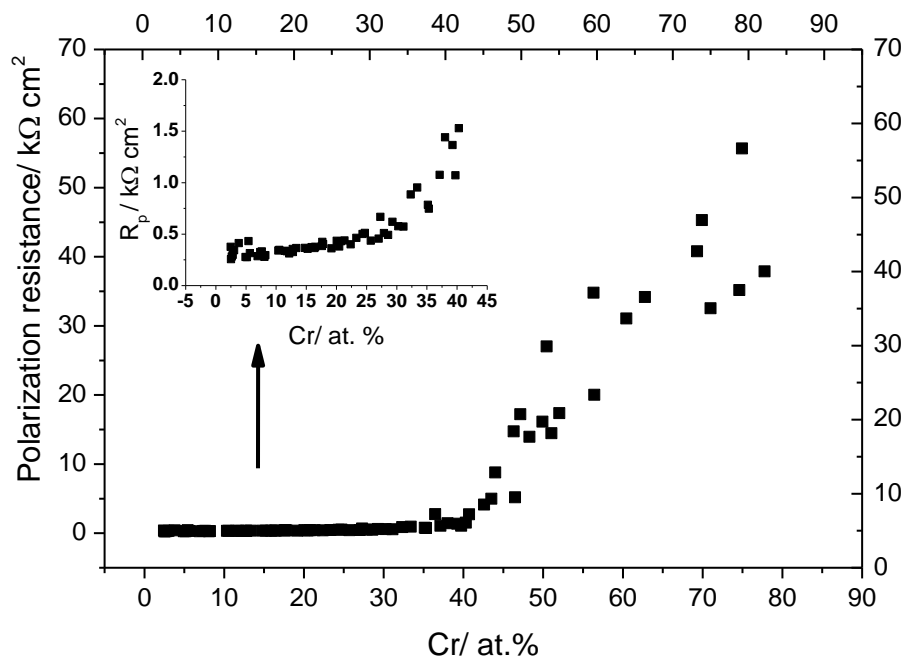


Figure 3.18: The polarization resistance extracted from voltametric data by LPR method from a single array of 100 fields studied in sodium chloride [50 mM] at 293 K. Chromium compositions were determined by EDS. Solution purged with Ar for 2 min.

The incorporation of Cr into the Ni-Cr matrix at lower than 20 %_{at.} Cr has not changed the polarisation resistance (**Figure 3.18**). This is in contrast to the observation obtained from the same composition for Ni-Cr alloys examined in phosphoric acid, where a small reduction of corrosion resistance has been observed (**Figure 3.10**). Nonetheless, it appears to be that polarisation resistance is correlated to Ni-Cr bulk structure. As a result, corrosion resistance increases sharply above 50 %_{at.} Cr in both corrosion electrolytes.

3.4.3.2 Polarization Resistance Obtained by LPR and Tafel Extrapolation

For further investigation of corrosion resistance of the Ni-Cr alloys, the polarisation resistances are determined by the Tafel extrapolation method and plotted as a function of chromium composition. Results are compared to the polarisation resistance obtained by linear polarisation resistance (LPR) for a number of NiCr alloys and presented in **Figure 3.19**. The compositional dependence of the polarisation resistance produced by both methods appears to be consistent, indicating the reproducibility of the methods.

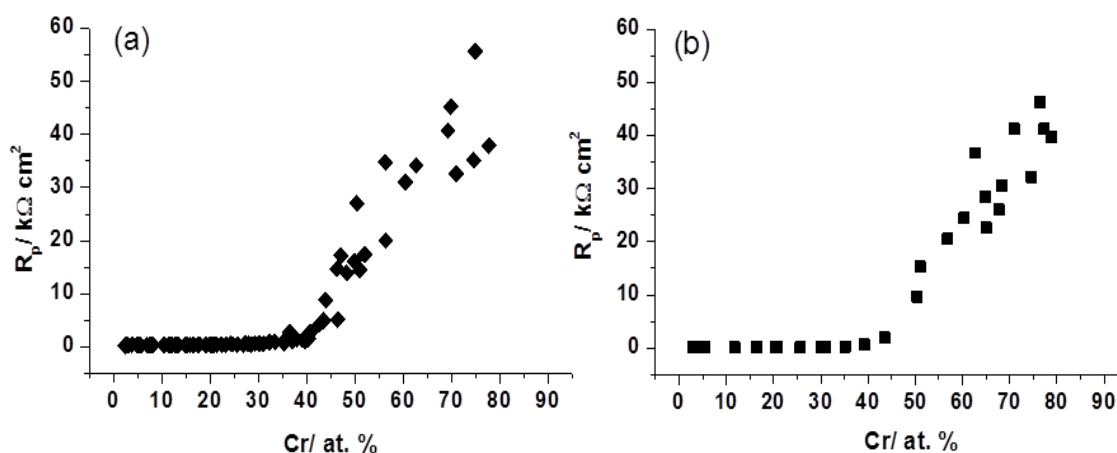


Figure 3.19: The polarization Resistance(s) (R_p) obtained by the LPR method (a), and from the Tafel extrapolation method assuming the $B = 26 \text{ mV}$ (b) for NiCr alloys of compositions in the range of 2-83 %_{at.} Cr. R_p was extracted after performing cyclic voltammetry in the potential range -1250 to $+1000$ vs. SCE/mV at a scan rate of 20 mV s^{-1} . The compositions were determined by EDS. The corrosion electrolyte is sodium chloride [50 mM] at 293 K.

3.5 Electrochemical Measurements of Bulk “Commercial” Samples in Sodium Chloride [50 mM] at 293 K.

3.5.1 Cyclic Voltammetry

It is worth investigating the corrosion resistance of equilibrium “bulk” Ni-Cr alloys in order to compare their results with those obtained from non-equilibrium “as-deposited” Ni-Cr thin film alloys. Consequently, a comprehensive view of Ni-Cr corrosion resistance will be attained. The bulk samples preparation and condition data can be found in detail in the experimental part of the study.

Cyclic voltammograms of Ni, Cr, and Ni-Cr alloys with different compositions are presented in **Figure 3.20**. The addition of chromium results in an obvious reduction of cathodic polarisation current densities as displayed by the Ni₈₉-Cr₁₁ alloy, which increases with increasing Cr content. Also, the anodic current densities significantly decrease, indicating enhancing corrosion performance.

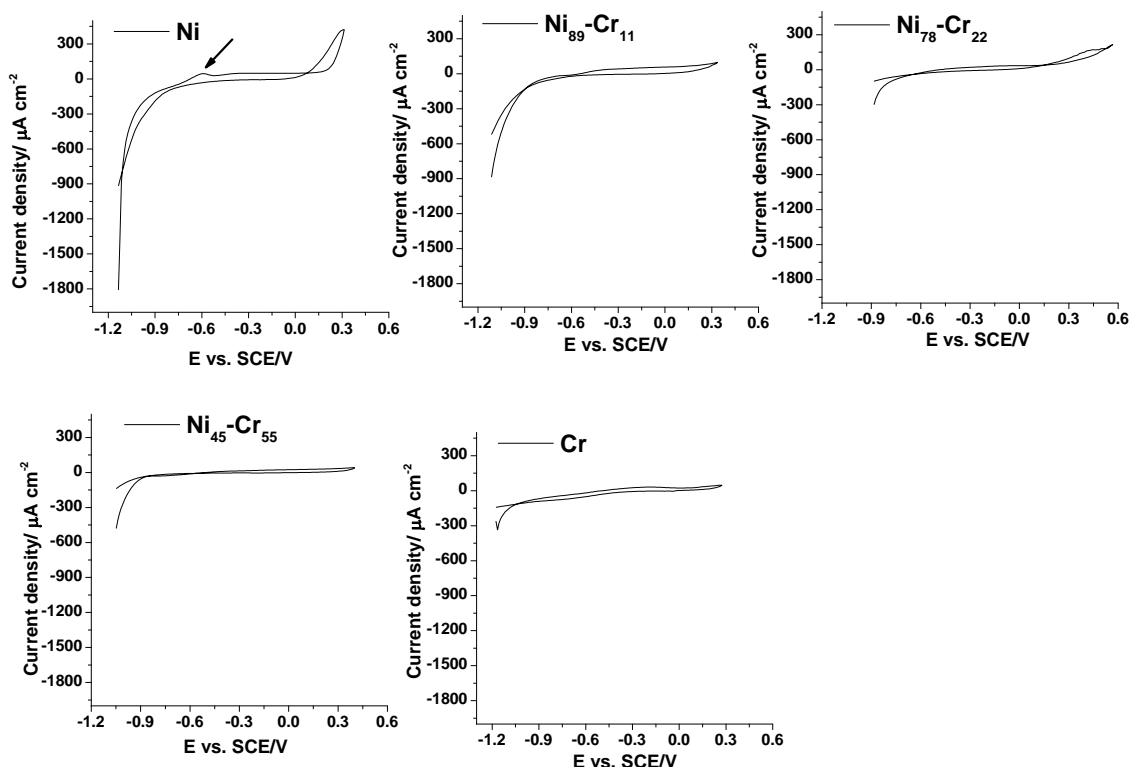


Figure 3.20: Cyclic voltammograms of nickel, chromium, and three Ni-Cr bulk alloys examined in aerated sodium chloride [50 mM] at 293 K. Arrow indicates Ni dissolution.

The previous cyclic voltammograms have been reproduced as Tafel plots or potentiodynamic curves (as shown in **Figure 3.21**) from which certain corrosion characteristics can be deduced such as passivity current, corrosion, and breakdown potentials.

The addition of 10 %_{wt.} Cr results in a reduction of anodic current densities. Additionally a large shift of the corrosion potential is observed as exhibited by Ni₉₀-Cr₁₀ alloy, which is ca. 200 mV higher than nickel's E_{corr} . More reduction of the anodic current densities has been achieved by adding 20 %_{wt.} Cr. The lowest anodic polarisation and highest passivation are shown by Ni₅₀-Cr₅₀ and chromium. The Ni shows early breakdown potential which is not far from its corrosion potential. In contrast to this, all Ni-Cr alloys comprised displayed positive breakdown potentials that occurred quite far from their corrosion potentials; this indicates that those alloys have better corrosion resistance than Ni and the alloying of Cr with Ni in any case is useful. The cathodic reactions more likely are under activation control except the Ni₅₀-Cr₅₀ at ca. -0.90 vs. SCE/V seems to be under diffusion control of oxygen reduction reaction (ORR). The corrosion and breakdown potentials are tabulated in the **Table 3.2**.

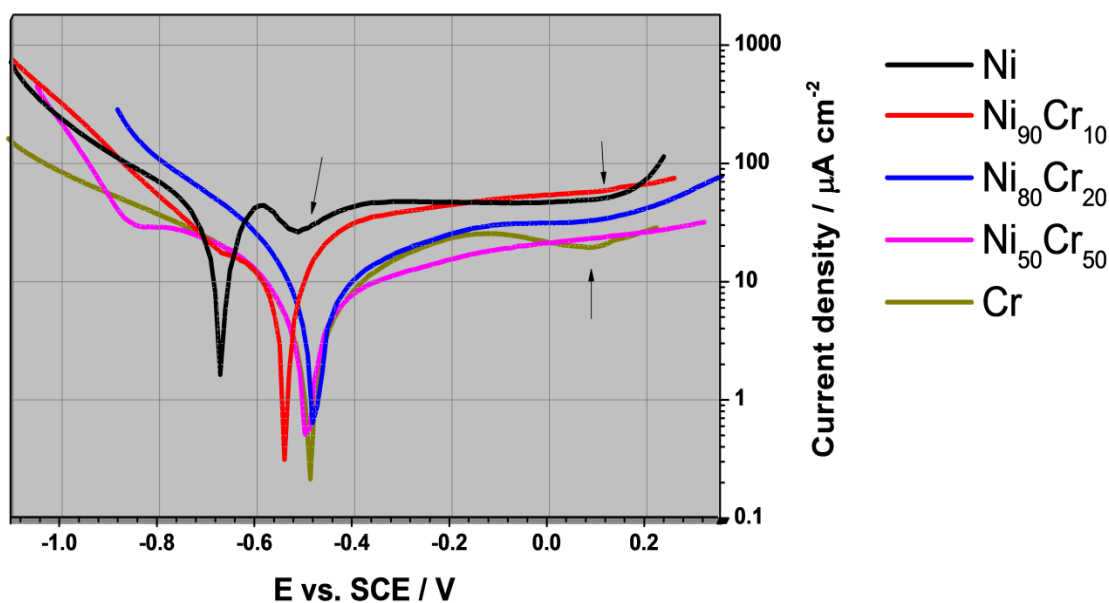


Figure 3.21: Potentiodynamic curves of Ni, Cr, and Ni-Cr bulk alloys studied in aerated sodium chloride [50 mM] at 293 K. Arrows indicate the breakdown potential (E_{bd}). Compositions are in (%_{wt.}).

3.5.2 Corrosion Resistance of Nickel, Chromium and Ni-Cr Bulk Alloys

The polarization resistance of bulk samples are extracted from voltametric data by LPR approach. Results are shown in **Figure 3.22**. Standard error (SE) data obtained from the linear regression has been added to R_p values. The incorporation of chromium clearly improves the corrosion resistance, which is expected since the addition of chromium has been accompanied by an apparent reduction of the anodic current densities as shown by potentiodynamic curves (**Figure 3.21**). The best corrosion resistance is displayed by the Ni₅₀-Cr₅₀ and chromium. The Ni₅₀-Cr₅₀ exhibits the lowest and steadiest passive current.

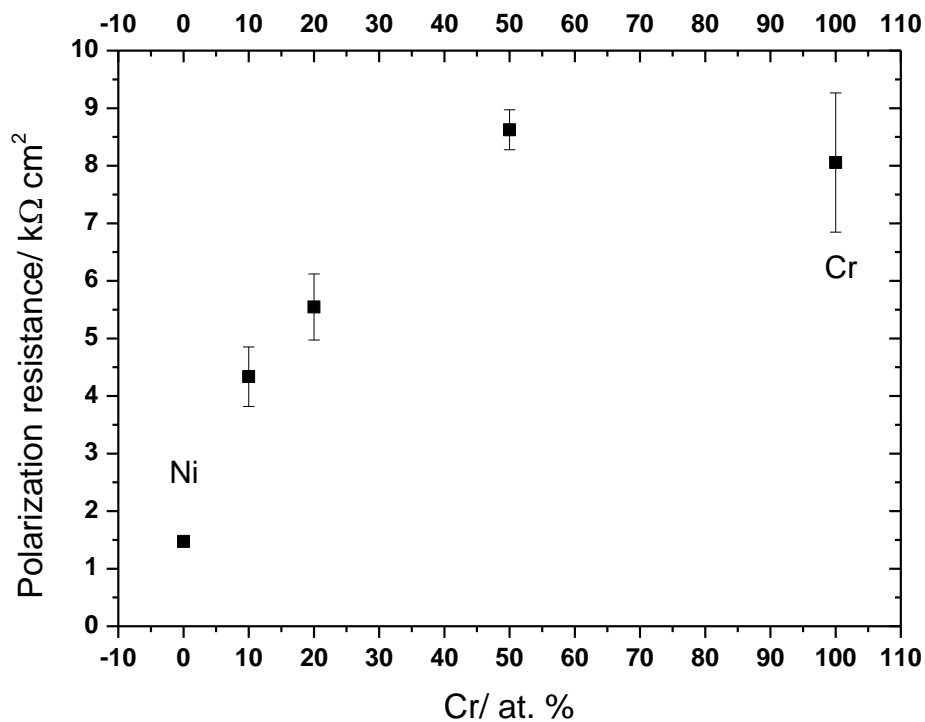


Figure 3.22: Polarization resistance of Ni, Cr, and Ni-Cr alloys examined in aerated sodium chloride solution [50 mM] at 293 K. The error bar reflects standard error (SE) obtained from linear regression.

The addition of 10 % Cr results in an enormous increase of the breakdown potential (E_{bd}) as shown in **Table 3.2**, which is consistent with corrosion resistance results where polarisation resistance increases as much as three times as displayed by Ni₉₀-Cr₁₀. In addition, the corrosion potential shifts by

130 mV to positive potentials. This is in contrast with results obtained from the same composition of as-deposited Ni-Cr alloys. Therefore, it is worthy to make a comparison between the two systems, which will be presented in the next section.

Table 3.2: The corrosion and breakdown potentials, and polarization resistance of Ni, Cr, and Ni-Cr alloys.

Alloys/ Metal	E_{corr} vs. SCE/V	E_{bd} vs. SCE/V	R_p / $\text{k}\Omega \text{ cm}^2$
Ni	-0.67	-0.56	1.472
Cr	-0.49	0.16	8.055
Ni-Cr(90:10)*	-0.54	0.16	4.336
Ni-Cr(80:20)*	-0.49	0.20	5.546
Ni-Cr(50:50)*	-0.49	...	8.625

* Composition in weight %

3.6 Comparison between Bulk and As-deposited NiCr Alloys Studied in Sodium Chloride.

The zero current (corrosion) potentials for bulk and deposited samples investigated in sodium chloride [50 mM] at 293K are extracted from voltametric data and plotted as functions of chromium composition (**Figure 3.23**). Incorporating Cr by lower than 20 %_{wt.} (i.e. =22 %_{at.}) results in a small reduction of the corrosion potential of the as-deposited Ni-Cr alloys. This is in contrast to what has been shown by the same alloy composition of Ni-Cr bulk alloys, where the corrosion potential shifts to positive potentials. Above 20 %_{wt.} Cr, the corrosion potential of bulk alloys shows no significant change. Conversely, an abrupt change of the corrosion potential is observed at ~ 45 %_{wt.} Cr in as-deposited Ni-Cr alloys. However, above 50 %_{wt.} Cr the corrosion potentials of both systems are similar, and appear constant (**Figure 3.23**).

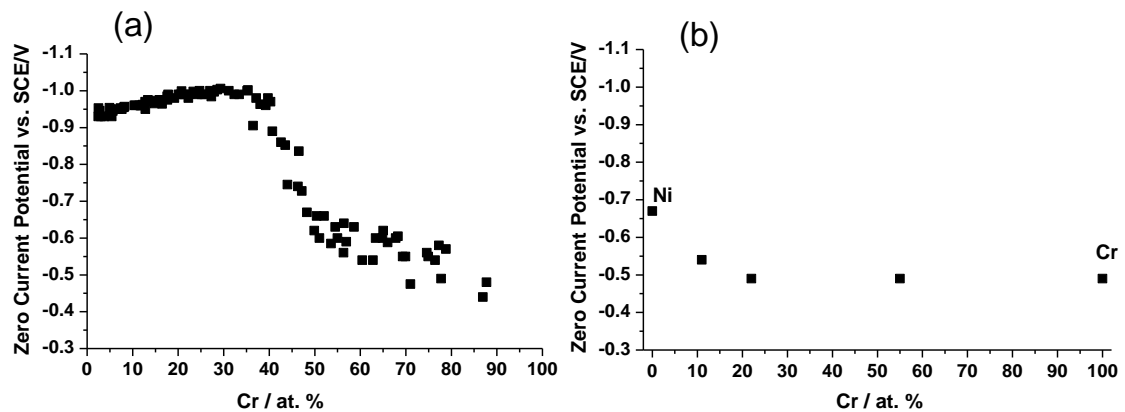


Figure 3.23: zero current (corrosion) potentials of (a) as-deposited NiCr alloys in the composition range 2-89 %_{at.} Cr, (b) nickel, chromium, and NiCr bulk alloys at different compositions in atomic percentage (%_{at.}).

The polarisation resistances determined by LPR for the two Ni-Cr systems are presented in **Figure 3.24**. Note that y scale i.e. polarisation resistance varies between the two systems.

Before examining the consequence of chromium incorporation in both Ni-Cr systems (i.e. equilibrium and non-equilibrium alloys), the absolute polarisation resistances appear dissimilar. At low chromium composition ≤ 20 %_{wt.} bulk alloys exhibit higher polarisation resistance while the opposite is true of an alloy with compositions of ≥ 50 %_{wt.} Cr.

The incorporation of chromium regardless of content increases the corrosion resistance of the Ni-Cr bulk alloys (**Figure 3.24 b**). The comparable increase, however, was observed at higher chromium composition viz. ca. 45 %_{wt.} Cr. The rich chromium alloys displays the best corrosion resistance for as-deposited Ni-Cr system while the superior corrosion resistance of bulk samples are shown by the Ni₅₀-Cr₅₀ alloy.

The differences of the corrosion resistance and potential between the bulk and as deposited Ni-Cr alloys are most likely attributed to phase(s) formation, changes within microstructure or forming an oxide protective layer; this has been reported and well-known in Ni-Cr alloys. For example, the Hastelloy C

alloy, which contained 15 %_{wt.} Cr, shows better corrosion resistance and passivity when compared to Hastelloy B, which ascribed to the creation of Cr₂O₃ [7]. Additionally, microstructural changes that often occur during heat exposure, such as annealing and casting have great influences on corrosion resistance behaviour[183]. Therefore, these two reasons are expected to be responsible for the corrosion resistance changes demonstrated by the Ni-Cr bulk alloys. To be more precise, since corrosion resistance of bulk alloys (**Figure 3.24 b**) increases constantly with increasing chromium content, the first reason (i.e. creation of Cr₂O₃) is the most probable one, which is in agreement with other observations [184, 185].

On the other hand, phase formation and modification is anticipated to be responsible for corrosion resistance and potential changes observed in the as-deposited Ni-Cr alloys. The XRD results shown in **Figure 3.2** reveal that at 28 Cr %, a preferred orientation of the γ -Ni (111) has been observed, which coincides with the onset of corrosion resistance increase as shown in the inset (**Figure 3.24 a**). Moreover, at 48 %_{at.} Cr evidence of the σ -Cr₃Ni₂ metastable phase has been identified, which also compares to the considerable increase of the corrosion resistance at the same composition. A similar observation has identified the σ -Cr₃Ni₂ phase within a composition of 40-60 %_{at.} [82-85, 89].

The polarisation resistance and corrosion potential behaviour appears to be related to the microstructural and phases characteristics of the NiCr alloy. However, structure and phases of Ni-Cr alloys are subjected to substrate temperature and nature [82, 88]. For example, the Ni₂Cr or γ^- phase is expected under equilibrium conditions in the range of 21 to 37 % Cr [81] while in the as-deposited i.e. non-equilibrium condition only the solid solution of Cr in Ni in the range of 0 to 45 %_{at.} Cr[88]. Therefore, a discrepancy of alloy compositional dependence of the polarisation resistance between Ni-Cr systems is expected.

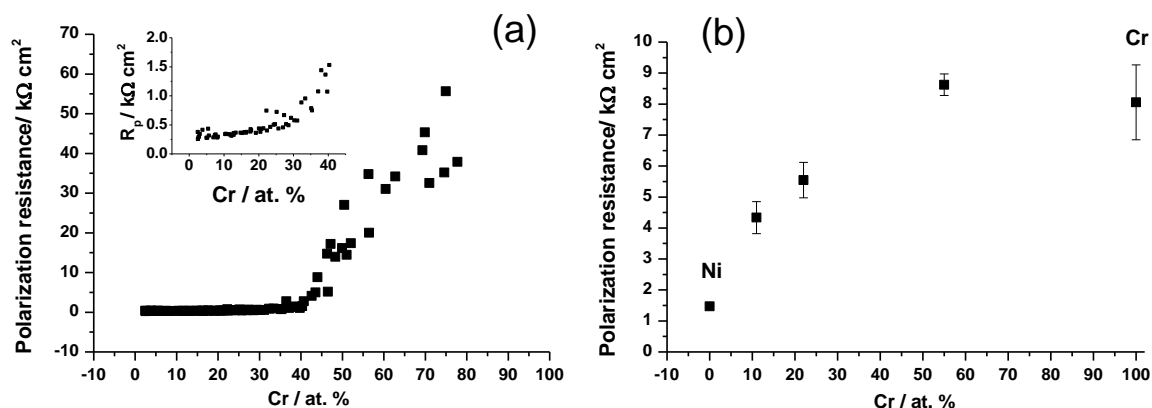


Figure 3.24: Polarisation resistance(s) extracted from cyclic voltammograms data by LRP approach (a) for as-deposited Ni-Cr alloys (b) for nickel, chromium, and NiCr bulk alloys. Both systems investigated in sodium chloride [50 mM] at 293 K.

3.7 Conclusion

High throughput XRD studies identify two regions of solid solutions of Cr in Ni (f.c.c.) and Ni in Cr (b.c.c.), and two metastable phases namely σ -Cr₃Ni₂ and σ -Cr₇Ni₃ at composition of 50-70 %_{at.} Cr.

The corrosion resistance of a series of NiCr thin film alloys is explored by the high-throughput electrochemical measurement of their polarisation resistance, which is achieved by simultaneous cyclic voltammetry on 100 alloy compositions in phosphoric acid pH 3 and sodium chloride [50 mM] at room temperature. Tafel extrapolation and linear polarisation resistance methods are used to determine polarisation resistance. Both methods have revealed the same alloy compositional dependence of the polarisation resistance.

Besides the b.c.c α -Cr (Im3m) phase and its Ni solid solutions in the compositional range of 75 to 100 %_{at.} Cr which exhibit the highest polarisation resistances as similarly observed by Betova and Boijnov [66], the σ Cr₃Ni₂ phase at 60 %_{at.} Cr exhibits the next best polarisation resistance in both corrosion electrolytes.

The co-existence of the σ Cr_3Ni_2 phase with the $\sigma\text{Cr}_7\text{Ni}_3$ phase at 60-75 %_{at.} Cr causes a decrease of the polarisation resistance of Ni-Cr thin film alloys explored in phosphoric acid.

The corrosion resistance of nickel, chromium, and selected Ni-Cr bulk alloys are examined in sodium chloride solution [50 mM]. Results are compared to the ones obtained from Ni-Cr thin film alloys. The overall behaviour of their compositional dependence of polarisation resistance is different, which is attributed to differences in their microstructure.

4. Ni-W Thin Film System

4.1 Introduction

Ni-W alloys have been the subject of interest due to their robust mechanical, wear and corrosion resistance [97] as an alternative to Ni-Cr alloys [92]. The Ni-W alloys also exhibit good catalytic activity for hydrogen evolution [101]. The alloy properties, however, noticeably depend on their composition and structure [101, 103, 105, 186]. Therefore a range of Ni-W thin film alloys have been synthesised by co-evaporation using combinatorial compositional gradient method. Those alloys are characterised by EDX and X-ray diffraction (XRD) including phase identification and crystallite size. The corrosion resistance of alloy compositions was extracted by LPR and Tafel extrapolation. This allows a comprehensive assessment of composition and structure influence on Ni-W alloys corrosion performance.

4.2 Structure Characterisation of As-deposited Ni-W Film Alloys

Figure 4.1 shows XRD patterns measured at selected alloy compositions on thin films of Ni-W alloys deposited at 300 K and with a thickness of ca. 100-150 nm. Under these conditions we expect the alloys formed will not be at full equilibrium [103, 105]. Two diffraction peaks are observed at ca. $2\theta = 44.4^\circ$ and 51.5° , and these are most intense for alloys with low W content, and correspond respectively to the $\langle 111 \rangle$ and Ni $\langle 200 \rangle$ Bragg peaks of the f.c.c. Ni (Fm3m) structure. Another diffraction peak only observed in composition of $\sim 26\%_{\text{at.}} \text{ W}$ appears at ca. $2\theta = 43.5^\circ$, and it corresponds to the $\langle 211 \rangle$ Bragg peak of the Ni_4W (I4/m) structure. This phase is expected to be formed at equilibrium [104], and it has also been obtained at non-equilibrium [103] films. This phase is observed in a very small composition range (around $26\%_{\text{at.}} \text{ W}$), just at the onset of the formation of the amorphous phase with increasing W content.

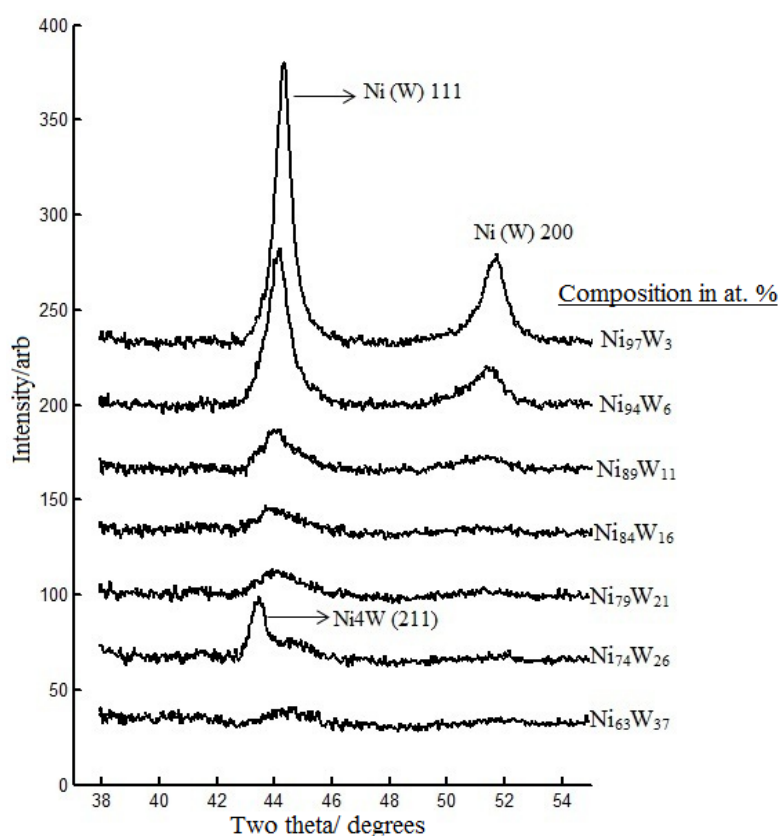


Figure 4.1: X-ray diffraction patterns of a series of as-deposited NiW thin film alloys of composition range from 3-37 %_{at.} W. The films were deposited on a silicon nitride substrate at ~ 300 K. Three phases were identified, namely Ni (W) solid solution γ -Ni (111) and Ni (200), Ni₄W (211), and amorphous phase where no peaks can be seen for a composition $\geq 26\%$ _{at.} W. Compositions in %_{at.} were determined by EDS.

The two Ni derived peaks shift from $2\theta = 44.4^\circ$ and 51.5° (3 %_{at.} W) to lower 2θ values with increasing W content (**Figure 4.2B**). This shift is associated with the formation of a solid solution of W in the Ni. A solid solution is known to form at equilibrium up to a composition of 10 %_{at.} W [104]. The increased scatter in the data above ca. 22 %_{at.} W is due to the broadening of the peaks at high W content, and the signal to noise ratio of the XRD measurement.

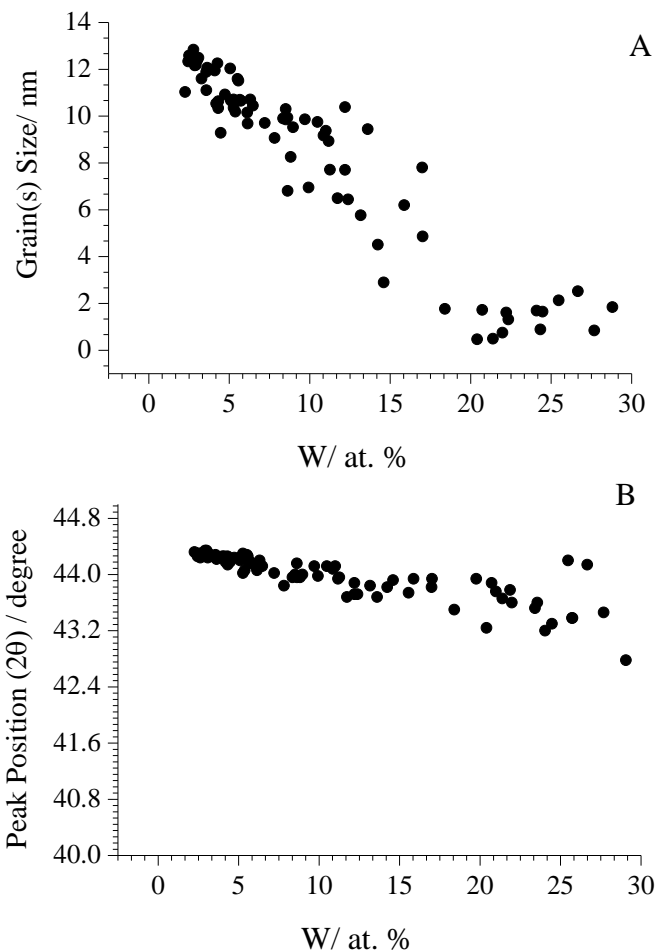


Figure 4.2: (A) The grain size of the NiW solid solution phase determined using the Scherrer equation from the half width of the $\langle 111 \rangle$ Bragg peak as a function of composition. (b) The peak position of the $\langle 111 \rangle$ Bragg peak of the NiW solid solution as a function of composition. Note that error will be higher close to zero nm.

The grain size of the NiW solid solution phase is determined using the Scherrer Equation 4-1 after extracting the full width of half maximum (FWHM) from the $\langle 111 \rangle$ peak at ca. $2\theta = 44.4^\circ$, and is shown in **Figure 4.2A**. The results are closely comparable to those obtained elsewhere for co-sputtered un-annealed (non-equilibrium) thin films [103] which also show a reduction in grain size from 15 nm to 1 nm as the W content increases in the range 0 - 30 %_{at.} W.

$$L = \frac{K\lambda}{\beta \cos \theta}$$

Equation 4-1

Where L, K, λ , β , θ are grain size, Scherer's constant (i.e. 0.94), wave length of X-ray beam, Full Width at Half Maximum (FWHM), and scattering angle respectively.

The dependence of grain size appears to flatten at ca. 2 nm for a composition > 20 %_{at.} W (**Figure 4.2A**), representing the limit of accuracy in grain size extraction from the very broad peaks, and heralds the onset of the formation of the amorphous phase: This has been observed previously [93] for non-equilibrium Ni-W alloys at composition > 20 %_{at.} W.

4.3 Electrochemical Measurements of As-deposited a 10x10 Ni-W Array in Phosphoric Acid Solution [pH 3] at 293 K.

4.3.1 Cyclic Voltammetry

Figure 4.3 shows the first cyclic voltammograms of a 10x10 Ni-W library where the potential was scanned from -900 mV to +800 mV vs. SCE. Electrochemical measurements were conducted in phosphoric acid (pH 3) solution purged with Ar for 3 min at 298 K. Film thicknesses are in the range 100 -150 nm. The currents in **Figure 4.3** are presented on a global scale (the same current scale for each square) at $\pm 6 \text{ mA cm}^{-2}$ around the current zero. Note that the tungsten content increases vertically across the array as indicated, and every horizontal row has nominally the same tungsten composition as a result of the deposition geometry expected for opposing source positions [170]. The result is that the cyclic voltammograms for each horizontal row are very similar (**Figure 4.3**). The Ni rich alloys (lowermost) display a large anodic polarisation when compared to the W rich alloys. There is little change in the general oxidation behaviour in the anodic polarisation for compositions below 15 %_{at.} W.

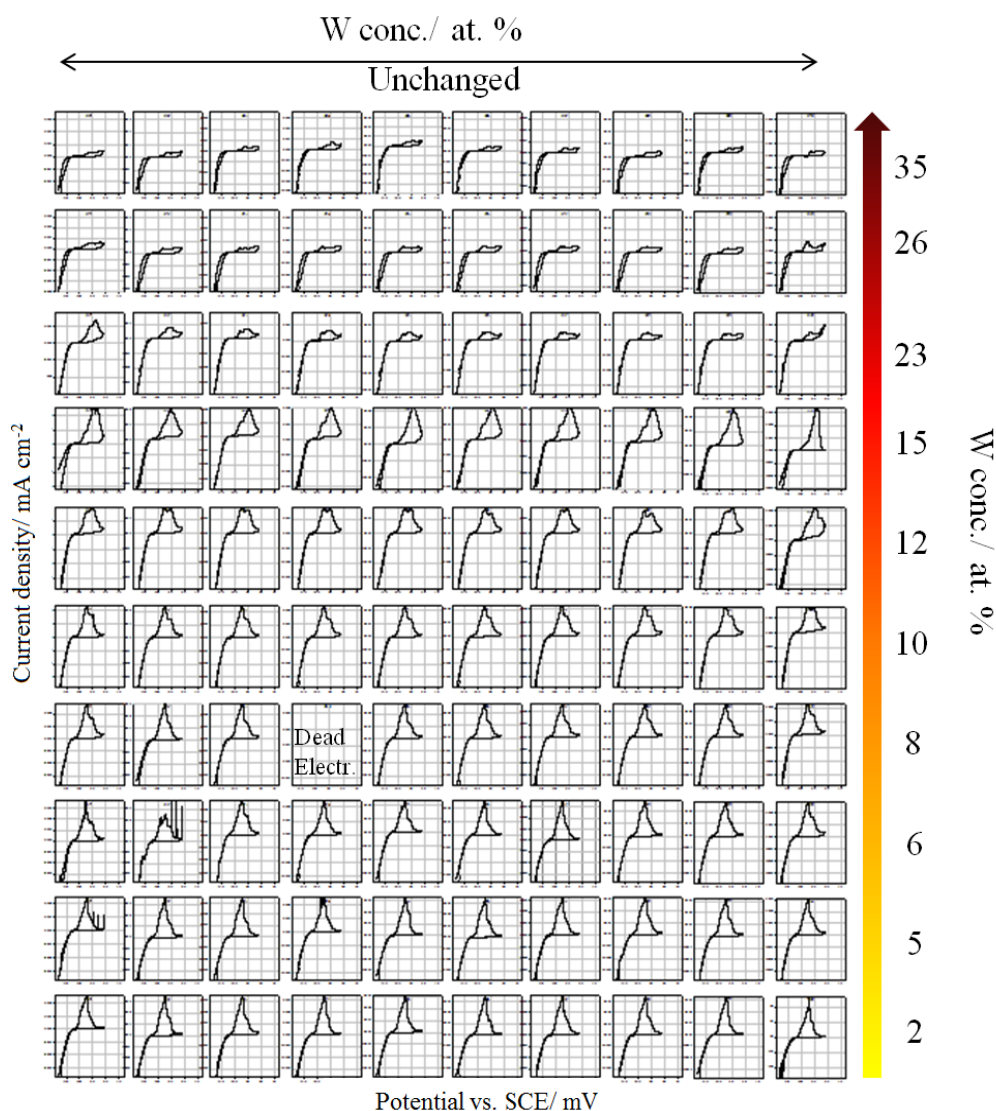


Figure 4.3: Cyclic voltammograms of a 10x10 Ni-W array studied in phosphoric acid pH 3 at 293 K. All the squares have same scale where x axis ranges from (- 900 to + 800 vs. SCE/ mV) and y varies by ± 6 mA cm⁻² around the zero current. The 20 mV s⁻¹ was used as scan rate. Gold was used as substrate for the electrochemical array. Tungsten compositions were determined by EDS and are enclosed above. Electrode with a coordinate (4, 4) from bottom left is dead electrode due to bad connection.

Figure 4.4 shows the cyclic potentiodynamic curves for Ni and selected Ni-W compositions in the range 6 to 33 %_{at.} W. The anodic polarisation of pure Ni is smaller than Ni-W alloys with W compositions ≤ 15 %_{at.}, and is shown in **Figure 4.4**; this indicates qualitatively that adding W at low concentrations

potentially deteriorates the alloys corrosion resistance, and this effect has been reported elsewhere [94] where Ni and Ni-W alloys in this composition range were explored in acidic sodium chloride solution. It is also evident from the potentiodynamic curves (**Figure 4.4**) that hydrogen evolution is promoted on Ni by the addition of low concentrations of W, and at higher W content it diminishes again. This appears qualitatively in good agreement with what is known about this system [101, 187].

The passivity improves by adding W particularly for the NiW alloys with W compositions $\geq 21\%_{\text{at}}$ (**Figure 4.4**). Consequently, the breakdown potential (E_{bd}), at which anodic current largely increases, shifts to positive potentials. Additionally the anodic activity decreases at the compositions $\geq 21\%_{\text{at}}$ W. Both Ni and Ni-W alloys display a negative hysteresis loop, which indicates that Ni and Ni-W alloys corrode uniformly. The absence of any positive hysteresis loop indicates that Ni and Ni-W alloys do not suffer from pitting corrosion in phosphoric acid.

The $\text{Ni}_{67}\text{W}_{33}$ alloy, i.e. at the highest tungsten composition investigated, displays the lowest anodic polarisation investigated. The qualitative conclusion that can be drawn from **Figure 4.2**, **Figure 4.3** and **Figure 4.4** is that in the composition region where the grain size in the Ni-W alloy is decreasing, there is a concomitant decrease in the anodic polarisation.

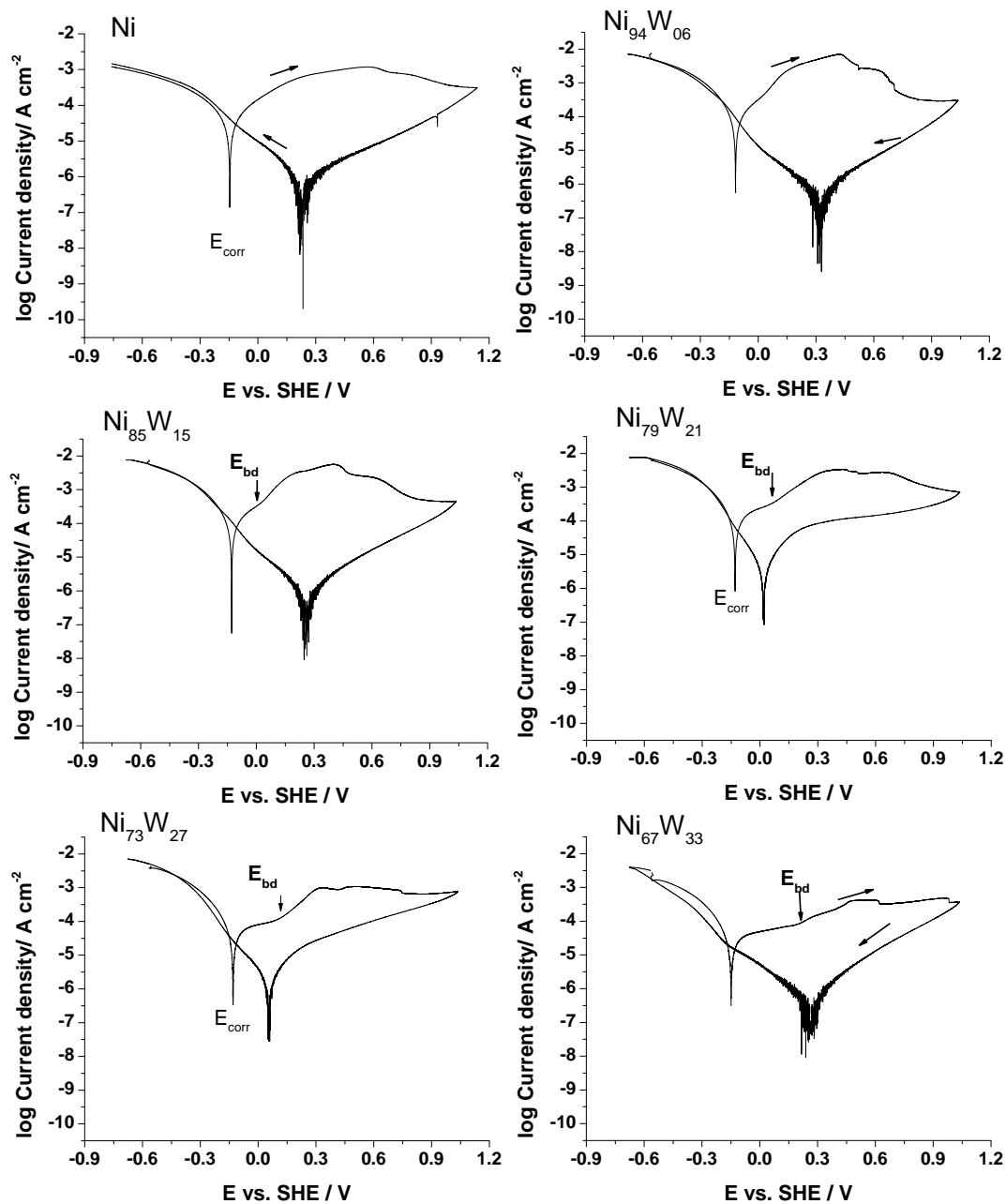


Figure 4.4: Selected cyclic potentiodynamic curves for a composition from 6–33 %_{at.} W and pure Ni. Currents are normalised to geometric area. The electrolyte is phosphoric acid pH 3. Anodic activity decreases for the compositions ≥ 21 %_{at.} W. The corrosion potential (E_{corr}) and breakdown potential (E_{bd}) are labelled.

4.3.2 Corrosion (zero current) potential

Figure 4.5 shows the corrosion potentials (E_{corr}) from 100 Ni-W alloys from a single array for the composition range 5 - 35 %_{at.} W. Two regions of composition display a reduction of the corrosion potential with increasing W content, and between these regions ($15 \geq W \%_{\text{at.}} \leq 28$) the E_{corr} appears to be constant. Those relate to the solid solution of tungsten in Ni and amorphous phase potentials respectively. The first reduction of the corrosion potential is caused by localised corrosion as result of preferential attack on active site (.i.e. where tungsten depleted). This is expected in heterogeneous phase such as the solid solution of tungsten in Ni. Also this in agreement with other observations [188]. The second reduction of the corrosion potential is due to formation of tungsten oxide (WO_3) which acts as an n-type semiconductor [189, 190]. The negative charge accumulates an included with the n-type oxide results in a negative shift in corrosion potentials. Further, the oxide (WO_3) is predictable to be thermodynamically stable under these conditions [109], also observed experimentally elsewhere [191, 192]. The negative electronic band gap of tungsten trioxide WO_3 increases by the formation of distorted amorphous WO_3 [193]. Consequently the corrosion potential moves to negative potentials as tungsten trioxide WO_3 becomes more amorphous. This is in agreement with observations which revealed that electronic bandgap increases with the reduction of grains size[194].

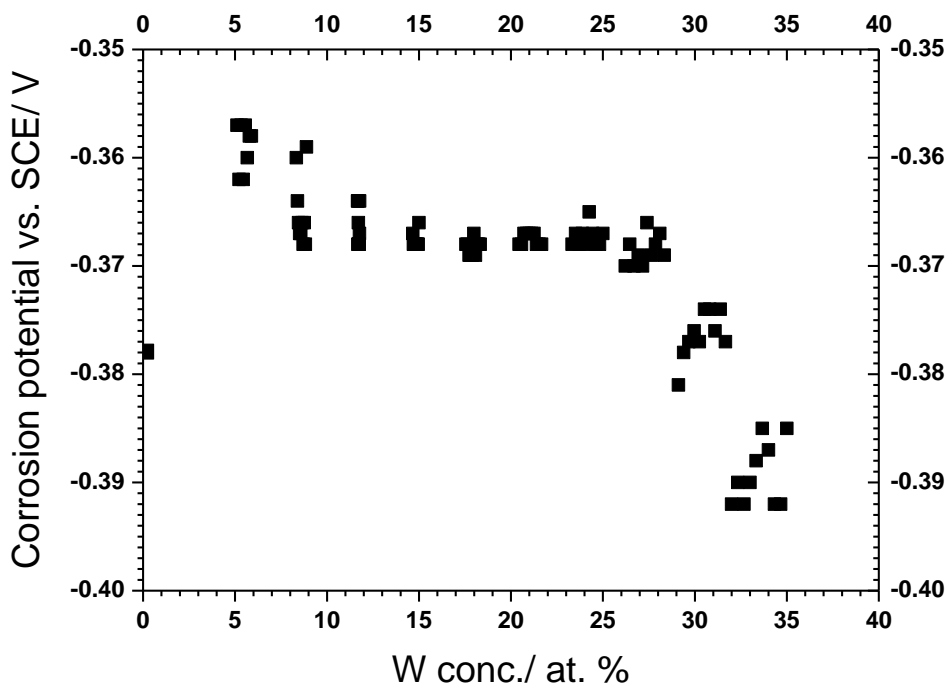


Figure 4.5: The corrosion potentials (E_{corr}) extracted from the potentiodynamic curves for a composition of 5-35 %at W and pure Ni.

4.3.3 Corrosion Resistance

Corrosion (polarisation) resistance extracted from cyclic voltammograms data were determined by linear polarisation resistance (LPR) and Tafel methods. **Figure 4.6** shows the corrosion resistances (obtained by LPR) as a function of alloy composition for the 100 fields of one of the Ni-W libraries. Due to similarity of the compositions of rows of electrodes (**Figure 4.3**) their corrosion resistances appear as clusters of ten. There is a slight reduction of the corrosion resistance(s) with increasing W content in the composition range of 5-20 %at W (**Figure 4.6**), which is a result of localised corrosion taken place in the solid solution of tungsten in Ni. This indicates the small reduction in the corrosion potentials (**Figure 4.5**). There is, however, above 24 %_{at.} W, a considerable increase in the corrosion resistance, which coincides with the onset of the formation of the amorphous phase; this was first observed at ca. 26 %_{at.} W, and which persists at higher W compositions (**Figure 4.1**). The increased corrosion resistance of the amorphous phase is in agreement with observations elsewhere [98]. It has been ascribed to the significant reduction

of segregation, and grain boundary energy, at compositions higher than 24 %_{at.} W for which there is clear evidence [99]. Nevertheless, the possible formation of tungsten oxide (WO₃) is most likely the principal cause of the significant change observed in the corrosion resistance and potential (**Figure 4.5** and **Figure 4.6**).

For further investigation selected corrosion resistances determined by the LPR method (**Figure 4.6**) are compared to those obtained by the Tafel method, and the results are shown in **Figure 4.7**. The error bars reflect a standard error obtained from three data points at similar compositions. The results obtained by the two methods are very consistent and exhibit very similar compositional dependent behaviour. There is a systematic increase in the absolute values of corrosion resistances extracted by LPR, which are likely to be a result of irreversible changes during the cathodic scan which precedes the linear polarisation resistance region. As a result a thin corrosion film is formed on alloy surfaces producing an increase of the corrosion resistances extracted by LPR, in agreement with the assessment of Mansfeld [28], not owing to the accusation made by Hoar [26] against the LPR method of giving superfluous electrical measurements despite measurement method and corrosion system. In addition to this, both the LPR and Tafel method are susceptible to the capacitive currents associated with the high scan rates applied in this study [1]. As pointed out earlier, the latter will give rise to a systematic error in the absolute values obtained (perhaps not equally for each method), but the relative values across composition will be much less susceptible to this contribution.

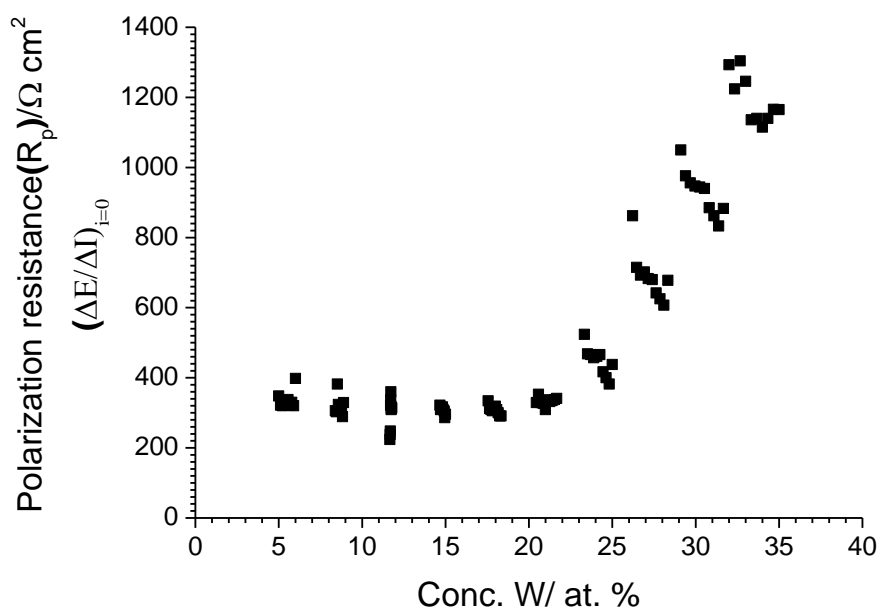


Figure 4.6: Polarisation resistances determined by LPR of as-deposited 100 pads on Ni-W array of a compositions range of 5-35 %_{at.} W. All electrochemical measurements are performed in phosphoric acid pH 3 electrolyte at 293 K. The electrolyte was purged with Ar for 3 min in the presence of the array. The error bar was obtained from standard error.

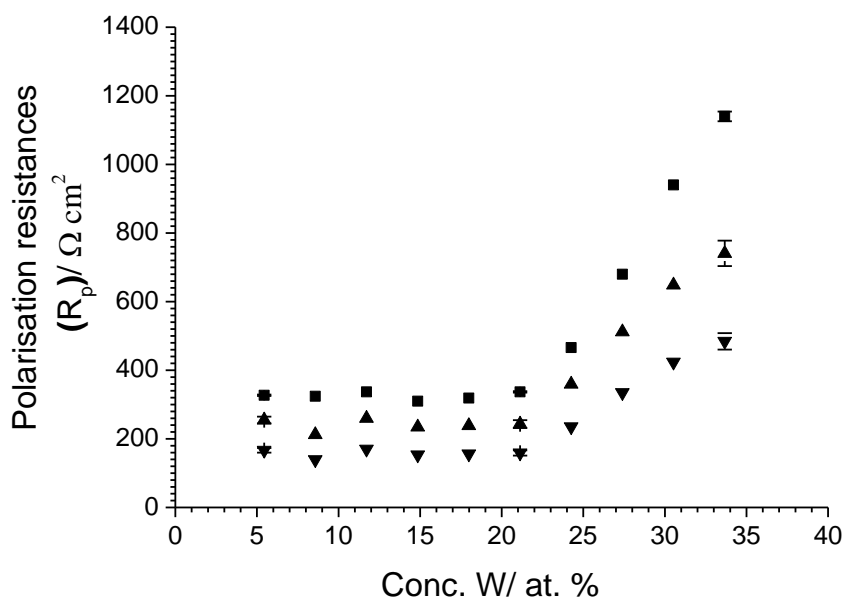


Figure 4.7: Selected polarisation resistances determined by LPR (■) compared to ones obtained by Tafel (▲, ▼) where B equals 13 and 26 mV respectively. The error bar was obtained from standard error.

4.4 Conclusion

High throughput corrosion screening measurement has successfully been applied to study the compositionally dependent corrosion resistance of non-equilibrium Ni-W alloys. High throughput XRD studies have allowed a correlation of the behaviour with composition and structure. The corrosion resistances (R_p) of the Ni-W alloy library have been extracted from the voltammetry using the linear polarisation resistance (LPR) and Tafel extrapolation methods. The results obtained by these methods are very consistent.

In the composition region $W < 24 \text{ \%}_{\text{at}}$, the grain size decreases strongly with increasing W content in the Ni-W solid solution phase, only a very small concomitant reduction in corrosion resistance and potential is observed.

At compositions of $W \geq 24 \text{ \%}_{\text{at}}$, the amorphous phase is observed whose formation is associated with a strong increase in the corrosion resistance and a large cathodic shift in corrosion potential.

5. Binary Al-Mg Alloys

5.1 Introduction

Libraries of binary Al-Mg alloys over the composition range of (5-80 %_{at.} Al, 10-95 %_{at.} Mg) have been prepared by physical vapour deposition (PVD). The alloy compositions and structures have been fully characterised using X-ray diffraction (XRD) and electron dispersive energy microscopy (EDX). Moreover the surface morphologies of selected alloys have been determined.

High-throughput electrochemical screening has also been performed. Subsequently the alloys corrosion resistances are plotted as a function of Al and Mg compositions. Also the corrosion potentials (E_{corr}) extracted from the potentiodynamic curves are plotted versus the Al and Mg compositions.

Also this chapter examines the microstructure and morphology effects on the corrosion resistances of the Al-Mg alloys in particular the role of the β phase.

5.2 X-ray diffraction of Binary Al-Mg Alloy

Figure 5.1 presents the X-ray diffraction patterns of Mg-Al alloys. The thin film alloys with a thickness of ca. 100-150 nm were deposited on Si/SiN substrates at 300 K. The $Al_{10}Mg_{90}$ alloy shows one peak at ca. $2\theta = 34.42^\circ$ which according to the PDF card [195] corresponds to the (002) Bragg peak of the hexagonal Mg with (P63/mmc) space group. By introducing more Al another peak appears at ca. $2\theta = 34.72^\circ$ as displayed by the $Al_{22}Mg_{78}$ in addition to the (002) peak which is moved to a slightly lower angle at ca. $2\theta = 34.26^\circ$. These two peaks persist at the compositions of 22-25 %_{at.} Al. However, the peak that appeared at ca. $2\theta = 34.26^\circ$ disappears at more than 25 %_{at.} Al as displayed by the $Al_{27}Mg_{73}$ and $Al_{34}Mg_{66}$ alloys. From compositional point of view the Al-Mg alloys which contain (40-70 %_{at.} Al, 30-60 %_{at.} Mg) show amorphous structure where no peaks have been observed. This can be seen in the diffraction of the $Al_{40}Mg_{60}$ alloy. At rich aluminium alloys comprised ≥ 74 %_{at.} Al a Bragg peak appears at ca. $2\theta = 38.36^\circ$ which corresponds to the solid solution of Mg in the f.c.c Al (111).

According to the Mg-Al phase diagram [104] presented in **Figure 5.2a**, the hexagonal Mg with (P63/mmc) space group exists from 0-13 %_{at.} Al; however the Al solid solution in Mg can extend up to 27 %_{at.} Al as shown in the modified Mg-Al phase diagram suggested by Hajjari et al. and presented in **Figure 5.2b**. The latter reveal that a mixture of γ Al₁₂Mg₁₇ intermetallic phase and the solid solution of Al in Mg phases have been obtained at the composition of 27 %_{at.} Al and 73 %_{at.} Mg. Similar observations have been reported by other authors [141, 145]. This compares to the peaks located at ca. $2\theta = 34.42^\circ$, 34.72° and displayed by Al₂₂Mg₇₈ and Al₂₅Mg₇₅ alloys as shown in **Figure 5.1**. At equilibrium the γ Al₁₂Mg₁₇ exists from 40-55 %_{at.} Al although an early review study of the Mg-Al phase diagram [196] suggests the γ Al₁₂Mg₁₇ at low temperature persist over a greater compositional range. This has been proved by Singh et al. [197] where the γ Al₁₂Mg₁₇ has been identified at a lower compositional range of 30-40 %_{at.} Al.

The alloys containing (40-70 %_{at.} Al) show amorphous structure as displayed by the Al₄₀Mg₆₀ alloy (**Figure 5.1**). Similar results obtained by Mukherjee et al. [198] revealed that the Al₆₅Mg₃₅ and Al₆₀Mg₄₀ alloys contain merely nanocrystalline phases and amorphization. Moreover they have proved that the amorphous metastable phase is the more stable phase from the thermodynamical point of view at the composition range of 35-60 %_{at.} Mg compared to crystalline solid solution phases.

According to the Mg-Al phase diagram [104], the f.c.c (111) Bragg peak of Al crystalline exists from ~ 80 to 100 %_{at.} Al. However a distinct crystalline of the f.c.c (111) Al has been obtained at 73.9 %_{at.} Al [141]. The latter associates with the onset of the Bragg peak which appears at ca. $2\theta = 38.36^\circ$ as displayed by the Al₇₄Mg₂₆ alloy shown in **Figure 5.1**. The intensity of this peak increases significantly at 79 %_{at.} Al.

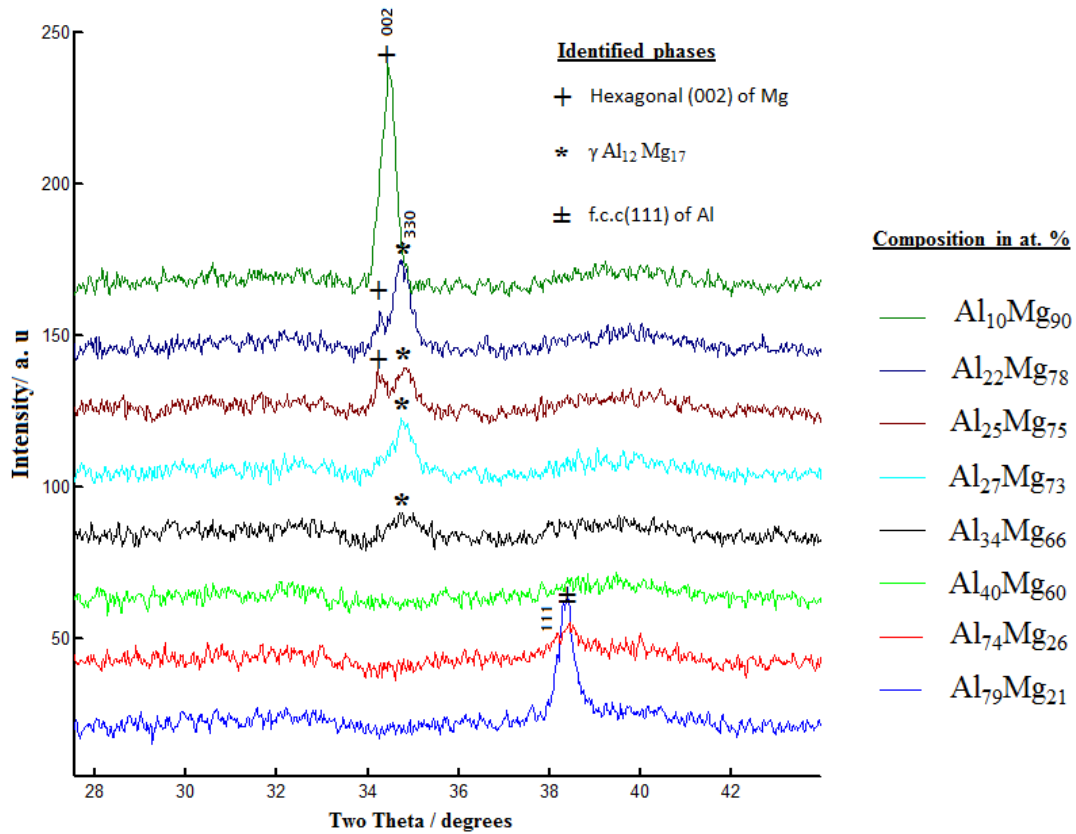


Figure 5.1: X-ray diffraction patterns of a series of as-deposited Mg-Al thin film alloys of composition range of 10-79 %_{at.} Al. The films were deposited on a silicon/ silicon nitride substrate at ~ 300 K (#7358). Three phases have been identified, namely solid solution of Al in Mg as hexagonal (002), γ $\text{Al}_{12}\text{Mg}_{17}$ with structure of (330), and Mg solid solution in Al of f.c.c (111). The alloys composition in %_{at.} was determined by EDS.

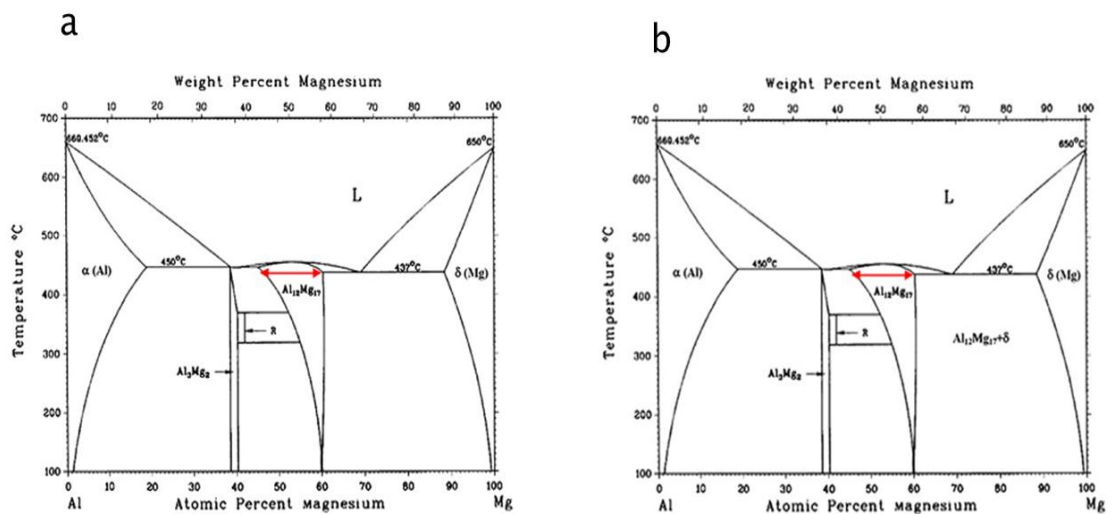


Figure 5.2: The Al-Mg phase diagram (a) ref.[104] and (b) ref.[143].

For further analysis, the area under the peaks located at ca. $2\theta = 34\text{--}35^\circ$ and presented in **Figure 5.1** have been integrated and plotted as a function of the Al compositions. Note that the peak area represents the peak size as well. Therefore the peak disappears if the peak area is equal to zero. Firstly, the area under the peaks located at ca. $2\theta = 34.42^\circ$ and 34.72° were plotted versus Al composition and are presented in **Figure 5.3**. These peaks are related to the Mg (Al) solid solution and the intermetallic γ $\text{Al}_{12}\text{Mg}_{17}$ phase.

The addition of Al from 5 to 10 %_{at.} decreases the peak area sharply as shown clearly in the inset figure. This compares to the significant decrease of the peak intensity at ca. $2\theta = 34.42^\circ$ which corresponds to the Mg (002) as displayed by $\text{Al}_{22}\text{Mg}_{78}$ (purple colour) as shown in **Figure 5.1**. However, at 15 %_{at.} Al a small shoulder has surfaced (**Figure 5.3**), which relates to the onset for the second peak appearing at ca. $2\theta = 34.72^\circ$ (**Figure 5.1**). At 40 %_{at.} Al the peak area flattens to zero. This indicates that no peaks exist at this composition, which is confirmed as displayed by $\text{Al}_{40}\text{Mg}_{60}$ alloy (coloured with green **Figure 5.1**).

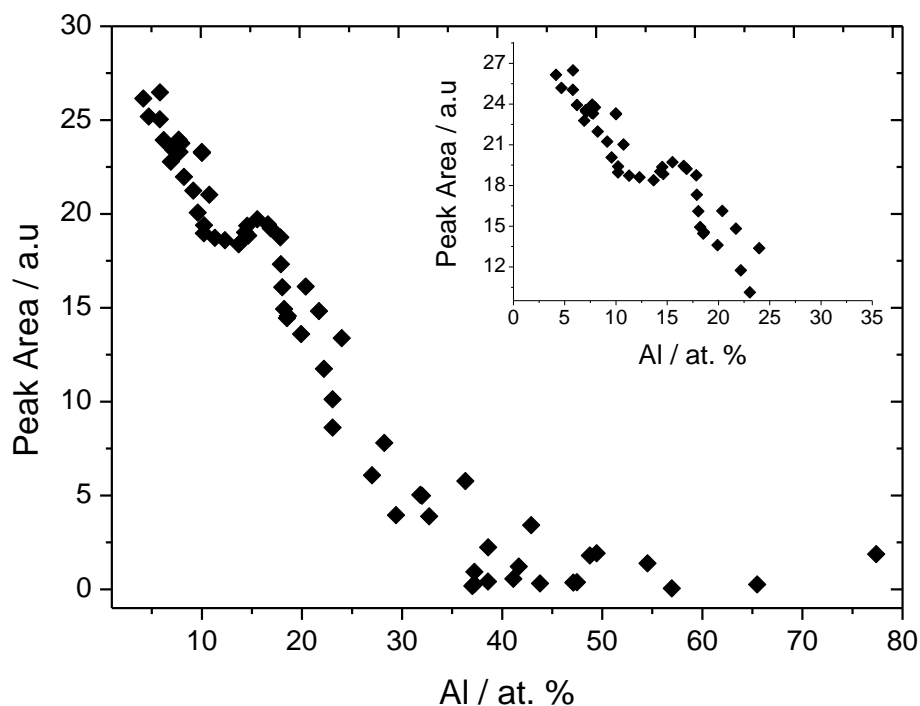


Figure 5.3: The integrated areas under the peaks located at ca. $2\theta = 34.42^\circ$ correspond to (002) of hexagonal Mg (Al) solid solution and 34.72° corresponds intermetallic γ $\text{Al}_{12}\text{Mg}_{17}$ phase as function of Al compositions.

The first reduction of the peak area observed at 5 to 10 %_{at.} Al (**Figure 5.3**) relates to the formation of an Al solid solution in Mg, which disappears at ~27 %_{at.} Al. The peak area (**Figure 5.3**) shows limited relaxation region between 12-14 %_{at.} Al, which is associated with the onset of the γ Al₁₂Mg₁₇ phase. There is, however, a little shoulder that arises at 15 %_{at.} Al after the relaxation region (as clearly shown in the inset figure in **Figure 5.3**); which indicates that the γ (Al₁₂Mg₁₇) is dominating the mixture consisting of the γ Al₁₂Mg₁₇ and the Al solid solution in Mg. This agrees with the observation presented in **Figure 5.4**, where the γ Al₁₂Mg₁₇ displays an obvious Bragg peak corresponding to the (330) structure and only a small peak appears for the Mg (002).

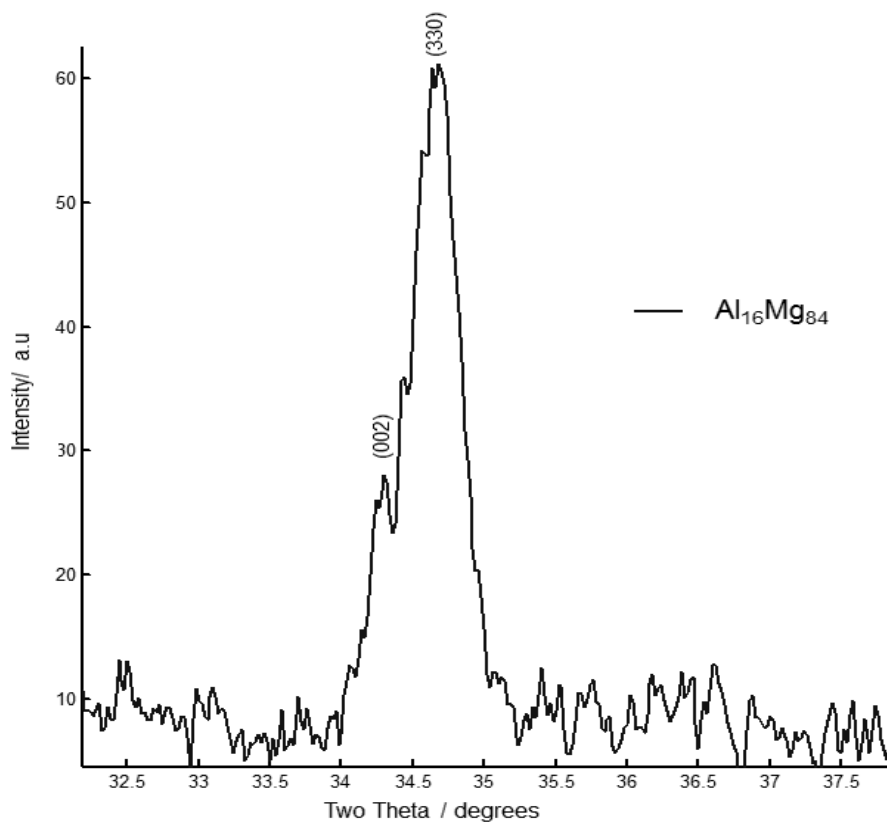


Figure 5.4: The X-ray diffraction pattern of the Al₁₆Mg₈₄ alloy. Two phases have been identified namely solid solution of Al in Mg as (002) and γ Al₁₂Mg₁₇ with structure of (330).

Figure 5.5 shows the peak area analysis under the third peak located at ca. $2\theta = 38.36^\circ$ and shown in **Figure 5.1**. There is no change of the peak area throughout the composition range of 5-70 %_{at.} Al, in which the peak area

equals zero. This means the peak located at ca. $2\theta = 38.36^\circ$ does not exist all over the previous compositions. But an obvious increase of the peak area appears at $\sim 75\%$ at. Al as shown in the inset figure in **Figure 5.5**. This increase relates to the onset of the solid solution of Mg in the Al. Consequently the peak area (= peak size) increases sharply at $\geq 79\%$ at. Al. This associate with the pronounced peak displayed by the $\text{Al}_{79}\text{Mg}_{21}$ alloys (labelled with blue colour) and located at ca. $2\theta = 38.36^\circ$ (**Figure 5.1**). This peak corresponds (111) of the Al f.c.c.

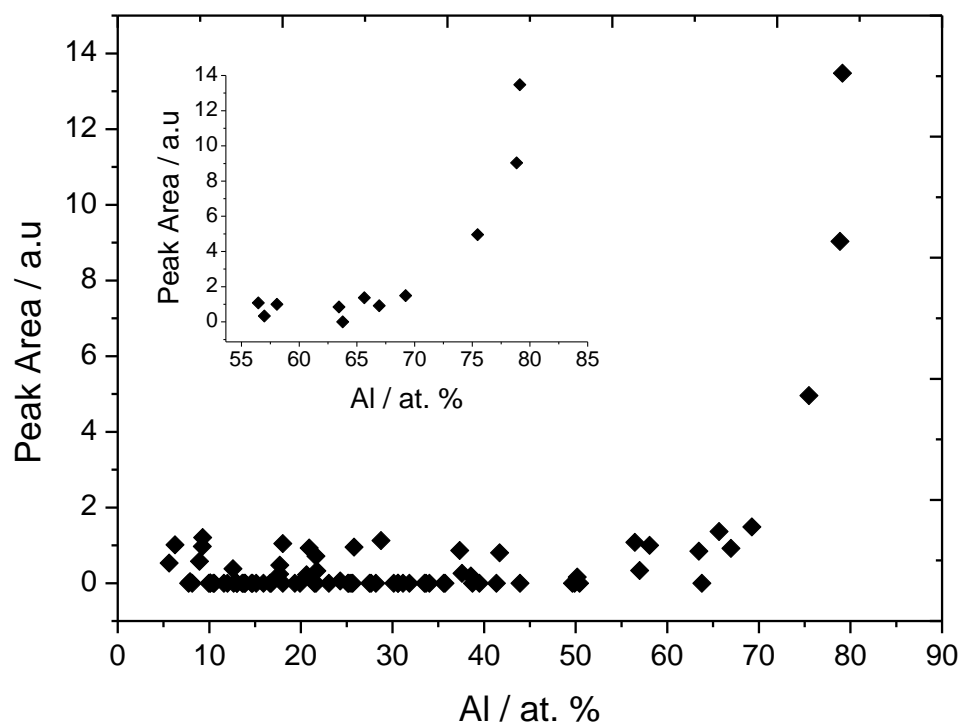


Figure 5.5: The integrated area under the peak located at $2\theta = 38.36^\circ$ which corresponds to the (111) of Al f.c.c. as function of Al compositions.

5.3 Corrosion Resistance (Polarisation) of the Al-Mg Alloys

The electrochemical measurements were performed in sodium chloride solution [0.005 M]. The pH and temperature were kept at 9 and 293 K respectively. The corrosion resistances have been obtained by LPR and Tafel extrapolation methods. The Tafel constant (B) used to convert corrosion currents (i_{corr}) extrapolated from Tafel plots to corrosion resistances (R_p) as described in (Equation 5-1) is 26 mV. The method by which Tafel constant (B) was obtained is presented at the end of this chapter.

$$R_p = \frac{B}{i_{corr}} \quad \Omega \text{ cm}^2 \quad \text{Equation 5-1}$$

Figure 5.6 shows the corrosion resistances as function of Al compositions. Similar corrosion resistances were obtained by both methods. There is no change in the corrosion resistance throughout the compositional range of 5–30 %_{at.} Al. The magnitude of the corrosion resistance also appears low. However, an apparent increase arises from 27–48 %_{at.} Al. Another increase of the corrosion resistance appears at rich Al ≥ 80 %_{at.} Al (**Figure 5.6 B**), although this increase was not obtained in the corrosion resistances determined by LPR (**Figure 5.6 A**). The best corrosion resistance is displayed by ~ 40 %_{at.} Al (or Al₄₀Mg₆₀) composition. A small reduction of the R_p appears between 50 to 60 %_{at.} Al.

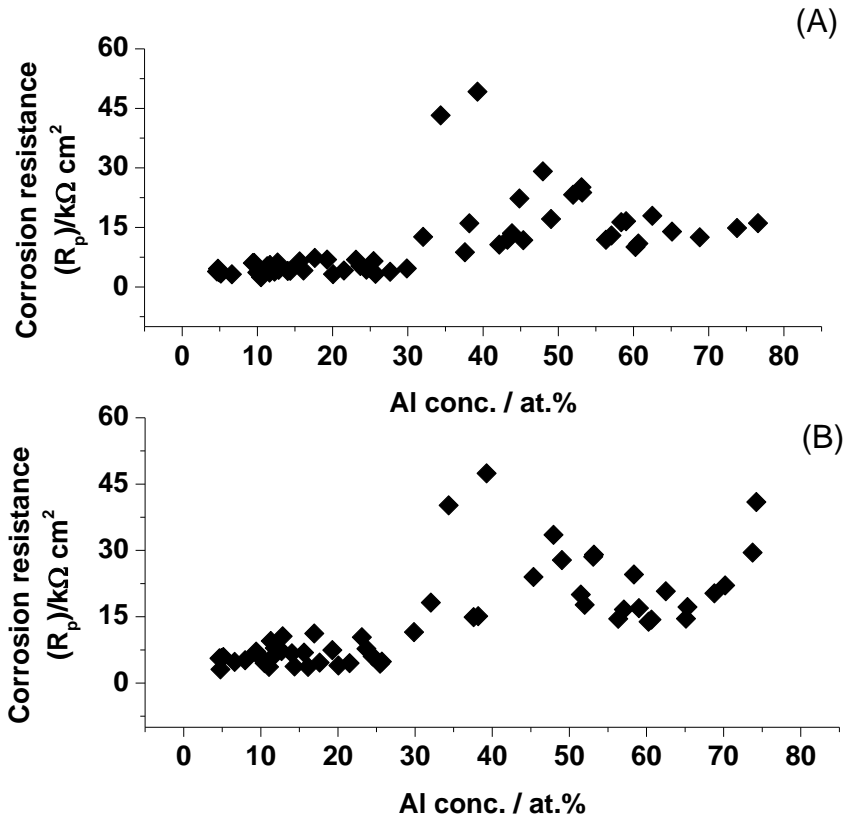


Figure 5.6 : The corrosion resistances of Al-Mg alloys (#7355) versus Al compositions (A) determined by LPR and (B) extracted from Tafel extrapolation, where $B = 26$ mV. The corrosion electrolyte is [0.005 M] of sodium chloride. The pH and temperature were kept at 9 and 293 K respectively.

From the Mg compositional point of view, at low Mg i.e. ≤ 25 %_{at.} the corrosion resistance shows good performance where the corrosion resistance is ≥ 15 kΩ cm² (**Figure 5.7**). At the compositions of 35–60 %_{at.} Mg the corrosion resistance increases noticeably before reaching a maximum at a 60 %_{at.}, above which a decrease in the R_p is viewed. There is, however, an apparent reduction in corrosion resistance that appears at 70 %_{at.} Mg. The Al-Mg alloys comprised Mg ≥ 70 %_{at.} displays similar corrosion resistances.

Consequently as presented in **Figure 5.6** and **Figure 5.7**, the best corrosion resistance is demonstrated by the compositions of (30–45 %_{at.} Al, Al ≥ 80 %_{at.}) or (35–60 %_{at.} Mg, Mg ≤ 25 %_{at.}). On the other hand the Al-Mg alloys contained rich Mg ≥ 70 %_{at.} show low corrosion resistance.

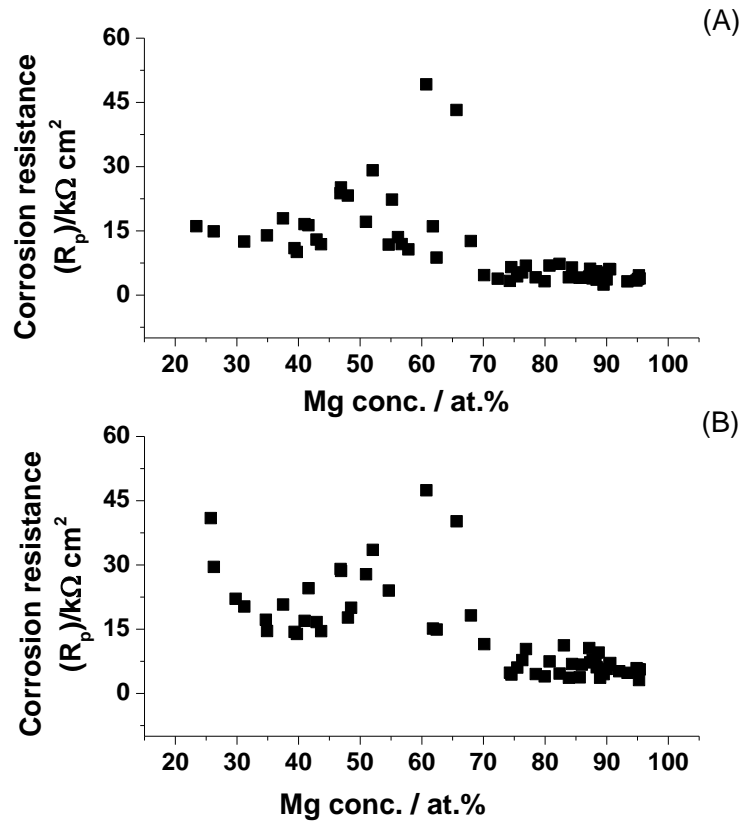


Figure 5.7 : The corrosion resistances of Al-Mg (#7355) alloys versus Mg compositions (A) determined by LPR and (B) extracted from Tafel extrapolation where $B = 26\text{ mV}$. The corrosion electrolyte is [0.005 M] of sodium chloride.

The pH and temperature were kept at 9 and 293 K.

In addition the corrosion potentials (E_{corr}) which are extracted from the cyclic voltammogram data at the zero current potential are presented in **Figure 5.8**. The addition of Al moves the corrosion potential towards more positive potentials (**Figure 5.8 B**). But at $35\%_{\text{at.}} \leq \text{Al} \leq 50\%_{\text{at.}}$ the E_{corr} has decreased to more negative potentials. The E_{corr} stays constant at ca. -1.4 V/ vs. SCE between 50 to 79 $\%_{\text{at.}}$ Al. Similar behaviour is demonstrated by the E_{corr} versus Mg compositions as shown in (**Figure 5.8 A**). The lowest corrosion potential i.e. (-1.00 V/ vs. SCE) is obtained at 70 $\%_{\text{at.}}$ Mg; which correlates with the corrosion potential obtained at 30 $\%_{\text{at.}}$ Al (**Figure 5.8 B**). The addition of $\text{Mg} \geq 75\%_{\text{at.}}$ switches the corrosion potential abruptly towards more negative potentials.

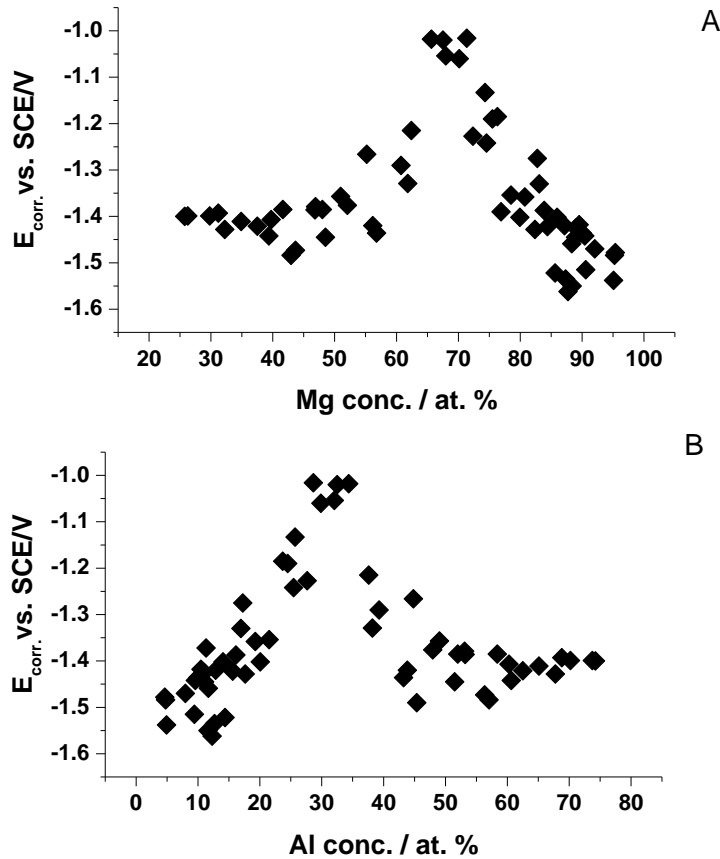


Figure 5.8: The corrosion potentials of the Al-Mg alloys (#7355) for the composition range of 5–79 %_{at.} Al and 25–95 %_{at.} Mg. The saturated calomel electrode (SCE) was used as reference electrode. The corrosion electrolyte is [0.005 M] of sodium chloride.

The more positive corrosion potential viz. -1.00 V/ vs. SCE has been obtained at the composition of (30 %_{at.} Al or 70 %_{at.} Mg) as shown in **Figure 5.8**. This associates with the exclusive formation of the γ $\text{Al}_{12}\text{Mg}_{17}$ as displayed by the $\text{Al}_{27}\text{Mg}_{73}$ alloy in the X-ray diffraction results (**Figure 5.1**). However, the most negative potential i.e. -1.5 V/ vs. SCE (**Figure 5.8**) was displayed by the rich Mg ≥ 90 %_{at.} alloys. Those alloys contain solely α -Al solid solution in Mg as in shown **Figure 5.1**. Consequently the alloys possessing the γ $\text{Al}_{12}\text{Mg}_{17}$ structure exclusively exhibit E_{corr} values 500 mV less negative than the alloys containing only the α -Al solid solution in Mg. This in agreement with the observation that has been previously identified by Song and Atrens [4], where the difference of

the E_{corr} between the alloys comprised of the γ ($\text{Al}_{12}\text{Mg}_{17}$) and those containing the α -Al solid solution in Mg is 400 mV.

The corrosion resistances results presented in **Figure 5.6** and **Figure 5.7** display similar behaviour. Low corrosion resistance was noticed at high Mg concentration viz. ≥ 80 %_{at.} which consist of γ ($\text{Al}_{12}\text{Mg}_{17}$) and Al solid solution in Mg. But an obvious increase of the corrosion resistance has been detected at 70 %_{at.} Mg, which compares to the great shift of the corrosion potential towards more positive potential (**Figure 5.8**). This is attributed to the exclusive form of the γ $\text{Al}_{12}\text{Mg}_{17}$ phase acting as corrosion barrier. The γ $\text{Al}_{12}\text{Mg}_{17}$ phase generally plays two roles. Firstly it could act as passive film hence lessens the number of active sites on the surface. As a result the corrosion resistance would improve. This occurs only when the γ $\text{Al}_{12}\text{Mg}_{17}$ phase or so called β phase distributes equally in large fraction. This relates to the obvious increase of the corrosion resistance noticed at 70 %_{at.} Mg. However, the β phase acts as a cathode when it exists in a small fraction into α phase i.e. Al solid solution in Mg. As a result it accelerates the corrosion rate and reduces the corrosion resistance. This associates with the low corrosion resistance displayed at high Mg concentration ≥ 80 %_{at.} as shown in **Figure 5.6**. The role of the β phase i.e. γ $\text{Al}_{12}\text{Mg}_{17}$ on corrosion resistance has been given enormous attention [4, 6, 20, 119-127, 199]. The conclusion is that the γ ($\text{Al}_{12}\text{Mg}_{17}$) phase inhibits corrosion progress when present in a large fraction forming a continuous network. This therefore lessens the number of the active sites on the surface. As a result the corrosion potential appears more positive than the α -phase viz. Al solid solution in Mg [4, 6, 124]. This compares to the more positive corrosion potential viz. -1.00 V/ vs. SCE obtained at the composition of (30 %_{at.} Al, 70 %_{at.} Mg) in which the γ $\text{Al}_{12}\text{Mg}_{17}$ phase dominates, as displayed by $\text{Al}_{27}\text{Mg}_{73}$ alloy (cyan colour) and presented in **Figure 5.1**. There is, however, a negative effect of the γ $\text{Al}_{12}\text{Mg}_{17}$ phase when existing in the form of nano-structure, which precipitates into a huge cluster of the α -phase. In this environment the γ $\text{Al}_{12}\text{Mg}_{17}$ acts as cathode where α phase acts as anode hence micro-galvanic corrosion would be created [6, 122]. However, this effect has not been observed and the corrosion resistance over the composition range of 75–97 %_{at.} Mg displays a uniform behaviour as shown in **Figure 5.7**. In other words, there is no reduction of the corrosion resistance observed at 87 %_{at.} Mg (=13 %_{at.} Al) at which the onset of the γ $\text{Al}_{12}\text{Mg}_{17}$ arises as clearly shown in **Figure 5.3**. This

agrees with Pardo et al. [120] observation of the surface potential mapping, which reveals no significant difference between the β and α phases galvanic coupling.

Figure 5.9 shows selected potentiodynamic curves of a series of Al-Mg alloys over the composition range of 5–77 %_{at.} Al and 23–95 %_{at.} Mg. The Al₇₇Mg₂₃ alloy (**Figure 5.9a**) demonstrates a rather positive corrosion potential (E_{corr}) and lower anodic current densities in comparison with the Al₅Mg₉₅ alloy.

The addition of 12 %_{at.} Al into the matrix has not made any difference on the electrochemical behaviour as displayed by Al₁₂Mg₈₈ (**Figure 5.9 b**). There is, however, a considerable change of the corrosion potential that occurs upon addition of 24 %_{at.} Al (**Figure 5.9c**), whereby the corrosion potential (E_{corr}) shifts 320 mV more positive in potential. This complies with the shift of the E_{corr} observed in **Figure 5.8**. The cathodic polarisation displays low activity over a wide potential range of -1.8 to -1.3 V/ SCE, but near to the corrosion potential high activity appears specifically at -1.25 V/SCE. Also the anodic polarisation shows active behaviour.

The lowest corrosion potential i.e. -1.05 V/ SCE is displayed by the Al₃₂Mg₆₈ alloy (**Figure 5.9d**). Additionally the Al₃₂Mg₆₈ alloy demonstrates low cathodic activity. Moreover it shows low anodic polarisation, although the anodic polarisation part was not entirely scanned because it sits out of the chosen potential window. This compares to the lowest corrosion resistance obtained at (40 %_{at.} Al and 60 %_{at.} Mg) and presented in **Figure 5.6** and **Figure 5.7**.

However, the compositions of (45–48 %_{at.} Al) exhibit a very negative E_{corr} potential viz. -1.55 V/ SCE compared to previous alloys. Moreover it suffers severe pitting corrosion initiated near to the E_{corr} potential as shown in **Figure 5.9f**. This coincides with the corrosion resistance reduction observed at ca. 48 %_{at.} Al as presented in **Figure 5.6**.

But at ≥ 52 %_{at.} Al the pitting corrosion has disappeared as displayed by the Al₅₂Mg₄₈. This coincides with the stability of the E_{corr} obtained at ≥ 52 %_{at.} Al as shown in **Figure 5.8**.

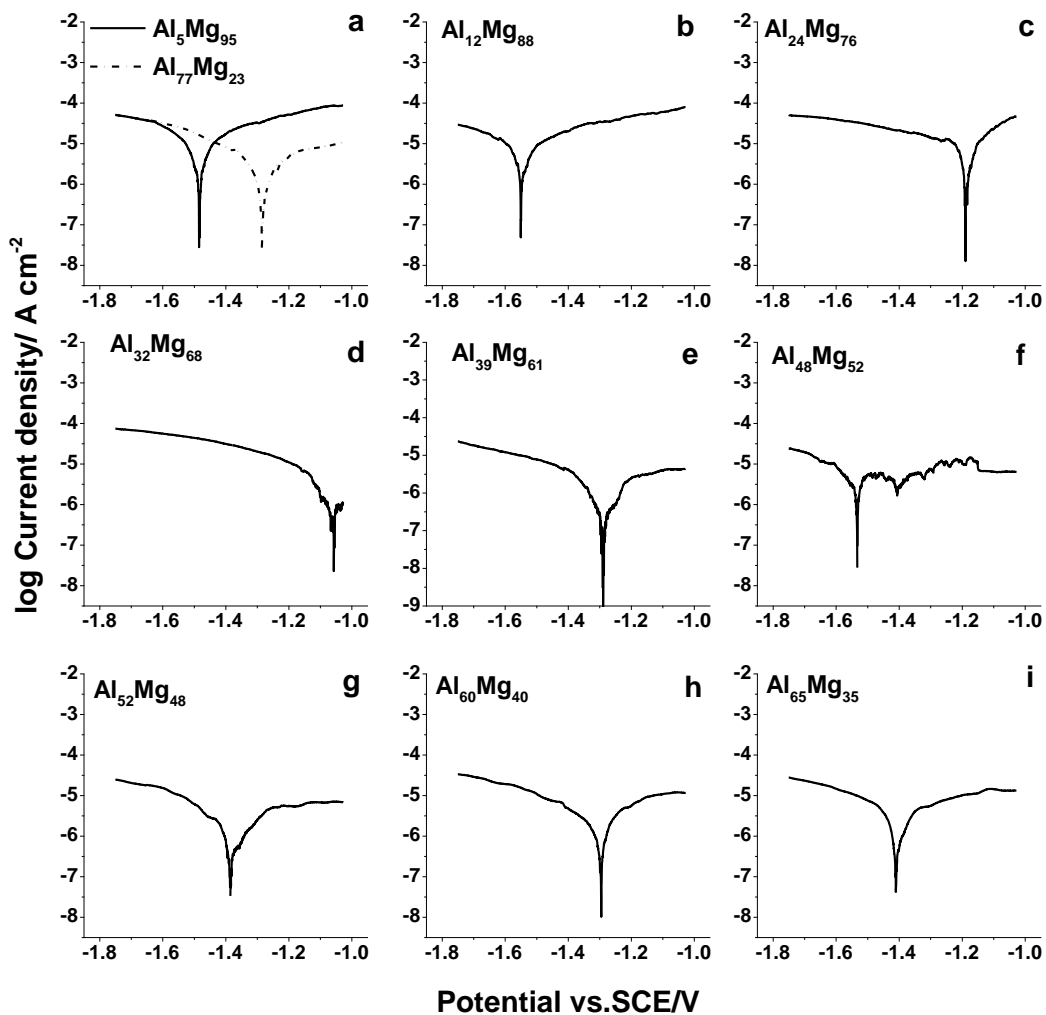


Figure 5.9: The potentiodynamic curves of series Al-Mg alloys for a composition range of 5-77 %_{at} Al. The corrosion electrolyte is sodium chloride [0.005 M] where the SCE is used as reference electrode. Compositions were determined by EDS.

In addition, surface morphologies after the electrochemical experimentation for the selected Al-Mg alloys have been obtained by the scanning electron microscope (SEM) and are presented in **Figure 5.10**. Note that all the samples appeared similar before the electrochemical screening test.

The Al₅Mg₉₅ alloy (**Figure 5.10a**) shows a large dark area on which corrosion has taken place. Only a few scattered white areas i.e. un-corroded areas were

observed. This relates to the high anodic polarisation observed for the same alloy in **Figure 5.9a**.

Although the appearance does not show corrosion products the $\text{Al}_{24}\text{Mg}_{76}$ alloys show obvious cracks (**Figure 5.10b**); which indicates the high anodic activity seen in **Figure 5.9c**.

The surface image of the $\text{Al}_{32}\text{Mg}_{68}$ alloys does not show any cracks (**Figure 5.10c**). Moreover the alloy surface is largely covered by an oxide layer which appeared as white in colour. Also small particles distribute over the surface. This alloy exhibits low corrosion potential (E_{corr}) and low anodic activity as displayed in the **Figure 5.9d**.

The potentiodynamic curve of the $\text{Al}_{48}\text{Mg}_{52}$ (**Figure 5.9f**) displays pitting corrosion; which compares to the small black pits (**Figure 5.10d**). The pits spread largely over the surface as presented in **Figure 5.10d**. Similar results were observed by Song and Atrens[4]. They believe the pitting corrosion mechanism of Al-Mg alloys differs from the stainless steel ones. In the latter pits grows deeply and aggressively with time, but in the Al-Mg pits tend to develop laterally and are self-healing with time.

However, the $\text{Al}_{52}\text{Mg}_{48}$ alloy does not suffer from any pitting corrosion (as shown in **Figure 5.9g**) although it contains a little more Al content ($\sim 5\%_{\text{at}}$). As a result no defects or corrosion products can be observed after the corrosion testing (as shown in **Figure 5.10e**). The X-ray diffraction results presented in **Figure 5.1** show only the amorphous phase at the compositions of (40-65 $\%_{\text{at}}$ Al). Besides the thermodynamic calculations made by Mukherjee et al. [198] prove that the amorphous phase is only stable over the composition range of 40–65 $\%_{\text{at}}$ Al. However, at equilibrium γ' metastable with a tetragonal structure has been identified over the composition range of 41.3–60 $\%_{\text{at}}$ Al by Murray [139]. Therefore there is no clear reason for the pitting corrosion seen in **Figure 5.10d**.

The surface morphology of the $\text{Al}_{77}\text{Mg}_{23}$ alloy displays neither corrosion products nor cracks as shown in **Figure 5.10f**. Also small fragments appear on the surface; which similarly has been noticed at the $\text{Al}_{32}\text{Mg}_{68}$ alloys

(Figure 5.10c). But the surface image of the $\text{Al}_{32}\text{Mg}_{68}$ alloys display white colour which was not seen in the $\text{Al}_{77}\text{Mg}_{23}$ alloy.

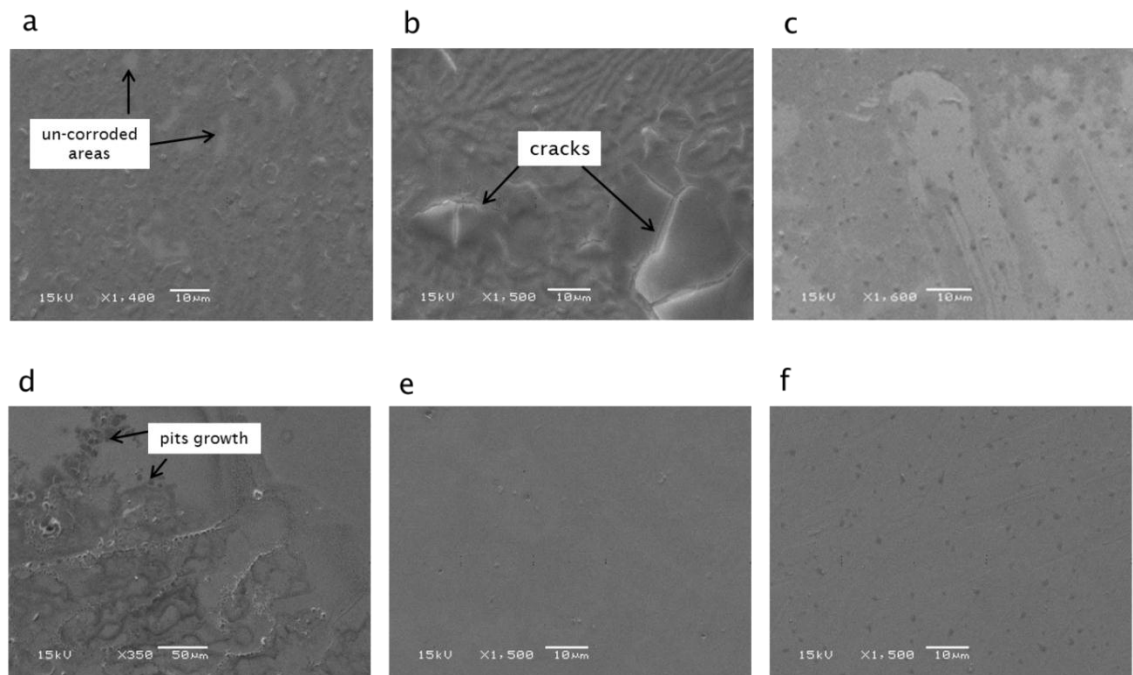


Figure 5.10: Scanning electron microscope (SEM) images of selected Al-Mg alloys after electrochemical screening (a) $\text{Al}_5\text{Mg}_{95}$ (b) $\text{Al}_{24}\text{Mg}_{76}$ (c) $\text{Al}_{32}\text{Mg}_{68}$ (d) $\text{Al}_{48}\text{Mg}_{52}$ (e) $\text{Al}_{52}\text{Mg}_{48}$ (f) $\text{Al}_{77}\text{Mg}_{23}$. The substrate is gold.

The elemental compositions (i.e. Al, Mg) after the electrochemical screening was analysed by the energy dispersive X-ray microscopy (EDX). The notion of this analysis is to find out the scale of the corrosion damage taken place after corrosion testing. The results are presented in **Table 5.1**.

The EDX analysis after exposure of the $\text{Al}_5\text{Mg}_{95}$ alloy displays a different chemical composition i.e. $\text{Al}_{14}\text{Mg}_{86}$. The Mg content decreases significantly; indicating an aggressive corrosion takes place. This can be seen at **Figure 5.10a**, where only few white areas were left not corroded.

The $\text{Al}_{24}\text{Mg}_{76}$ alloy exhibits a lower difference in the chemical composition compared to the $\text{Al}_5\text{Mg}_{95}$ alloy. The surface morphology of the $\text{Al}_{24}\text{Mg}_{76}$ alloy (**Figure 5.10b**) appears less coarse although it contains apparent cracks. According to the X-ray diffraction results the $\text{Al}_{24}\text{Mg}_{76}$ alloy contains γ $\text{Al}_{12}\text{Mg}_{17}$ (= β phase) and the Al solid solution in Mg (= α phase). Therefore the cracks

more likely result from the preferential attack on α phase which acts as an anode, while the β phase acts as the cathode. This conforms to the high anodic polarisation demonstrated by the $\text{Al}_{24}\text{Mg}_{76}$ alloy potentiodynamic curve shown in **Figure 5.9c**.

The $\text{Al}_{32}\text{Mg}_{68}$ alloy displays higher Mg concentration after electrochemical screening (i.e. $\text{Al}_{24}\text{Mg}_{76}$). This indicates the predominance of γ $\text{Al}_{12}\text{Mg}_{17}$ phase which enhances corrosion resistance. The $\text{Al}_{32}\text{Mg}_{68}$ alloy shows the lowest anodic polarisation and highest positive corrosion potential (E_{corr}) as shown in (**Figure 5.9d**). Moreover the best corrosion resistances have been obtained at the compositions (about 35 %_{at.} Al and 65 %_{at.} Mg) as shown in **Figure 5.6** and **Figure 5.7**. The optical appearance of the $\text{Al}_{32}\text{Mg}_{68}$ alloy presented in **Figure 5.10c** shows white and light grey colour. Besides small fragments or particles which are dispersed across the surface. There are no signs of cracks or any defects. The X-ray diffraction results shown in **Figure 5.1** reveal the $\text{Al}_{32}\text{Mg}_{68}$ alloy contains only β phase (γ ($\text{Al}_{12}\text{Mg}_{17}$)). Similar results were observed by Hajjari et al. [143]. Also at equilibrium the β phase is expected to form at the composition of 40 %_{at.} Al [104]. The β phase here acts as corrosion barrier and forms a protective layer which prevents corrosion to take place. Consequently the Mg concentration of the exposed $\text{Al}_{32}\text{Mg}_{68}$ alloy appears higher the as-deposited alloy. The white layer shown in **Figure 5.10c** confirms that the β phase acts here as a corrosion barrier because it diffuses evenly and dominates in the alloy structure (**Figure 5.1**). Also the $\text{Al}_{32}\text{Mg}_{68}$ alloy (**Figure 5.9d**) shows very positive (noble) corrosion potential compared to the $\text{Al}_{12}\text{Mg}_{88}$ containing the α phase (**Figure 5.9b**). Further insight about the role of β phase can be found elsewhere [6, 122, 124, 199].

The $\text{Al}_{48}\text{Mg}_{52}$ alloy shows very similar concentration although the $\text{Al}_{48}\text{Mg}_{52}$ alloy suffers from severe pitting corrosion as shown in **Figure 5.10d**. The pitting corrosion may result due to the existence of a nano-phase of β obtained at 34 %_{at.} Al (**Figure 5.1**), although the X-ray diffraction results show no such evidence and only amorphous structure over the compositions of 40 to 60 %_{at.} Al as displayed by the $\text{Al}_{40}\text{Mg}_{60}$ alloy (**Figure 5.1**). If the nano-particles of the β phase exist, they would induce corrosion pit initiation. This is a negative consequence of the β phase on the corrosion resistance when it is present in small centred fractions. However, there is no clear evidence to support this

conclusion apart from the pitting corrosion displayed by the $\text{Al}_{48}\text{Mg}_{52}$ alloy and shown in **Figure 5.9f**.

The $\text{Al}_{52}\text{Mg}_{48}$ alloy shows similar consequence to the one observed at $\text{Al}_{32}\text{Mg}_{68}$ alloy where Mg content increases after corrosion test. Also this alloy shows no defects and the surface remains intact as presented in **Figure 5.10e**. This associates with the good corrosion resistance exhibited by the $\text{Al}_{52}\text{Mg}_{48}$ alloy (**Figure 5.7**). Also the potentiodynamic curve of the $\text{Al}_{52}\text{Mg}_{48}$ alloy displays passive behaviour over a wide potential range as shown in **Figure 5.9g**.

The $\text{Al}_{77}\text{Mg}_{23}$ alloy exhibits similar chemical composition. There are, however, black spots on the SEM image of the $\text{Al}_{77}\text{Mg}_{23}$ alloy as presented in **Figure 5.10f**; which may be a result of pitting corrosion.

Table 5.1: The EDX analysis before and after the electrochemical screening of the Al-Mg alloys deposited on gold substrate.

Alloy composition in (% _{at.}) before	Alloy composition in (% _{at.}) after the electrochemical screening
$\text{Al}_5\text{Mg}_{95}$	$\text{Al}_{14}\text{Mg}_{86}$
$\text{Al}_{24}\text{Mg}_{76}$	$\text{Al}_{19}\text{Mg}_{81}$
$\text{Al}_{32}\text{Mg}_{68}$	$\text{Al}_{24}\text{Mg}_{76}$
$\text{Al}_{48}\text{Mg}_{52}$	$\text{Al}_{47}\text{Mg}_{53}$
$\text{Al}_{52}\text{Mg}_{48}$	$\text{Al}_{43}\text{Mg}_{57}$
$\text{Al}_{77}\text{Mg}_{23}$	$\text{Al}_{74}\text{Mg}_{26}$

The Tafel constant (B) in (Equation 5-1) usually were assumed to be 26 mV for the Al-Mg system [120]. However, this constant can be experimentally obtained by plotting the log corrosion resistances (R_p) obtained by LPR versus the log corrosion currents (i_{corr}) extrapolated from Tafel plot as described in (Equation 5-2). Consequently a linear relationship should result between the corrosion resistances and corrosion current densities with a slope of -1 and an intercept of log B.

$$\log R_p = \log B - \log i_{corr} \quad \text{Equation 5-2}$$

Figure 5.11 shows data for different Al-Mg alloy compositions on a single array: The slope of the line obtained by linear regression is -1.04 and $B = 26$ mV. Therefore this confirms that 26 mV is appropriate to be used as Tafel constant (B) for Al-Mg system. Moreover this provides an assessment of the validity of the corrosion resistances obtained by LPR method.

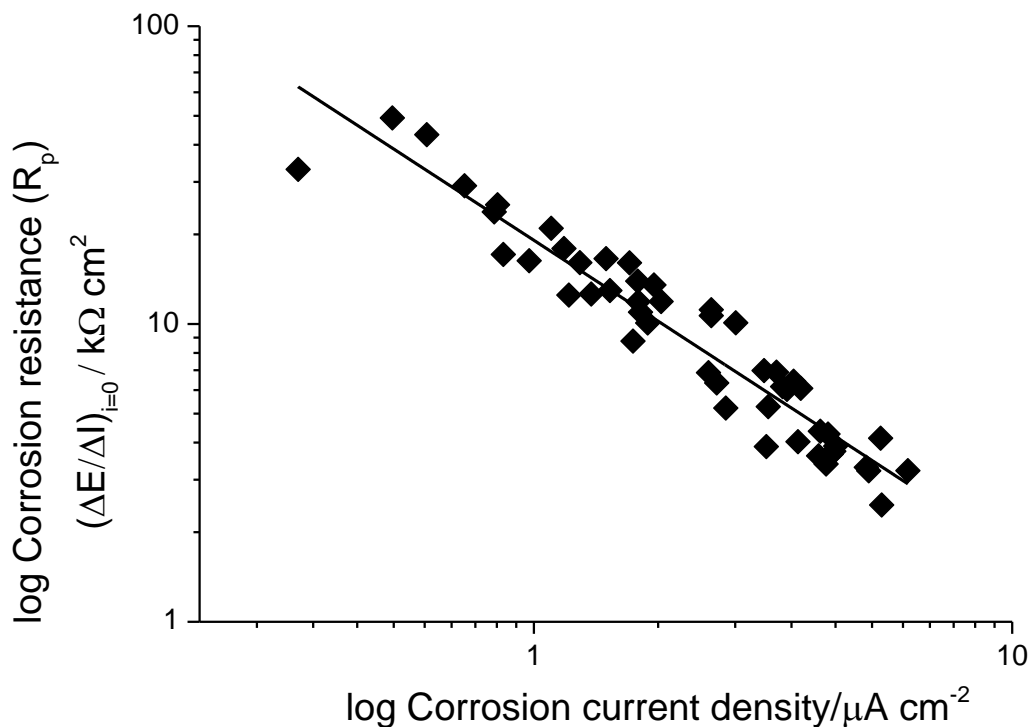


Figure 5.11: A plot of $\log R_p$ vs. $\log (i_{corr})$ for a series of Al-Mg alloys: The slope and B derived from (Equation 5-2) are -1.04 and 26 mV respectively. The electrolyte is sodium chloride [0.005 M] at 293 K.

5.4 Conclusion

Binary Al-Mg alloys have been obtained over the composition range of (5-80 %_{at.} Al, 10-95 %_{at.} Mg). The X-ray diffraction results reveal three phases namely the two extreme solid solutions and the β phase (i.e. γ Al₁₂Mg₁₇). The compositions between 2-12 %_{at.} Al comprise only Al solid solution in Mg. The mixture of β phase and Al solid solution in Mg extends from 12 to 25 %_{at.} Al. The β phase has been isolated in the compositions 27-35 %_{at.} Al. The compositions from 40-70 %_{at.} Al contained only the amorphous phase. The solid solution of Mg in Al extends beyond equilibrium limits and forms from ≥ 75 %at Al or $25 \leq$ %_{at.} Mg. In contrast to equilibrium the Al₂Mg₃ expected at ~ 39 %_{at.} Al has not been observed.

The corrosion resistance increased from 30 to 50 %_{at.} Al. The best corrosion resistance was obtained at ~ 35 %_{at.} Al. Moreover the more positive corrosion potential (E_{corr}) has been obtained at the same percentage viz. 35 %_{at.} Al. There is an apparent correlation between the β phase existence and changes observed in the corrosion resistance and corrosion potential. The alloys which comprised only β phase show the best corrosion resistance; however, the alloys containing a mixture of β phase and Al solid solution in Mg demonstrates low corrosion resistance. Also evidence of cracks has been observed in the alloys containing a mixture of β phase and Al solid solution in Mg.

The SEM images after the electrochemical studies reveal that the Al₃₂Mg₆₈ alloy shows no defects, where a white layer covers the alloy surface. Also the Al₅₂Mg₄₈ alloy displays no sign of corrosion products and shows an intact surface. Aggressive uniform corrosion was observed in the Al₅Mg₉₅ alloy, whereas only pitting corrosion was noticed on the Al₄₈Mg₅₂ alloys. This largely agrees with the EDX analysis after corrosion testing. The highest magnesium concentration was exhibited by the Al₃₂Mg₆₈ and Al₅₂Mg₄₈ alloys; which show intact surfaces. The Al₅Mg₉₅ displays the lower magnesium concentration after corrosion test; which complies with the SEM image showing aggressive uniform corrosion.

6. Ternary Al-Mg-Zr Alloys

6.1 Introduction

The Al-Mg-Zr alloys have not been widely studied. However, the Al and Mg which are the main constituents of these alloys are widely investigated. Magnesium has several distinctive characteristics such as abundant, high strength/ weight ratio, good machinability, thermal conductivity, and mechanical properties[106]; however, it has low corrosion resistance limiting its application. On the other hand aluminium has good corrosion resistance. Therefore it has been suggested to improve Mg corrosion resistance but Al-Mg alloys suffer from intergranular corrosion (IGC) and intergranular stress corrosion cracking (IGSCC) when exposed to heat treatments even at low temperature, which is usually referred to as sensitization[15]. Zirconium is often used as a grain refiner by adding small amount (i.e. 0.1 up to 2 %_{wt.}) to Mg alloys[148] to improve corrosion resistance[149, 150] by stabilising the Mg matrix. Adding Zr to Al decreases the corrosion rate significantly in [1M] HCl solution[153]. There are, however, few studies concerning the structure and corrosion resistance of the ternary Al-Mg-Zr alloys [151, 152].

Accordingly this chapter presents a comprehensive study of the microstructure and morphology of the ternary Al-Mg-Zr alloys at different compositions. The second part presents the corrosion resistances extracted from cyclic voltammograms data using the linear polarisation resistance (LPR) method and Tafel extrapolation technique. As a result the compositional dependence of corrosion resistance and potential is measured and correlated with the alloy structure and morphology.

Finally a general comparison between the annealed and as-deposited Al-Mg-Zr alloys is provided.

6.1.1 X-ray Diffraction of Al-Mg-Zr Alloys

Table 6.1 shows the summary of X-ray diffraction results of Al-Mg-Zr alloys. The alloys are classified based on the compositional range to eight zones. Five Al-Zr metastable phases are identified within these zones, i.e. (Al_3Zr , Al_2Zr , Al_3Zr_2 , Al_4Zr_5 , and Al_3Zr_5). Also at high Mg content (i.e. 30-35 %_{at.}) the solid solution of Zr in magnesium has been obtained.

As shown in **Table 6.1 (Zone A)** and **Figure 6.1** the rich aluminium ≥ 80 %_{at.} alloy (e.g. $\text{Al}_{80}\text{Mg}_1\text{Zr}_{19}$) exhibits five diffraction peaks. The peaks located at ca. $2\theta = 28^\circ$, 36.01° , and 40.36° are indexed to the hexagonal Al_2Zr with space group ($\text{P6}_3/\text{mmc}$) according to the PDF card[200]. Other peaks are found at ca. $2\theta = 37.32^\circ$ and 38.7° and are indexed to the tetragonal Al_3Zr corresponding to ($\text{I4}/\text{mmm}$) space group as in the PDF card[201]. According to the Zr-Al phase diagram, these two phases of Al_2Zr and Al_3Zr_2 exist in equilibrium at the composition range of 67 to 75 %_{at.} Al [160, 161]. This is in agreement with observations reported elsewhere [154], where Al_2Zr and Al_3Zr_2 have been identified in the arc-melted Al-Zr alloys which contain up to 24 %_{at.} Zr.

Zone B (Table 6.1) contains unknown phase. The obtained peaks are small and have not matched any PDF cards available from JCPDS.

Zone C (Table 6.1) displays two alloys. The $\text{Al}_{61}\text{Mg}_2\text{Zr}_{37}$ shows four Bragg peaks at ca. $2\theta = 36^\circ$, 36.7° , 37.85° , and 40.7° . These peaks are indexed to Al_2Zr and Al_3Zr_2 [200, 201], as indicated in **Figure 6.1**. The $\text{Al}_{61}\text{Mg}_{13}\text{Zr}_{26}$ shows three peaks: two peaks correspond to Al_2Zr and one peak corresponds to Al_3Zr_2 [202]. The alloy containing more Zr is dominated by Al_3Zr_2 . This is expected; according to the Zr-Al phase diagram[159], the Al_3Zr_2 intermetallic forms at Zr $\sim \geq 40$ %_{at.} Zr whereas Al_2Zr forms at 33 %_{at.} Zr. Also, the Al_2Zr transforms to Al_3Zr_2 according to thermodynamic reaction as $\text{L} + \text{Al}_2\text{Zr} \rightarrow \text{Al}_3\text{Zr}_2$ at 1590 °C, with compositions of 59, 66.7, and 60 %_{at.} Al respectively [162].

Zone D (Table 6.1) displays three Bragg peaks at ca. $2\theta = 35.7^\circ$, 38.2° , 40.1° . These peaks have not matched any PDF cards available from JCPDS or mentioned in literature.

Table 6.1: Summary of the x-ray diffraction results of Al-Mg-Zr alloys.

Zone	Compositional range in (% _{at.})	Example	Peak(s) position (2θ)/ degree	Identified phases(s)	Structure	Space group	References
A	Al ₇₉₋₈₅ Mg ₁₋₂ Zr ₁₅₋₂₀	Al ₈₀ Mg ₁ Zr ₁₉	28, 36.01, 40.36 37.32, 38.7	Al ₂ Zr Al ₃ Zr	Hexagonal Tetragonal	P6 ₃ /mmc I4/mmm	[200] [201],[160, 161]
B	Al ₆₅₋₈₅ Mg ₁₅₋₂₅ Zr ₅₋₁₅	Al ₈₀ Mg ₁₀ Zr ₁₀	38.12, 39.46, 40.1	unknown	unknown	unknown	
C	Al ₆₀₋₇₀ Mg ₁₋₃ Zr ₂₀₋₃₇	Al ₆₁ Mg ₂ Zr ₃₇ Al ₆₁ Mg ₁₃ Zr ₂₆	36, 40.7 36.7, 37.85 34, 36 37.45	Al ₂ Zr Al ₃ Zr ₂ Al ₂ Zr Al ₃ Zr ₂	Hexagonal Orthorhombic Hexagonal Orthorhombic	P6 ₃ /mmc Fdd2(43) P6 ₃ /mmc Fdd2(43)	[200, 201] [202] [200] [202]
D	Al ₅₅₋₆₀ Mg ₁₀₋₃₀ Zr ₁₀₋₃₀	Al ₅₅ Mg ₂₅ Zr ₂₀	35.7, 38.2, 40.1	unknown	unknown	unknown	
E	Al ₄₄₋₄₆ Mg ₁₆₋₁₈ Zr ₄₀₋₄₂	Al ₄₄ Mg ₁₆ Zr ₄₀	36,37.6	Al ₄ Zr ₅	Hexagonal	P6 ₃ /mcm	[203]
F	Al ₄₁₋₄₂ Mg ₂₁₋₂₃ Zr ₃₅₋₃₈	Al ₄₁ Mg ₂₁ Zr ₃₈	34, 35.15, 36.55, 40	Al ₃ Zr ₅	Tetragonal	I4/mcm	[204]
G	Al ₂₀₋₂₅ Mg ₃₀₋₃₅ Zr ₄₀₋₄₅	Al ₂₃ Mg ₃₂ Zr ₄₅	32.4, 34.5, and 36.55	Mg _{0.996} Zr _{0.004}	Hexagonal	P6 ₃ /mmc	[205],[151]
H	Al ₃₀₋₃₅ Mg ₁₀₋₁₅ Zr ₅₀₋₅₅	Al ₃₁ Mg ₁₅ Zr ₅₄	35.5 31.88, 34.88, 36.3 37.58	α-Zr (as-deposited) α-Zr (annealed) Al ₃ Zr ₅	Hexagonal Tetragonal	P6 ₃ /mmc I4/mcm	[206] [163]

Zone E (Table 6.1) e.g. $\text{Al}_{44}\text{Mg}_{16}\text{Zr}_{40}$ shows two Bragg peaks at ca. $2\theta = 36^\circ$ and 37.6° , which correspond to (211) and (112) for the hexagonal Al_4Zr_5 with the ($\text{P6}_3/\text{mcm}$) space group[203]. Also the diffraction pattern is presented in **Figure 6.1**. The Al_4Zr_5 phase has been identified at equilibrium for the Al-Zr alloys containing compositions of 42.7 and 49.1%_{at.} Al [207]. This compares to the $\text{Al}_{44}\text{Mg}_{16}\text{Zr}_{40}$ alloy, which contains a very similar composition of 44 %_{at.} Al.

Zone F (Table 6.1) displays four peaks at ca. $2\theta = 34^\circ$, 35.15° , 36.55° , and 40° . These peaks correspond to (321), (112), (420), (222) of the tetragonal Al_3Zr_5 [204]. Two examples i.e. $\text{Al}_{41}\text{Mg}_{21}\text{Zr}_{38}$ and $\text{Al}_{42}\text{Mg}_{23}\text{Zr}_{35}$ from this zone are presented in **Figure 6.1**. This phase has been identified and reported frequently at composition ~ 37 %_{at.} Al. There is, however, disagreement concerning the crystal structure type of the Al_3Zr_5 phase. This issue has been discussed in detail by Murray et al [160], with some researchers suggesting a hexagonal Mn_5Si_3 as a type of the structure. However, others have argued that the crystal structure of the Al_3Zr_5 is a tetragonal Si_3W_5 type, proving that contamination with interstitial impurities works as a stabiliser to the hexagonal Mn_5Si_3 type. A recent study revealed that the Al_3Zr_5 has a tetragonal structure at high temperature $> 800^\circ\text{C}$, while it has a hexagonal structure at low temperatures as metastable[166]. Schuster et al [166] confirm that the Al_3Zr_5 phase with a Mn_5Si_3 type structure is stable only in the low temperature phase.

Zone G (Table 6.1) contains rich magnesium content compared to Al (i.e. $\text{Al}_{23}\text{Mg}_{32}\text{Zr}_{45}$) and exhibits three diffraction peaks at ca. $2\theta = 32.4^\circ$, 34.5° , and 36.55° as presented in **Figure 6.1**. These peaks relate to Bragg diffractions of (100), (002), and (101) of the hexagonal $\text{Mg}_{0.996}\text{Zr}_{0.004}$ phase[205]. Zirconium solubility in Mg is limited to 1 %_{at.} Zr according to the Mg-Zr alloy phase diagram[104]. However, supersaturating of magnesium with zirconium has been achieved using a sputter deposition[151]. Also similar X-ray diffraction patterns have been observed for $\text{Al}_2\text{Mg}_{48}\text{Zr}_{50}$ alloy where two overlapped peaks can be seen at ca. $2\theta = 34.5^\circ$, 35.3° in addition to one at ca. $2\theta = 36.5^\circ$.

Zone H (Table 6.1) which contains rich Zr e.g. $\text{Al}_{31}\text{Mg}_{15}\text{Zr}_{54}$ alloy shows only one peak at ca. $2\theta = \sim 35.5^\circ$ (**Figure 6.1**). This relates to the situation of Al solid solution in zirconium, which itself relates to (110) of the solid solution of Al in the α -Zr according to the PDF card[206].

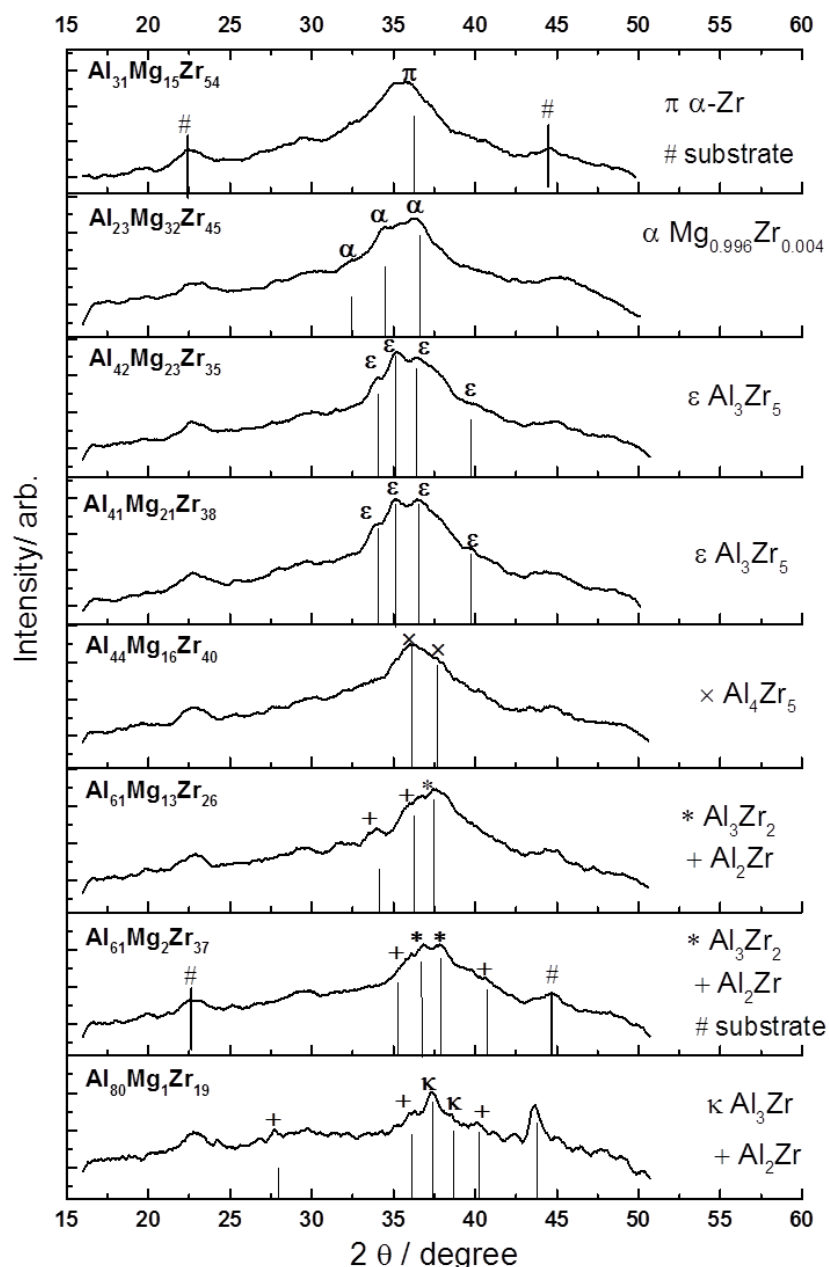


Figure 6.1: X-ray diffraction patterns of as-deposited Al-Mg-Zr alloys (#7541). Silicon nitride was used as the substrate. The detected phases are designated and included (at the right). Compositions, in atomic %, were determined by EDX.

However, the annealed alloy contains the Al_3Zr_5 besides the solid solution of Al in the α -Zr phase. Similar results have been observed at equilibrium where the Al_3Zr_5 and the solid solution of Al in the α -Zr phase were obtained at composition of 23.5 %_{at.} Al using the arc-melting method [163]. In contrast an

amorphous phase was obtained at a composition range of 15 to 40 %_{at.} Al for Al-Zr alloys manufactured by mechanical alloying[208]. Therefore, the existence of the Zr-Al intermetallic phase seems largely depend on the alloy preparation method, as clearly shown by Yoshioka et al.[154].

Figure 6.2 shows the X-ray diffractions of annealed Al-Mg-Zr alloys. These alloys were annealed immediately after deposition at 423 K for 30 minutes in a vacuum. In general, the annealed alloys show similar diffraction patterns to the as-deposited alloys. There are, however, some differences. For instance, the Al₂Zr phase observed at rich aluminium ≥ 60 %_{at.} Al as seen in **Figure 6.1** has disappeared after annealing. On the other hand, an additional peak associated with the (411) of the Al₃Zr₅ phase has been identified in the annealed Al₃₁Mg₁₅Zr₅₄, where only the α -Zr phase has been obtained in the as-deposited Al₃₁Mg₁₅Zr₅₄ alloy. Further analysis is presented in **Figure 6.3**.

Figure 6.3 shows a comparison between as-deposited and annealed Al-Mg-Zr alloys. The annealed alloys are at the left-hand side and the as-deposited ones are at the right. Although the annealed alloys' spectrum appears rather broad in shape, it shows more and sharper peaks. The as-deposited Al₄₄Mg₁₆Zr₄₀ (**Figure 6.3 E**) shows only one peak, which relates to (211) of the Al₄Zr₅ phase. However, after annealing more peaks relating to the same phase have surfaced (**Figure 6.3 A**).

The annealed and as-deposited Al₄₂Mg₂₃Zr₃₅ alloy (**Figure 6.3 B, F**) exhibit the same diffraction peaks, with only a little change in the (411) peak intensity.

Both the annealed and as-deposited Al₂₃Mg₃₂Zr₄₅ alloys (**Figure 6.3 C, G**) have only supersaturating zirconium solid in the magnesium phase, which has a hexagonal structure and (P6₃/mmc) as the space group. The (002) peak intensity has increased after annealing. It is well known that magnesium solubility in zirconium is limited[104] and the Al₂₃Mg₃₂Zr₄₅ alloy contains more Mg and Zr contents in comparison with Al. This explains why no Al-Zr phase appears.

The as-deposited Al₃₁Mg₁₅Zr₅₄ alloy exhibits only one Bragg peak associated with an α -Zr phase (**Figure 6.3 H**). However, two more peaks relating to the α -Zr phase are raised after annealing (**Figure 6.3 D**). An additional peak is located at ca. $2\theta = 37.5^\circ$ and corresponds to (411) of the tetragonal Al₃Zr₅. This is in

agreement with observations at equilibrium obtained by Kematick and Franzen[163].

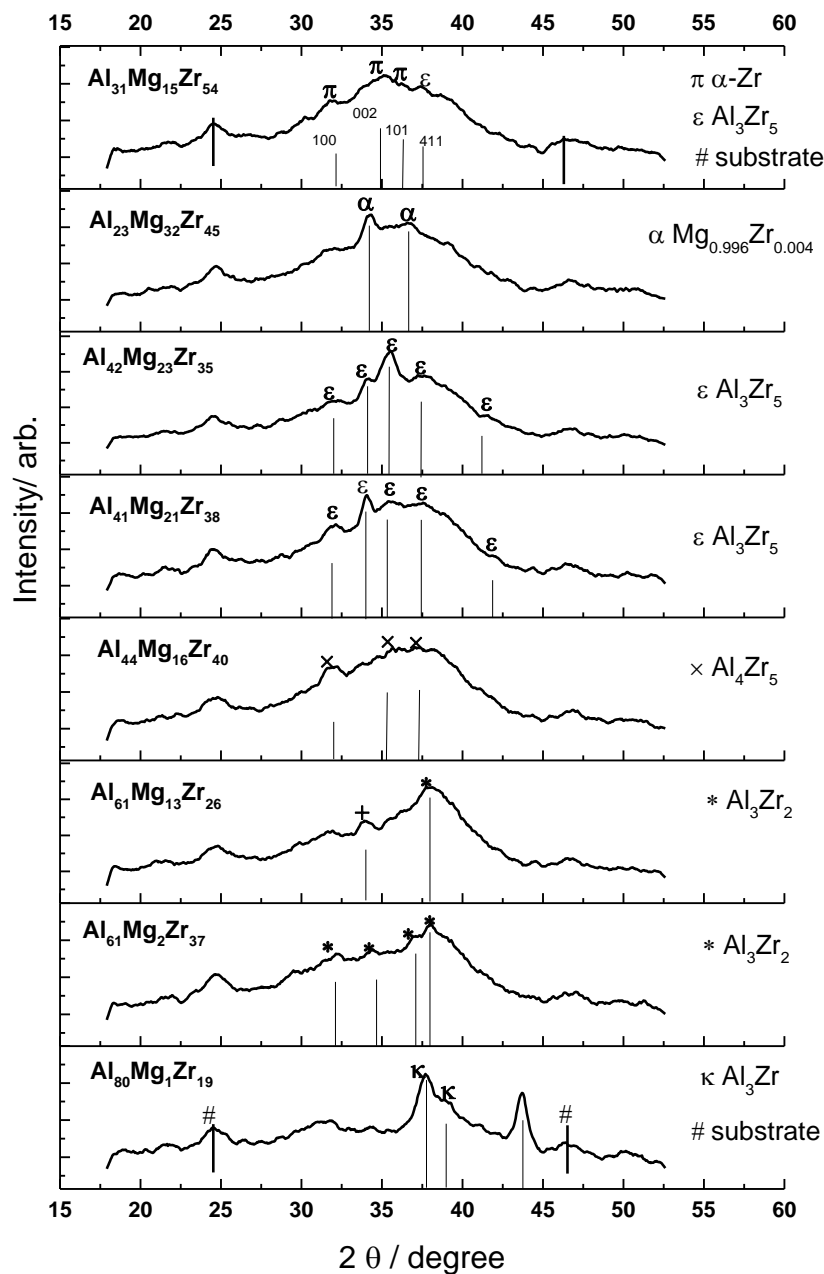


Figure 6.2: X-ray diffraction patterns of annealed Al-Mg-Zr alloys (#7544). Silicon nitride was used as the substrate. The detected phases are designated and included (at the right). Compositions, in atomic %, were determined by EDX. Array annealed at 423 K for 30 min.

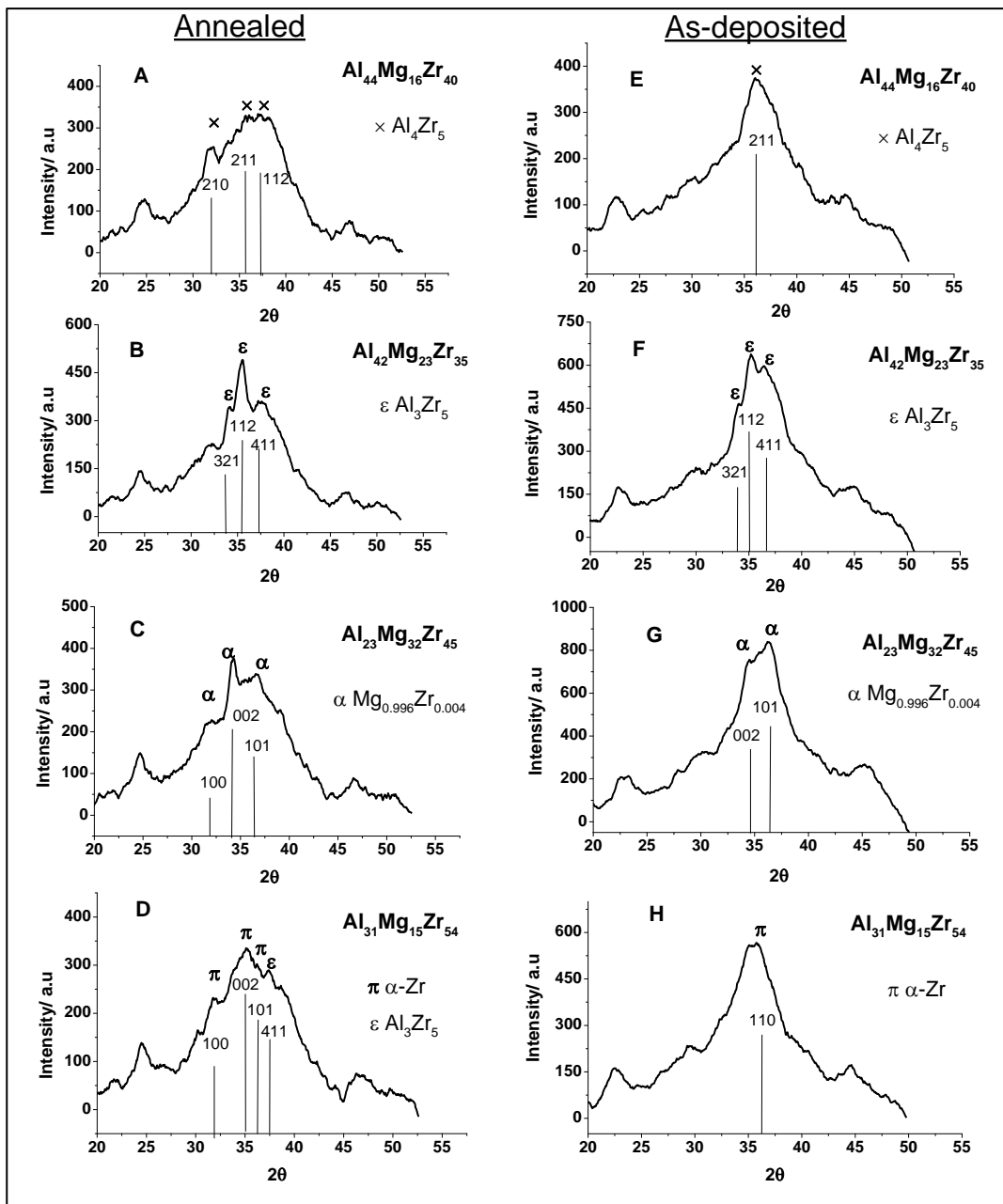


Figure 6.3: X-ray diffraction of selected Al-Mg-Zr alloys as-annealed (A, B, C, D) and as-deposited (E, F, G, H). Silicon nitride was used as the substrate. The annealed alloys were heated linearly at 423 K for 30 minutes in a vacuum.

All the x-ray diffraction results of ternary Al-Mg-Zr systems are summarised in **Figure 6.4**. Also the identified phase(s) at different composition range of the binary Al-Mg system are included in **Figure 6.4**. Note that colour is used just to differentiate between phases for better clarification. The ternary plot

(Figure 6.4) allows fast and simple correlation between alloy's structure and their corrosion resistance in the next section.

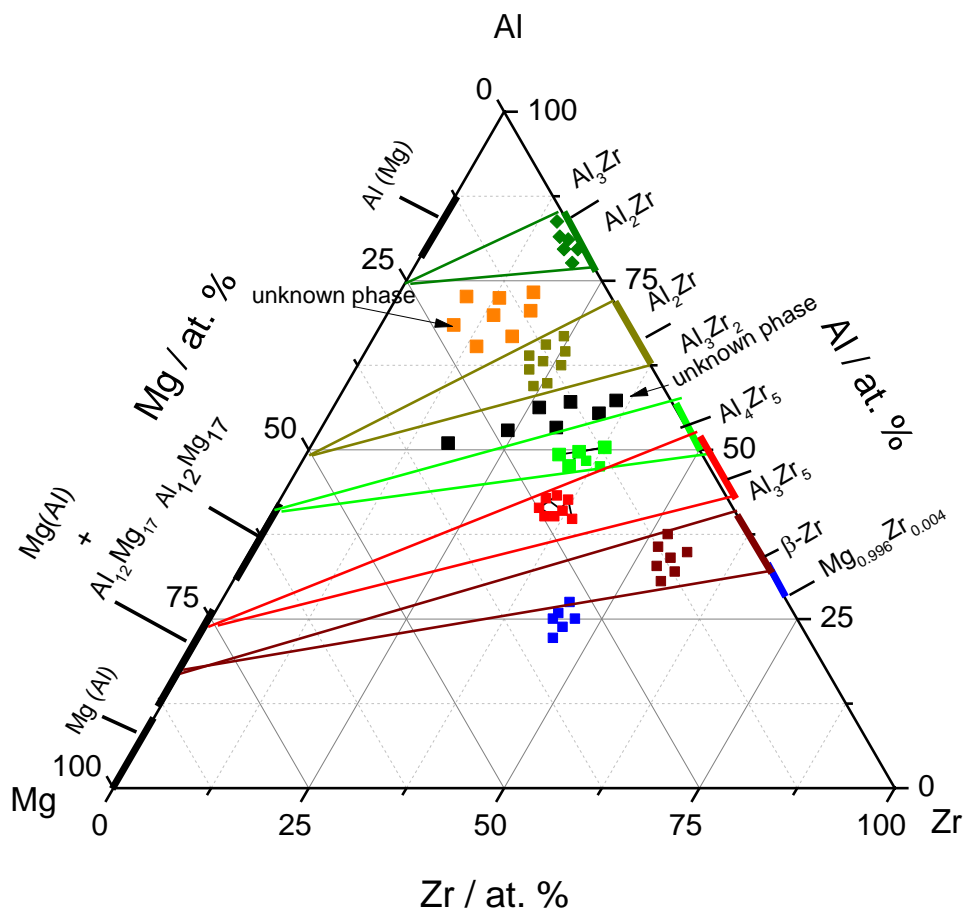


Figure 6.4: Summary of the phases identified in the binary Al-Mg and ternary Al-Mg-Zr systems.

6.2 Electrochemical Screening of Al-Mg-Zr Alloys

6.2.1 Electrochemical Screening of As-deposited Al-Mg-Zr Alloys

The electrochemical measurements were recorded at a 20 mV s^{-1} scan rate. The corrosion electrolyte was made of sodium chloride solution. Two concentrations were used: 0.1 and 0.02 M. The pH of the solutions was adjusted at 6.35. In addition, the solution was purged with N_2 gas for five minutes in order to dispel oxygen before performing the electrochemical screening. All measurements were obtained at 293 K.

6.2.1.1 The Corrosion Resistance (R_p) Screening of As-deposited Al-Mg-Zr Alloys

The corrosion resistance data are extracted from the cyclic voltammograms by the LPR and Tafel extrapolation methods. The data presented here are obtained from two 10×10 arrays on which the library of Al-Mg-Zr alloys were deposited and examined in sodium chloride solutions [0.1 and 0.02 M] at 293 K. The compositions were determined by electron energy dispersive spectroscopy (EDX), and an example using the first array is presented in **Figure 6.5**. It is worth noting that aluminium and magnesium compositions grow in opposite directions while zirconium grows from the right top corner. This effect has been observed in the corrosion resistance behaviour.

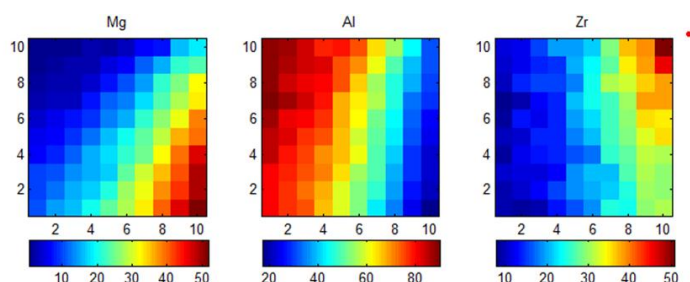


Figure 6.5: The composition maps of the components of Al-Mg-Zr alloys (#7537) across the 10×10 array. The compositions were determined by EDX. Gold pads on silicon/silicon nitride chip were used as the substrate. The film thicknesses are 100–150 nm.

Figure 6.6 shows the corrosion resistance values extracted by LPR methods as a function of the constituents of the ternary Al-Mg-Zr alloys. From a compositional point of view, the rich aluminium alloys $> 85\%_{\text{at}}$ display good corrosion resistance, as presented in **Figure 6.6(A, C)**. However, the corrosion resistance declines with the introduction of a low amount of Mg, as seen in the blue colour in **Figure 6.6(A)**, with a sharp decrease shown in **Figure 6.6(B)**. Another increase of the corrosion resistance appears at the compositions ca. (10-30 $\%_{\text{at}}$ Mg, 40-70 $\%_{\text{at}}$ Al), appearing as a wide peak as shown in **Figure 6.6(B, C)** and in **Figure 6.6(A)** as green colour at compositions of 15-30 $\%_{\text{at}}$ Zr. Besides the corrosion resistance displayed by rich Al alloys, the alloys containing (10-30 $\%_{\text{at}}$ Mg, 40-70 $\%_{\text{at}}$ Al, and 15-30 $\%_{\text{at}}$ Zr) shows the next best corrosion resistance as labelled in green colour (**Figure 6.6A**). The corrosion resistance (R_p) as a function of the Al and Mg compositions demonstrates the same trend but in the opposite direction, as shown in **Figure 6.6(B, C)**. This can be attributed to the way that magnesium and aluminium ingredients grow across the 10x10 array as presented in **Figure 6.5**.

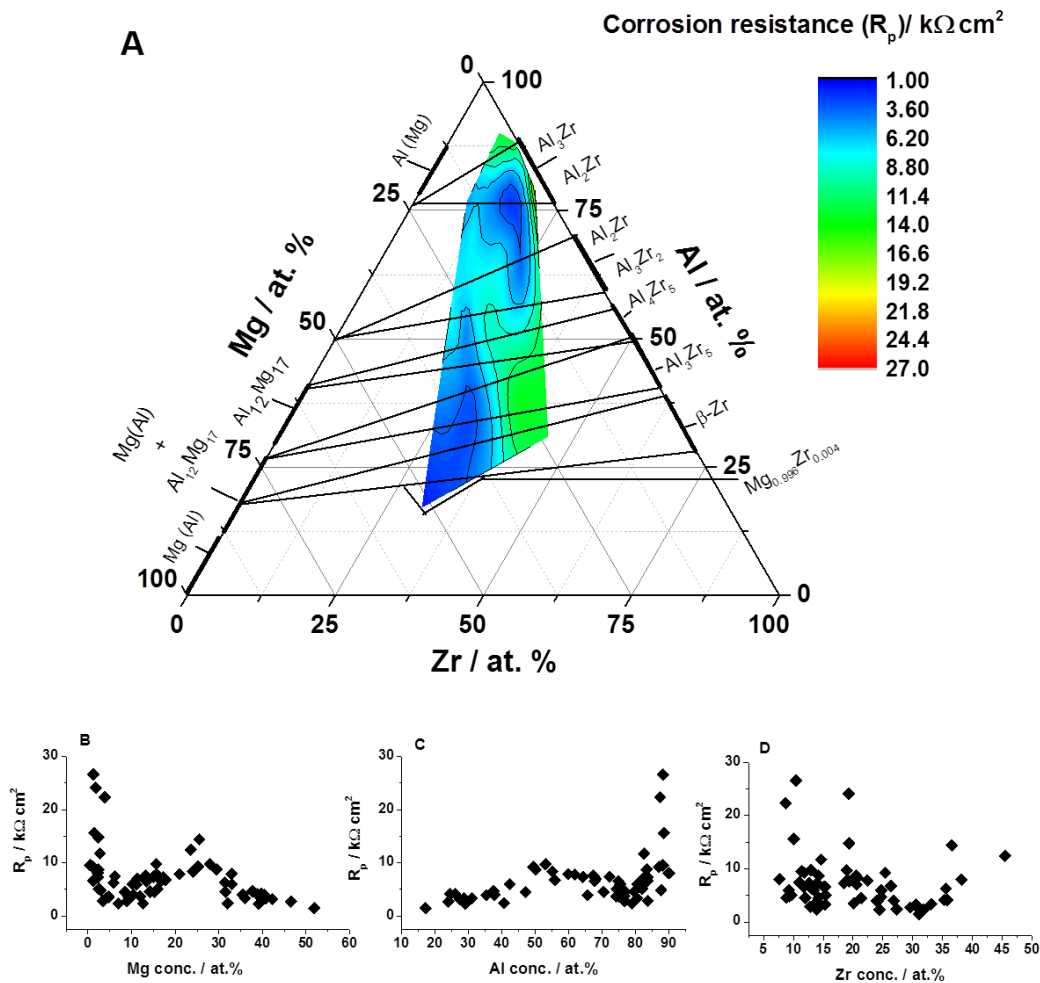


Figure 6.6: The corrosion resistance values as a function of the constituents of Al-Mg-Zr alloys (#7537). The data were determined using the LPR method. De-aerated sodium chloride [0.1 M] was used as the corrosion electrolyte. Measurements were obtained at 293 K. The XRD results are included.

The corrosion resistance values have also been obtained using Tafel extrapolation ($B = 24\text{ mV}$), and are presented in **Figure 6.7**. Tafel constant (B) is experimentally calculated as shown in **Figure 6.17**.

The corrosion resistance results are very similar to the ones obtained by LPR presented in **Figure 6.6**. The best performance of the corrosion resistance appears at high Al content $> 85\%_{\text{at}}$ and at the compositions of (10-30 $\%_{\text{at}}$ Mg, 40-70 $\%_{\text{at}}$ Al, and 15-30 $\%_{\text{at}}$ Zr). The latter appears in the middle as the green colour in **Figure 6.7(A)**. There is, however, a systematic difference in the absolute values of the corrosion resistances extracted by the two methods,

wherein the ones obtained by LPR appear higher than the ones determined using the Tafel extrapolation. There are two reasons for this discrepancy. The first reason is the irreversible changes (e.g. corrosion film) that take place during the wide potential scans, which increase the corrosion resistance values obtained by the LPR. Secondly is the possibility of intervene small current densities such as background and double layer charging current into the corrosion resistance values obtained by LPR, which depends on small current densities measurements near the zero current potential. Further insights regarding this issue can be found elsewhere [28, 209].

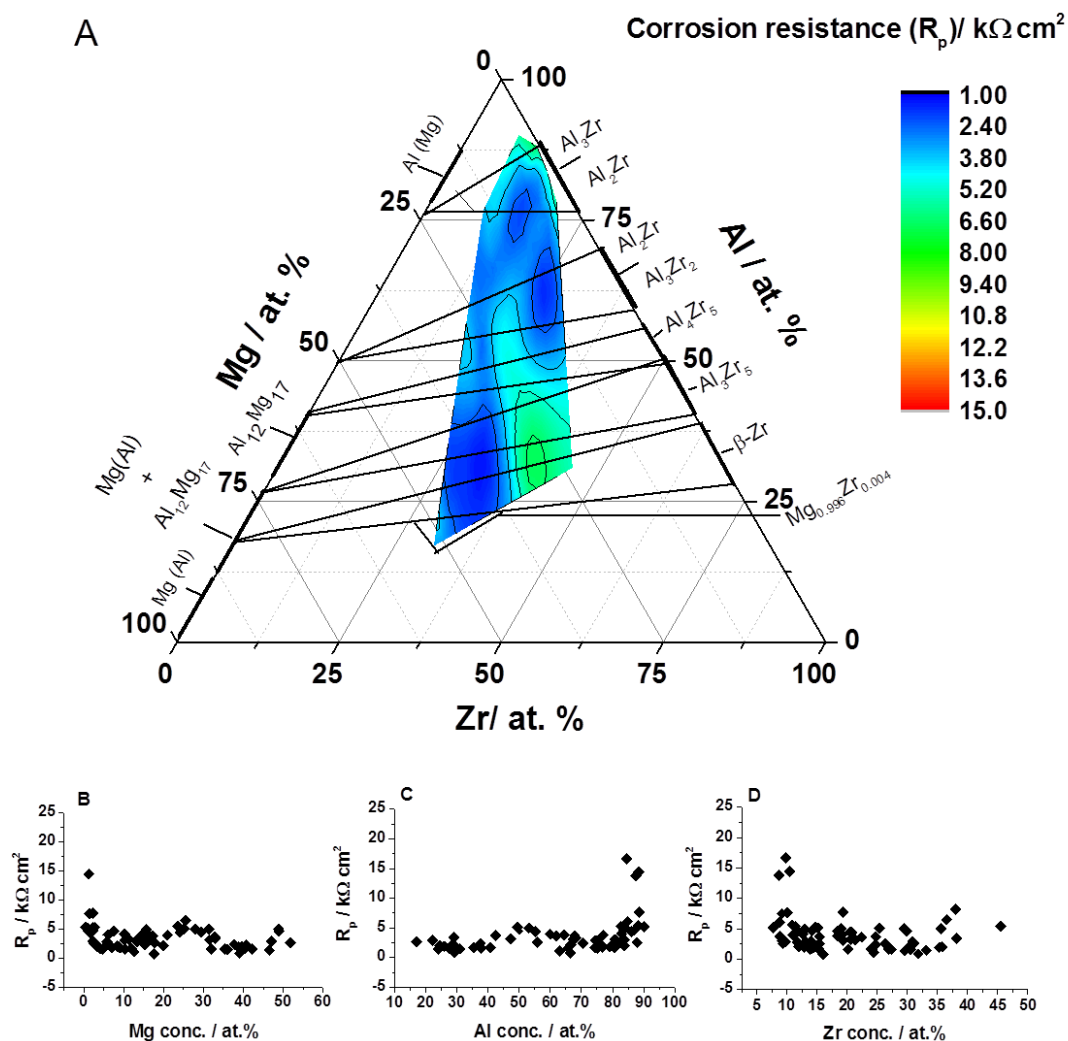


Figure 6.7: The corrosion resistance values as a function of the constituents of Al-Mg-Zr alloys (#7537). The data were determined using the Tafel extrapolation method assuming $B = 24$ mV. De-aerated sodium chloride [0.1 M] was used as the corrosion electrolyte. Measurements were obtained at 293 K.

The corrosion resistance dependence as a function of Al, Mg can clearly be observed from **Figure 6.6** and **Figure 6.7** (B, C) but the corrosion resistances versus Zr compositions as in **Figure 6.6** and **Figure 6.7**(D) show no clear behaviour, apart from the vertical change. Although as in the **Figure 6.6** and **Figure 6.7** (A) alloys contain low Zr and 15-45 %_{at.} Zr show high corrosion resistance (as the green colouring shows).

The changes in the corrosion resistance (R_p) performance as a function of Al, Mg, Zr compositions observed in **Figure 6.6** and **Figure 6.7** result from either a change in the alloy structure (e.g. form new phases) or as result of morphological changes that take place on the alloys' surfaces. The latter effect is more likely to exist at low and high zirconium contents. This associates with the lowest roughness factor, which is equal to ca. = 3.45 nm, and shown by $Al_{80}Mg_1Zr_{19}$ and $Al_{31}Mg_{15}Zr_{54}$ alloys as clearly seen in **Figure 6.8**. This effect is usually called grain refining, which is believed to improve the corrosion resistance as reported by Song et al[150]. Similarly, other studies have revealed that the addition of Zr with less than 10%_{at} increases corrosion resistance [151, 152].

Moreover, the existence of new phases (i.e. Al_3Zr_5 and Al_2Zr_3) has led to improvement in the corrosion resistance performance. The onset of those phases existed at the compositions of (10-30 %_{at.} Mg, 38-70 %_{at.} Al, and 15-30 %_{at.} Zr) corresponds to the increase in the corrosion resistance as shown in **Figure 6.6** and **Figure 6.7**. The Al_2Zr_3 and Al_3Zr_5 phases use as reversible hydrogen getter [166]. Moreover, the Al_3Zr_5 phase stabilises through the presence of even a low amount of oxygen, as Mn_5Si_3 structure type[167]. This probably explains the high corrosion resistance exhibited by those composition ranges. There are no studies specifically investigating the effect of the Al_3Zr_5 and Al_2Zr_3 phases on corrosion resistance. The anodic polarisation behaviour of sputtered and arc-melted Al-Zr alloys have been explored at neutral chloride solution [154]. The XRD results revealed that the sputtered alloys only contain an amorphous phase whereas numbers of intermetallic phases have been identified in the ark-melted alloys. Also, the electrochemical results revealed that sputtered alloys demonstrate more passivation and pitting resistance performance than the ark-melted alloys. However, it is worth mentioning that the Al_3Zr_5 and Al_2Zr_3 phases are not among those phases which

have been identified at the ark-melted alloys. Another study revealed that the addition of Zr with low Zr viz. 2, 5 %_{at.} reduces to a remarkable degree the anodic polarisation, while adding high Zr content (i.e. 12 and 25 %_{at.}) increases anodic activity. The latter is believed to be accelerated by the nanostructured Zr phase, which acts as a cathode in relation to the Mg-Al-Zr alloy containing 25 %_{at.} Zr[152]. Therefore, the corrosion resistance is susceptible to the morphological and structural changes.

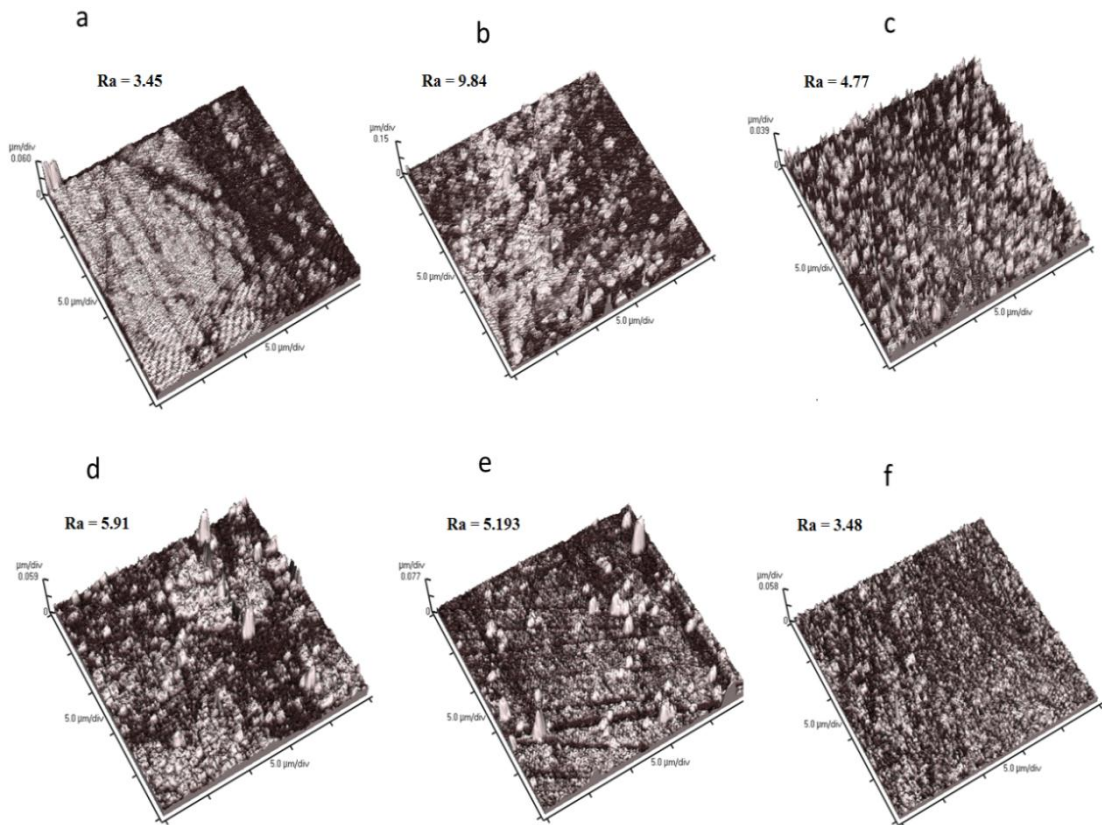


Figure 6.8: Topography of as-deposited Al-Mg-Zr alloys obtained by AFM where (a) $Al_{80}Mg_1Zr_{19}$ (b) $Al_{65}Mg_9Zr_{26}$ (c) $Al_{44}Mg_{16}Zr_{40}$ (d) $Al_{42}Mg_{23}Zr_{35}$ (e) $Al_{23}Mg_{32}Zr_{45}$ and (f) $Al_{31}Mg_{15}Zr_{54}$. Silicon nitride was used as the substrate. The roughness factor unit is nm.

The previous corrosion resistance behaviour has been reproduced in another Al-Mg-Zr array as shown in **Figure 6.9**. This array is examined in much milder corrosion solution, which is [0.02 M] of sodium chloride. The corrosion resistance performance is comparable to the ones seen in the previous array as presented in **Figure 6.6** and **Figure 6.7** (B, C, D). As one would expect, the

corrosion resistance values obtained in the milder condition appear to be higher. The rich aluminium alloys at $> 90 \text{ \%}_{\text{at.}}$ Al display high corrosion resistance, at $\sim 80 \text{ k}\Omega \text{ cm}^2$ on average. Therefore, those values have been excluded from **Figure 6.9** in order to get the best comparison. The alloys containing compositions of (10-30 $\text{\%}_{\text{at.}}$ Mg, 40-70 $\text{\%}_{\text{at.}}$ Al) show the second best corrosion resistance (**Figure 6.9**). This compares to what has been observed in **Figure 6.6** and **Figure 6.7** (B, C, D) at equivalent compositions.

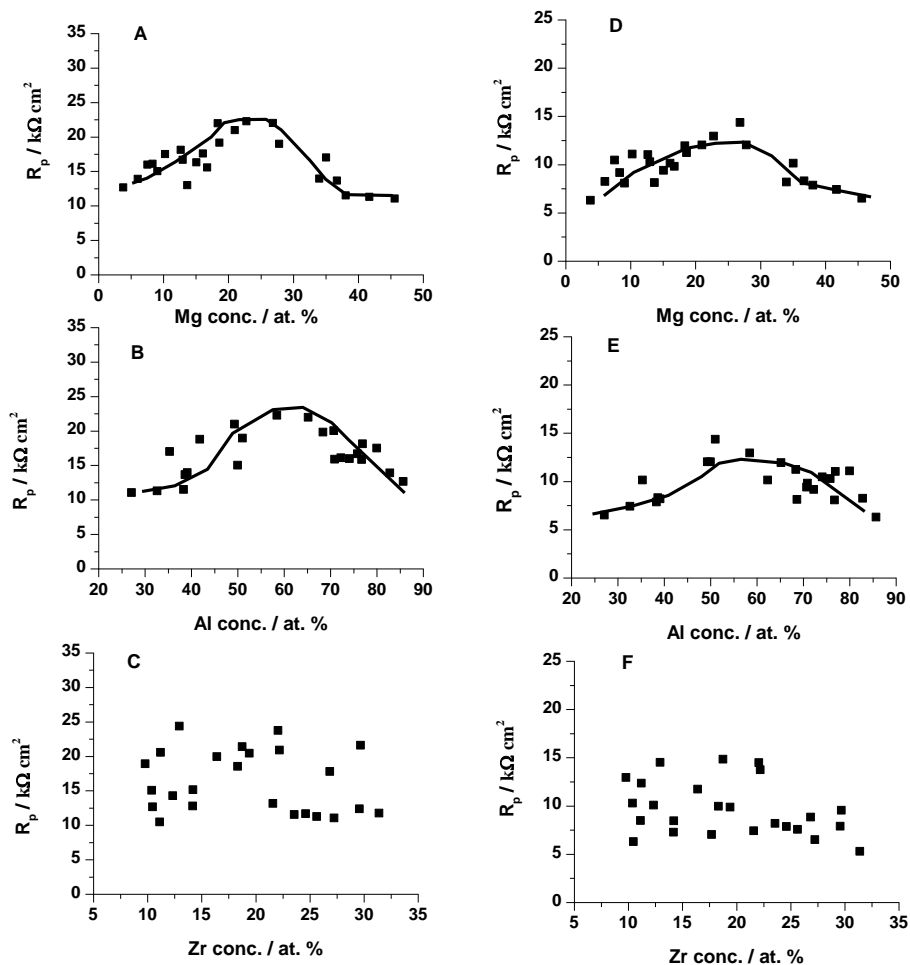


Figure 6.9: The corrosion resistance values as a function of the constituents of Al-Mg-Zr alloys (#7534) where (A, B, C) are determined using the LPR method and (D, E, F) are determined using the Tafel method assuming $B = 24 \text{ mV}$. The corrosion electrolyte solution was de-aerated sodium chloride [0.02 M].

Measurements were obtained at 293K.

The corrosion resistance behaviour as a function of Zr compositions can be estimated if a single compositional line over the Mg and Al growth is chosen,

as displayed in **Figure 6.10**. This gives a continuous constant ratio of Al/Mg over a wide compositional range.

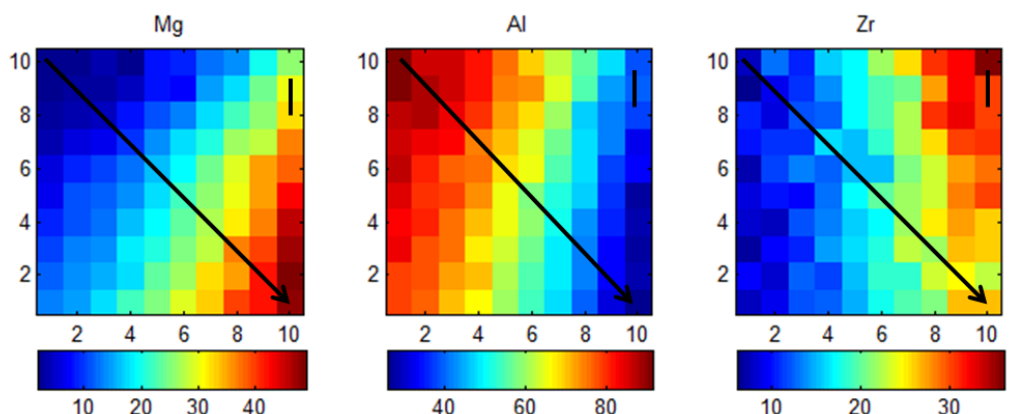


Figure 6.10: The composition maps of the components of Al-Mg-Zr alloys (#7534) across the 10x10 array. The compositions were determined by EDX and silicon nitride was used as the substrate. Black arrows show the selected compositions.

The corrosion resistance values of the selected alloys from **Figure 6.10** are presented in **Figure 6.11**. The results disclose that at rich Al and Zr compositions corrosion resistance shows an obvious increase. Another increase in the corrosion resistance appears at the compositions of (10-30 %_{at.} Mg, 38-70 %_{at.} Al, and 10-25 %_{at.} Zr). This generally agrees with what has been seen before. This consistency of the corrosion resistance results extracted from two separate arrays as presented in **Figure 6.6** and **Figure 6.7** (B, C, D) and **Figure 6.9** demonstrate clearly the good reproducibility of the method used.

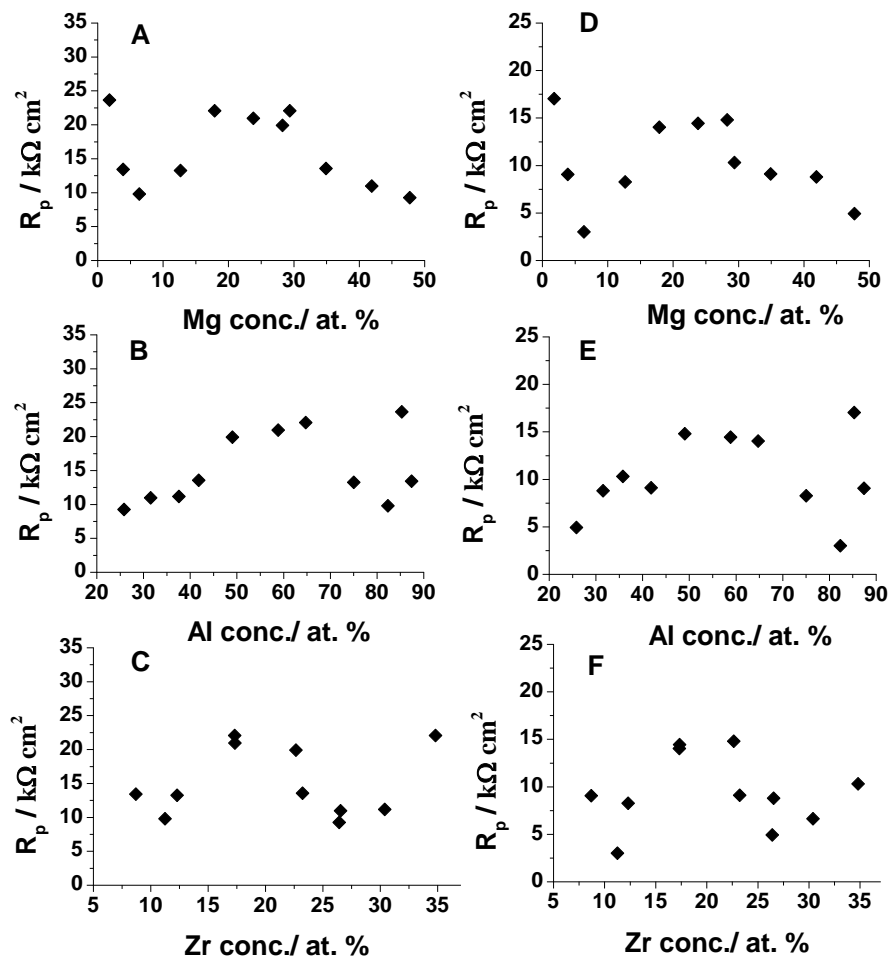


Figure 6.11: The selected corrosion resistances as a function of the components of Al-Mg-Zr alloys (#7534) where (A, B, C) are determined using the LPR method and (D, E, F) are determined using the Tafel method. The corrosion electrolyte solution was de-aerated sodium chloride [0.02 M]. Measurements were obtained at 293 K.

For further investigation, the potentiodynamic curves of selected Al-Mg-Zr alloys across a wide compositional range (17-89 %_{at.} Al, 1-52 %_{at.} Mg, 10-46 %_{at.} Zr) are presented in **Figure 6.12**. The $\text{Al}_{89}\text{Mg}_1\text{Zr}_{10}$ (labelled with black colour) demonstrates the lowest anodic activity. Besides it shows large passive region. This indicates the high corrosion resistance observed in rich Al alloys as shown in **Figure 6.6** and **Figure 6.7** (A, C). The addition of more Mg, as displayed by the $\text{Al}_{77}\text{Mg}_9\text{Zr}_{14}$ (red line), results in high anodic and cathodic polarisations, although its corrosion potential has slightly shifted toward positive potential in

comparison to the $\text{Al}_{89}\text{Mg}_1\text{Zr}_{10}$ (black line) as shown in **Figure 6.13**. This mimics the sharp reduction of the corrosion resistance noted after adding more Mg as seen in **Figure 6.6** and **Figure 6.7(A, B)**.

The highest cathodic polarisation current densities (associated with a hydrogen evolution reaction (HER)) are exhibited by the $\text{Al}_{64}\text{Mg}_{17}\text{Zr}_{19}$, $\text{Al}_{55}\text{Mg}_{24}\text{Zr}_{21}$, $\text{Al}_{38}\text{Mg}_{26}\text{Zr}_{36}$, and $\text{Al}_{31}\text{Mg}_{24}\text{Zr}_{46}$ alloys, which are labelled in green, blue, cyan, and brown colours respectively. Moreover, these alloys show low anodic activity and very positive corrosion potentials, as presented in **Figure 6.12** and **Figure 6.13**. This indicates the good performance of the corrosion resistance observed at the composition of (10-30 %_{at.} Mg, 38-70 %_{at.} Al, and 15-30 %_{at.} Zr) as shown in the corrosion resistance results as a function of the Al, Mg, Zr compositions (i.e. **Figure 6.6**, **Figure 6.7** and **Figure 6.9**). The $\text{Al}_{17}\text{Mg}_{52}\text{Zr}_{31}$ alloy (pink line) shows the highest anodic current densities. This alloy contains 52 %_{at.} Mg content at which an apparent decrease of corrosion resistance clearly appears in **Figure 6.6**, **Figure 6.7 (B)**, and **Figure 6.9**.

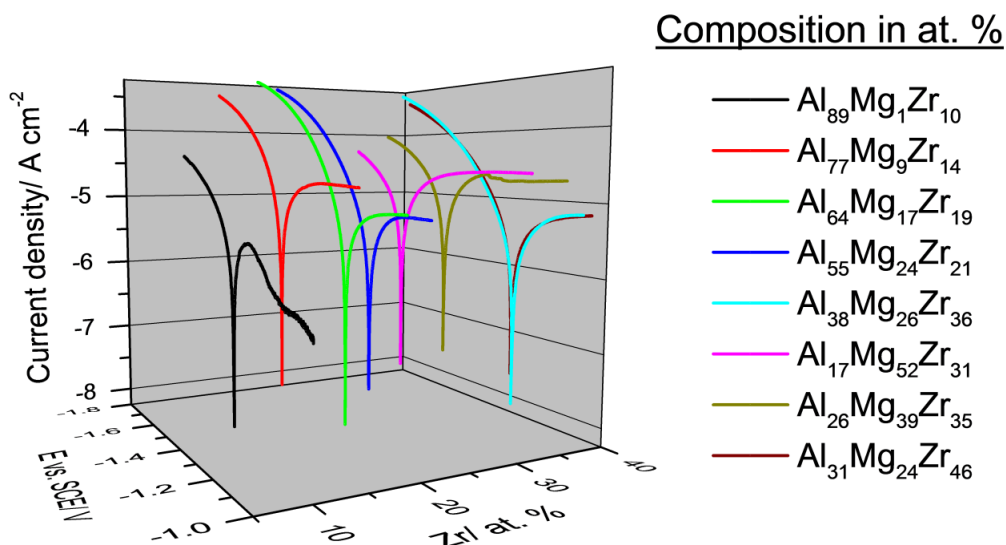


Figure 6.12: Potentiodynamic curves of as-deposited Al-Mg-Zr alloys (#7537) studied in sodium chloride solution [0.1 M]. The scan rate was 20 mVs⁻¹. The solution was purged with N₂ for five minutes. The pH and temperature were adjusted at 6.35 and 293 K. Alloys composition was determined by EDX.

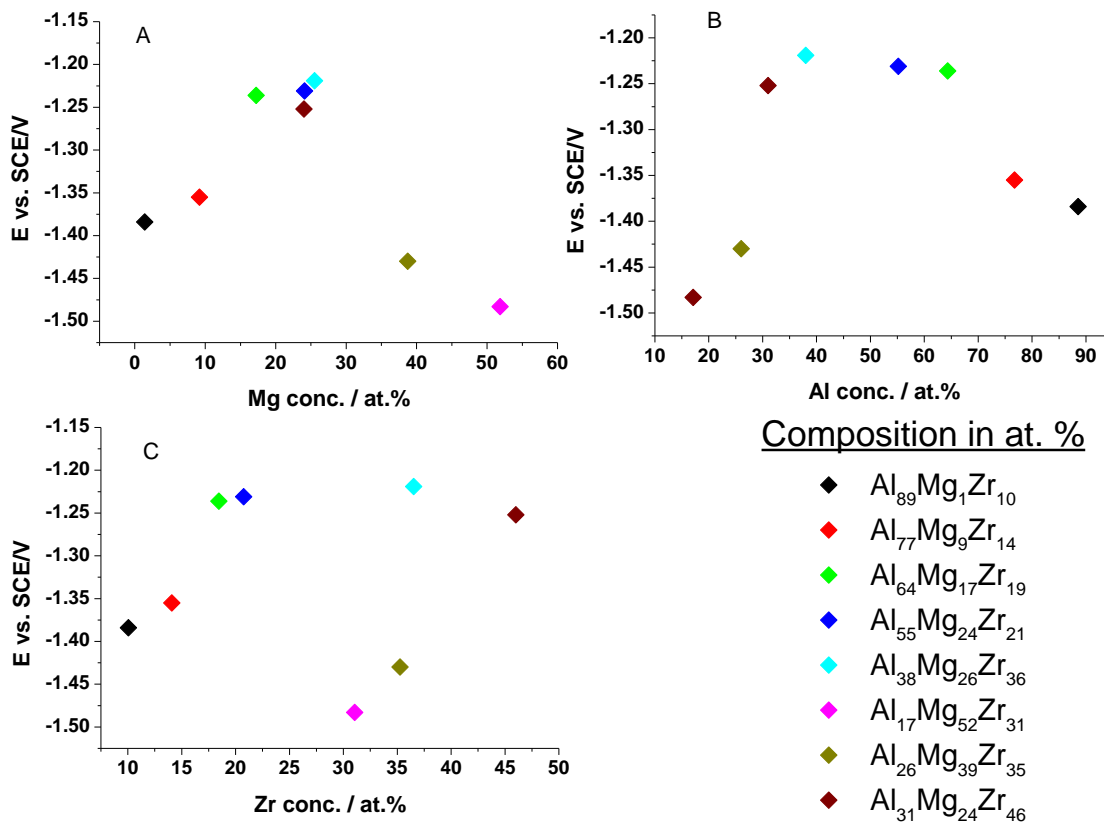


Figure 6.13: Corrosion potentials of the selected Al-Mg-Zr alloys (#7537) versus (A) Mg, (B) Al, and (C) Zr compositions.

There is a good agreement between the corrosion resistance results and the potentiodynamic curves. The changes in the potentiodynamic curves and corrosion resistance performance originate from two factors. The first is the morphological effect influenced and controlled by zirconium. This effect is responsible for the low anodic activity and high corrosion resistance displayed by the $\text{Al}_{89}\text{Mg}_1\text{Zr}_{10}$ alloy, where the zirconium acts as a grain refiner and improves corrosion resistance, which is in agreement with the observations of Song et al [150]. Moreover, the low roughness factor (i.e. 3.45 nm) exhibited by $\text{Al}_{89}\text{Mg}_1\text{Zr}_{19}$, which has a very similar composition, clearly indicates the grain refining effect as shown in **Figure 6.8(a)**. According to the Al-Zr phase diagram, only zirconium solid solution in aluminium exists in such a composition [159]. Furthermore, the addition of a low amount of Mg has increased the roughness by roughly three times from 3.45 nm to 9.84 nm, as displayed by the

$\text{Al}_{89}\text{Mg}_1\text{Zr}_{19}$ and $\text{Al}_{65}\text{Mg}_9\text{Zr}_{26}$ alloys respectively (**Figure 6.8** a, b). This compares to the high anodic activity displayed by the $\text{Al}_{77}\text{Mg}_9\text{Zr}_{14}$ alloy (red line) shown in **Figure 6.12**, as well as to the considerable decrease in the corrosion resistance that appeared at low Mg contents in **Figure 6.6** and **Figure 6.7**. The addition of Mg with a low content has led Mg to precipitate out of the Al (Zr) solid solution. As a result, the precipitated Mg acts as an anode and thus corrodes rapidly, which indicates the high anodic activity revealed by the $\text{Al}_{77}\text{Mg}_9\text{Zr}_{14}$ alloy (red line) as in **Figure 6.12**. This phenomenon has also been observed by Al-Aqeeli et al [210].

In addition to the morphological effect, the alloy structure forming new phases has played a significant role in increasing the corrosion resistance performance. For example, the $\text{Al}_{64}\text{Mg}_{17}\text{Zr}_{19}$, $\text{Al}_{55}\text{Mg}_{24}\text{Zr}_{21}$, $\text{Al}_{38}\text{Mg}_{26}\text{Zr}_{36}$ alloys shown in **Figure 6.12** and labelled in green, blue, and cyan respectively demonstrate very obvious cathodic current densities viz. hydrogen evolution. Additionally, they exhibit low anodic current densities. According to the X-ray diffraction results presented in **Figure 6.1**, those alloys comprise the Al_3Zr_2 and Al_3Zr_5 phases. These phases are commonly used as a hydrogen getter or absorber, and they react reversibly with hydrogen [168]. This explains their high activity in terms of the cathodic current densities. In addition, the Al_3Zr_5 phase has a strong affinity toward oxygen, whose presence stabilises the Al_3Zr_5 phase as the hexagonal $\text{D}8_8 \text{Zr}_5\text{Al}_3 \text{O}_{1-x}$ structure [169]. Consequently, this indicates the low anodic polarisation exhibited by those alloys.

On the other hand, the alloys comprising $>30\%_{\text{at.}}$ Mg contain only the solid solution of zirconium in magnesium Mg (Zr), as has been identified in the XRD patterns presented in **Figure 6.1**. The existence of this phase has a negative impact on the corrosion resistance as shown in **Figure 6.6**, **Figure 6.7** and **Figure 6.9**. Moreover, the alloys comprising $>30\%_{\text{at.}}$ Mg display the highest anodic current densities such as the $\text{Al}_{26}\text{Mg}_{39}\text{Zr}_{35}$ and $\text{Al}_{17}\text{Mg}_{52}\text{Zr}_{31}$ alloys labelled in gold and pink colour respectively and shown **Figure 6.12**. Also, their corrosion potentials (**Figure 6.13**) are very negative compared to other alloys.

The corrosion potential (E_{corr}) map of the Al-Mg-Zr alloys (#7537) is presented in **Figure 6.14**. The corrosion potential moves to negative potentials when

forming the solid solution of Zr in magnesium (i.e. $\text{Mg}_{0.996}\text{Zr}_{0.004}$). Also a similar consequence appears by forming the solid solution of Mg in aluminium. As shown earlier in **Figure 6.13** the addition of more Mg causes the corrosion potential to shift toward negative potentials. Contrary to this adding more Zr moves the corrosion potential to positive potentials (**Figure 6.14**). Besides the formation of Al-Zr intermetallics shift the corrosion potential to positive potentials; indicating good corrosion resistance as shown in **Figure 6.6**.

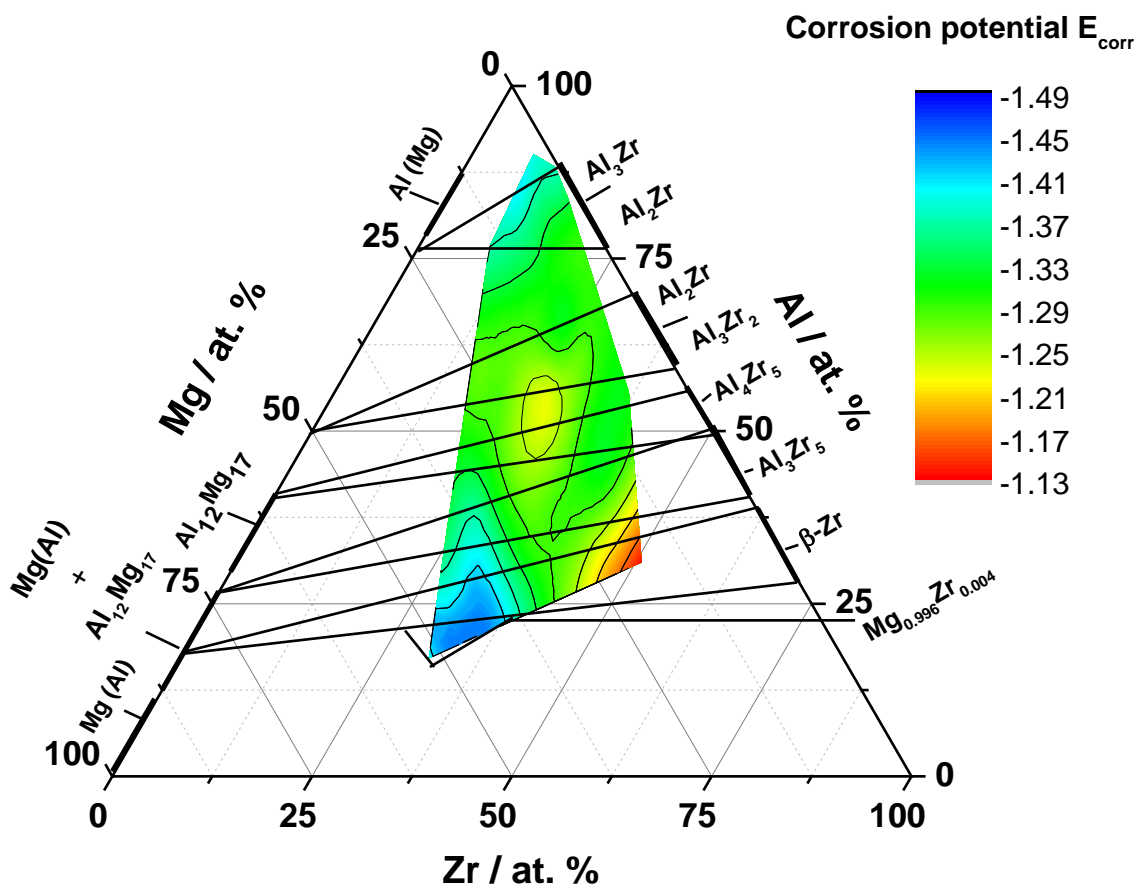


Figure 6.14: The corrosion potentials (E_{corr}) extracted from the potentiodynamic curves of Al-Mg-Zr alloys (#7537). The electrolyte is sodium chloride solution [0.1 M]. Alloys composition was determined by EDX. The XRD results are included.

6.2.2 Electrochemical Screening of Annealed Al-Mg-Zr Alloys

The electrochemical measurements were recorded at a 20 mV s^{-1} scan rate where de-aerated sodium chloride [0.05 M] was used as the corrosion electrolyte. All measurements were performed at 293 K. The potentiodynamic curves of selected annealed Al-Mg-Zr alloys are presented in **Figure 6.15**. The rich aluminium alloy (black colour) shows a rather high anodic and cathodic polarisation, which is ranked second after the rich magnesium alloy (pink colour). The anodic activity decreases slightly after adding more Mg and Zr as shown by the $\text{Al}_{70}\text{Mg}_{12}\text{Zr}_{18}$ alloy (green colour). More reduction in the anodic activity is exhibited by the $\text{Al}_{52}\text{Mg}_{25}\text{Zr}_{23}$ and $\text{Al}_{37}\text{Mg}_{26}\text{Zr}_{37}$ alloys, labelled using the blue and cyan colours respectively. Moreover, the latter also shows more cathodic activity. The rich Zr alloys (namely the $\text{Al}_{30}\text{Mg}_{26}\text{Zr}_{44}$ and $\text{Al}_{45}\text{Mg}_{11}\text{Zr}_{44}$) display large cathodic current densities. Moreover, they produce the lowest anodic current densities. The $\text{Al}_{45}\text{Mg}_{11}\text{Zr}_{44}$ alloy, which contains more Al and has a low Mg content compared to the $\text{Al}_{30}\text{Mg}_{26}\text{Zr}_{44}$, demonstrates an obvious passive behaviour shape.

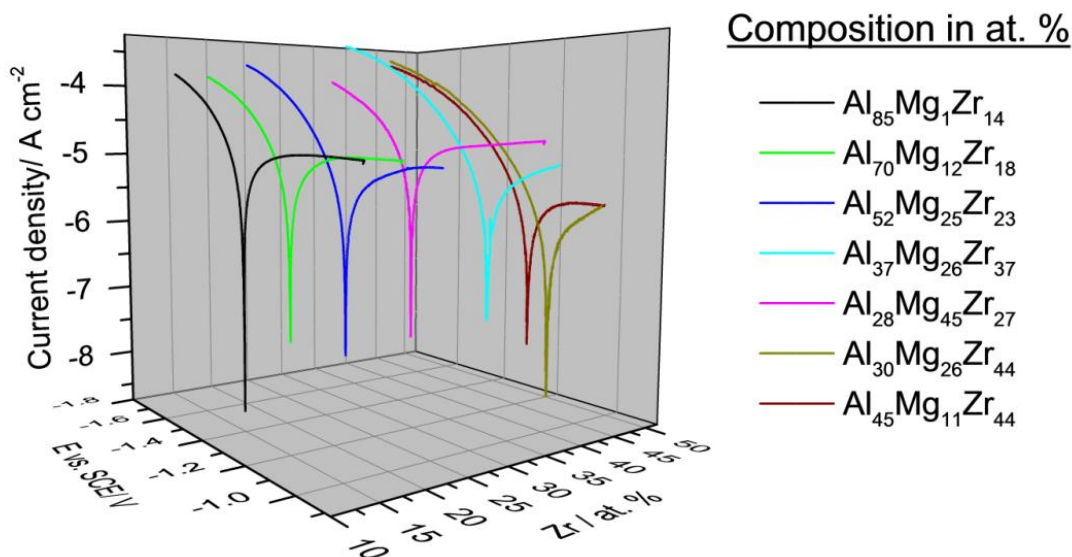


Figure 6.15: Potentiodynamic curves of annealed Al-Mg-Zr alloys investigated in de-aerated sodium chloride solution [0.05 M]. The scan rate was 20 mVs^{-1} . The pH and temperature were adjusted at 6.35 and 293 K. Alloy composition was determined by EDX.

The corrosion potentials (**Figure 6.16**) of the former alloys reflect what appears in the potentiodynamic curves. In another words, the alloys that displayed low anodic activity show more positive corrosion potentials viz. the $\text{Al}_{37}\text{Mg}_{26}\text{Zr}_{37}$, $\text{Al}_{30}\text{Mg}_{26}\text{Zr}_{44}$, and $\text{Al}_{45}\text{Mg}_{12}\text{Zr}_{44}$ alloys displayed in cyan, gold, and brown colour respectively. Adding Zr usually shifts the corrosion potential toward positive potential, whereas adding Mg in high quantity $\text{Mg} > 30\%_{\text{at}}$ shifts the potential to the negative side.

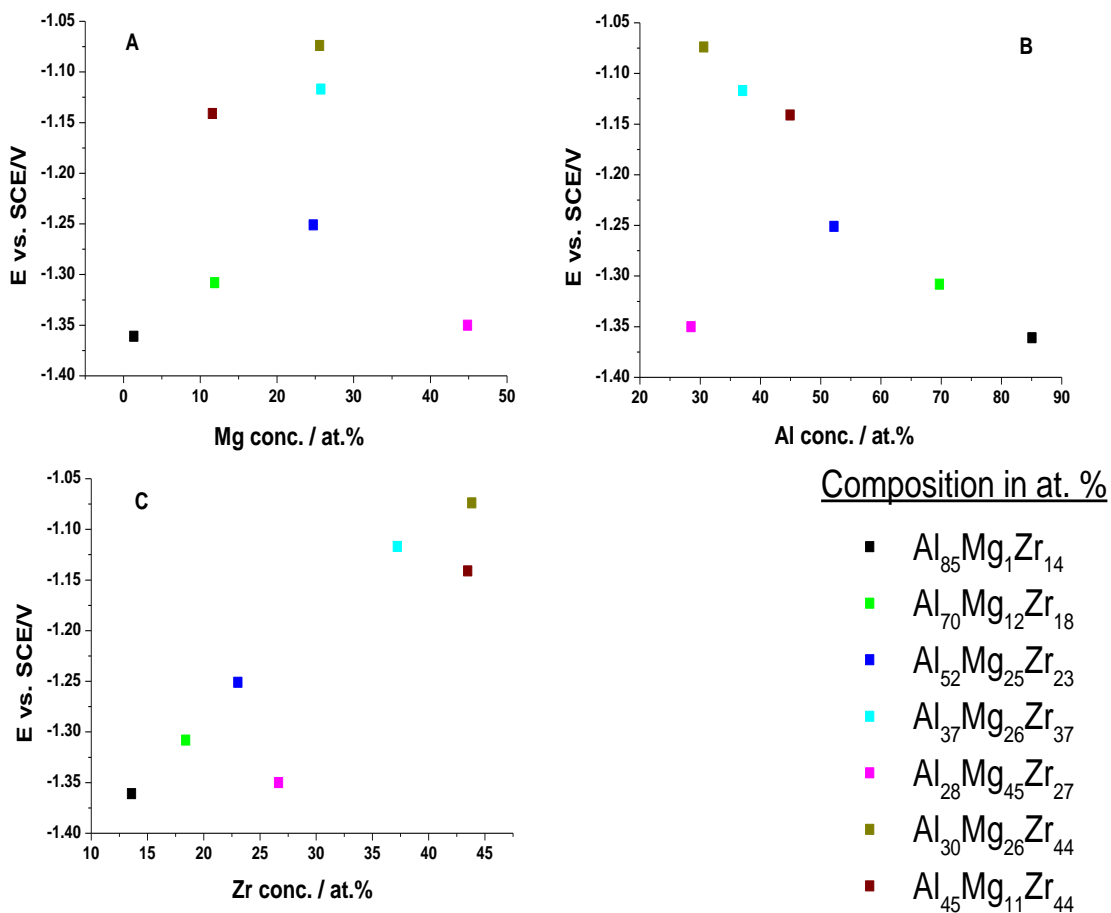


Figure 6.16: Corrosion potentials of the selected Al-Mg-Zr alloys versus (A) Mg, (B) Al, and (C) Zr compositions

As pointed earlier Tafel constant is determined using Equation 6-1 where a linear relationship between polarisation resistances obtained by LPR and corrosion currents extracted from Tafel plots persists over three decades as shown in **Figure 6.17**.

$$\log R_p = \log B - \log i_{\text{corr}}$$

Equation 6-1

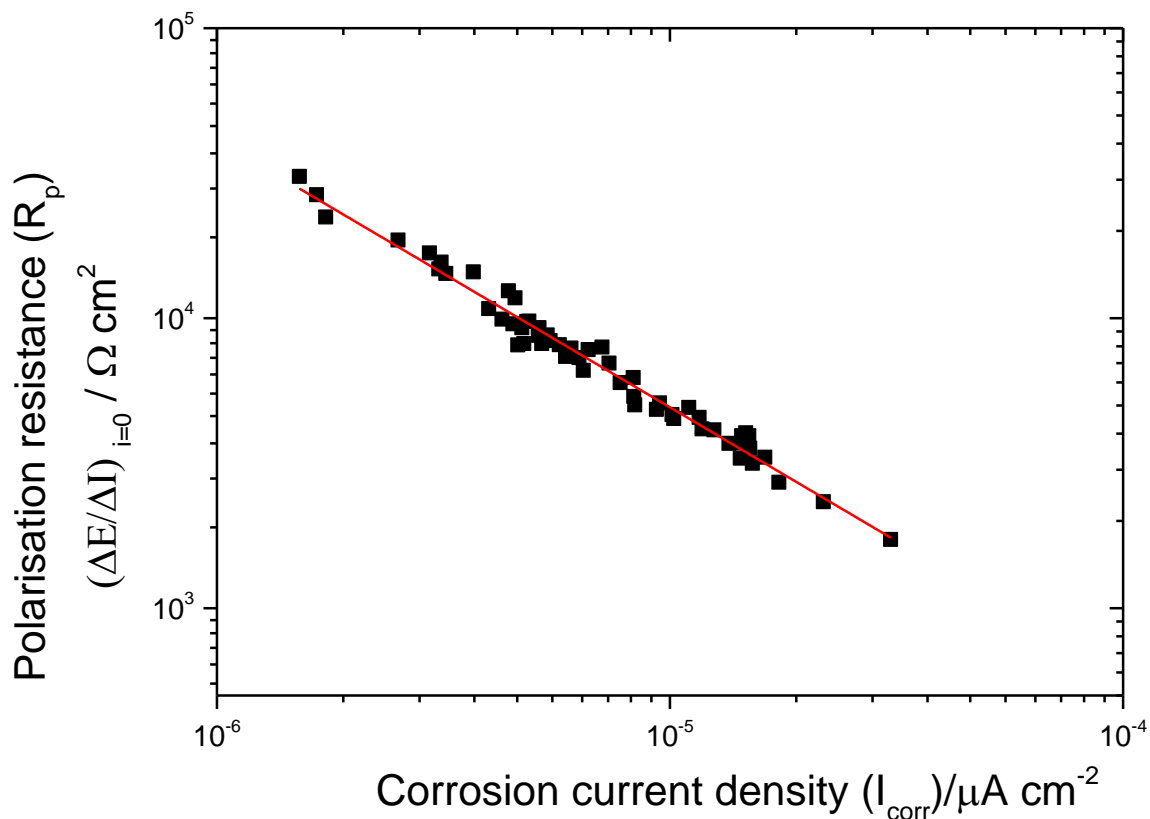


Figure 6.17: A plot of $\log R_p$ vs. $\log (i_{\text{corr}})$ for a series of Al-Mg-Zr alloys: The slope and B derived from (Equation 6-1) are -0.922 and 24 mV respectively. The electrolyte is sodium chloride [0.1 M] at room temperature.

6.2.2.1 The Corrosion Resistance (R_p) of the Annealed Al-Mg-Zr Alloys

The corrosion resistance data obtained from 100 fields on a single 10x10 array are shown in **Figure 6.18**. At rich Al $> 75\%_{\text{at}}$, the corrosion resistance appears low (see the light blue colour). Similarly, the alloys containing rich Mg $> 30\%_{\text{at}}$ show a low level of corrosion resistance. This can also be seen clearly in **Figure 6.18(B, C)**. The best corrosion resistance is displayed by the compositions of (10- 30 $\%_{\text{at}}$ Mg, 30-65 $\%_{\text{at}}$ Al, 20-30 $\%_{\text{at}}$ Zr). This compares to the low anodic current densities demonstrated by the $\text{Al}_{52}\text{Mg}_{25}\text{Zr}_{23}$ and $\text{Al}_{37}\text{Mg}_{26}\text{Zr}_{37}$ alloys labelled in blue and cyan as shown in **Figure 6.15**. According to the X-ray diffraction results presented in **Figure 6.2**, those compositions contain the Al_2Zr_3 , Al_4Zr_5 , and Al_3Zr_5 phases.

In addition, the alloys containing rich Zr $> 35\%_{\text{at}}$ show good corrosion resistance performance. In addition, they exhibit the lowest anodic activity as shown by the $\text{Al}_{30}\text{Mg}_{26}\text{Zr}_{44}$ alloy (**Figure 6.15**). Their structure comprises the Al_3Zr_5 and $\alpha\text{-Zr}$ phases as shown in **Figure 6.3**.

In general, the corrosion resistance performances of the annealed alloys (**Figure 6.18**) are similar to those observed in the as-deposited alloys (**Figure 6.6** and **Figure 6.7**). There is, however, one difference between the two performances, which appears at a low amount of Zr and Mg. The corrosion resistance profile of the as-deposited alloys show an obvious increase at low Mg and Zr compositions (as shown in **Figure 6.6** and **Figure 6.7**) while no increase appears at low Mg and Zr compositions of the annealed alloys (as shown in **Figure 6.18**), where instead a flat resistance appears. The origin of this difference likely relates to zirconium behaviour before and after the annealing in the presence of the Mg. This is discussed in more detail in the next section in which a general comparison between the annealed and as-deposited Al-Mg-Zr alloys is given.

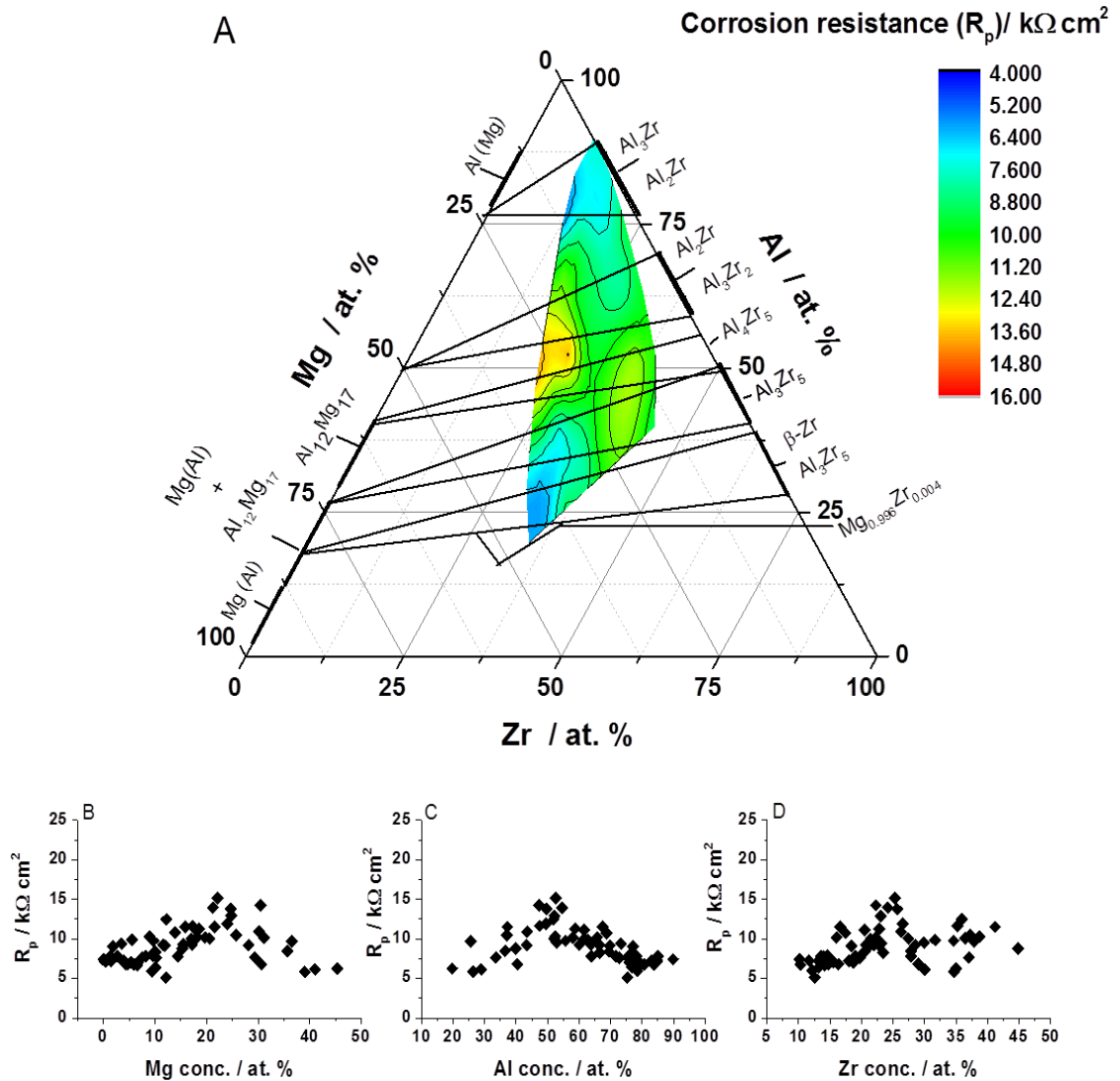


Figure 6.18: The corrosion resistance values obtained by LPR as a function of the components of Al-Mg-Zr alloys. De-aerated sodium chloride solution [0.05 M] was used as corrosion electrolyte. The pH and temperature were kept at 6.30 and 293 K. The XRD results are included.

6.3 Comparison between the As-deposited and Annealed Al-Mg-Zr Alloys

Generally, both the as-deposited and annealed alloys demonstrate similar trends in their corrosion resistance performance as functions of the compositions as shown in **Figure 6.6**, **Figure 6.7** and **Figure 6.18**. Nevertheless, the as-deposited alloys containing a low amount of Zr and Mg display a good performance where an evident increase appears at low Zr and Mg or rich Al compositions as shown in **Figure 6.6** and **Figure 6.7**. This is in contrast to the corrosion resistance of the annealed alloys at low Zr and Mg compositions showing a low and constant profile, where a light blue colour appears at the top of the ternary plot (**Figure 6.18**). There are two possible explanations for this difference. First, a change in the alloy structure may have occurred due to annealing, thus producing a structure with poor corrosion resistance performance. However, this is not the reason because the XRD results show no difference between the as-deposited and annealed alloy structures, with both being dominated by the Al_3Zr phase as shown in **Figure 6.1** and **Figure 6.2**. The other reason that may have led to the variation in the corrosion resistance is the morphological effect that has taken place at the surface. The latter is more likely to be the origin of the discrepancy in the corrosion resistance performance observed at low Zr and Mg compositions between the as-deposited and annealed alloys. Firstly, the annealing increases the surface roughness from 3.45 to 5 nm as seen in **Figure 6.19**. Secondly, according to the Mg-Zr diagram[104], Zr has very limited solubility in Mg at equilibrium Zr. Therefore, the annealing treatment made Mg to precipitate out of the existed phase viz. Al_3Zr and thus hampered Zr's effect as a grain refiner.

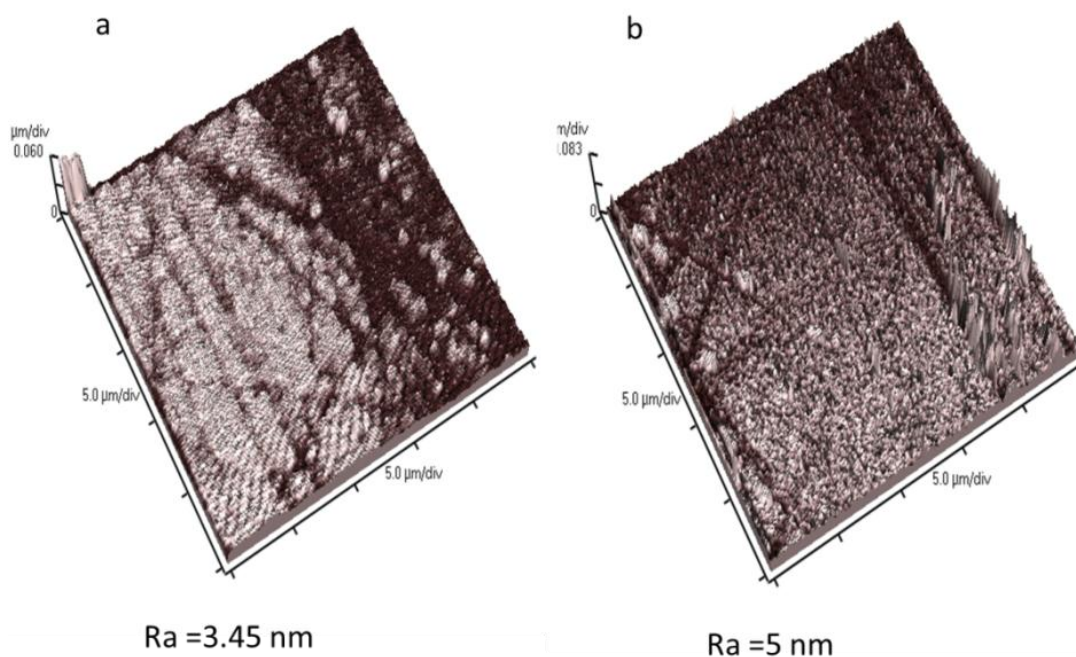


Figure 6.19: Topography of (a) as-deposited and (b) annealed $\text{Al}_{80}\text{Mg}_1\text{Zr}_{19}$ alloy. Silicon nitride was used as the substrate.

As a result, the corrosion resistance of the annealed alloys comprised of low Zr and Mg display low corrosion resistance with a flat profile (**Figure 6.18**). This is associated with the large anodic current densities displayed by the annealed $\text{Al}_{85}\text{Mg}_1\text{Zr}_{14}$ alloy (green colour) compared to the as-deposited $\text{Al}_{89}\text{Mg}_1\text{Zr}_{10}$ alloy (red colour) as shown in **Figure 6.20**. The high anodic activity exhibited by the annealed alloy is ascribed to the selective dissolution of the precipitated Mg.

On the other hand, the as-deposited $\text{Al}_{52}\text{Mg}_{24}\text{Zr}_{21}$ and annealed $\text{Al}_{52}\text{Mg}_{25}\text{Zr}_{23}$ alloys have the same structure. Therefore, they exhibit similar polarisation behaviour as shown in **Figure 6.20**. Moreover, their corrosion performance is similar to those presented in **Figure 6.6**, **Figure 6.7** and **Figure 6.18**. Also, both the annealed and as-deposited systems show an increase in the corrosion resistance performance at rich Zr $\geq 35\%_{\text{at}}$, although the annealed alloys demonstrate slightly higher corrosion resistance (**Figure 6.6**, **Figure 6.7** and **Figure 6.18**). This indicates the lower anodic current densities displayed by the annealed alloy (brown colour) compared to the as-deposited alloy (pink colour).

However, it is worth mentioning that the as-deposited alloy (pink colour) shows better passive behaviour than the annealed alloy (brown colour). This is probably because the annealed alloys contain rich Zr ≥ 35 %_{at.} composed of two phases (i.e. the α -Zr and Al_3Zr_5) while only the α -Zr phase exists in the as-deposited alloys, as shown by the XRD results (Figure 6.3 (D, H)). Consequently, the existence of the two phases simultaneously may prevent the passivity behaviour due to the occurrence of micro-galvanic corrosion.

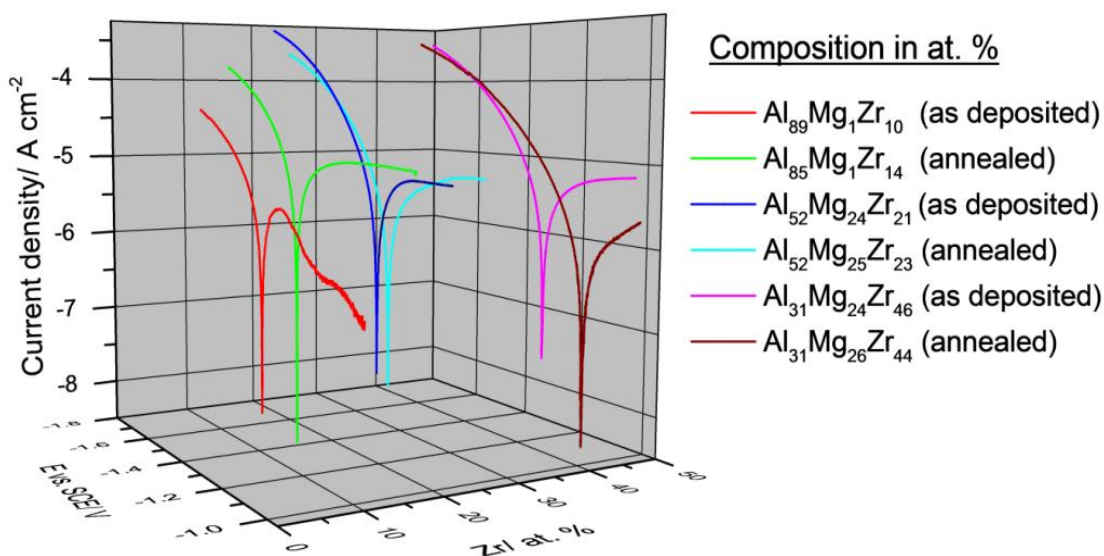


Figure 6.20: Potentiodynamic curves of selected as-deposited and annealed Al-Mg-Zr alloys investigated in de-aerated sodium chloride solution [0.05M]. The scan rate was 20 mVs^{-1} . The pH and temperature were adjusted at 6.35 and 293K. Alloys composition was determined by EDX.

6.4 Conclusion

Five Al-Zr metastable phases are found i.e. (Al_3Zr , Al_2Zr , Al_3Zr_2 , Al_4Zr_5 , and Al_3Zr_5) besides Zr solid solution in magnesium. No ternary intermetallics of the Al-Mg-Zr have been obtained, which is in agreement with literature [157]. The relationship between corrosion resistance and alloys structure and morphology is observable.

The annealed and as-deposited alloys with compositions of (10- 30 %_{at.} Mg, 30- 65 %_{at.} Al, 20-30 %_{at.} Zr) have a similar structure and corrosion resistance performance. Two phases have been identified in those composition ranges, namely the Al_3Zr_2 and Al_3Zr_5 . They noticeably increase cathodic activity, i.e. HER, and reduce anodic activity as well. Besides the rich zirconium alloys contained ≥ 44 %_{at.} Zr, those alloys composition also display the best passivity.

The addition of small amount of zirconium into Mg-rich Al alloy result in good grain refining effect of the as-deposited alloys. Therefore they have shown good corrosion resistance. However, this effect was not observed at the same alloys composition of annealed alloys owing to heat treatment which causes Mg to segregate out of Al-Zr phases. As a result, the annealed alloys display a coarser surface and they exhibit a low corrosion resistance compared to the equivalent compositions of the as-deposited alloys. Moreover, its passivity has greatly deteriorated

The addition of Zr shifts corrosion potential to positive potentials while adding Mg by ≥ 35 %_{at.} moves the corrosion potential negative.

7. General Conclusion

A high throughput screening methodology, employing multi-channel current followers [46] and a silicon micro-fabricated array of independently addressable electrodes [41], has been successfully applied to the screen corrosion characteristics of thin film alloys. The screening methodology is compatible with the high-throughput physical vapour deposition (HT-PVD) methodology, which were based on the MBE sources [170]. This allows the controllable deposition of compositional gradients of a large range of thin film materials. Furthermore, high throughput XRD and EDS measurements have been employed before conducting electrochemical screening. This allows a correlation of the alloys composition, structure (phase(s)) and morphology dependence of the corrosion behaviour. As a result, multiple findings have been identified.

For example, the polarisation resistance behaviour is shown to be directly related to the bulk alloy structures in the NiCr alloys, where the b.c.c α -Cr (Im3m) phase and the σ Cr_3Ni_2 phase observed 60 %_{at.} Cr display the best polarisation resistance. In another case, the formation of a solid solution of tungsten in nickel Ni (W) resulted in a low polarisation resistance, whereas the formation of the amorphous phase (observed at compositions of $W \geq 24\%_{\text{at}}$) display higher corrosion resistance. Therefore, this methodology can be used for materials selection, which will eventually assist in reducing the economic costs of corrosion.

The high throughput characterisation also allows a correlation of the alloys composition and structure dependence of the corrosion potential (E_{corr}). This provides information concerning intermetallics. For example, the grains boundary impact on corrosion behaviour for complicated alloys system as Al-Mg alloys. The Al-Mg alloys corrosion resistance is very susceptible to intermetallics formation, such as Al_3Mg_2 and γ $\text{Al}_{12}\text{Mg}_{17}$. Since these intermetallics have a different electrochemical activity, they can be monitored by their corrosion potential. This has been observed, and the formation of γ $\text{Al}_{12}\text{Mg}_{17}$ coincides with a very significant shift of corrosion potential to positive potentials, which is in agreement with observations obtained by XRD results.

The corrosion (polarisation) resistance (R_p) is extracted using both the Tafel extrapolation and linear polarisation resistance (LPR) methods. Both methods revealed the same alloy compositional dependence of the polarisation resistance. There is a systematic increase in the absolute values of corrosion resistances extracted by LPR, which is likely to be the result of the irreversible changes that occurred during the cathodic scan, which preceded the linear polarisation resistance region. As a result, a thin corrosion film was formed on the surface of the alloys, producing an increase of the corrosion resistances extracted by LPR, which is in agreement with the assessment of Mansfeld [28].

Finally, this methodology of corrosion screening provides the ability to explore a considerable number of samples (up to a 100 fields per single array), while previous high-throughput approaches could only assess a quarter of this number, like the multi-electrode method [53, 54], for instance. In addition, the simultaneous parallel electrochemical screening ensures not only a simple procedure but also an identical electrochemical environment, which is more difficult to achieve in the sequential measurements of a scanning droplet cell (SDC) [49].

7.1 Future Work

There are two important issues arising from this work that have not been extensively addressed due to time limits. However, they are significant. The next section provides a brief discussion of these two issues and suggestions regarding future work in these areas.

7.1.1 Open Circuit Potential (E_{opc})

For a single electrode, the open circuit potential can be measured easily by using a digital voltammeter (DVM). However, for high-throughput measurements, things are more complicated. A voltage follower comprised of a 100 channel needs to be constructed. This has been achieved to some extent with the help of Ilika Technologies Ltd, and some measurements have been obtained (see Appendix 2). Nevertheless, the device still needs further tests. The zero current potential has alternatively been obtained from the CV data, which should be similar.

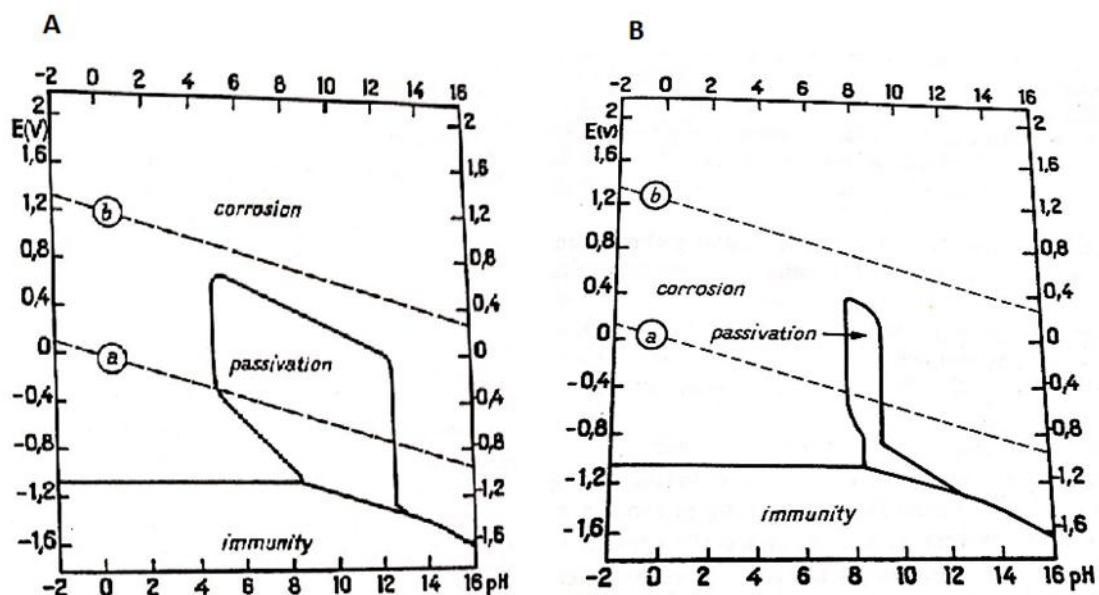
7.1.2 The Potential Scan Rate

Electrochemical screening was achieved by carrying out parallel cyclic voltammetry measurements at a scan rate of 20 mV s^{-1} . The 20 mV s^{-1} scan rates are somewhat high for conventional corrosion measurements, and it should ideally not exceed 0.16 mV s^{-1} [1]. The high scan rates will lead to a capacitance current contribution. As a result, the zero current potential ($E_{i=0}$) or corrosion potential (E_{corr}) will not necessarily be equal to the open circuit potential. Consequently, this will influence the absolute accuracy of corrosion currents extrapolated from the potentiodynamic curves, and corrosion resistances obtained by the LPR method [24, 34]. Nonetheless, the 20 mV s^{-1} scan rate was used for two main reasons. Firstly, this resulted in higher measurable currents, and in this respect provided the necessary signal-to-noise when measuring simultaneously cyclic voltammograms on 100 small electrodes. Moreover, this scan rate was conservatively low in comparison to other combinatorial measurements [47], where even higher scan rates are used to study corrosion. Secondly, this approach minimised irreversible changes in the thin films caused during longer periods in the electrolyte when using a slow scan rate $\leq 1 \text{ mV s}^{-1}$.

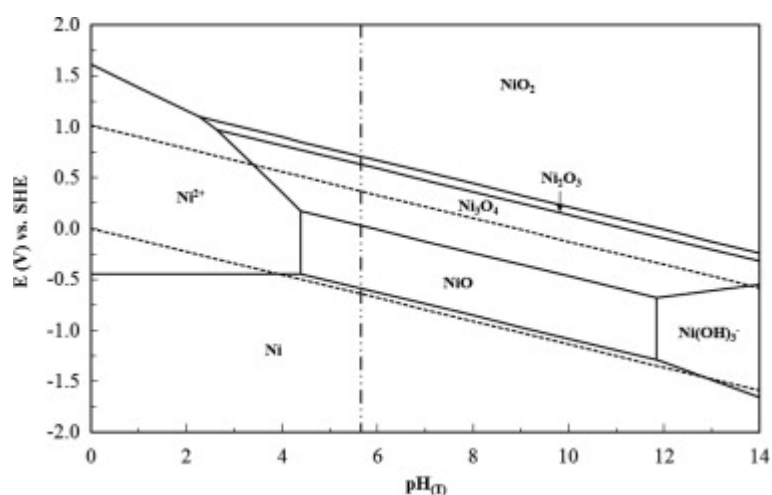
Nevertheless, slow scan rates can be achieved. In order to do this, sample or film thickness has to be more than $0.5 \text{ }\mu\text{m}$, and this is achievable only via a longer deposition course. Also, the current can be maximised by increasing the electrode (field) area on the 10×10 array. Therefore, higher measurable currents can be obtained when using slow scan rates. This leads to the need to design and manufacture a new array.

Appendices

Appendix 1

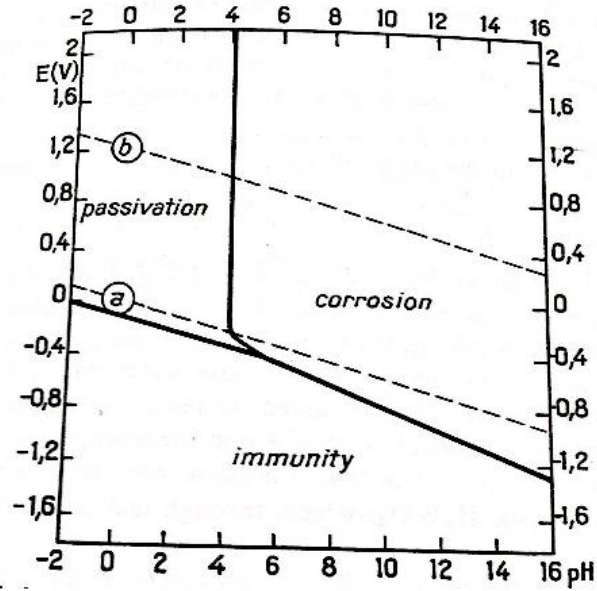


Theoretical conditions of corrosion, immunity and passivation of chromium, at 25 °C (A) in solution not contains chloride (B) in solution contains chloride. Adapted from[109]. The potential is vs. RHE.

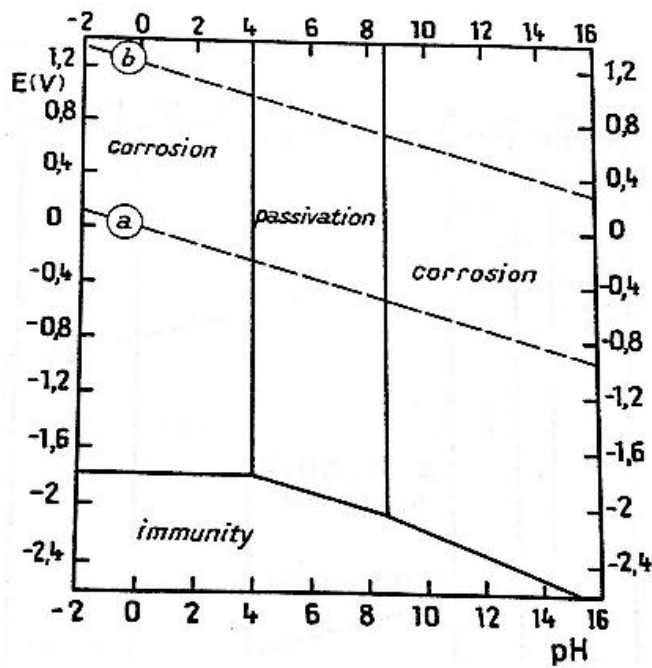


Theoretical conditions of corrosion, immunity and passivation of nickel at 25 °C. Adapted from[109].

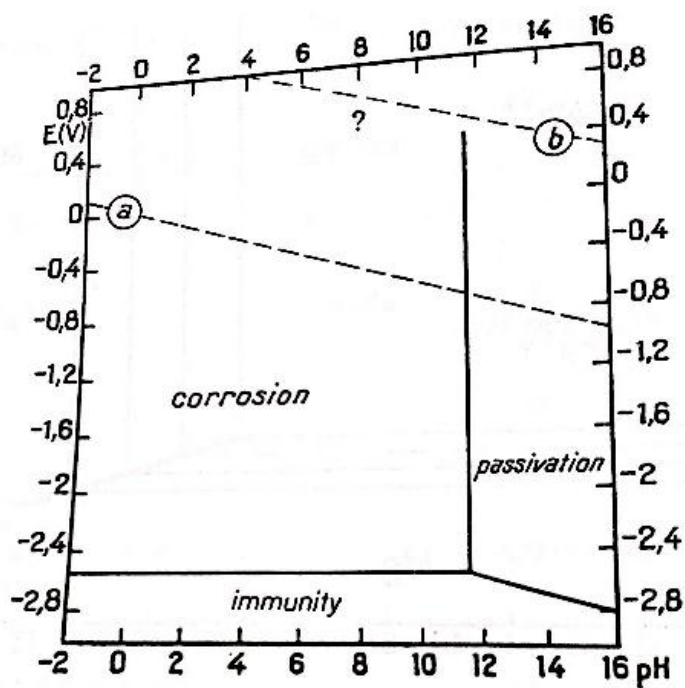
Appendix 1



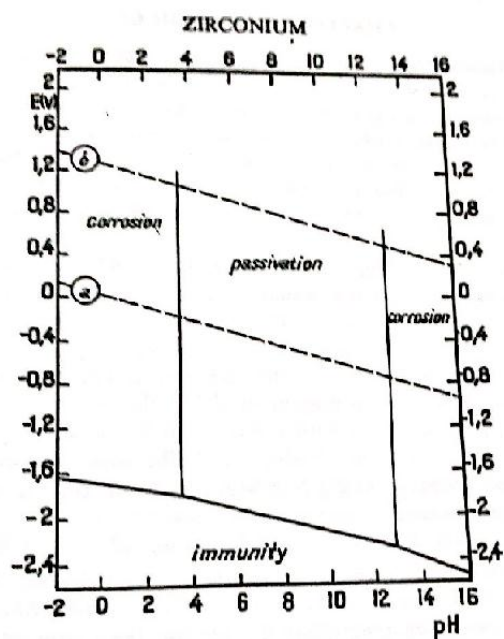
Theoretical conditions of corrosion, immunity and passivation of tungsten, at 25 °C. Adapted from[109]. The potential is vs. RHE.



Theoretical conditions of corrosion, immunity and passivation of aluminium, at 25 °C. Adapted from[109]. The potential is vs. RHE.

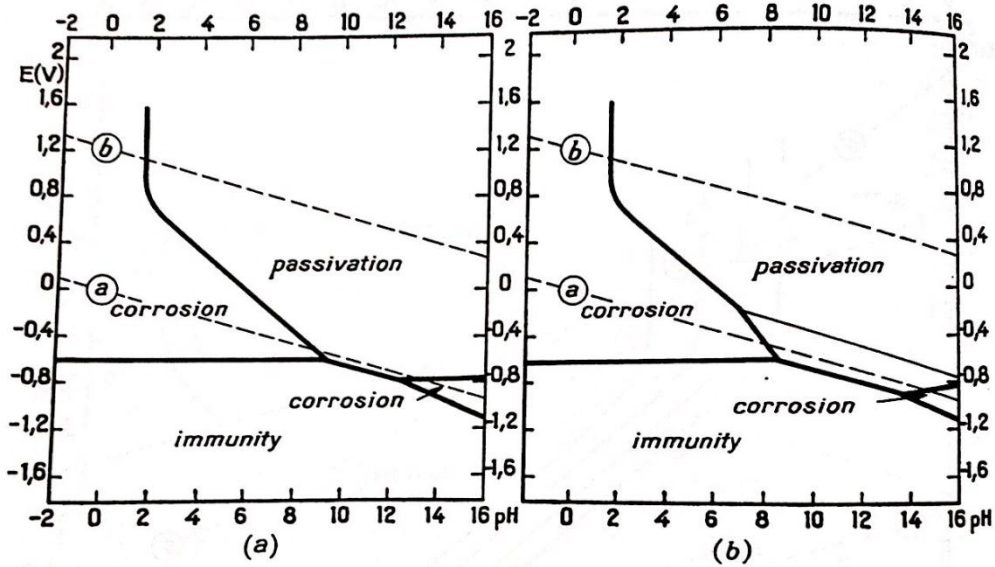


Theoretical conditions of corrosion, immunity and passivation of magnesium, at 25 °C. Adapted from[109]. The potential is vs. RHE.



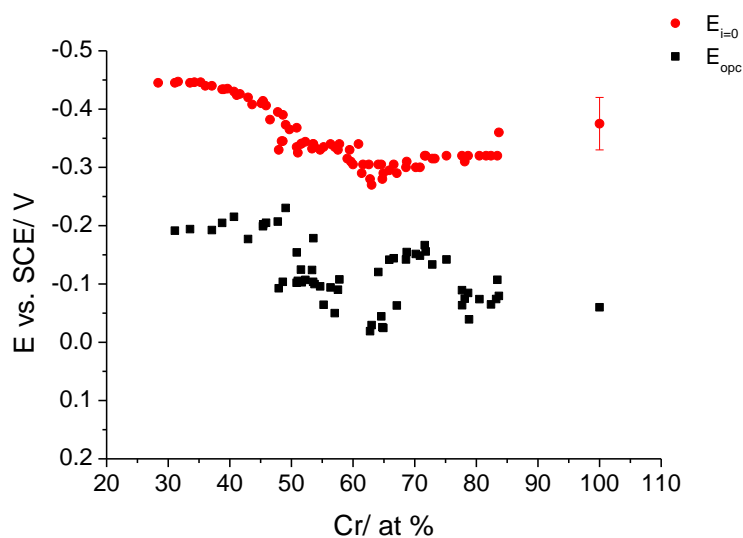
Theoretical conditions of corrosion, immunity and passivation of zirconium, at 25 °C. Adapted from[109]. The potential is vs. RHE.

Appendix 1

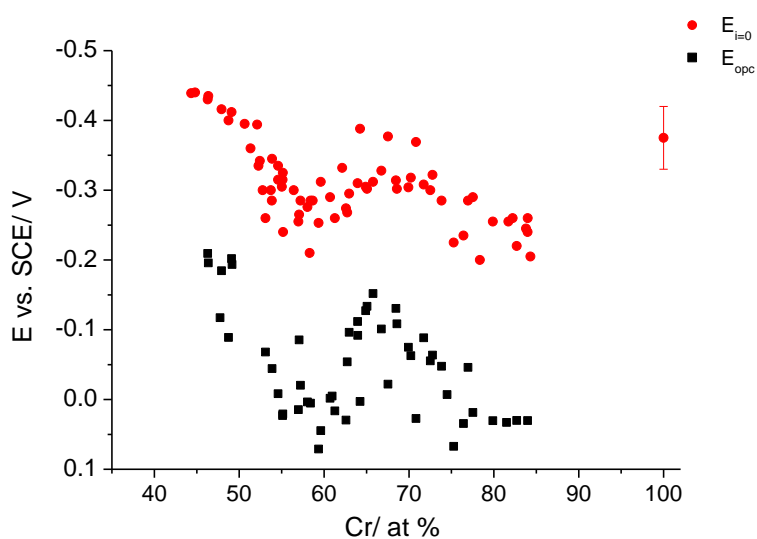


Theoretical conditions of corrosion, immunity and passivation of Iron, where in (a) assuming passivation by a film of Fe_2O_3 and (b) in present of Fe_2O_3 and Fe_3O_4 . The potential is vs. RHE.

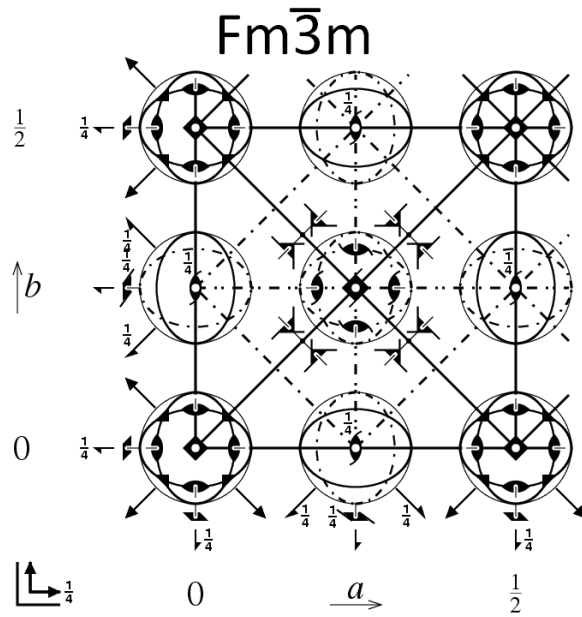
Appendix 2



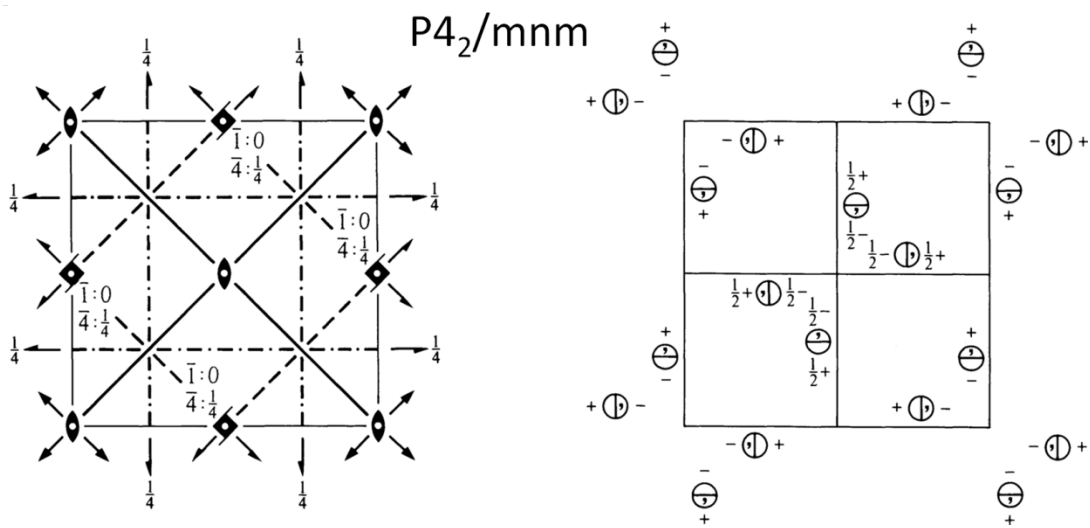
Comparison between open circuit and zero current potential for Ni-Cr alloys of compositions in the range of 31–83 % Cr, array A (#7149). The open circuit potentials were obtained after 20 min. The electrolyte is phosphoric acid pH 3 at 293 K.



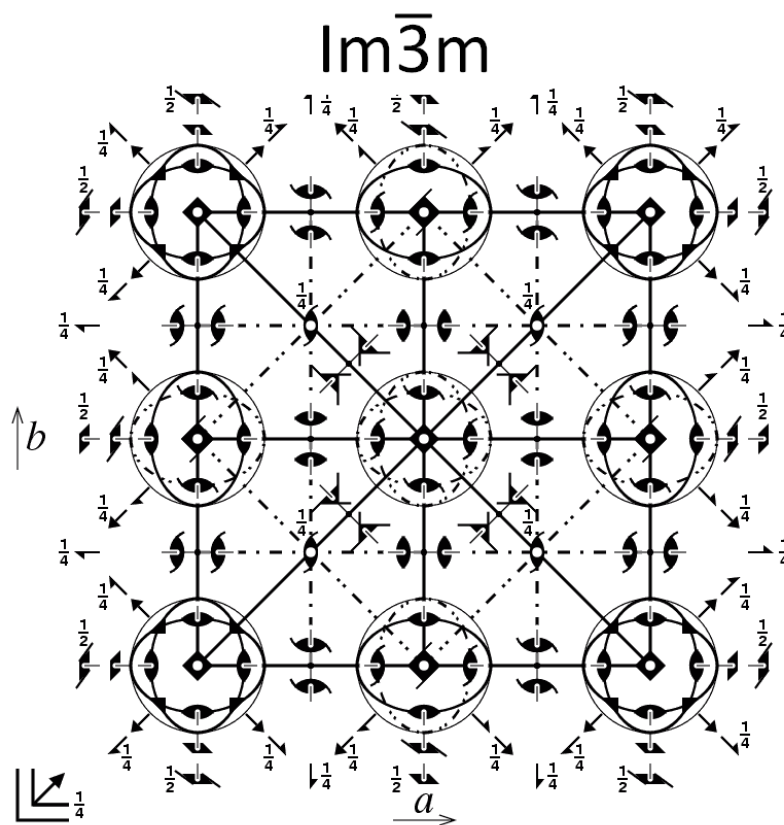
Comparison between open circuit and zero current potential for Cr and Ni-Cr alloys of compositions in the range of 42–85 % Cr, array B (#7150). The open circuit potentials were obtained after 20 min. The electrolyte is phosphoric acid pH 3 at 293 K.



Space group diagram of cubic Fm $\bar{3}$ m.



Space group diagram of tetragonal P4 $_2$ /mnm.

Space group diagram of cubic $\text{Im}\bar{3}\text{m}$.

Bibliography

- [1] R. Kelly, J. Scully, D. Shoesmith, R. Buchheit, *Electrochemical Techniques in Corrosion Science and Engineering*, CRC press, Taylor & Francis Group, 2003.
- [2] G.L. Song, A. Atrens, *Corrosion Mechanisms of Magnesium Alloys*, *Advanced Engineering Materials*, 1 (1999) 11-33.
- [3] M.G. Fontana, *Corrosion Engineering*, Third Edition ed., McGraw-Hill, New York, 1978.
- [4] G. Song, A. Atrens, *Understanding Magnesium Corrosion—A Framework for Improved Alloy Performance*, *Advanced Engineering Materials*, 5 (2003) 837-858.
- [5] P. Zhang, X. Nie, D.O. Northwood, *Influence of coating thickness on the galvanic corrosion properties of Mg oxide in an engine coolant*, *Surface and Coatings Technology*, 203 (2009) 3271-3277.
- [6] M.-C. Zhao, M. Liu, G. Song, A. Atrens, *Influence of the β -phase morphology on the corrosion of the Mg alloy AZ91*, *Corrosion Science*, 50 (2008) 1939-1953.
- [7] D.A. Jones, *Principles and prevention of corrosion*, Prentice Hall, United States of America, 1996.
- [8] J. Kruger, *Corrosion of Metals: Overview*, in: K.H.J.B. Editors-in-Chief: , W.C. Robert, C.F. Merton, I. Bernard, J.K. Edward, M. Subhash, V. Patrick (Eds.) *Encyclopedia of Materials: Science and Technology (Second Edition)*, Elsevier, Oxford, 2001, pp. 1701-1706.
- [9] Z. Szklarska-Smialowska, *Insight into the pitting corrosion behavior of aluminum alloys*, *Corrosion Science*, 33 (1992) 1193-1202.
- [10] S. Maitra, G.C. English, *Mechanism of localized corrosion of 7075 alloy plate*, *MTA*, 12 (1981) 535-541.
- [11] R.H. Jones, D.R. Baer, M.J. Danielson, J.S. Vetrano, *Role of Mg in the stress corrosion cracking of an Al-Mg alloy*, *Metall and Mat Trans A*, 32 (2001) 1699-1711.
- [12] S. Jain, M.L.C. Lim, J.L. Hudson, J.R. Scully, *Spreading of intergranular corrosion on the surface of sensitized Al-4.4Mg alloys: A general finding*, *Corrosion Science*, 59 (2012) 136-147.
- [13] E.L. Hall, C.L. Briant, *Chromium depletion in the vicinity of carbides in sensitized austenitic stainless steels*, *MTA*, 15 (1984) 793-811.
- [14] C. Tedmon, D. Vermilyea, J. Rosolowski, *Intergranular corrosion of austenitic stainless steel*, *Journal of The Electrochemical Society*, 118 (1971) 192-202.
- [15] I.N.A. Oguocha, O.J. Adigun, S. Yannacopoulos, *Effect of sensitization heat treatment on properties of Al-Mg alloy AA5083-H116*, *J Mater Sci*, 43 (2008) 4208-4214.
- [16] J.L. Searles, P.I. Gouma, R.G. Buchheit, *Stress corrosion cracking of sensitized AA5083 (Al-4.5Mg-1.0Mn)*, *Metall and Mat Trans A*, 32 (2001) 2859-2867.
- [17] J.R. Galvele, S.M. de De Micheli, *Mechanism of intergranular corrosion of Al-Cu alloys*, *Corrosion Science*, 10 (1970) 795-807.
- [18] G.S. Frankel, *Electrochemical Techniques in Corrosion: Status, Limitations, and Needs*, *Journal of ASTM International*, 5 (2008).
- [19] M. Jönsson, D. Persson, C. Leygraf, *Atmospheric corrosion of field-exposed magnesium alloy AZ91D*, *Corrosion Science*, 50 (2008) 1406-1413.

Bibliography

- [20] A. Pardo, M.C. Merino, A.E. Coy, R. Arrabal, F. Viejo, E. Matykina, Corrosion behaviour of magnesium/aluminium alloys in 3.5 wt.% NaCl, *Corrosion Science*, 50 (2008) 823-834.
- [21] ASTM, Standard Practice for Operating Salt Spray (Fog) Testing Apparatus, American society for testing and materials, Standard B117-97.
- [22] G.S. Frankel, M. Rohwerder, Electrochemical Techniques for Corrosion, in: *Encyclopedia of Electrochemistry*, Wiley-VCH Verlag GmbH & Co. KGaA, 2007.
- [23] C. Wagner, W. Traud, *Elektrochem*, 44 391.
- [24] X.L. Zhang, Z.H. Jiang, Z.P. Yao, Y. Song, Z.D. Wu, Effects of scan rate on the potentiodynamic polarization curve obtained to determine the Tafel slopes and corrosion current density, *Corrosion Science*, 51 (2009) 581-587.
- [25] M. Stern, Geary, A. L., *Journal of Electrochemical Society*, 104 (1957) 56.
- [26] T.P. Hoar, On the relation between corrosion rate and polarization resistance, *Corrosion Science*, 7 (1967) 455-458.
- [27] F. Mansfeld, K.B. Oldham, A modification of the Stern--Geary linear polarization equation, *Corrosion Science*, 11 (1971) 787-796.
- [28] F. Mansfeld, Tafel slopes and corrosion rates obtained in the pre-Tafel region of polarization curves, *Corrosion Science*, 47 (2005) 3178-3186.
- [29] F. Mansfeld, Simultaneous Determination of Instantaneous Corrosion Rates and Tafel Slopes from Polarization Resistance Measurements, *Journal of The Electrochemical Society*, 120 (1973) 515-518.
- [30] S. Barnartt, Two-point and three-point methods for the investigation of electrode reaction mechanisms, *Electrochimica Acta*, 15 (1970) 1313-1324.
- [31] M. Periassamy, P.R. Krishnaswamy, Corrosion rate and tafel slopes from polarization curves, *Journal of Electroanalytical Chemistry and Interfacial Electrochemistry*, 61 (1975) 349-352.
- [32] J. Jankowski, R. Juchniewicz, A four-point method for corrosion rate determination, *Corrosion Science*, 20 (1980) 841-851.
- [33] K.B. Oldham, F. Mansfeld, Corrosion rates from polarization curves: A new method, *Corrosion Science*, 13 (1973) 813-819.
- [34] M. Kouril, P. Novak, M. Bojko, Limitations of the linear polarization method to determine stainless steel corrosion rate in concrete environment, *Cement and Concrete Composites*, 28 (2006) 220-225.
- [35] M.P.H.B. Gerhardus H. Koch, Neil G. Thompson, Virmani Y Paul, Payer J. H., *Corrosion Costs and Preventative strategies in the United States*, NACE, (2001).
- [36] T.P. Hoar, Report of the Committee on Corrosion and Protection
Department of Trade and Industry, UK, (1971).
- [37] A. Al-Hashem, in: P.R.a.S. Center (Ed.), *Kuwait Institute for Scientific Research*, Kuwait.
- [38] L.H. Bennett, J. Kruger, R. Parker, E. Passaglia, C. Reimann, A. Ruff, H. Yakowitz, E. Berman, Economic effects of metallic corrosion in the United States. Part 1, in, National Bureau of Standards, Washington, DC (USA); Berman (Edward B.) Associates, Inc., Marblehead, MA (USA), 1978.
- [39] B. Chisholm, D. Webster, The development of coatings using combinatorial/high throughput methods: a review of the current status, *Journal of Coatings Technology and Research*, 4 (2007) 1-12.
- [40] R. Potyrailo, K. Rajan, K. Stoeve, I. Takeuchi, B. Chisholm, H. Lam, Combinatorial and High-Throughput Screening of Materials Libraries: Review of State of the Art, *ACS Combinatorial Science*, 13 (2011) 579-633.
- [41] S. Guerin, B.E. Hayden, C.E. Lee, C. Mormiche, A.E. Russell, High-throughput synthesis and screening of ternary metal alloys for electrocatalysis, *Journal of Physical Chemistry B*, 110 (2006) 14355-14362.

- [42] B.E. Hayden, D.V. Malevich, D. Pletcher, Platinum catalysed nanoporous titanium dioxide electrodes in H₂SO₄ solutions, *Electrochemistry Communications*, 3 (2001) 395-399.
- [43] B.E. Hayden, D. Pletcher, M.E. Rendall, J.P. Suchsland, CO oxidation on gold in acidic environments: Particle size and substrate effects, *Journal of Physical Chemistry C*, 111 (2007) 17044-17051.
- [44] B.E. Hayden, D. Pletcher, J.P. Suchsland, Enhanced activity for electrocatalytic oxidation of carbon monoxide on titania-supported gold nanoparticles, *Angewandte Chemie-International Edition*, 46 (2007) 3530-3532.
- [45] P.M. Tucker, M.J. Waite, B.E. Hayden, Electrocatalytic reduction of nitrate on activated rhodium electrode surfaces, *Journal of Applied Electrochemistry*, 34 (2004) 781-796.
- [46] S. Guerin, B.E. Hayden, C.E. Lee, C. Mormiche, J.R. Owen, A.E. Russell, B. Theobald, D. Thompsett, Combinatorial electrochemical screening of fuel cell electrocatalysts, *Journal of Combinatorial Chemistry*, 6 (2004) 149-158.
- [47] S.O. Klemm, J.P. Kollender, A.W. Hassel, Combinatorial corrosion study of the passivation of aluminium copper alloys, *Corrosion Science*, 53 (2011) 1-6.
- [48] J.S. Cooper, M.K. Jeon, P.J. McGinn, Combinatorial screening of ternary Pt-Ni-Cr catalysts for methanol electro-oxidation, *Electrochemistry Communications*, 10 (2008) 1545-1547.
- [49] M.M. Lohrengel, A. Moehring, M. Pilaski, Electrochemical surface analysis with the scanning droplet cell, *Fresenius' Journal of Analytical Chemistry*, 367 (2000) 334-339.
- [50] A.I. Mardare, A. Savan, A. Ludwig, A.D. Wieck, A.W. Hassel, A combinatorial passivation study of Ta-Ti alloys, *Corrosion Science*, 51 (2009) 1519-1527.
- [51] A.I. Mardare, A. Savan, A. Ludwig, A.D. Wieck, A.W. Hassel, High-throughput synthesis and characterization of anodic oxides on Nb-Ti alloys, *Electrochimica Acta*, 54 (2009) 5973-5980.
- [52] A.I. Mardare, A. Ludwig, A. Savan, A.D. Wieck, A.W. Hassel, Combinatorial investigation of Hf-Ta thin films and their anodic oxides, *Electrochimica Acta*, 55 (2010) 7884-7891.
- [53] T.H. Muster, A.E. Hughes, S.A. Furman, T. Harvey, N. Sherman, S. Hardin, P. Corrigan, D. Lau, F.H. Scholes, P.A. White, M. Glenn, J. Mardel, S.J. Garcia, J.M.C. Mol, A rapid screening multi-electrode method for the evaluation of corrosion inhibitors, *Electrochimica Acta*, 54 (2009) 3402-3411.
- [54] S.J. García, T.H. Muster, Ö. Özkanat, N. Sherman, A.E. Hughes, H. Terryn, J.H.W. de Wit, J.M.C. Mol, The influence of pH on corrosion inhibitor selection for 2024-T3 aluminium alloy assessed by high-throughput multielectrode and potentiodynamic testing, *Electrochimica Acta*, 55 2457-2465.
- [55] S. Guerin, B.E. Hayden, D. Pletcher, M.E. Rendall, J.P. Suchsland, A combinatorial approach to the study of particle size effects on supported electrocatalysts: Oxygen reduction on gold, *Journal of Combinatorial Chemistry*, 8 (2006) 679-686.
- [56] S. Guerin, B.E. Hayden, D. Pletcher, M.E. Rendall, J.P. Suchsland, L.J. Williams, Combinatorial approach to the study of particle size effects in electrocatalysis: Synthesis of supported gold nanoparticles, *Journal of Combinatorial Chemistry*, 8 (2006) 791-798.
- [57] Y. Kwon, N.-H. Kim, G.-P. Choi, W.-S. Lee, Y.-J. Seo, J. Park, Structural and surface properties of NiCr thin films prepared by DC magnetron sputtering under variation of annealing conditions, *Microelectronic Engineering*, 82 (2005) 314-320.

Bibliography

- [58] L.I. Belič, K. Požun, M. Remškar, AES, AFM and TEM studies of NiCr thin films for capacitive humidity sensors, *Thin Solid Films*, 317 (1998) 173-177.
- [59] W.R. Hardy, D.K. Murti, Electrical and structural properties of NiCr thin film resistors reactively sputtered in O₂, *Thin Solid Films*, 20 (1974) 345-362.
- [60] S.S. Chatha, H.S. Sidhu, B.S. Sidhu, High temperature hot corrosion behaviour of NiCr and Cr₃C₂-NiCr coatings on T91 boiler steel in an aggressive environment at 750 °C, *Surface and Coatings Technology*, 206 (2012) 3839-3850.
- [61] S.S. Chatha, H.S. Sidhu, B.S. Sidhu, The effects of post-treatment on the hot corrosion behavior of the HVOF-sprayed Cr₃C₂-NiCr coating, *Surface and Coatings Technology*, 206 (2012) 4212-4224.
- [62] Z. Dong, X. Peng, Y. Guan, L. Li, F. Wang, Optimization of composition and structure of electrodeposited Ni-Cr composites for increasing the oxidation resistance, *Corrosion Science*, 62 (2012) 147-152.
- [63] L. Reclaru, R.E. Unger, C.J. Kirkpatrick, C. Susz, P.Y. Eschler, M.H. Zuercher, I. Antoniac, H. Lüthy, Ni-Cr based dental alloys; Ni release, corrosion and biological evaluation, *Materials Science and Engineering: C*, 32 (2012) 1452-1460.
- [64] M.I. Solonin, A.B. Alekseev, Y.I. Kazennov, V.F. Khramtsov, V.P. Kondrat'ev, T.A. Krasina, V.N. Rechitsky, V.N. Stepankov, S.N. Votinov, XHM-1 alloy as a promising structural material for water-cooled fusion reactor components, *Journal of Nuclear Materials*, 233-237 (1996) 586-591.
- [65] M.I. Solonin, A.B. Alekseev, S.A. Averin, Y.A. Burenkov, V.M. Chernov, B.K. Kardashev, V.P. Kondrat'ev, A.V. Kozlov, V.N. Rechitsky, S.N. Votinov, Cr-Ni alloys for fusion reactors, *Journal of Nuclear Materials*, 258-263 (1998) 1762-1766.
- [66] I. Betova, M. Bojinov, T. Tzvetkoff, Oxidative dissolution and anion-assisted solubilisation in the transpassive state of nickel-chromium alloys, *Electrochimica Acta*, 49 (2004) 2295-2306.
- [67] N. Saito, I. Nakaaki, H. Iwata, K. Nishioka, Structural and electrical properties of Ni-Cr oxide films prepared by magnetron sputtering, *Thin Solid Films*, 520 (2012) 3031-3034.
- [68] N. Bala, H. Singh, S. Prakash, High-temperature oxidation studies of cold-sprayed Ni-20Cr and Ni-50Cr coatings on SAE 213-T22 boiler steel, *Applied Surface Science*, 255 (2009) 6862-6869.
- [69] I. Cvijovic, M.T. Jovanovic, D. Perusko, Cyclic oxidation behaviour of Ti₃Al-based alloy with Ni-Cr protective layer, *Corrosion Science*, 50 (2008) 1919-1925.
- [70] N. Bala, H. Singh, S. Prakash, Accelerated hot corrosion studies of cold spray Ni-50Cr coating on boiler steels, *Materials & Design*, 31 (2010) 244-253.
- [71] T.S. Sidhu, S. Prakash, R.D. Agrawal, Hot corrosion performance of a NiCr coated Ni-based alloy, *Scripta Materialia*, 55 (2006) 179-182.
- [72] K. Yamada, Y. Tomono, J. Morimoto, Y. Sasaki, A. Ohmori, Hot corrosion behavior of boiler tube materials in refuse incineration environment, *Vacuum*, 65 (2002) 533-540.
- [73] M.F. Morks, C.C. Berndt, Corrosion and oxidation properties of NiCr coatings sprayed in presence of gas shroud system, *Applied Surface Science*, 256 (2010) 4322-4327.
- [74] A. Mitsuhashi, K. Asami, A. Kawashima, K. Hashimoto, The corrosion behavior of amorphous nickel base alloys in a hot concentrated phosphoric acid, *Corrosion Science*, 27 (1987) 957-970.

- [75] M. Bojinov, T. Tzvetkoff, The Influence of Solution Anion on the Mechanism of Transpassive Dissolution of Ferrous- and Nickel-Based Alloys, *Journal of Physical Chemistry B*, 107 (2003) 5101-5112.
- [76] N. Shigeto, T. Yanagihara, T. Hamada, E. Budtz-Jørgensen, Corrosion properties of soldered joints. Part I: Electrochemical action of dental solder and dental nickel-chromium alloy, *The Journal of Prosthetic Dentistry*, 62 (1989) 512-515.
- [77] V.S. Saji, H.-C. Choe, Electrochemical behavior of Co-Cr and Ni-Cr dental cast alloys, *Transactions of Nonferrous Metals Society of China*, 19 (2009) 785-790.
- [78] M. Sharma, A.V.R. Kumar, N. Singh, Electrochemical corrosion behaviour of dental/implant alloys in saline medium, *Journal of Materials Science - Materials in Medicine*, 19 (2008) 2647-2653.
- [79] J. Geis-Gerstorfer, H. Weber, In vitro corrosion behavior of four Ni-Cr dental alloys in lactic acid and sodium chloride solutions, *Dental Materials*, 3 (1987) 289-295.
- [80] S. Viswanathan, H. Choe, Preferential dissolution behaviour in Ni-Cr dental cast alloy, *Bulletin of Materials Science*, 33 (2010) 463-468.
- [81] P. Nash, Phase Diagrams of Binary Nickel Alloys, in, ASM International (USA), Materials Park, OH, 1991, pp. 75-84.
- [82] C. Sârbu, Ra, S.A. u, N. Popescu-Pogrion, M.I. Bîrjega, The structure of flash-evaporated Cr---Ni (65:35) and Cr---Ni (50:50) thin films, *Thin Solid Films*, 28 (1975) 311-322.
- [83] M.B. Vollaro, D.I. Potter, Phase formation in coevaporated Ni---Cr thin films, *Thin Solid Films*, 239 (1994) 37-46.
- [84] M.I. Bîrjega, N. Popescu-Pogrion, C. Sarbu, S. Râu, Metastable phases in vacuum-evaporated Cr-Ni thin films, *Thin Solid Films*, 34 (1976) 153-155.
- [85] M.I. Bîrjega, C.A. Constantin, I.T. Florescu, C. Sârbu, Crystallization of amorphous sputtered 55%Cr-45%Ni thin films, *Thin Solid Films*, 92 (1982) 315-322.
- [86] M. Danisman, N. Cansever, Effect of Cr content on mechanical and electrical properties of Ni-Cr thin films, *Journal of Alloys and Compounds*, 493 (2008) 649-653.
- [87] J. Saaedi, T.W. Coyle, S. Mirdamadi, H. Arabi, J. Mostaghimi, Phase formation in a Ni-50Cr HVOF coating, *Surface and Coatings Technology*, 202 (2008) 5804-5811.
- [88] S. Vinayak, H.P. Vyas, V.D. Vankar, Microstructure and electrical characteristics of Ni-Cr thin films, *Thin Solid Films*, 515 (2007) 7109-7116.
- [89] P. Mengucci, M. Costato, G. Majni, Substrate effect on texturized microstructures in Ni---Cr thin films, *Thin Solid Films*, 209 (1992) 67-72.
- [90] L. Lassak, K. Hieber, Structural and electrical properties of evaporated Cr-Ni films as a function of gas pressure, *Thin Solid Films*, 17 (1973) 105-111.
- [91] N. Saunders, A.P. Miodownik, The use of free energy vs composition curves in the prediction of phase formation in codeposited alloy thin films, *Calphad*, 9 (1985) 283-290.
- [92] R.M. Krishnan, C.J. Kennedy, S. Jayakrishnan, S. Sriveeraraghavan, S.R. Natarajan, P.G. Venkatakrishnan, Electrodeposition of nickel-tungsten alloys, *Metal Finishing*, 93 (1995) 33-39.
- [93] H. Wang, R. Liu, F. Cheng, Y. Cao, G. Ding, X. Zhao, Electrodepositing amorphous Ni-W alloys for MEMS, *Microelectronic Engineering*, 87 (2010) 1901-1906.

Bibliography

- [94] A. Chianpairot, G. Lothongkum, C.A. Schuh, Y. Boonyongmaneerat, Corrosion of nanocrystalline Ni-W alloys in alkaline and acidic 3.5 wt.% NaCl solutions, *Corrosion Science*, 53 (2011) 1066-1071.
- [95] H. Alimadadi, M. Ahmadi, M. Aliofkhaezai, S.R. Younesi, Corrosion properties of electrodeposited nanocrystalline and amorphous patterned Ni-W alloy, *Materials & Design*, 30 (2009) 1356-1361.
- [96] K.R. Sriraman, S.G.S. Raman, S.K. Seshadri, Corrosion behaviour of electrodeposited nanocrystalline Ni-W and Ni-Fe-W alloys, *Materials Science and Engineering: A*, 460-461 (2007) 39-45.
- [97] P. de Lima-Neto, A.N. Correia, R.A.C. Santana, R.P. Colares, E.B. Barros, P.N.S. Casciano, G.L. Vaz, Morphological, structural, microhardness and electrochemical characterisations of electrodeposited Cr and Ni-W coatings, *Electrochimica Acta*, 55 (2010) 2078-2086.
- [98] S. Yao, S. Zhao, H. Guo, M. Kowaka, A new amorphous alloy deposit with high corrosion resistance, *Corrosion*, 52 (1996) 183-186.
- [99] A.J. Detor, C.A. Schuh, Grain boundary segregation, chemical ordering and stability of nanocrystalline alloys: Atomistic computer simulations in the Ni-W system, *Acta Materialia*, 55 (2007) 4221-4232.
- [100] M.F. Morks, N.F. Fahim, A. Kobayashi, Microstructure, corrosion behavior, and microhardness of plasma-sprayed W-Ni composite coatings, *Journal of Manufacturing Processes*, 10 (2008) 6-11.
- [101] M. Metikos-Hukovic, Z. Grubac, N. Radic, A. Tonejc, Sputter deposited nanocrystalline Ni and Ni-W films as catalysts for hydrogen evolution, *Journal of Molecular Catalysis A: Chemical*, 249 (2006) 172-180.
- [102] Y. Yao, S. Yao, L. Zhang, H. Wang, Electrodeposition and mechanical and corrosion resistance properties of Ni-W/SiC nanocomposite coatings, *Materials Letters*, 61 (2007) 67-70.
- [103] C. Borgia, T. Scharowsky, A. Furrer, C. Solenthaler, R. Spolenak, A combinatorial study on the influence of elemental composition and heat treatment on the phase composition, microstructure and mechanical properties of Ni-W alloy thin films, *Acta Materialia*, 59 (2011) 386-399.
- [104] ASM Handbook, Alloy Phase Diagrams, Metals Park OH, 1992.
- [105] T. Yamasaki, P. Schloßmacher, K. Ehrlich, Y. Ogino, Formation of amorphous electrodeposited Ni-W alloys and their nanocrystallization, *Nanostructured Materials*, 10 (1998) 375-388.
- [106] B.L. Mordike, T. Ebert, Magnesium: Properties — applications — potential, *Materials Science and Engineering: A*, 302 (2001) 37-45.
- [107] F. Witte, I. Abeln, E. Switzer, V. Kaese, A. Meyer-Lindenberg, H. Windhagen, Evaluation of the skin sensitizing potential of biodegradable magnesium alloys, *Journal of Biomedical Materials Research Part A*, 86A (2008) 1041-1047.
- [108] W. Frank, The history of biodegradable magnesium implants: A review, *Acta Biomaterialia*, 6 (2010) 1680-1692.
- [109] M. Pourbaix, Atlas of electrochemical equilibria in aqueous solution, Cebelcor, Houston, 1974.
- [110] W.S. Miller, L. Zhuang, J. Bottema, A.J. Wittebrood, P. De Smet, A. Haszler, A. Vieregge, Recent development in aluminium alloys for the automotive industry, *Materials Science and Engineering: A*, 280 (2000) 37-49.
- [111] G.M. Scamans, N.J.H. Holroyd, C.D.S. Tuck, The role of magnesium segregation in the intergranular stress corrosion cracking of aluminium alloys, *Corrosion Science*, 27 (1987) 329-347.
- [112] J.J. Burton, E.S. Machlin, Prediction of Segregation to Alloy Surfaces from Bulk Phase Diagrams, *Physical Review Letters*, 37 (1976) 1433-1436.

- [113] P. Doig, J.W. Edington, Stress Corrosion Susceptibility of As-Quenched Al-5.9 wt-% Zn-3.2 wt-% Mg Alloy, *British Corrosion Journal*, 9 (1974) 220-222.
- [114] D.R. Baer, J.C.F. Windisch, M.H. Engelhard, M.J. Danielson, R.H. Jones, J.S. Vetrano, Influence of Mg on the corrosion of Al, *Journal of Vacuum Science & Technology A: Vacuum, Surfaces, and Films*, 18 (2000) 131-136.
- [115] K. Urushino, K. Sugimoto, Stress-corrosion cracking of aged Al-Cu-Mg alloys in NaCl solution, *Corrosion Science*, 19 (1979) 225-236.
- [116] J.A. Lyndon, R.K. Gupta, M.A. Gibson, N. Birbilis, Electrochemical behaviour of the β -phase intermetallic (Mg_2Al_3) as a function of pH as relevant to corrosion of aluminium-magnesium alloys, *Corrosion Science*, 70 (2013) 290-293.
- [117] S. Lin, Z. Nie, H. Huang, B. Li, Annealing behavior of a modified 5083 aluminum alloy, *Materials & Design*, 31 (2010) 1607-1612.
- [118] R.H. Jones, Vetrano, J. S. , and Windisch, C. F., Stress Corrosion Cracking of Al-Mg and Mg-Al Alloys., *Corrosion*, 60 (2004) 1144-1154.
- [119] Y.-l. Cheng, T.-w. Qin, H.-m. Wang, Z. Zhang, Comparison of corrosion behaviors of AZ31, AZ91, AM60 and ZK60 magnesium alloys, *Transactions of Nonferrous Metals Society of China*, 19 (2009) 517-524.
- [120] A. Pardo, M.C. Merino, A.E. Coy, F. Viejo, R. Arrabal, S. Feliú Jr, Influence of microstructure and composition on the corrosion behaviour of Mg/Al alloys in chloride media, *Electrochimica Acta*, 53 (2008) 7890-7902.
- [121] L. Zhu, G. Song, Improved corrosion resistance of AZ91D magnesium alloy by an aluminium-alloyed coating, *Surface and Coatings Technology*, 200 (2006) 2834-2840.
- [122] G. Song, A. Atrens, X. Wu, B. Zhang, Corrosion behaviour of AZ21, AZ501 and AZ91 in sodium chloride, *Corrosion Science*, 40 (1998) 1769-1791.
- [123] S. Mathieu, C. Rapin, J. Hazan, P. Steinmetz, Corrosion behaviour of high pressure die-cast and semi-solid cast AZ91D alloys, *Corrosion Science*, 44 (2002) 2737-2756.
- [124] S. Mathieu, C. Rapin, J. Steinmetz, P. Steinmetz, A corrosion study of the main constituent phases of AZ91 magnesium alloys, *Corrosion Science*, 45 (2003) 2741-2755.
- [125] A.D. Sudholz, N.T. Kirkland, R.G. Buchheit, N. Birbilis, Electrochemical Properties of Intermetallic Phases and Common Impurity Elements in Magnesium Alloys, *Electrochemical and Solid-State Letters*, 14 (2011) C5-C7.
- [126] M.C. Merino, A. Pardo, R. Arrabal, S. Merino, P. Casajús, M. Mohedano, Influence of chloride ion concentration and temperature on the corrosion of Mg-Al alloys in salt fog, *Corrosion Science*, 52 (2010) 1696-1704.
- [127] M. He, L. Liu, Y. Wu, C. Zhong, W. Hu, Influence of microstructure on corrosion properties of multilayer Mg-Al intermetallic compound coating, *Corrosion Science*, 53 (2011) 1312-1321.
- [128] S. Bender, J. Goellner, A. Heyn, S. Schmigalla, A new theory for the negative difference effect in magnesium corrosion, *Materials and Corrosion*, (2011) n/a-n/a.
- [129] J. Chen, J. Dong, J. Wang, E. Han, W. Ke, Effect of magnesium hydride on the corrosion behavior of an AZ91 magnesium alloy in sodium chloride solution, *Corrosion Science*, 50 (2008) 3610-3614.
- [130] G.G. Perrault, The potential-pH diagram of the magnesium-water system, *Journal of Electroanalytical Chemistry and Interfacial Electrochemistry*, 51 (1974) 107-119.
- [131] E. Gulbrandsen, Anodic behaviour of Mg in HCO_3^-/CO_3^{2-} buffer solutions. Quasi-steady measurements, *Electrochimica Acta*, 37 (1992) 1403-1412.

Bibliography

- [132] G. Song, A. Atrens, D. StJohn, J. Nairn, Y. Li, The electrochemical corrosion of pure magnesium in 1 N NaCl, *Corrosion Science*, 39 (1997) 855-875.
- [133] G. Baril, N. Pébère, The corrosion of pure magnesium in aerated and deaerated sodium sulphate solutions, *Corrosion Science*, 43 (2001) 471-484.
- [134] S. Bender, J. Goellner, A. Atrens, Corrosion of AZ91 in 1N NaCl and the Mechanism of Magnesium Corrosion, *Advanced Engineering Materials*, 10 (2008) 583-587.
- [135] G. Song, A. Atrens, Recent Insights into the Mechanism of Magnesium Corrosion and Research Suggestions, *Advanced Engineering Materials*, 9 (2007) 177-183.
- [136] G. Williams, H.N. McMurray, Localized Corrosion of Magnesium in Chloride-Containing Electrolyte Studied by a Scanning Vibrating Electrode Technique, *Journal of The Electrochemical Society*, 155 (2008) C340-C349.
- [137] J. Światowska, P. Volovitch, K. Ogle, The anodic dissolution of Mg in NaCl and Na₂SO₄ electrolytes by atomic emission spectroelectrochemistry, *Corrosion Science*, 52 (2010) 2372-2378.
- [138] G.L. Makar, J. Kruger, Corrosion Studies of Rapidly Solidified Magnesium Alloys, *Journal of The Electrochemical Society*, 137 (1990) 414-421.
- [139] J. Murray, The Al-Mg (Aluminum-Magnesium) system, *Bulletin of Alloy Phase Diagrams*, 3 (1982) 60-74.
- [140] K.F. Kobayashi, T. Awazu, P.H. Shingu, New metastable phases in the Al-Mg system, *Journal of Materials Science Letters*, 6 (1987) 781-783.
- [141] C.H. Olk, D.B. Haddad, Growth and structure of a combinatorial array of mixed-phase magnesium-aluminum thin-film alloys, *Appl. Phys. A-Mater. Sci. Process.*, 88 (2007) 249-253.
- [142] S. Scudino, S. Sperling, M. Sakaliyska, C. Thomas, M. Feuerbacher, K.B. Kim, H. Ehrenberg, J. Eckert, Phase transformations in mechanically milled and annealed single-phase β -Al₃Mg₂, *Acta Materialia*, 56 (2008) 1136-1143.
- [143] E. Hajjari, M. Divandari, S.H. Razavi, T. Homma, S. Kamado, Intermetallic compounds and antiphase domains in Al/Mg compound casting, *Intermetallics*, 23 (2012) 182-186.
- [144] M.X. Zhang, H. Huang, K. Spencer, Y.N. Shi, Nanomechanics of Mg-Al intermetallic compounds, *Surface and Coatings Technology*, 204 (2010) 2118-2122.
- [145] A.S. El-Amoush, An X-ray investigation of hydrogenated Mg-30Al magnesium alloy, *Journal of Alloys and Compounds*, 441 (2007) 278-283.
- [146] K. Spencer, M.X. Zhang, Heat treatment of cold spray coatings to form protective intermetallic layers, *Scripta Materialia*, 61 (2009) 44-47.
- [147] H.L. Su, M. Harmelin, P. Donnadieu, C. Baetzner, H.J. Seifert, H.L. Lukas, G. Effenberg, F. Aldinger, Experimental investigation of the Mg-Al phase diagram from 47 to 63 at.% Al, *Journal of Alloys and Compounds*, 247 (1997) 57-65.
- [148] Y. Tamura, N. Kono, T. Motegi, E. Sato, Grain refining mechanism and casting structure of Mg-Zr alloy, *Japan Institute of Light Metals, Journal*, 48 (1998) 185-189.
- [149] G. Song, Recent progress in corrosion and protection of magnesium alloys, *Advanced Engineering Materials*, 7 (2005) 563-586.
- [150] G. Song, D. StJohn, The effect of zirconium grain refinement on the corrosion behaviour of magnesium-rare earth alloy MEZ, *Journal of Light Metals*, 2 (2002) 1-16.

- [151] E. Juzeliūnas, A. Grigučevičienė, K. Leinartas, R. Juškėnas, Sputter deposited Mg-Al-Zr alloys – structure, surface morphology and anodic activity, *Electrochemistry Communications*, 6 (2004) 678-682.
- [152] A. Grigučevičienė, K. Leinartas, R. Juškėnas, E. Juzeliūnas, Structure and initial corrosion resistance of sputter deposited nanocrystalline Mg-Al-Zr alloys, *Materials Science and Engineering: A*, 394 (2005) 411-416.
- [153] H. Yoshioka, H. Habazaki, A. Kawashima, K. Asami, K. Hashimoto, The corrosion behavior of sputter-deposited Al-Zr alloys in 1 M HCl solution, *Corrosion Science*, 33 (1992) 425-436.
- [154] H. Yoshioka, H. Habazaki, A. Kawashima, K. Asami, K. Hashimoto, Anodic polarization behaviour of sputter-deposited Al-Zr alloys in a neutral chloride-containing buffer solution, *Electrochimica Acta*, 36 (1991) 1227-1233.
- [155] H. Yoshioka, Q. Yan, H. Habazaki, A. Kawashima, K. Asami, K. Hashimoto, Passivity and its breakdown on sputter-deposited amorphous Al-early transition metal alloys in 1 M HCl at 30°C, *Corrosion Science*, 31 (1990) 349-354.
- [156] A. Johansen, MICROSTRUCTURES AND PROPERTIES OF ALUMINIUM-MAGNESIUM ALLOYS WITH ADDITIONS OF MANGANESE, ZIRCONIUM AND SCANDIUM . in, *The Norwegian University of Science and Technology (NTNU)*, 2000, pp. 230.
- [157] Al-Mg-Zr (Aluminium - Magnesium - Zirconium), in: G. Effenberg, S. Ilyenko (Eds.) *Light Metal Systems. Part 3*, Springer Berlin Heidelberg, 2005, pp. 1-5.
- [158] G. Garcés, M.C. Cristina, M. Torralba, P. Adeva, Texture of magnesium alloy films growth by physical vapour deposition (PVD), *Journal of Alloys and Compounds*, 309 (2000) 229-238.
- [159] H. Okamoto, Al-Zr (Aluminum-Zirconium), *JPE*, 23 (2002) 455-456.
- [160] J. Murray, A. Peruzzi, J.P. Abriata, The Al-Zr (aluminum-zirconium) system, *JPE*, 13 (1992) 277-291.
- [161] N. Saunders, V.G. Rivlin, Thermodynamic characterization of Al-Cr, Al-Zr, and Al-Cr-Zr alloy systems, *Materials Science and Technology*, 2 (1986) 520-527.
- [162] T. Wang, Z. Jin, J.-C. Zhao, Thermodynamic assessment of the Al-Zr binary system, *JPE*, 22 (2001) 544-551.
- [163] R.J. Kematich, H.F. Franzen, Thermodynamic study of the zirconium-aluminum system, *Journal of Solid State Chemistry*, 54 (1984) 226-234.
- [164] L.-E. Edshammar, Crystal Structure Investigations on the Zr-Al and Hf-Al Systems., *Acta Chemica Scandinavica*, 16 (1962) 20-30.
- [165] M.P.a.K. Schubert, On the Construction of Some“ T4-B3 Homologous and Quasihomologous Systems. II. The Ti-Al, Zr-Al, Hf-Al, Mo-Al and Some Ternary Systems., *Z. Metallkd*, 53 (1962) 548-561
- [166] J.C. Schuster, J. Bauer, J. Debuigne, Investigation of phase equilibria related to fusion reactor materials: I. The ternary system Zr-Al-Nn, *Journal of Nuclear Materials*, 116 (1983) 131-135.
- [167] S.J. Kim, R.J. Kematich, S.S. Yi, H.F. Franzen, On the stabilization of Zr₅Al₃ in the Mn₅Si₃-type structure by interstitial oxygen, *Journal of the Less Common Metals*, 137 (1988) 55-59.
- [168] R.J. Knize, J.L. Cecchi, H.F. Dylla, Compatibility of the Zr-Al alloy with a tokamak plasma environment, *Journal of Nuclear Materials*, 103 (1981) 539-543.
- [169] N.J. Clark, E. Wu, Hydrogen absorption by M₅X₃ phase Zr-Al compounds, *Journal of the Less Common Metals*, 142 (1988) 145-154.

Bibliography

- [170] S. Guerin, B.E. Hayden, Physical vapor deposition method for the high-throughput synthesis of solid-state material libraries, *Journal of Combinatorial Chemistry*, 8 (2006) 66-73.
- [171] M. Stern, Wiesert, E. D., Experimental observations on the relation between polarization resistance and corrosion rate, *ASTM proceedings*, American society for testing and materials, 59 (1959) 1280.
- [172] R. ICPDS card No. 040850, Swanson, Tatge, *Natl. Bur. Stand.(US), Cir. 539*, 1,13 (1953), (1953).
- [173] A. Belu-Marian, R. Mănăilă, G. Korony, C. Constantin, A. Devenyi, Electrical properties and structural defects of Ni-Cr thin films, *Thin Solid Films*, 139 (1986) 15-24.
- [174] JCPDS, International Centre for Diffraction Data, PDF#00-051-0637 (2005).
- [175] JCPDS, International Centre for Diffraction Data, PDF#510637 (1983).
- [176] JCPDS, International Centre for Diffraction Data, PDF# 060694 (1955).
- [177] C.M. Wylie, R.M. Shelton, G.J.P. Fleming, A.J. Davenport, Corrosion of nickel-based dental casting alloys, *Dental Materials*, 23 (2007) 714-723.
- [178] J. R.Scully, *Encyclopedia of Electrochemistry*, Wiley-VCH Verlag GmbH & Co. KGaA., 2007.
- [179] V.Z. Lev, Mechanism of the intergranular corrosion of cast nickel-chromium-molybdenum alloy, *Chem Petrol Eng*, 12 (1976) 429-431.
- [180] S. Jain, N.D. Budiansky, J.L. Hudson, J.R. Scully, Surface spreading of intergranular corrosion on stainless steels, *Corrosion Science*, 52 (2010) 873-885.
- [181] N.S. Zadorozne, C.M. Giordano, M.A. Rodríguez, R.M. Carranza, R.B. Rebak, Crevice corrosion kinetics of nickel alloys bearing chromium and molybdenum, *Electrochimica Acta*, 76 (2012) 94-101.
- [182] P. Los, A. Rami, A. Lasia, Hydrogen evolution reaction on Ni-Al electrodes, *Journal of Applied Electrochemistry*, 23 (1993) 135-140.
- [183] J.H. Potgieter, P.A. Olubambi, L. Cornish, C.N. Machio, E.-S.M. Sherif, Influence of nickel additions on the corrosion behaviour of low nitrogen 22% Cr series duplex stainless steels, *Corrosion Science*, 50 (2008) 2572-2579.
- [184] A.C. Lloyd, J.J. Noël, S. McIntyre, D.W. Shoesmith, Cr, Mo and W alloying additions in Ni and their effect on passivity, *Electrochimica Acta*, 49 (2004) 3015-3027.
- [185] H.-H. Huang, Effect of chemical composition on the corrosion behavior of Ni-Cr-Mo dental casting alloys, *Journal of Biomedical Materials Research*, 60 (2002) 458-465.
- [186] Y. Wu, D. Chang, D. Kim, S.-C. Kwon, Influence of boric acid on the electrodepositing process and structures of Ni-W alloy coating, *Surface and Coatings Technology*, 173 (2003) 259-264.
- [187] E. Navarro-Flores, Z. Chong, S. Omanovic, Characterization of Ni, NiMo, NiW and NiFe electroactive coatings as electrocatalysts for hydrogen evolution in an acidic medium, *Journal of Molecular Catalysis A: Chemical*, 226 (2005) 179-197.
- [188] C.H. Lee, K.O. Min, Effects of heat treatment on the microstructure and properties of HVOF-sprayed Ni-Cr-W-Mo-B alloy coatings, *Surface and Coatings Technology*, 132 (2000) 49-57.
- [189] S.R. Biaggio, R.C. Rocha-Filho, J.R. Vilche, F.E. Varela, L.M. Gassa, A study of thin anodic WO₃ films by electrochemical impedance spectroscopy, *Electrochimica Acta*, 42 (1997) 1751-1758.
- [190] D. Vernardou, H. Drosos, E. Spanakis, E. Koudoumas, N. Katsarakis, M.E. Pemble, Electrochemical properties of amorphous WO₃ coatings grown on

- polycarbonate by aerosol-assisted CVD, *Electrochimica Acta*, 65 (2012) 185-189.
- [191] M. Anik, K. Osseo-Asare, Effect of pH on the Anodic Behavior of Tungsten, *Journal of The Electrochemical Society*, 149 (2002) B224-B233.
- [192] M. Anik, Effect of concentration gradient on the anodic behavior of tungsten, *Corrosion Science*, 48 (2006) 4158-4173.
- [193] H. Zheng, J.Z. Ou, M.S. Strano, R.B. Kaner, A. Mitchell, K. Kalantar-zadeh, Nanostructured Tungsten Oxide – Properties, Synthesis, and Applications, *Advanced Functional Materials*, 21 (2011) 2175-2196.
- [194] S.K. Gullapalli, R.S. Vemuri, C.V. Ramana, Structural transformation induced changes in the optical properties of nanocrystalline tungsten oxide thin films, *Applied Physics Letters*, 96 (2010) 171903-171903.
- [195] JCPDS, International Centre for Diffraction Data, PDF# 00-035-0821 (1984).
- [196] N. Saunders, A review and thermodynamic assessment of the Al-Mg and Mg-Li systems, *Calphad*, 14 (1990) 61-70.
- [197] D. Singh, C. Suryanarayana, L. Mertus, R.H. Chen, Extended homogeneity range of intermetallic phases in mechanically alloyed Mg-Al alloys, *Intermetallics*, 11 (2003) 373-376.
- [198] D. Mukherjee, V. Ande, R. Manna, B.S. Murty, N.K. Mukhopadhyay, Formation of nanostructured and amorphous β -Al₃Mg₂ based alloys by rapid solidification and mechanical milling, *Materials Science and Engineering: A*, 527 (2010) 5078-5083.
- [199] T. Zhang, Y. Li, F. Wang, Roles of β phase in the corrosion process of AZ91D magnesium alloy, *Corrosion Science*, 48 (2006) 1249-1264.
- [200] JCPDS, International Centre for Diffraction Data, PDF# 01-073-8026 (2010).
- [201] JCPDS, International Centre for Diffraction Data, PDF# 01-072-9258 (2010).
- [202] JCPDS, International Centre for Diffraction Data, PDF# 03-065-1431 (2005).
- [203] JCPDS, International Centre for Diffraction Data, PDF# 00-048-1382 (1996).
- [204] JCPDS, International Centre for Diffraction Data, PDF# 00-048-1379 (1996).
- [205] JCPDS, International Centre for Diffraction Data, PDF# 01-071-9629 (2010).
- [206] JCPDS, International Centre for Diffraction Data, PDF# 01-078-2921 (2010).
- [207] D.J.M. Phersons, M. Hansen, The system Zr-Al, *Transactions ASM*, 46 (1954) 354-374.
- [208] H.J. Fecht, G. Han, Z. Fu, W.L. Johnson, Metastable phase formation in the Zr-Al binary system induced by mechanical alloying, *Journal of Applied Physics*, 67 (1990) 1744-1748.
- [209] T.A. Aljohani, B.E. Hayden, A. Anastasopoulos, The high throughput electrochemical screening of the corrosion resistance of Ni-Cr thin film alloys, *Electrochimica Acta*, 76 (2012) 389-393.
- [210] N. Al-Aqeeli, G. Mendoza-Suarez, A. Labrie, R.A.L. Drew, Phase evolution of Mg-Al-Zr nanophase alloys prepared by mechanical alloying, *Journal of Alloys and Compounds*, 400 (2005) 96-99.